

Cover Page



Universiteit Leiden



The handle <http://hdl.handle.net/1887/39392> holds various files of this Leiden University dissertation

Author: Engels, Marc Christian

Title: Cellular modifications and interventions for the damaged heart

Issue Date: 2016-05-11



**Cellular Modifications and
Interventions for the
Damaged Heart**

Marc C. Engels

Cellular Modifications and Interventions for the Damaged Heart

Marc C. Engels

Colophon

Cellular Modifications and Interventions for the Damaged Heart

Marc C. Engels

The studies described in this thesis were performed at the Laboratory of Experimental Cardiology of the Department of Cardiology of the Leiden University Medical Center, Leiden, the Netherlands, and the Cardiovascular Research Center of the Massachusetts General Hospital, Boston, MA, U.S.A.

Copyright © 2016 Marc C. Engels

All rights reserved. No parts of this thesis may be reproduced, stored in a retrieval system of any nature or transmitted in any form or by any means, photocopied, recorded or otherwise, without prior written permission of the author, or when appropriate, the publishers of the papers.

ISBN: 978-90-9029675-3

Support: The research described in this thesis was supported by the Netherlands Organization for Scientific Research (NWO) through a Mosaic grant (017.007.064).

Cover: Deirdre Waski

Lay-out and printed by: Gildeprint, Enschede, the Netherlands

Cellular Modifications and Interventions for the Damaged Heart

Proefschrift

ter verkrijging van
de graad van Doctor aan de Universiteit Leiden,
op gezag van Rector Magnificus prof. mr. C.J.J.M. Stolker,
volgens besluit van het College voor Promoties
te verdedigen op woensdag 11 mei 2016
klokke 16:15 uur

door

Marc Christian Engels
geboren te Willemstad, Curaçao
in 1984

Promotor:

Prof. dr. M.J. Schalijs

Co-Promotores:

Dr. D.A. Pijnappels

Dr. A.A.F. de Vries

Promotiecommissie:

Prof. dr. D.E. Atsma

Prof. dr. V.M. Christoffels (Universiteit van Amsterdam)

Dr. S.M. Wu (Stanford University, Stanford, CA, U.S.A.)

Prof. Dr. K. Zeppenfeld

Stay hungry. Stay foolish.

-Steve Jobs (excerpt from Stanford commencement address, 12 June 2005)

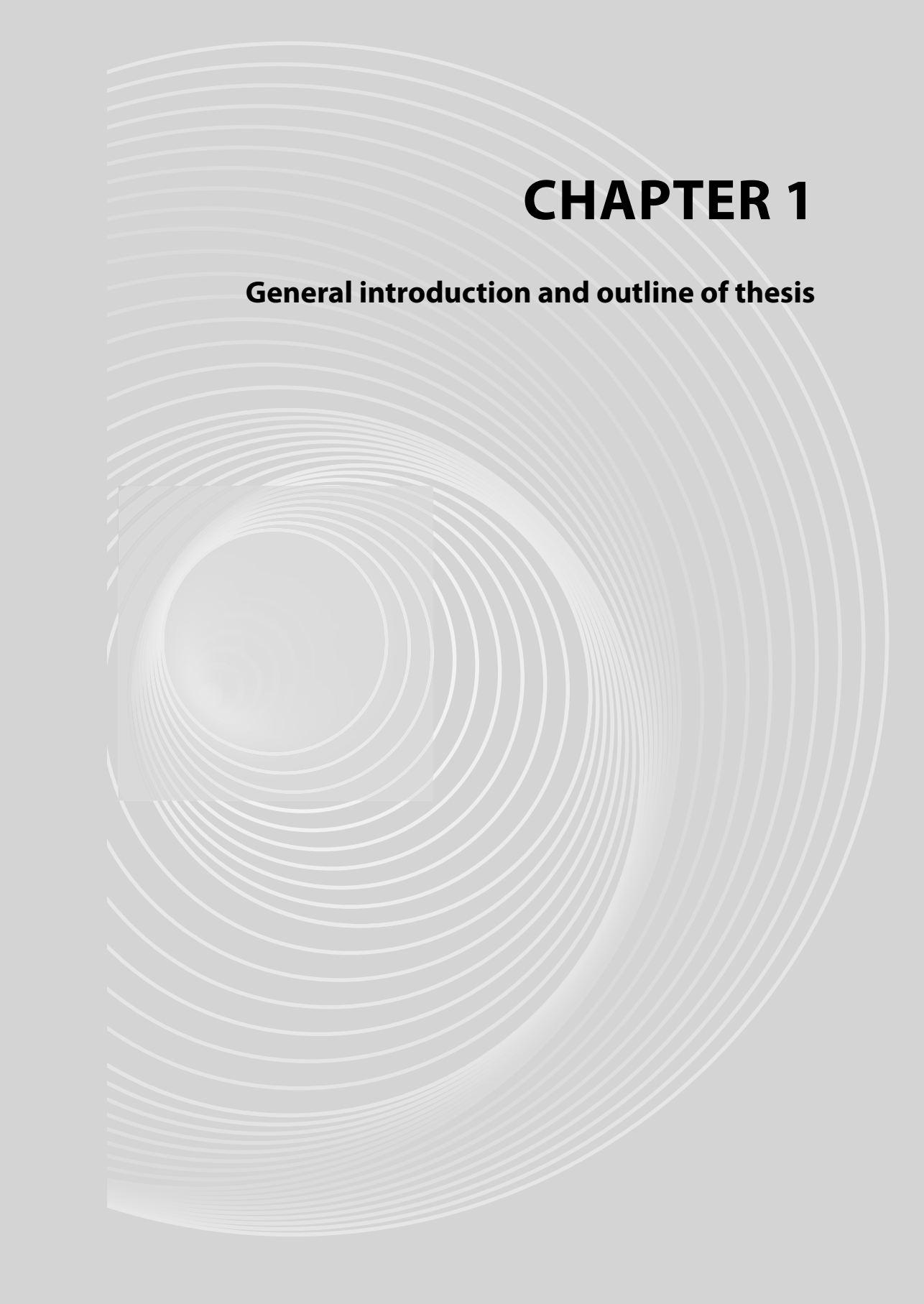
In loving memory of my grandparents

To my parents

For Becca

Contents

Chapter 1	General introduction and outline of thesis	9
Chapter 2	Reprogramming of mouse, rat, pig, and human fibroblasts into iPS cells Rajarajan K, Engels MC, Wu SM Current Protocols in Molecular Biology 2012;Chapter 23:Unit 23.15	25
Chapter 3	Insulin-like growth factor promotes cardiac lineage induction in vitro by selective expansion of early mesoderm Engels MC, Rajarajan K, Feistritz R, Sharma A, Nielsen UB, Schalij MJ, de Vries AA, Pijnappels DA, Wu SM Stem Cells 2014;32:1493-1502	67
Chapter 4	Forced fusion of human ventricular scar cells with cardiomyocytes suppresses arrhythmogenicity in a co-culture model Engels MC, Askar SF, Jangsangthong W, Bingen BO, Feola I, Liu J, Majumder R, Versteegh MI, Braun J, Klautz RJ, Ypey DL, De Vries AA, Pijnappels DA Cardiovascular Research 2015;107:601-612	93
Chapter 5	Islands of spatially discordant APD alternans underlie arrhythmogenesis by promoting electrotonic dyssynchrony in models of fibrotic rat ventricular myocardium Engels MC, Majumder R, de Vries AA, Panfilov AV, Pijnappels DA Scientific Reports 2016;6:24334	131
Chapter 6	Light-induced termination of spiral wave arrhythmias by optogenetic engineering of atrial cardiomyocytes Bingen BO, Engels MC, Jangsangthong W, Neshati Z, Feola I, Ypey DL, Askar SF, Panfilov AV, Pijnappels DA, de Vries AA Cardiovascular Research 2014;104:194-205	169
Chapter 7	Summary, conclusions and future perspectives	197
	Nederlandse samenvatting	205
	List of Publications	211
	Acknowledgements	213
	Curriculum Vitae	215



CHAPTER 1

General introduction and outline of thesis

Background

The heart is a vital organ, which is of great importance for the maintenance of tissue homeostasis. Millions of years of evolution have culminated in the heart in its current state, a well-orchestrated and efficient pump that supplies the body with nutrient- and oxygen-rich blood. While evolutionarily well-designed, the heart is also a delicate organ with very limited regenerative capacity. This implies that the slightest injury or adverse effect can have serious detrimental outcomes, such as acutely lethal arrhythmias or chronically lethal heart failure. Recent advances in the field of cardiology, such as the development of percutaneous coronary interventional procedures, ventricular assist devices and implantable cardioverter defibrillator devices, have led to major breakthroughs in preventing or limiting the extent of these adverse effects. This has resulted in a drastic lowering of heart disease related mortality and morbidity. Despite of these tremendous developments, cardiovascular disease still has the highest mortality rate worldwide.¹ It is therefore important to continue developing new and improved therapeutic modalities. A promising strategy for treating heart disease is by harnessing the potentials of molecular medicine, such as genetic or cellular therapies.

Normal cardiac function

The adult human heart consist of about five to ten billion cells. These comprise the smallest building blocks, of which the most important cardiac cell types are the cardiac muscle cells (cardiomyocytes), smooth muscle cells, endothelial cells, (myo)fibroblasts, Purkinje fibers, sinoatrial pacemaker cells and atrioventricular nodal cells. Each individual cell type has its unique contribution to normal pump function. In order for the rhythmic contractions to occur, cells need to be electrically activated at the right moment. This allows synchronous mechanical contraction and relaxation to occur in a timely fashion, which is important for optimal and efficient blood movement through the organism. The electrical activation of the heart is a hierarchically structured and coordinated process, which starts in the cardiac pacemaker cells of the sinoatrial node in the right atrium. These nodal cells derive their pacemaker activity from their funny current channels (I_f), an inward current which opens upon hyperpolarization, as well as the sodium-calcium exchanger (NCX) current, which produces a net inward current. These currents contribute to the membrane clock (contribution of ion channels in plasma membrane) and calcium clock (contribution of calcium release from sarcoplasmic reticulum) respectively, which both allow for spontaneous depolarizations, thereby starting the action potential in the heart. From here, the electrical wave is transmitted to the surrounding cardiomyocytes in the atria and reaches the atrioventricular node. This specialized tissue slows down conduction,

allowing sufficient time for full contraction and blood expulsion from atria through the mitral and tricuspid valves into the left and right ventricles, respectively. The action potential then travels through the Purkinje fibers, which consist of specialized cells that rapidly transmit the electrical wave down the His bundles to activate the ventricles. This sequential multistep process culminates in ventricular contraction, propulsion of deoxygenated blood through the pulmonary valve into the pulmonary arteries on the right side of the heart, and oxygenated blood through the aortic valve into the aorta on the left side of the heart.

Electrical Wave Propagation

In order for electrical wave propagation to occur, there is an extensive intercellular communication system through gap junctional coupling. These gap junctions form intercellular channels, which, amongst others, allow for electrotonic interaction through low-resistance trafficking of ionic currents from cell to cell. Gap junctions are formed when one hemichannel (i.e. connexon) of one cell is coupled to one hemichannel of an adjacent cell. Connexons consist of an assembly of six proteins of the connexin family. The contributing connexin (Cx) subtypes can vary per connexon, and are spatially organized in the heart, so that each specific cardiac tissue type has its own unique biophysical properties.²⁻⁴ In the human heart, the distribution pattern is mainly (from highest to lowest) Cx43 and Cx45 in the ventricles and Cx40, Cx43 and Cx45 in the atria.^{5,6} Once an activation front reaches an excitable cell, an elaborate mechanism of multiple steps produces an action potential in the cell. This process of excitation consists of five distinct phases. During phase 0, transient depolarization by movement of ionic current through gap junction channels from an adjacent cell activates fast sodium (Na^+) channels, leading to influx of Na^+ ions (I_{Na}) and rapid depolarization. At phase 1, the depolarization is self-limiting as fast Na^+ channels become inactivated and there is transient net outward current of potassium (K^+) and chloride (Cl^-) ions carried by the I_{to} channels. Phase 2 is also known as the plateau phase, as activation of L-type calcium (Ca^{2+}) channels causes inward movement of Ca^{2+} ions, while simultaneously there is a counterbalancing effect of outward K^+ current through K_v channels such as slow delayed rectifier K^+ channels (I_{Ks}), thereby offsetting the effect of the inward movement of Ca^{2+} current. This creates the plateau in the action potential. The high intracellular Ca^{2+} concentration makes Ca^{2+} ions more readily available for Ca^{2+} -binding troponin molecules of the tropomyosin complex in the contraction apparatus of cardiomyocytes. Therefore, it is during this phase (phase 2) that the cell is able to contract. Meanwhile, the NCX channel, as well as Na^+/K^+ -ATPase begin to restore intra- and extracellular ion concentrations. Phase 3 is characterized by the rapid repolarization phase of the action potential, due to inactivation of the Ca^{2+} channels, while I_{Ks} channels remain open. This results in a net outward

positive current, which facilitates a negative change in the membrane potential, so that also other K^+ channels become active, like the rapid delayed rectifier K^+ channels (I_{Kr}) and inwardly rectifying K^+ channels (I_{K1}). This net outward positive current further repolarizes the cell. I_{Kr} channels become inactivated around the membrane potential, while I_{K1} is still conductive through phase 4, thereby establishing resting membrane potential. Meanwhile, ionic pumps like NCX and Na^2+/K^+ -ATPase continue to restore ionic balances corresponding to resting state. Phase 4 is the resting membrane potential, which is maintained by activity of NCX and Na^2+/K^+ -ATPase, as well as I_{K1} . Once a wavefront reaches the cell, electrotonic interaction by means of K^+ entering the cell through gap junction channels causes slight depolarization, thereby activating fast Na^+ channels, and the action potential starts again at phase 0.⁷

Ischemic heart disease

Myocardium is an aerobic tissue, relying almost exclusively on aerobic oxidation for its energy consumption.⁸ Ischemic heart disease is defined by an imbalance between myocardial oxygen demand and supply from the coronary arteries.⁹ A myocardial infarction is a process where an atherosclerotic plaque in a coronary artery ruptures, exposing subendothelial collagen and thrombogenic necrotic material. Thrombocytes rapidly adhere and aggregate to form a platelet thrombus, thereby occluding the vessel lumen. This sudden loss of blood supply to the myocardium leads to rapid cardiomyocyte death, a process which is further aggravated by ischemia reperfusion injury when the vessel is opened.^{10, 11} Cardiomyocytes are a permanent cell type, and possess very limited proliferation capacity, if any, at the adult stage.¹²⁻¹⁶ In the event of injury, tissue integrity is maintained by an inflammatory response, where damaged or deceased cardiomyocytes are replaced by rapidly proliferating cardiac fibroblasts. This is followed by extensive tissue remodelling and myocardial scar formation, consisting of mainly fibrotic tissue.^{17, 18} These changes have detrimental effects on both tissue contractility as well as excitability. As cardiomyocytes are the force-generating units of the heart, replacement of these cells by non-contractile fibroblasts leads to a reduction in contractile force, and thus a decreased ejection fraction. Furthermore, increased tissue stiffness causes diastolic dysfunction and these mechanisms can ultimately lead to heart failure.¹⁹⁻²¹

Cardiac fibrosis also has many detrimental effects from an electrophysiological point of view. The cardiac syncytium, which consists of well-aligned fibers of cardiomyocytes, surrounded by a meshwork of collagen-producing fibroblasts, is normally able to rapidly conduct action potentials over long distances. Cardiac fibroblasts are inexcitable cells and are poorly coupled to their excitable counterparts (*i.e.* cardiomyocytes), at least *in vitro*.²²⁻²⁴ Fibroblasts are not

able to propagate action potentials over large distances.²⁵ Replacement of excitable and well-coupled cardiomyocytes by inexcitable and poorly-coupled fibroblasts therefore creates disruptions in the cardiac syncytium, which becomes interrupted by poorly aligned and poorly conducting cells. This causes asynchronous and inefficient electrical impulse propagation.²⁶ Ultimately, these effects cause conduction slowing and unidirectional block, which increases the likelihood of re-entrant activity.^{24, 27-29}

Ischemic injury is associated with a massive inflammatory response, which activates cardiac fibroblast proliferation and differentiation. A fibroblastic cell subset transdifferentiates to a myofibroblast phenotype, due to certain pro-inflammatory signalling, such as the TGF beta pathway.^{30, 31} These myofibroblasts mimic certain features of cardiomyocytes, such as having a contractile apparatus and expressing smooth muscle actin stress fibers. In addition, myofibroblasts have more abundant expression of connexins, which enable them to better couple to their surrounding cardiomyocytes.³² However, this compensatory mechanism is to a great extent detrimental to the electrophysiological function of the heart, as myofibroblasts are inexcitable cells, and have a more positive resting membrane potential than cardiomyocytes.³³ Improved intercellular coupling causes partial depolarization of the surrounding cardiomyocytes, thereby leading to conduction slowing.^{24, 32} Furthermore, coupling of cardiomyocytes with inexcitable cells prolongs the action potential duration because of a larger shared cell capacitance.^{34, 35} A prolonged action potential duration is associated with increased incidence of early after-depolarizations, because of the prolonged time that the membrane potential is in the calcium window; the membrane potential window at which the Ca²⁺ channels are active. This increases the chance of abnormally early influx of Ca²⁺ ions into the cell, thereby creating a new ectopic action potential from one or a few neighbouring cells. This irregular extra beat is out of phase with the normal wave fronts, and can therefore run into tissue that is still in its refractory phase. If other areas are repolarized faster, this could lead to unidirectional block and formation of a re-entrant circuit.³⁶⁻³⁸ Increased coupling of (myo) fibroblasts to cardiomyocytes also decreases the source-sink mismatch normally present in cardiac tissue. This mismatch is protective, since its hierarchical nature causes synchronized action potential propagation and thereby prevents the occurrence of early or delayed after-depolarizations. In case of fibrosis, this source-sink mismatch is decreased, thereby contributing to increased early and delayed after-depolarizations and thus arrhythmogenicity.^{28, 39}

In conclusion, ischemic heart disease causes cardiomyocyte damage and/or death. Due to limited regenerative capacity, cardiac remodelling occurs, which is characterized by replacement of dead or diseased cardiomyocytes by inexcitable, non-contractile fibroblasts. This leads to a reduction in contractile force, which is clinically translated to a decrease in

stroke volume. When the heart cannot meet the demands of maintaining adequate blood flow to the tissues in the body, there is a state of heart failure. Heart failure is usually a non-reversible, (slowly or rapidly) deteriorating process, with a high mortality rate.⁴⁰ Cardiomyocyte damage and fibrosis furthermore contribute to an arrhythmogenic substrate, which can lead to fatal arrhythmias like ventricular tachycardia (VT) or ventricular fibrillation (VF). One of the hallmarks of post-ischemic cardiac remodelling is changes in gap junctional coupling.⁴¹⁻⁴³ Damaged cardiomyocytes express lower levels of phosphorylated connexin 43; the active protein which forms gap junctional channels. In addition, there is lateralization of connexins, meaning that connexins are predominantly expressed perpendicularly to cardiac myofiber direction, thereby decreasing their functional effectivity in electrical signal relaying.^{44,45}

Current treatment options and their limitations

Recent scientific breakthroughs have revolutionized treatment of ischemic heart disease. Novel insight into the atherosclerotic process have contributed to improved preventive measures, such as the use of lipid lowering agents (e.g. statins), but also lifestyle adjustments such as smoking cessation, adhering a low-fat diet and regular exercise have all shown significant lowering effects on the incidence of ischemic heart disease.^{46, 47} Furthermore, improved diagnostic tools have enabled clinicians to detect atherosclerotic lesions at an early stage. These lesions can be opened and stented by means of percutaneous coronary intervention (PCI) or bypassed by coronary artery bypass graft (CABG) procedures. During acute occlusion, these interventions are used to acutely re-establish blood-flow to the ischemic myocardium, thereby reducing infarct size, which has beneficial effect on long-term prognosis, such as morbidity and mortality.⁴⁸⁻⁵¹

Once an ischemic event has occurred, cardiac performance can be optimized by pharmacotherapy, thereby offsetting or delaying clinical manifestations of heart failure. Mainstay therapies are angiotensin converting enzyme inhibitors, angiotensin II receptor blockers, diuretics, beta blocking agents, all drugs that reduce pre- and afterload.^{46, 52-55} Anti-arrhythmic agents are used to prevent or treat cardiac arrhythmias, but are frequently associated with paradoxical arrhythmogenic effects.⁵⁶ Recently catheter ablation techniques have been applied to treat scar-tissue associated arrhythmogenic foci.^{57, 58} In addition, implantable cardioverter defibrillators (ICDs) are used to monitor patients' heart rhythm and apply a defibrillating shock when an arrhythmia is detected. Although a tremendous amount of progress has been made in the prevention and treatment of (the effects of) ischemic heart disease, morbidity and mortality still remains remarkably high. These numbers justify the search and exploration of better, more sophisticated treatment modalities.

Regenerative therapy for ischemic heart disease

Since the heart is a poorly regenerating organ, a lot of effort has been invested into strategies and techniques that could eventually lead to effective cell replacement or tissue adaptation therapy. The ability to culture pluripotent stem cells (PSCs), such as embryonic stem cells (ESCs), and subsequently differentiate them into specialized cell types raised anticipation for generating tissue in a dish. This transplantable graft could replace a patient's myocardium once it becomes damaged or diseased. This promise grew further with the discovery of a technique to induce a terminally-differentiated cell type (e.g. fibroblast) into an induced pluripotent stem cell (iPSC), which allowed the production of patient-specific pluripotent stem cells.^{59, 60} This breakthrough discovery made possible that patient-specific cells could be used to eventually replace their own diseased heart, without the need for donor matching or immunosuppressive therapies. In addition, these developments laid the foundation for establishing cell fate switching by means of transdifferentiation. Here, terminally-differentiated cell types directly convert into a different terminally differentiated cell type (e.g. fibroblast to cardiomyocyte).^{61, 62} This reprogramming of one cell type to another has also been shown *in vivo* by direct transdifferentiation in the heart.^{63, 64}

Despite these advances, much of the early optimism has now been replaced by scepticism with the realization that many important hurdles need to be overcome before these techniques could one day lead to a significant therapeutic intervention.

Limited directed differentiation has precluded generation of vast amounts of the cell type of interest (e.g. cardiomyocytes). There is a considerable amount of inter-PSC-line variability in terms of cardiac differentiation potential. What is more, differentiated PSC-derived cardiomyocytes show generally an immature phenotype compared to endogenous cardiomyocytes for important characteristics, such as gene expression profiles, action potential morphology and force generation.^{65, 66} These problems are even worse for cardiac transdifferentiation, where the current reprogramming protocols give rise to inefficiently and incompletely reprogrammed cells, (*i.e.* cardiomyocyte-like cells).^{67, 68}

Early transplantation studies have shown transient beneficial effects at an early stage, but these effects were lost after a few weeks.^{69, 70} Furthermore, cellular homing to the heart after systemic administration has been extremely limited.⁷¹ Both systemic and local administration resulted in poor long-term cell survival, thereby supporting the hypothesis that the beneficial effects were mainly due to transient paracrine effects.^{72, 73}

Recently, a study showed robust ESC-derived cardiomyocyte engraftment in a primate model of myocardial infarction.⁷⁴ However, ventricular tachycardia was an important and frequent adverse effect after successful transplantation, likely due to poor cellular alignment and integration in the host tissue.⁷⁵ Electrophysiological integration and prevention of arrhythmogenicity are therefore important problems to overcome.

In order for regenerative therapies to one day become clinical practice, it is important to address several issues. First, elucidating and controlling the factors that determine differentiation potential and cellular maturation would be an important step to generate sufficient amounts of cardiomyocytes necessary for tissue graft transplantation. Second, differentiation protocols should be modified to improve cardiomyocyte maturation, yielding cells that are capable of generating sufficient contractile force and also electrophysiologically resemble endogenous cardiomyocytes. Many lessons can be learned from the developing embryonic heart. Orchestrated expression of key transcription factors by spatial and temporal activation of signalling pathways underlies heart development.^{76, 77} This process can be mimicked *in vitro* by timed addition and removal of growth factors or signalling molecules.⁷⁸⁻⁸¹ Unravelling this process in detail can greatly make the process of cardiac differentiation more efficient.

Third, efforts need to be made to increase cellular integration into host tissue in order to prevent arrhythmogenicity of engrafted tissue. Cells could be further modified by genetic engineering to equip them with properties for improved cellular function. This could be done by increasing their contractile force, but also tailoring their electrophysiological behaviour. One such function is the ability of cells to self-terminate arrhythmias once they occur. Therefore, further investigation is required in order to produce transplantable quantities of cardiomyocytes. Additionally, these cells could be genetically modified to enhance several functions, such as their functional integration into the host tissue, thereby decreasing transplant arrhythmogenicity or fitting these cells with the capacity to intrinsically terminate arrhythmias when they occur.

Aims and outline of thesis

In order to meet the therapeutic promise of cellular modification and interventions for ischemic heart disease, it is important to overcome a number of challenges that preclude harnessing their full therapeutic potential, see **Chapter 1**. Therefore, the aim of this thesis was to explore from an electrophysiological point of view, pathological cellular modification processes in cardiac disease, and to establish novel cell-modifying genetic interventions to prevent or treat

arrhythmia. In addition, cardiac differentiation was studied in an embryonic stem cell model, to gain new insight into cardiac lineage commitment. Improved *in vitro* cardiac differentiation can give rise to robust and mature cardiomyocytes, which could ultimately serve for cellular transplantation therapies.

In order to capitalize on induced pluripotent stem cell technology for regenerative applications, efficient reprogramming technique is a prerequisite to allow easy access to patient- or model animal-specific pluripotent stem cells. In **Chapter 2**, the generation of iPSC by transcription factor reprogramming is described for fibroblasts of mouse, rat, pig and human origin, respectively.

iPSCs, like ESCs could be subsequently differentiated into any somatic cell type of interest, including cardiac lineage cells. A thorough understanding of the developmental processes that direct pluripotent stem cells towards the cardiac lineage is essential for efficient cardiac differentiation. Identifying which signalling pathways are active or repressed at specific time windows during cardiac development can be used for directed lineage induction and therefore greater cardiomyocyte yield. **Chapter 3** describes the results of a systematic screen of cytokines and signalling molecules for their ability to enhance Nkx2.5⁺ cardiac progenitor cells in an ESC differentiation model. Insulin-like growth factors (IGFs) were identified to promote cardiac lineage induction by selective proliferation in early mesodermal lineage cells, which are precursors to the cardiac lineage.

Although these cells could be used for grafting viable myocardial tissue after removal of a patch of scar tissue, this approach becomes problematic in diffuse fibrosis, where large areas of the myocardium are generally affected. Fibroblasts exert detrimental effects in part due to their suboptimal integration into the myocardium. In **Chapter 4** these effects were counteracted by forced cellular fusion of human ventricular scar cells (hVSCs) with neonatal rat ventricular myocytes (NRVMs). Resulting heterokaryons derived from fusion of NRVMs and hVSCs showed enhanced repolarization force by increased outward K_v current. This corrected fibrosis-mediated action potential duration (APD) prolongation and occurrence of EADs. In addition, fused cultures showed increased gap junctional coupling between cells, as well as a more negative membrane diastolic potential compared to unfused cultures. These results could provide a framework for understanding fibrosis-mediated arrhythmogenesis and lead to new strategies for its prevention.

Although prevention of cardiac arrhythmia is a holy grail, it is still far removed and cardiac arrhythmias are still everyday reality. Insights into re-entry initiation and dynamics in vulnerable tissue can improve therapeutic strategies, including genetic and cell therapeutic interventions. In **Chapter 5** complimentary *in silico* and *in vitro* models of conduction slowing were used to study both quantitatively as well as mechanistically, the process of re-entry induction and stability. Increased conduction slowing due to increased knock-down of Cx43, resulted in occurrence of spatially discordant APD alternans phase islands. Wavebreaks and phase singularities formed at boundaries of adjacent alternans phase islands of opposite phase. Increased re-entry complexity resulted from increased alternans phase islands. These results give new insight into the dynamics of re-entry formation and maintenance in remodelled ventricular tissue.

Once stable re-entry occurs, it can be terminated by pharmacotherapy or application of a biphasic electrical shock. Anti-arrhythmic drugs are often paradoxically associated with pro-arrhythmia, whereas electroshock therapy can cause serious patient discomfort and tissue damage. A more elegant approach is if the myocardium could self-terminate arrhythmic activity, without the need for an external current. A prerequisite hereto would be for the cardiomyocytes to generate a current strong enough to meet the defibrillation threshold, and current activation should be highly controllable both spatially as well as temporally. Therefore, in **Chapter 6** the re-entry terminating ability of optogenetically engineered atrial tissue was investigated. To this purpose, atrial cardiomyocytes were equipped with a channelrhodopsin, an ion channel normally found in algae, thereby making them light-sensitive and allowing for high spatiotemporal control of depolarization with an intrinsic current.

Finally, **Chapter 7** describes the summary and conclusions of this thesis, as well as future perspectives of cellular and genetic interventions for treatment of heart disease.

References

1. WHO. World health statistics. 2014. Geneva: World Health Organization; 2014e. 2015.
2. Rohr S. Role of gap junctions in the propagation of the cardiac action potential. *Cardiovasc Res.* 2004;62:309-322.
3. John S, Cesario D, Weiss JN. Gap junctional hemichannels in the heart. *Acta Physiol Scand.* 2003;179:23-31.
4. Moreno AP. Biophysical properties of homomeric and heteromultimeric channels formed by cardiac connexins. *Cardiovasc Res.* 2004;62:276-286.
5. Kanter HL, Saffitz JE, Beyer EC. Cardiac myocytes express multiple gap junction proteins. *Circ Res.* 1992;70:438-444.
6. Davis LM, Kanter HL, Beyer EC, Saffitz JE. Distinct gap junction protein phenotypes in cardiac tissues with disparate conduction properties. *J Am Coll Cardiol.* 1994;24:1124-1132.
7. Zipes DP, Jalife J. Cardiac Electrophysiology: From Cell to Bedside. 2013.
8. Knaapen P, Germans T, Knuuti J, Paulus WJ, Dijkmans PA, Allaart CP, Lammertsma AA, Visser FC. Myocardial energetics and efficiency: current status of the noninvasive approach. *Circulation.* 2007;115:918-927.
9. Davies MJ. A macro and micro view of coronary vascular insult in ischemic heart disease. *Circulation.* 1990;82:1138-1146.
10. Braunwald E, Kloner RA. Myocardial reperfusion: a double-edged sword? *J Clin Invest.* 1985;76:1713-1719.
11. Yellon DM, Hausenloy DJ. Myocardial reperfusion injury. *N Engl J Med.* 2007;357:1121-1135.
12. Senyo SE, Steinhauser ML, Pizzimenti CL, Yang VK, Cai L, Wang M, Wu TD, Guerquin-Kern JL, Lechene CP, Lee RT. Mammalian heart renewal by pre-existing cardiomyocytes. *Nature.* 2013;493:433-436.
13. Soonpaa MH, Field LJ. Assessment of cardiomyocyte DNA synthesis in normal and injured adult mouse hearts. *Am J Physiol.* 1997;272:H220-H226.
14. Bergmann O, Bhardwaj RD, Bernard S, Zdunek S, Barnabe-Heider F, Walsh S, Zupicich J, Alkass K, Buchholz BA, Druid H, Jovinge S, Frisen J. Evidence for cardiomyocyte renewal in humans. *Science.* 2009;324:98-102.
15. Walsh S, Ponten A, Fleischmann BK, Jovinge S. Cardiomyocyte cell cycle control and growth estimation in vivo—an analysis based on cardiomyocyte nuclei. *Cardiovasc Res.* 2010;86:365-373.
16. Laflamme MA, Murry CE. Heart regeneration. *Nature.* 2011;473:326-335.
17. van den Borne SW, Diez J, Blankesteyn WM, Verjans J, Hofstra L, Narula J. Myocardial remodeling after infarction: the role of myofibroblasts. *Nat Rev Cardiol.* 2010;7:30-37.
18. Sun Y, Weber KT. Infarct scar: a dynamic tissue. *Cardiovasc Res.* 2000;46:250-256.
19. MacKenna DA, Omens JH, McCulloch AD, Covell JW. Contribution of collagen matrix to passive left ventricular mechanics in isolated rat hearts. *Am J Physiol.* 1994;266:H1007-H1018.
20. Kass DA, Bronzwaer JG, Paulus WJ. What mechanisms underlie diastolic dysfunction in heart failure? *Circ Res.* 2004;94:1533-1542.
21. Lal H, Ahmad F, Zhou J, Yu JE, Vagnozzi RJ, Guo Y, Yu D, Tsai EJ, Woodgett J, Gao E, Force T. Cardiac fibroblast glycogen synthase kinase-3beta regulates ventricular remodeling and dysfunction in ischemic heart. *Circulation.* 2014;130:419-430.
22. Rohr S. Arrhythmogenic implications of fibroblast-myocyte interactions. *Circ Arrhythm Electrophysiol.* 2012;5:442-452.
23. Miragoli M, Gaudesius G, Rohr S. Electrotonic modulation of cardiac impulse conduction by myofibroblasts. *Circ Res.* 2006;98:801-810.

24. Thompson SA, Copeland CR, Reich DH, Tung L. Mechanical coupling between myofibroblasts and cardiomyocytes slows electric conduction in fibrotic cell monolayers. *Circulation*. 2011;123:2083-2093.
25. Gaudesius G, Miragoli M, Thomas SP, Rohr S. Coupling of cardiac electrical activity over extended distances by fibroblasts of cardiac origin. *Circ Res*. 2003;93:421-428.
26. Nguyen TP, Qu Z, Weiss JN. Cardiac fibrosis and arrhythmogenesis: the road to repair is paved with perils. *J Mol Cell Cardiol*. 2014;70:83-91.
27. Xie Y, Garfinkel A, Camelliti P, Kohl P, Weiss JN, Qu Z. Effects of fibroblast-myocyte coupling on cardiac conduction and vulnerability to reentry: A computational study. *Heart Rhythm*. 2009;6:1641-1649.
28. Xie Y, Sato D, Garfinkel A, Qu Z, Weiss JN. So little source, so much sink: requirements for afterdepolarizations to propagate in tissue. *Biophys J*. 2010;99:1408-1415.
29. Nguyen TP, Xie Y, Garfinkel A, Qu Z, Weiss JN. Arrhythmogenic consequences of myofibroblast-myocyte coupling. *Cardiovasc Res*. 2012;93:242-251.
30. Desmouliere A, Geinoz A, Gabbiani F, Gabbiani G. Transforming growth factor-beta 1 induces alpha-smooth muscle actin expression in granulation tissue myofibroblasts and in quiescent and growing cultured fibroblasts. *J Cell Biol*. 1993;122:103-111.
31. Rosenkranz S. TGF-beta1 and angiotensin networking in cardiac remodeling. *Cardiovasc Res*. 2004;63:423-432.
32. Rohr S. Myofibroblasts in diseased hearts: new players in cardiac arrhythmias? *Heart Rhythm*. 2009;6:848-856.
33. Chilton L, Ohya S, Freed D, George E, Drobic V, Shibukawa Y, MacCannell KA, Imaizumi Y, Clark RB, Dixon IM, Giles WR. K⁺ currents regulate the resting membrane potential, proliferation, and contractile responses in ventricular fibroblasts and myofibroblasts. *Am J Physiol Heart Circ Physiol*. 2005;288:H2931-H2939.
34. MacCannell KA, Bazzazi H, Chilton L, Shibukawa Y, Clark RB, Giles WR. A mathematical model of electrotonic interactions between ventricular myocytes and fibroblasts. *Biophys J*. 2007;92:4121-4132.
35. Jacquemet V, Henriquez CS. Loading effect of fibroblast-myocyte coupling on resting potential, impulse propagation, and repolarization: insights from a microstructure model. *Am J Physiol Heart Circ Physiol*. 2008;294:H2040-H2052.
36. Qu Z, Xie LH, Olcese R, Karagueuzian HS, Chen PS, Garfinkel A, Weiss JN. Early afterdepolarizations in cardiac myocytes: beyond reduced repolarization reserve. *Cardiovasc Res*. 2013;99:6-15.
37. Chang MG, Chang CY, de LE, Xu L, O'Rourke B, Karagueuzian HS, Tung L, Marban E, Garfinkel A, Weiss JN, Qu Z, Abraham MR. Dynamics of early afterdepolarization-mediated triggered activity in cardiac monolayers. *Biophys J*. 2012;102:2706-2714.
38. Kohl P, Camelliti P, Burton FL, Smith GL. Electrical coupling of fibroblasts and myocytes: relevance for cardiac propagation. *J Electrocardiol* 2005 October;38(4 Suppl):45-50.
39. Weiss JN, Garfinkel A, Karagueuzian HS, Chen PS, Qu Z. Early afterdepolarizations and cardiac arrhythmias. *Heart Rhythm*. 2010;7:1891-1899.
40. Yusuf S, Rangarajan S, Teo K, Islam S, Li W, Liu L, Bo J, Lou Q, Lu F, Liu T, Yu L, Zhang S, Mony P, Swaminathan S, Mohan V, Gupta R, Kumar R, Vijayakumar K, Lear S, Anand S, Wielgosz A, Diaz R, Avezum A, Lopez-Jaramillo P, Lanus F, Yusuf K, Ismail N, Iqbal R, Rahman O, Rosengren A, Yusufali A, Kelishadi R, Kruger A, Puoane T, Szuba A, Chifamba J, Oguz A, McQueen M, McKee M, Dagenais G. Cardiovascular risk and events in 17 low-, middle-, and high-income countries. *N Engl J Med*. 2014;371:818-827.
41. de Diego DC, Pai RK, Chen F, Xie LH, De LJ, Weiss JN, Valderrabano M. Electrophysiological consequences of acute regional ischemia/reperfusion in neonatal rat ventricular myocyte monolayers. *Circulation* 2008;118:2330-2337.

42. Kostin S, Rieger M, Dammer S, Hein S, Richter M, Klovekorn WP, Bauer EP, Schaper J. Gap junction remodeling and altered connexin43 expression in the failing human heart. *Mol Cell Biochem.* 2003;242:135-144.
43. Cabo C, Yao J, Boyden PA, Chen S, Hussain W, Duffy HS, Ciaccio EJ, Peters NS, Wit AL. Heterogeneous gap junction remodeling in reentrant circuits in the epicardial border zone of the healing canine infarct. *Cardiovasc Res.* 2006;72:241-249.
44. Duffy HS. The molecular mechanisms of gap junction remodeling. *Heart Rhythm.* 2012;9:1331-1334.
45. Danik SB, Liu F, Zhang J, Suk HJ, Morley GE, Fishman GI, Gutstein DE. Modulation of cardiac gap junction expression and arrhythmic susceptibility. *Circ Res.* 2004;95:1035-1041.
46. Law MR, Wald NJ, Rudnicka AR. Quantifying effect of statins on low density lipoprotein cholesterol, ischaemic heart disease, and stroke: systematic review and meta-analysis. *BMJ.* 2003;326:1423.
47. Kromhout D, Menotti A, Kesteloot H, Sans S. Prevention of coronary heart disease by diet and lifestyle: evidence from prospective cross-cultural, cohort, and intervention studies. *Circulation.* 2002;105:893-898.
48. Keeley EC, Boura JA, Grines CL. Primary angioplasty versus intravenous thrombolytic therapy for acute myocardial infarction: a quantitative review of 23 randomised trials. *Lancet.* 2003;361:13-20.
49. de Boer MJ, Hoorntje JC, Ottervanger JP, Reiffers S, Suryapranata H, Zijlstra F. Immediate coronary angioplasty versus intravenous streptokinase in acute myocardial infarction: left ventricular ejection fraction, hospital mortality and reinfarction. *J Am Coll Cardiol.* 1994;23:1004-1008.
50. Hueb W, Lopes N, Gersh BJ, Soares PR, Ribeiro EE, Pereira AC, Favarato D, Rocha AS, Hueb AC, Ramires JA. Ten-year follow-up survival of the Medicine, Angioplasty, or Surgery Study (MASS II): a randomized controlled clinical trial of 3 therapeutic strategies for multivessel coronary artery disease. *Circulation.* 2010;122:949-957.
51. de Boer MJ, Suryapranata H, Hoorntje JC, Reiffers S, Liem AL, Miedema K, Hermens WT, van den Brand MJ, Zijlstra F. Limitation of infarct size and preservation of left ventricular function after primary coronary angioplasty compared with intravenous streptokinase in acute myocardial infarction. *Circulation.* 1994;90:753-761.
52. Flather MD, Yusuf S, Kober L, Pfeffer M, Hall A, Murray G, Torp-Pedersen C, Ball S, Pogue J, Moye L, Braunwald E. Long-term ACE-inhibitor therapy in patients with heart failure or left-ventricular dysfunction: a systematic overview of data from individual patients. ACE-Inhibitor Myocardial Infarction Collaborative Group. *Lancet.* 2000;355:1575-1581.
53. Wald NJ, Law MR. A strategy to reduce cardiovascular disease by more than 80%. *BMJ.* 2003;326:1419.
54. Freemantle N, Cleland J, Young P, Mason J, Harrison J. beta Blockade after myocardial infarction: systematic review and meta regression analysis. *BMJ.* 1999;318:1730-1737.
55. LaRosa JC, He J, Vupputuri S. Effect of statins on risk of coronary disease: a meta-analysis of randomized controlled trials. *JAMA.* 1999;282:2340-2346.
56. Nattel S. Experimental evidence for proarrhythmic mechanisms of antiarrhythmic drugs. *Cardiovasc Res.* 1998;37:567-577.
57. Zeppenfeld K, Kies P, Wijffels MC, Bootsma M, van EL, Schalij MJ. Identification of successful catheter ablation sites in patients with ventricular tachycardia based on electrogram characteristics during sinus rhythm. *Heart Rhythm.* 2005;2:940-950.
58. Sacher F, Tedrow UB, Field ME, Raymond JM, Koplan BA, Epstein LM, Stevenson WG. Ventricular tachycardia ablation: evolution of patients and procedures over 8 years. *Circ Arrhythm Electrophysiol.* 2008;1:153-161.
59. Takahashi K, Yamanaka S. Induction of pluripotent stem cells from mouse embryonic and adult fibroblast cultures by defined factors. *Cell.* 2006;126:663-676.
60. Yu J, Vodyanik MA, Smuga-Otto K, Antosiewicz-Bourget J, Frane JL, Tian S, Nie J, Jonsdottir GA, Ruotti V, Stewart R, Slukvin II, Thomson JA. Induced pluripotent stem cell lines derived from human somatic cells. *Science.* 2007;318:1917-1920.

61. Vierbuchen T, Ostermeier A, Pang ZP, Kokubu Y, Sudhof TC, Wernig M. Direct conversion of fibroblasts to functional neurons by defined factors. *Nature*. 2010;463:1035-1041.
62. Ieda M, Fu JD, Delgado-Olguin P, Vedantham V, Hayashi Y, Bruneau BG, Srivastava D. Direct reprogramming of fibroblasts into functional cardiomyocytes by defined factors. *Cell*. 2010;142:375-386.
63. Qian L, Huang Y, Spencer CI, Foley A, Vedantham V, Liu L, Conway SJ, Fu JD, Srivastava D. In vivo reprogramming of murine cardiac fibroblasts into induced cardiomyocytes. *Nature*. 2012;485:593-598.
64. Song K, Nam YJ, Luo X, Qi X, Tan W, Huang GN, Acharya A, Smith CL, Tallquist MD, Neilson EG, Hill JA, Bassel-Duby R, Olson EN. Heart repair by reprogramming non-myocytes with cardiac transcription factors. *Nature*. 2012;485:599-604.
65. Yang X, Pabon L, Murry CE. Engineering adolescence: maturation of human pluripotent stem cell-derived cardiomyocytes. *Circ Res*. 2014;114:511-523.
66. Halbach M, Peinkofer G, Baumgartner S, Maass M, Wiedey M, Neef K, Krausgrill B, Ladage D, Fatima A, Saric T, Hescheler J, Muller-Ehmsen J. Electrophysiological integration and action potential properties of transplanted cardiomyocytes derived from induced pluripotent stem cells. *Cardiovasc Res*. 2013;100:432-440.
67. Chen JX, Krane M, Deutsch MA, Wang L, Rav-Acha M, Gregoire S, Engels MC, Rajarajan K, Karra R, Abel ED, Wu JC, Milan D, Wu SM. Inefficient reprogramming of fibroblasts into cardiomyocytes using Gata4, Mef2c, and Tbx5. *Circ Res*. 2012;111:50-55.
68. Qian L, Berry EC, Fu JD, Ieda M, Srivastava D. Reprogramming of mouse fibroblasts into cardiomyocyte-like cells in vitro. *Nat Protoc*. 2013;8:1204-1215.
69. van Laake LW, Passier R, Monshouwer-Kloots J, Verkleij AJ, Lips DJ, Freund C, den OK, Ward-van OD, Korving J, Tertoolen LG, van Echteld CJ, Doevendans PA, Mummery CL. Human embryonic stem cell-derived cardiomyocytes survive and mature in the mouse heart and transiently improve function after myocardial infarction. *Stem Cell Res*. 2007;1:9-24.
70. van Laake LW, Passier R, Doevendans PA, Mummery CL. Human embryonic stem cell-derived cardiomyocytes and cardiac repair in rodents. *Circ Res*. 2008;102:1008-1010.
71. Li SH, Lai TY, Sun Z, Han M, Moriyama E, Wilson B, Fazel S, Weisel RD, Yau T, Wu JC, Li RK. Tracking cardiac engraftment and distribution of implanted bone marrow cells: Comparing intra-aortic, intravenous, and intramyocardial delivery. *J Thorac Cardiovasc Surg*. 2009;137:1225-1233.
72. Zhang M, Methot D, Poppa V, Fujio Y, Walsh K, Murry CE. Cardiomyocyte grafting for cardiac repair: graft cell death and anti-death strategies. *J Mol Cell Cardiol*. 2001;33:907-921.
73. Laflamme MA, Chen KY, Naumova AV, Muskheli V, Fugate JA, Dupras SK, Reinecke H, Xu C, Hassanipour M, Police S, O'Sullivan C, Collins L, Chen Y, Minami E, Gill EA, Ueno S, Yuan C, Gold J, Murry CE. Cardiomyocytes derived from human embryonic stem cells in pro-survival factors enhance function of infarcted rat hearts. *Nat Biotechnol*. 2007;25:1015-1024.
74. Chong JJ, Yang X, Don CW, Minami E, Liu YW, Weyers JJ, Mahoney WM, Van BB, Cook SM, Palpant NJ, Gantz JA, Fugate JA, Muskheli V, Gough GM, Vogel KW, Astley CA, Hotchkiss CE, Baldessari A, Pabon L, Reinecke H, Gill EA, Nelson V, Kiem HP, Laflamme MA, Murry CE. Human embryonic-stem-cell-derived cardiomyocytes regenerate non-human primate hearts. *Nature*. 2014;510:273-277.
75. Pijnappels DA, Schalij MJ, Atsma DE, de Vries AA. Cardiac anisotropy, regeneration, and rhythm. *Circ Res*. 2014;115:e6-e7.
76. Murry CE, Keller G. Differentiation of embryonic stem cells to clinically relevant populations: lessons from embryonic development. *Cell*. 2008;132:661-680.
77. Van Vliet P, Wu SM, Zaffran S, Puceat M. Early cardiac development: a view from stem cells to embryos. *Cardiovasc Res*. 2012;96:352-362.
78. Kattman SJ, Witty AD, Gagliardi M, Dubois NC, Niapour M, Hotta A, Ellis J, Keller G. Stage-specific optimization of activin/nodal and BMP signaling promotes cardiac differentiation of mouse and human pluripotent stem cell lines. *Cell Stem Cell*. 2011;8:228-240.

79. Cai W, Guzzo RM, Wei K, Willems E, Davidovics H, Mercola M. A Nodal-to-TGFbeta cascade exerts biphasic control over cardiopoiesis. *Circ Res.* 2012;111:876-881.
80. Willems E, Cabral-Teixeira J, Schade D, Cai W, Reeves P, Bushway PJ, Lanier M, Walsh C, Kirchhausen T, Izpisua Belmonte JC, Cashman J, Mercola M. Small molecule-mediated TGF-beta type II receptor degradation promotes cardiomyogenesis in embryonic stem cells. *Cell Stem Cell.* 2012;11:242-252.
81. Burridge PW, Matsa E, Shukla P, Lin ZC, Churko JM, Ebert AD, Lan F, Diecke S, Huber B, Mordwinkin NM, Plews JR, Abilez OJ, Cui B, Gold JD, Wu JC. Chemically defined generation of human cardiomyocytes. *Nat Methods.* 2014;11:855-860.

CHAPTER 2

Reprogramming of mouse, rat, pig, and human fibroblasts into induced pluripotent stem cells

Kuppusamy Rajarajan^{1,†}, Marc C. Engels^{1,†}, Sean M. Wu^{1,2}

[†]These authors contributed equally to this work.

¹Cardiovascular Research Center, Division of Cardiology, Department of Medicine, Massachusetts General Hospital, Boston, Massachusetts, USA.

²Harvard Stem Cell Institute, Cambridge, Massachusetts, USA.

Adapted from: Current Protocols in Molecular Biology. 2012;Chapter 23: Unit 23.15.

Abstract

The induction of pluripotency in somatic cells by transcription factor overexpression has been widely regarded as one of the major breakthroughs in stem cell biology within this decade. The generation of these induced pluripotent stem cells (iPSCs) has enabled investigators to develop *in vitro* disease models for biological discovery and drug screening, and in the future, patient-specific therapy for tissue or organ regeneration. While new technologies for reprogramming are continuously being discovered, the availability of iPSCs from different species is also increasing rapidly. Comparison of iPSCs across species may provide new insights into key aspects of pluripotency and early embryonic development. iPSCs from large animals may enable the generation of genetically modified large animal models or potentially transplantable donor tissues or organs. This unit describes the procedure for the generation of iPSCs from mouse, rat, pig and human fibroblasts.

Introduction

With the overexpression of just four transcription factors, Oct4, Sox2, Klf-4, and c-Myc, Takahashi and Yamanaka showed that terminally differentiated fibroblasts could be reprogrammed into becoming pluripotent, embryonic stem cell-like cells, which they called induced pluripotent stem cells (iPSCs).¹ These cells are able to proliferate indefinitely and have been shown to differentiate into subtypes of all three germ layers. iPSCs thus harbor potential for disease modeling as well as conducting patient-specific drug screens *in vitro*, without the ethical and technical challenges associated with embryonic stem cells (ESCs). This unit describes the generation of iPSCs from four species: mouse, rat, pig, and human. To lower the barrier for new investigators to enter this exciting area of biology, the focus is on lenti- and retroviral infection-based strategies for somatic cell reprogramming, since these approaches remain the easiest for generating iPSC lines.

Although by no means exclusive, this unit describes in detail the full procedure required for iPSC generation. Basic Protocol 1 describes the isolation and culture of fibroblasts, with a Support Protocol for lentiviral production. Basic Protocol 2 describes the viral infection of fibroblasts, which can be applied to all four species. After this section, the procedure diverges for various species: Basic Protocol 3 describes the establishment and maintenance of mouse iPSCs and Alternate Protocols 1, 2, and 3 respectively describe the same procedure in rat, pig and human cells.

Note: All solutions and equipment coming into contact with cells must be sterile, and aseptic technique should be used accordingly.

Note: All culture incubations are performed in a humidified 37°C, 5% CO₂ incubator unless otherwise specified.

Note: All protocols using live animals must first be reviewed and approved by an Institutional Animal Care and Use Committee (IACUC) and must follow officially approved procedures for the care and use of laboratory animals.

Basic Protocol 1

Isolation and culture of fibroblasts

This protocol describes the isolation and culturing of mouse embryonic fibroblasts (MEFs). However, a slightly modified protocol can be followed for mouse dermal fibroblasts or tail-tip fibroblasts, as well as rat embryonic fibroblasts, rat dermal fibroblasts, rat tail-tip fibroblasts, pig dermal fibroblasts, and human dermal fibroblasts.

Note: When using either skin fibroblasts or tail tip fibroblasts, the same procedure can be followed as described below after finely mincing the sample using a sterile scalpel or razor blade.

Note: For rat samples the same procedure can be followed as described below using pregnant female rats at 14.5 to 15.5 days post coitum (dpc) for embryonic rat fibroblasts. Alternatively, skin samples can be used for dermal fibroblasts or tail tip fibroblasts.

Note: For pig and human samples a punch skin biopsy should be performed to obtain skin tissues. The same procedure can be followed as described below.

Materials

Pregnant female mice

Sterile Dulbecco's PBS (DPBS; with CaCl_2 and MgCl_2 ; Invitrogen, cat. no. 14040141)

Penicillin and streptomycin (Invitrogen, cat. no. 15140-155)

0.25% trypsin/0.53 mM EDTA (Invitrogen, cat. no. 25200-056)

MEF medium (see recipe)

Freezing/cryopreservation medium (see recipe)

Liquid N_2

Dissecting equipment including sterile forceps and sterile scalpel blades

100-mm petri dishes (BD Falcon 351029)

15- and 50-mL conical tubes

Centrifuge

Pipettors with 1000- μl (P1000) pipet tips

100-mm cell culture dishes (Corning 430167), pre-coated with 0.1% gelatin (see recipe)

Cryovials

Additional reagents and equipment for counting cells (*Appendix 3F*)

Preparation of mouse embryonic fibroblasts

1. Euthanize pregnant female mice at 13.5 to 15.5 dpc by cervical dislocation.² Isolate the gravid uterus and briefly wash with DPBS supplemented with antibiotics (penicillin at 5000 IU/mL and streptomycin at 5000 µg/mL final concentration).
2. Dissect through the placenta and uterus until embryos are within view. Separate embryos from their placenta and surrounding fetal membranes with sterile forceps. Carefully remove the head, visceral organs, and gonads from the embryos.
3. Wash bodies of the embryos thoroughly in a 100-mm petri dish containing fresh DPBS supplemented with antibiotics (penicillin and streptomycin at 5000 IU each per mL). Mince well with sterile scalpel blade, digest the embryos in 1 mL of 0.25% trypsin/EDTA in a 15-mL conical tube, and incubate at 37°C for 15 minutes (min). Pipetting up and down with a 1000-µL (P1000) pipet tip, gently triturate intermittently to allow the cells to disperse from the large tissue clumps.
4. Add 9 mL of MEF medium to neutralize the trypsin. Again pipet up and down gently to dissociate as many cells as possible.
5. Incubate the samples for 5 min at room temperature (20° to 25°C) to allow the tissue debris to settle at the bottom and transfer the supernatant into a sterile 50-mL conical tube. Centrifuge 4 min at 200 × *g*, at room temperature, discard the supernatant, and resuspend the pellet in 10 mL fresh MEF medium.
6. Simply count cells with a hemocytometer (see *Appendix 3F*; trypan blue test not needed) and adjust the concentration to 1 × 10⁶ cells per mL with MEF medium (generally, 1 × 10⁷ cells can be obtained from a single embryo). Transfer the cell suspension to gelatinized 100-mm tissue culture dishes (1 × 10⁷ cells per dish) with 10 mL of MEF medium and incubate in a 37°C, 5% CO₂ humidified incubator.
This is considered passage number 0.
7. Remove non-adherent cells after 48 hours by washing with DPBS (with calcium and magnesium) or MEF medium, then replenish with MEF medium.
Cells should be replenished with fresh MEF medium every 48 hours until confluent.
8. When the cells have become confluent, remove MEF medium, wash once with DPBS (with calcium and magnesium), and trypsinize with 2 mL of 0.25% trypsin/EDTA for 4 min at 37°C. After detaching, add 9 mL of MEF medium and resuspend the cells by pipetting. Passage to new 100-mL dishes at 1:4 dilution (passage no. 1).
Now these cells can be used for viral infection to make iPSCs. It is recommended to conduct a mycoplasma test before use.

Important note: For the generation of iPSCs, it is advisable to use MEFs (mouse embryonic fibroblasts) up to and including passage no. 3 to avoid replicative senescence. As an alternative, other easily

accessible tissues can be used for reprogramming, such as adult skin cells, tail tip fibroblasts, blood, and cells from biopsy tissues,³ but these cells show less reprogramming efficiency than embryonic fibroblasts within the first 5 to 7 passages.

Freezing mouse embryonic fibroblasts (optional)

When working with DMSO-containing freezing medium, it is essential to work as quickly as possible and to transfer the freezing stock rapidly into a -80°C freezer in order to initiate the freezing procedure. To minimize exposure at room temperature, you should pre-label the cryovials and have the freezing container ready.

9. Let cells grow until they reach 90% confluency.
10. Aspirate the cell culture medium and wash cells with 5 mL of sterile DPBS (with calcium and magnesium).
11. Remove DPBS completely, add 2 mL of 0.25% trypsin/EDTA and incubate at 37°C with 5% CO_2 for 4 min.
12. Add 2.5 mL of MEF medium and resuspend the cells by pipetting up and down to a single-cell suspension.
13. Transfer the cell suspension to a 15-mL tube and add MEF medium for a total volume of 10 mL. Count cells using a hemocytometer (*APPENDIX 3F*). Centrifuge 4 min at $200 \times g$.
14. Aspirate the supernatant, resuspend the pellet in freezing/cryopreservation medium (10% DMSO in FBS) to obtain a concentration of 2×10^6 cells per mL.
15. Transfer the cell suspension to prelabeled cryovials at 1 mL per cryovial.
Labeling should include cell line, passage number, and date.
16. Quickly store the cryovials in a chilled cell-freezing container (4°C or on wet ice) and freeze at -80°C overnight.
Cells should be transferred to -80°C rapidly, since DMSO is toxic to cells in liquid phase.
17. The next day, remove cryovials from freezing container and store in the gas phase of a liquid nitrogen tank for long-term storage.

Production of lentivirus

This protocol describes the production of viral constructs in a lentiviral system. The protocols for infecting mouse, rat, pig, and human fibroblasts with lenti- and retroviruses are similar. Therefore the following applies to all four animal species.

NOTE: For retroviral production, use PLAT-E cells with FuGENE HD Transfection Reagent.

Materials

293FT cells (Invitrogen, cat. no. R700-07)

293FT medium (see recipe)

FuGENE HD Transfection Reagent (Roche, cat. no. 04 709 705 001)

DMEM/high glucose (Invitrogen, cat. no. 11965092)

VSV-G plasmid (Addgene, cat. no. 8454)

D8.9/psPAX2 plasmid (Addgene, cat. no. 12260)

STEMCCA (OKSM) Lentivirus Reprogramming Kit (Millipore, cat. no. SCR511)

10% bleach disinfectant

Serum-free DMEM medium (e.g., Invitrogen)

100-mm cell culture dishes (Corning, cat. no. 430167) pre-coated with 0.1% gelatin

0.45- μ m disposable filters

Ultracentrifugation tubes (Beckman, cat. no. 344058)

Beckman Coulter Optima L-90K ultracentrifuge with SW-32 rotor

1. Culture 293FT cells in a gelatinized 100-mm dish in 293FT medium until cells reach 80% to 90% confluency. Use 1 dish per viral construct or several if harvesting more virus.
2. Pre-warm DMEM/high glucose and FuGENE HD Transfection Reagent to room temperature and combine in a microcentrifuge tube. Use 770 μ l DMEM/high glucose and 50 μ l FuGENE Reagent per 100-mm dish.
3. Incubate at room temperature for 5 min.
4. For each infection, add 5.5 μ l VSV-G (5.5 μ g/infection) and 8.25 μ l D8.9 (8.25 μ g/infection) to each microcentrifuge tube and mix well.

Listed below are typical infection ratios of lentiviral helper plasmids for production of lentiviral vectors by FuGENE transfection:

1 \times VSV-G

1.5 \times D8.9

2 \times vector

5. Add a total of 11 μ g vector DNA (STEMCCA Lentivirus Reprogramming Vector– pluripotent transcription factors at 11 μ g/infection).
6. Mix by gently tapping tube several times (do not vortex).
7. Incubate 30 min at room temperature.
8. During incubation, add 10 mL of fresh 293FT medium to 293FT cells.
9. Add entire FUGENE/DNA complex to the 100-mm dish containing the 293FT cells in a dropwise fashion around the dish. Gently rotate the plate to mix the contents. Incubate for 12 to 24 hours (hr) at 37°C with 5% CO₂.

10. After the 12- to 24-hr incubation, change the 293FT medium. Add 10 mL of fresh medium at each medium-replenishing step.
11. After 24 hr, collect all medium into a 50-mL conical tube and store at 4°C until the collection procedure is completed. Add 10 mL of fresh 293FT medium to the dish. Repeat every subsequent 24 hr for a total of three collections. After completion, discard cells using proper viral waste disposal procedures.
This will allow a collection of 30 mL of virus medium per 100-mm dish.
12. Filter collected viral medium through a 0.45- μ m filter.
13. Transfer collected media into ultracentrifugation tubes at 30 mL per tube and centrifuge 1.5 hr at 50,000 $\times g$ and 4°C. Turn brakes off to avoid disturbance of pellet.
14. Decant supernatant into 10% bleach, then briefly place tube upside down onto tissue paper to remove supernatant completely.
This will take up to 1 to 2 min.
15. Add 200 μ L of serum-free DMEM medium to the pellet and let stand overnight at 4°C.
16. Resuspend by carefully pipetting up and down and aliquot the virus in small volumes (e.g. 20 μ L per aliquot). Store aliquots up to 1 year at -80°C .

Basic Protocol 2

Infection of fibroblasts using pluripotency factors

This protocol describes the infection of fibroblasts using viral constructs of the four pluripotency factors. This protocol can be applied to all four species described using the viral method detailed in Basic Protocol 1.

Caution: When working with virus, use a designated laminar flow hood for virus-related work. Always wear protective disposable gowns and double gloves. Make sure to discard any viral waste into designated viral waste bins and rinse any disposables with bleach before disposing of them. The contents of a viral waste bin should be autoclaved in an autoclavable bag for 45 min in a standard autoclave using the sterilization program.

Materials

Embryonic fibroblasts or dermal fibroblasts (passage ≤ 3 ; see Basic Protocol 1)

MEF medium (see recipe)

Sterile Dulbecco's PBS (DPBS; with CaCl_2 and MgCl_2 ; Invitrogen, cat. no. 14040141)

0.25% trypsin/0.53 mM EDTA (Invitrogen, cat. no. 25200-056)

Polybrene (Millipore TR-1003-G)

Pre-aliquoted virus (see Support Protocol 1)

6-well plate pre-coated with 0.1% gelatin

15-mL conical centrifuge tubes

Additional reagents and equipment for counting cells (APPENDIX 3F)

Note: Using fresh virus gives dramatically better infection efficiency. Virus should not be stored for longer than 1 week at 4°C before use. Virus should never undergo more than 1 freeze/thaw cycle, as multiple freeze/thaw cycles considerably reduce infection efficiency.

Note: For mouse and rat fibroblasts, mouse four factor plasmids are most widely used for making iPSCs. For pig and human fibroblasts it is preferable to use human four-in-one factor constructs, but individual human factors can also be used. A STEMCCA Cre-Excisable Constitutive Polycistronic (OKSM) Lentivirus Reprogramming Kit is commercially available (Millipore).

Note: For increased viral infection rate, multiple infections can be performed by aspirating and replenishing medium with fresh virus-containing medium every 12 hr up until 36 hr after initial infection.

Note: As a feeder layer for iPSCs, MEFs can be used for all four species. The MEFs should be growth-inhibited by irradiation or mitomycin C treatment. For best results, a single monolayer of feeder cells should be plated onto gelatinized culture plates (for mouse and rat) or Matrigel-coated culture plates (for pig and human).

1. Culture embryonic fibroblasts or dermal fibroblasts (passage ≤ 3) to $\sim 90\%$ confluency in a single well of a gelatin-coated 6-well plate in 2 mL MEF medium. *This will yield more than 1×10^4 cells per dish.*
2. Aspirate the culture medium from the MEF cells and wash with 2 mL of DPBS.
3. Aspirate PBS, add 0.5 mL per well of 0.25% trypsin-EDTA, and incubate at 37°C for 4 min.
4. Add 2 mL MEF medium to inactivate the trypsin, triturate to obtain a single-cell suspension, and transfer to a 15-mL tube.
5. Centrifuge 4 min at $200 \times g$, at room temperature, discard the supernatant and resuspend the pellet in 1 mL of MEF medium.
6. Simply count the number of cells using a hemocytometer (trypan blue test not needed) and adjust the cell concentration to 1×10^4 cells (see *Appendix 3F*) with MEF medium.
7. Add 1 μ L of 8 mg/mL polybrene per mL of cell-containing medium. Mix by gently pipetting up and down. *The final concentration of polybrene in the mixture should be 8 μ g/mL.*
8. Thaw and freshly combine all four factor lenti- or retroviruses (Oct-3/4, Sox2, Klf4, and c-Myc) into a cocktail and add freshly into the cell mixture for mouse and rat iPSC generation. Mix by gently pipetting up and down.

For pig and human iPSCs, a four-in-one mono-cassette virus is recommended. If using a doxycycline-inducible TetO viral system, a separate rtTa expressing virus should also be added at this point. Additionally, doxycycline should be added immediately and with each medium change at a final concentration of 1 µg/mL to induce gene expression. The amount of virus added should be calculated by making use of the equation mentioned below, using a Multiplicity of Infection (MOI) of at least 20.

The following equation can be used to determine the volume of virus required to achieve a Multiplicity of Infection (MOI) of at least 20.

Virus volume (µL) required = [(# MEFs seeded for infection)/virus titer (U/mL)] × [(desired MOI)/1 mL] × 1000 µL.

For example, if the number of cells in the well at the time of transduction is 1×10^5 cells, the viral titer is 3×10^8 IFU/mL, and a desired MOI is 20, then the volume of virus required is:

$(1 \times 10^5 \text{ cells}) / (3 \times 10^8 \text{ U/mL}) \times [20 / 1 \text{ mL} \times 1000 \text{ µL}] = 6.6 \text{ µL}$ virus required for 1 well of a 6-well plate.

9. Plate 1 mL of the cell/virus mixture onto a single well of a gelatin-coated 6-well plate and incubate the cells for 24 hr at 37°C with 5% CO₂.
10. After 24 hr, wash with warm MEF medium and replenish with 2 mL of fresh MEF medium. Continue incubation at 37°C with 5% CO₂.
11. For post-infection iPSC colony selection and maintenance procedures, see the respective protocol below (Basic Protocol 3 for mouse, Basic Protocol 4 and Alternate Protocol 1 for rat, Alternate Protocol 2 for pig, and Alternate Protocol 3 for human) for each species of interest to be reprogrammed.

Basic Protocol 3

Establishment and maintenance of mouse iPSCs

This protocol describes the establishment and maintenance of mouse iPSCs. See Basic Protocol 2 for the viral infection procedure. *Figure 1* is a schematic diagram showing the process of generating mouse iPSCs.

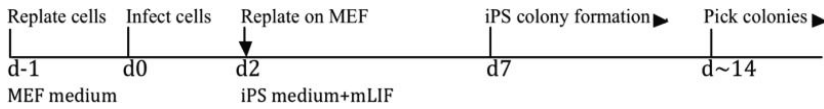


Figure 1. Schematic diagram of mouse iPSC generation.

Materials

Mouse fibroblasts infected with pluripotency factors (Basic Protocol 2); for timing see *Figure 1*.

MEF medium (see recipe)

0.25% trypsin/0.53 mM EDTA (Invitrogen, cat. no. 25200-056)

Mouse iPSC medium (see recipe) with double concentration of LIF and with normal concentration of mouse LIF as specified in Reagents and Solutions

Doxycycline (Sigma, cat. no. D9891); optional

24- and 6-well plates of inactivated mouse fibroblast feeder cells (*UNIT 23.2*)

Phosphate-buffered saline (PBS) without CaCl₂ and MgCl₂ (Invitrogen 14190-250)

Freezing/cryopreservation medium (see recipe)

Isopropanol

Liquid N₂

70% ethanol

15-mL conical centrifuge tubes

Centrifuge

Light microscope with camera

Marker pen

20- μ L (P20) and 1000- μ L (P1000) pipet tips

2.0-mL cryovials

Freezing chamber (e.g., Mr. Frosty; Thermo Scientific, cat. no. 5100-0001)

Liquid nitrogen storage tank

Cryogenic handling gloves and eye protectors

Forceps

Additional reagents and equipment for preparing inactivated mouse embryonic fibroblast feeder cells (*Unit 23.2*) and counting cells using a hemocytometer (*Appendix 3F*)

Post-infection Culturing of Infected Fibroblasts

1. After 48 hr of viral infection or when cells reach confluency, aspirate the medium from the infected cells and dissociate by adding 0.5 mL of 0.25% trypsin/0.53 mM EDTA and incubating for 4 min at 37°C with 5% CO₂. Add 2 mL of warm MEF medium, then pipet up and down to obtain a single-cell suspension. Transfer to a 15-mL tube containing 9 mL of warm MEF medium and centrifuge 4 min at 200 \times *g* and room temperature.

2. Discard the supernatant and resuspend the pellet in 8 mL of mouse iPSC culture medium. For initial culture use double the concentration of mouse LIF. After 2 to 3 passages, use the regular dose of mouse LIF.
3. Aspirate the medium from four single wells of a 6-well plate that has been gelatin-coated and pre-seeded with irradiated or mitomycin C–treated MEF cells (prepared as described in UNIT 23.2). Add 2 mL of the infected cell mixture per well onto the MEF feeder layer so that the infected cells are passaged in a 1:4 ratio. Incubate at 37°C with 5% CO₂.
4. Change iPSC medium supplemented with doxycycline (final concentration, 1 µg/mL if using a TetO lentiviral system) every 24 hr and check for colony formation. *Colonies should start becoming microscopically visible approximately 7 to 10 days post-infection.*
5. Let colonies grow into a reasonable size (roughly 50 to 100 cells/colony).
This should take approximately 14 or 15 days post-infection.

Picking and establishing mouse iPSC clones

6. One hour before picking iPSC colonies, pre-feed the cells by replenishing with fresh mouse iPSC medium.
This is especially important when the medium has turned acidic (indicated by yellow color), since pre-feeding will increase cell survival after dissociation.
7. Prepare a microscope inside a laminar hood to maintain sterile conditions for picking colonies (*Figure 2*).
8. Before picking, select up to 40 good colonies by circling the colony with a marker pen on the bottom of the plate to be able to retrieve the selected colonies when the actual picking procedure is started. *Suitable colonies should appear translucent and circular. See Figure 3 for examples of suitable mouse iPSC colonies.*
9. Pipet 50 µL of 0.25% trypsin/0.53 mM EDTA into each of several 15-mL tubes.
10. Use a 20-µL pipet tip for the picking procedure. Pick one individual colony by gently scratching with the pipet tip. Make sure not to touch any neighboring colonies.
11. Transfer each picked colony into an individual 15-mL tube containing 50 µL of 0.25% trypsin/0.53 mM EDTA. Dissociate the colony by gently pipetting up and down and incubate at 37°C in a water bath for 4 min.
12. After 4 min of incubation, add 5 mL of iPSC medium to each 15-mL tube containing one single colony and pipet up and down to dissociate the colony further into a single-cell suspension. Centrifuge 4 min at 200 × *g*, at room temperature.
13. Aspirate the supernatant and resuspend the pellet in 1 mL of mouse iPSC medium. Transfer the cell suspension from each picked colony into a single well of a 24-well plate that has been gelatin-coated and pre-seeded with growth-inactivated MEF cells (prepared as described in UNIT 23.2). Incubate at 37°C with 5% CO₂ and replenish medium every 24 hr until nearly confluent. *Cells are now ready to be passaged into a 6-well plate.*

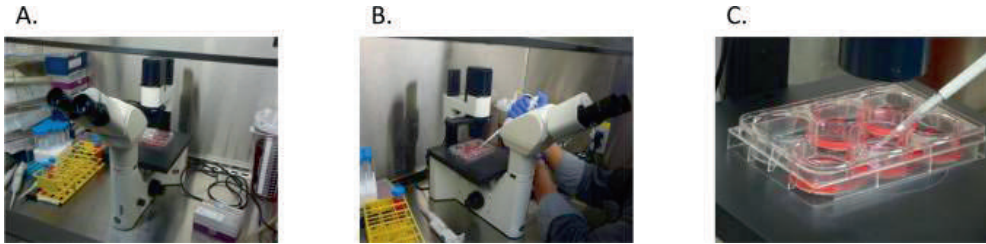


Figure 2. Procedural set up for iPSC colony picking. (A) Setup for picking iPSC colonies under a microscope in a laminar flow hood. (B) Process of iPSC colony picking. Note that the forearm is fixed against the microscope stage while looking through microscope (C) Close-up of picking. Make sure not to touch any neighboring colonies.

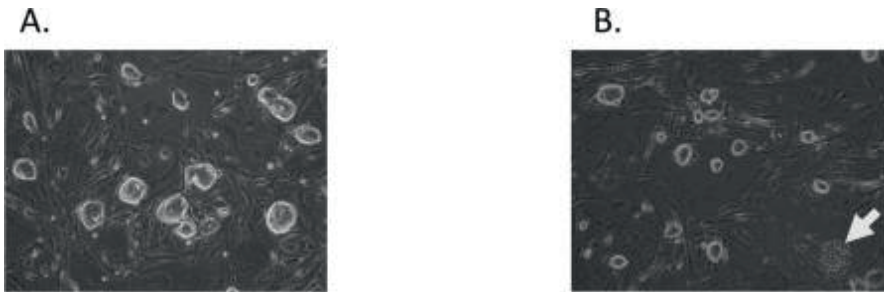


Figure 3. Typical morphology of good and bad mouse iPSC colonies. (A) A good mouse iPSC colony. Note the translucent appearance and sharp borders. (B) Mouse iPSCs. Notice the one bad mouse iPSC colony (arrow) on the bottom right. This colony looks heterogeneous and differentiated.

In vitro culture and expansion of mouse iPSCs

When reprogramming cells using a doxycycline-inducible system, wean the cells off doxycycline gradually after picking colonies. As a guideline, the following schedule can be applied: use 1/2 concentration of doxycycline after the first passage. Then, gradually lower the concentration with each passage to 1/4 concentration, and finally completely wean off doxycycline. If cell morphology begins to degrade, slow the rate of weaning. Do not change medium conditions at the time of passaging; rather, wait until the cells have attached (usually after 12 to 24 hr) before making changes to the doxycycline concentration.

14. When iPSC colonies reach 80% to 90% confluency in the dish or when individual iPSC colonies become large (approximately >100 cells/colony), aspirate the medium from the dish, and pre-feed the cells with mouse iPSC medium 1 hr before passaging. *For mouse iPSCs, a 1:6 passaging ratio is usually easily tolerated.*
15. After 1 hr aspirate the medium and wash the cells with 2 mL of PBS (no Ca or Mg).
16. Aspirate the PBS, add 0.5 mL of 0.25% trypsin/0.53 mM EDTA and incubate at 37°C with 5% CO₂ for 4 min.
17. Add 1 mL of the mouse iPSC medium and dissociate the colonies by pipetting up and down to create a single-cell suspension.

18. Transfer into a 15-mL tube containing 9 mL of warm mouse iPSC medium and centrifuge 4 min at $200 \times g$, at room temperature.
19. Discard the supernatant and resuspend the pellet in 12 mL of mouse iPSC medium.
20. Aspirate MEF medium from 6-well plates containing mitomycin C growth- inactivated or irradiated MEFs (prepared as described in *UNIT 23.2*) and add 2 mL of cell suspension per well. Incubate the cells at 37°C with 5% CO_2 until cells reach 80% to 90% confluency. Replenish with fresh mouse iPSC medium every 24 hr. *It is advisable to prepare frozen stocks of newly reprogrammed iPSCs at low passage for future use.*

Freezing mouse iPSCs

21. Let cells grow until they reach 80% to 90% confluency. Before beginning the freezing procedure, label 2-mL cryovials with information on cell line, passage number, and date. *Generally two 2-mL cryovials are used per well of a 6-well plate.*
22. Aspirate the cell culture medium from each well and wash cells with 2 mL of sterile PBS.
23. Remove PBS completely, add 0.5 mL of 0.25% trypsin/0.53 mM EDTA and incubate at 37°C and 5% CO_2 for 4 min (for 10-cm plate use 2 mL of 0.25% trypsin/0.53 mM EDTA).
24. Add 2.5 mL of serum-containing mouse iPSC medium and resuspend the cells by pipetting up and down to create a single-cell suspension.
25. Transfer the cell suspension to a 15-mL tube and add in mouse iPSC medium to a total volume of 10 mL. Count cells using a hemocytometer (*APPENDIX 3F*). Centrifuge 4 min at $200 \times g$, at room temperature
26. Aspirate the supernatant, then resuspend the pellet in freezing/cryopreservation medium (10% DMSO in FBS) to obtain a concentration of 2×10^6 cells per mL.
27. Transfer the cell suspension to pre-labeled cryovials at 1 mL per cryovial. *Labeling should include cell line, passage number, and date. Generally two cryovials are used per well of a 6-well plate.*
28. Quickly transfer the cryovials to a chilled isopropanol-containing cell-freezing container (4°C or on wet ice) and freeze at -80°C overnight. *Cells should be transferred to -80°C rapidly, since DMSO is toxic to cells in liquid phase.*
29. On the next day, remove cryovials from freezing container and store in the gas phase of a liquid nitrogen tank for long-term storage (may be kept frozen for many years).

Thawing mouse iPSCs

30. Using cryogenic hand gloves and eye protectors, remove the cryovial from the liquid nitrogen tank using forceps. *Caution: These safety measures are required, since cryovials stored in the liquid nitrogen tank may explode unexpectedly when exposed to rapid thawing.*

30. Immerse the vial in a 37°C water bath without submerging the cap.
31. Thaw vial rapidly until just a few ice crystals are left.
32. Record the sample name and passage number and spray 70% ethanol on the outer surface of the vial, then air dry quickly for a few seconds in a sterile laminar flow tissue culture hood.
33. Transfer the thawed cells to a 15-mL conical tube using a pipet with a P1000 pipet tip. Rinse the freezing vial once with 1 mL of mouse iPSC medium and add back to the 15-mL tube.
34. Add 10 mL of cold mouse iPSC medium drop-wise to cells in the 15-mL conical tube. While adding the medium, gently move the tube back and forth to mix the cells. *This step reduces osmotic shock to the cells.*
35. Centrifuge the cells 4 min at $200 \times g$, at room temperature.
36. Aspirate the supernatant and resuspend the cell pellet in 2 mL of mouse iPSC medium.
37. Slowly add the cell suspension in a dropwise fashion to a well of a gelatin-coated 6-well plate, pre-seeded with growth-inhibited MEF cells (prepared as in *UNIT 23.2*).
38. Culture cells as described above in a 37°C, 5% CO₂ incubator.

Alternate Protocol 1

Establishment and maintenance of Rat iPSCs

This protocol describes the establishment and maintenance of rat iPSCs. See Basic Protocol 2 for the viral infection procedure. *Figure 4* is a schematic diagram showing the process of generating rat iPSCs.

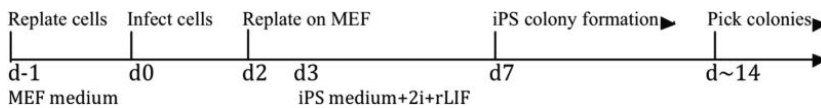


Figure 4. Schematic diagram of rat iPSC generation.

Materials

Rat fibroblasts infected with pluripotency factors (Basic Protocol 2); for timing, see *Figure 4* MEF medium (see recipe)

0.25% trypsin/0.53 mM EDTA (Invitrogen, cat. no. 25200-056)

Rat iPSC medium (see recipe for serum-free rat iPSC medium or KOSR-containing rat iPSC medium) with double concentration of LIF and with normal concentration of mouse LIF as specified in Reagents and Solutions

Doxycycline (Sigma, cat. no. D9891); optional

24- and 6-well plates of inactivated mouse fibroblast feeder cells (*UNIT 23.2*)

Phosphate-buffered saline (PBS) without CaCl₂ and MgCl₂ (Invitrogen 14190-250)
Freezing/cryopreservation medium (see recipe)
Isopropanol
Liquid N₂
70% ethanol
15-mL conical centrifuge tubes
Centrifuge
Light microscope with camera
Marker pen
20- μ L (P20) and 1000- μ L (P1000) pipet tips
2.0-mL cryovials
Freezing chamber (e.g., Mr. Frosty; Thermo Scientific, cat. no. 5100-0001)
Liquid nitrogen storage tank
Cryogenic handling gloves and eye protectors
Additional reagents and equipment for preparing inactivated mouse embryonic fibroblast feeder cells (*Unit 23.2*) and counting cells using a hemocytometer (*Appendix 3F*)

Note: There are two recipes for rat iPSC medium (see Reagents and Solutions): one for serum-free rat iPSC medium and one for KOSR-containing rat iPSC medium. Either of these media can be used for culturing rat iPSCs.

Post-infection Culturing of infected fibroblasts

1. After 48 hr of viral infection, or when cells reach confluency, aspirate the medium from the infected cells and dissociate by adding 0.5 mL of 0.25% trypsin/0.53 mM EDTA and incubating for 4 min at 37°C with 5% CO₂. Add 2 mL of warm MEF medium, then pipet up and down to obtain a single-cell suspension. Transfer to a 15-mL tube containing 9 mL of warm MEF medium and centrifuge 4 min at 200 \times *g*, room temperature.
2. Discard the supernatant and resuspend the pellet in 8 mL of MEF medium.
3. Aspirate the medium from four single wells of a 6-well plate that has been gelatin-coated and pre-seeded with growth-inhibited MEF cells (prepared as described in *UNIT 23.2*). Add 2 mL of the infected cell mixture per well onto the MEF feeder layer so that the infected cells are passaged in a 1:4 ratio. Incubate at 37°C with 5% CO₂.
4. After 12 to 24 hr change the medium to rat iPSC culture medium (supplemented with doxycycline at a final concentration of 1 μ g/mL, if using a TetO lentiviral system). For initial culture conditions, use double the concentration of rat LIF. After two to three passages, use the regular dose of LIF (1000 U/mL). *Colonies should start becoming microscopically visible approximately 7 to 10 days post-infection.*

5. Change rat iPSC medium supplemented with doxycycline (final concentration, 1 $\mu\text{g}/\text{mL}$ if using a TetO lentiviral system) every 24 hr and check for colony formation.
6. Let colonies grow into a reasonable size (>50 to 100 cells/colony).
This should take until approximately day 14 or 15 post-infection.
Cell death is a common problem when cells are transferred directly from serum-containing medium to serum-free medium or KOSR-containing medium, like rat iPSC medium. This may appear quite dramatic initially, as up to 50% of cells may fail to attach, but abundant viable and proliferative cells should be apparent after medium change.

Picking and establishing rat iPSC clones

7. One hour before picking iPSC colonies, pre-feed the cells by replenishing with fresh rat iPSC medium. *This is especially important when the medium has turned acidic (indicated by yellow color), since pre-feeding will increase cell survival after dissociation.*
8. Prepare a microscope inside a laminar hood to maintain sterile conditions for picking colonies (Figure 2).
9. Before picking, select up to 40 good colonies by circling the colony with a marker pen on the bottom of the plate to be able to retrieve the selected colonies when the actual picking procedure is started. *Suitable colonies should appear translucent and circular. See Figure 5 for examples of suitable rat iPSC colonies.*
10. Add 50 μL of 0.25% trypsin/0.53 mM EDTA into each of several 15-mL tubes.
11. Use a 20- μL (P20) pipet tip for the picking procedure. Pick one individual colony by gently scratching with the pipet tip. Make sure not to touch any neighboring colonies.
12. Transfer each picked colony into an individual 15-mL tube containing 50 μL of 0.25% trypsin/0.53 mM EDTA. Dissociate the colony by gently pipetting up and down and incubate at 37°C in water bath for 4 min.
13. After 4 min of incubation, add 5 mL of rat iPSC medium to each 15-mL tube containing one single colony and pipet up and down to dissociate the colony further into a single cell suspension. Centrifuge 4 min at 200 $\times g$, at room temperature.
14. Aspirate the supernatant and resuspend the pellet in 1 mL of rat iPSC medium. Transfer the cell suspension from each picked colony into a single well of a 24-well plate that has been gelatin-coated and pre-seeded with irradiated or mitomycin C-treated MEF cells (prepared as in UNIT 23.2). Incubate at 37°C with 5% CO_2 and replenish medium every 24 hr until nearly confluent. *Cells are now ready to be passaged into a 6-well plate.*

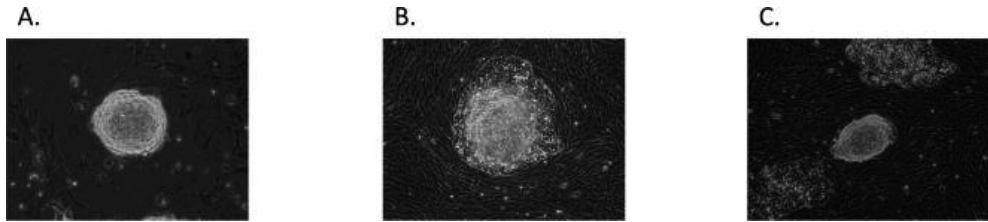


Figure 5. Examples of rat iPSC colonies. **(A)** A good rat iPSC colony. Note the translucent appearance and sharp borders. **(B)** a partially differentiated rat iPSC colony. This colony looks heterogeneous and differentiated. **(C)** One good rat iPSC colony (center) among two differentiated iPSC colonies (top and bottom). Care should be taken when picking the center colony not to touch the differentiated colonies.

In vitro culture and expansion of rat iPSCs

If reprogramming cells using a doxycycline-inducible system, wean the cells off doxycycline gradually after picking colonies. As a guideline, use the following schedule: use 1/2 concentration of doxycycline and then lower the concentration with each passage, to 1/4 concentration, then no doxycycline. If cell morphology begins to degrade, slow the rate of weaning. Do not change medium conditions at the time of passaging; rather, wait until the cells have attached (usually after 12 to 24 hr) before making changes to the doxycycline concentration.

15. When iPSC colonies reach 80% to 90% confluency in the dish or when individual iPSC colonies become large (approximately >100 cells/colony), aspirate the medium from the dish, and pre-feed the cells with rat iPSC medium 1 hr before passaging. *For rat iPSCs, a 1:6 passaging ratio is usually easily tolerated.*
16. After 1 hr aspirate the medium and wash the cells with 2 mL of PBS (no Ca or Mg).
17. Aspirate the PBS, add 0.5 mL of 0.25% trypsin/0.53 mM EDTA, and incubate at 37°C with 5% CO₂ for 4 min.
18. Add 1 mL of rat iPSC medium and dissociate the colonies by pipetting up and down into a single-cell suspension.
19. Transfer into a 15-mL tube containing 9 mL of warm rat iPSC medium and centrifuge 4 min at 200 × *g*, room temperature.
20. Discard the supernatant and resuspend the pellet in 12 mL of rat iPSC medium.
21. Aspirate the medium from 6-well plates containing mitomycin C–inactivated MEF (prepared as in *UNIT 23.2*), and add 2 mL of cell suspension per well. Incubate the cells at 37°C with 5% CO₂ until cells reach 80% to 90% confluency. Replenish with fresh rat iPSC medium every 24 hr. *It is advisable to prepare frozen stocks of newly reprogrammed iPSCs at low passage for future reference.*

Freezing rat iPSCs

22. Let cells grow until they reach 80% to 90% confluency. Before beginning the freezing procedure, label 2-mL cryovials with information on cell line, passage number, and date. *Generally two 2-mL cryovials are used per well of a 6-well plate.*
23. Aspirate the cell culture medium from each well and wash cells with 2 mL of sterile PBS.
24. Remove PBS completely, add 0.5 mL of 0.25% trypsin/0.53 mM EDTA, and incubate at 37°C with 5% CO₂ for 4 min (for 10-cm plate use 2 mL of 0.25% trypsin/0.53 mM EDTA).
25. Add 2.5 mL of serum containing rat iPSC medium and suspend the cells by pipetting up and down to create a single-cell suspension.
26. Transfer the cell suspension to a 15-mL tube and add in rat iPSC medium to a total volume of 10 mL. Count cells using a hemocytometer (*APPENDIX 3F*). Centrifuge 4 min at 200 × *g*, at room temperature.
27. Aspirate the supernatant, then resuspend the pellet in freezing/cryopreservation medium to obtain a concentration of 2 × 10⁶ cells per mL.
28. Transfer the cell suspension to pre-labeled cryovials at 1 mL per cryovial. *Generally two cryovials are used per well of a 6-well plate.*
29. Quickly store the cryovials in a chilled isopropanol-containing cell-freezing container (4°C or on wet ice) and freeze at –80°C overnight. Transfer cells to –80°C rapidly, since DMSO is toxic to cells in liquid phase.
30. On the next day, remove cryovials from freezing container and store in the gas phase of a liquid nitrogen tank for long-term storage (may be kept frozen for many years).

Thawing rat iPSCs

31. Using cryogenic hand gloves and eye protectors remove the cryovial from the liquid nitrogen tank using forceps.
CAUTION: These safety precautions are required since cryovials stored in the liquid nitrogen tank may explode unexpectedly when exposed to rapid thawing.
32. Immerse the vial in a 37°C water bath without submerging the cap.
33. Thaw vial rapidly until just a few ice crystals are left.
34. Record the sample name and passage number and spray 70% ethanol on the outer surface of the vial, then air dry quickly for a few seconds in a sterile laminar flow tissue culture hood.
35. Transfer thawed cells to a 15-mL conical tube using a pipet with a P1000 tip. Rinse freezing vial with 1 mL of rat iPSC medium and add to the 15-mL tube.
36. Add 10 mL of cold rat iPSC medium drop-wise to cells in the 15-mL conical tube. While adding the medium, gently move the tube back and forth to mix the cells. *This step reduces osmotic shock to the cells.*

37. Centrifuge the cells 4 min at $200 \times g$, at room temperature.
38. Aspirate the supernatant and resuspend the cell pellet in 2 mL of rat iPSC medium.
39. Slowly add the cell suspension in a drop-wise fashion into a well of a gelatin-coated 6-well plate, pre-seeded with growth-inhibited MEF cells (prepared as in *Unit 23.2*).
40. Culture cells as described above in a 37°C , 5% CO_2 incubator.

Alternate Protocol 2

Establishment and maintenance of pig iPSCs

This protocol describes the establishment and maintenance of pig iPSCs. See Basic Protocol 2 for the viral infection procedure. *Figure 6* is a schematic diagram showing the process of generating pig iPSCs.



Figure 6. Schematic diagram of pig iPSC generation.

Materials

Pig fibroblasts infected with pluripotency factors (Basic Protocol 2); for timing, see *Figure 6*.

MEF medium (see recipe)

0.25% trypsin/0.53 mM EDTA (Invitrogen, cat. no. 25200-056)

24- and 6-well plates of inactivated mouse fibroblast feeder cells (*UNIT 23.2*)

Matrigel-coated plates (see recipe; optional)

Pig iPSC culture medium (see recipe)

mTeSR1 medium (optional)

Doxycycline (Sigma, cat. no. D9891); optional

Phosphate-buffered saline (PBS) without CaCl_2 and MgCl_2 (Invitrogen, cat. no. 14190-250)

Collagenase IV

Accutase (optional)

Dispase (optional)

ROCK inhibitor Y27632 (Calbiochem, cat. no. 688000)

TeSR2 (STEMCELL Technologies, cat. no. 05860; optional)

mFreSR (STEMCELL Technologies, cat. no. 05855; optional)

Freezing/cryopreservation medium (see recipe)

Isopropanol

Liquid N_2

70% ethanol

15-mL conical tubes
Marker pen
Light microscope with camera
20- μ L (P20) and 1000- μ L (P1000) pipet tips
Cell lifter (Corning, cat. no. 3008)
Eppendorf Model 5810R benchtop centrifuge (or equivalent)
2.0-mL cryovials
Freezing chamber (e.g., Mr. Frosty; Thermo Scientific)
Liquid nitrogen storage tank
Cryogenic handling gloves and eye protectors
Forceps
Additional reagents and equipment for preparing inactivated mouse embryonic fibroblast feeder cells (*Unit 23.2*) and counting cells using a hemocytometer (*Appendix 3F*)

Post-infection culturing of infected fibroblasts

1. After 48 hr, or when cells reach confluency, aspirate the medium from the infected cells and dissociate by adding 0.5 mL of 0.25% trypsin/0.53 mM EDTA and incubating for 4 min at 37°C with 5% CO₂. Add 2 mL of warm MEF medium, then pipet up and down to obtain a single-cell suspension. Transfer to a 15-mL tube containing 9 mL of warm MEF medium, and centrifuge 4 min at 200 \times *g*, at room temperature.
2. Discard the supernatant and resuspend the pellet in 8 mL of MEF medium.
3. Aspirate the medium from four single wells of a 6-well plate that has been gelatin-coated and pre-seeded with growth-inhibited MEF cells as described in *Unit 23.2*. Add 2 mL of the infected cell mixture per well on to the MEF feeder layer so that the infected cells are passaged in a 1:4 ratio. Incubate at 37°C with 5% CO₂. *It is recommended to culture pig iPSCs on MEFs initially. Once stable colonies are established, the cells can be transferred to feeder-free conditions. If using MEFs, plate 1 million MEFs per 10-cm plate or approximately 170,000 MEFs per well of a 6-well plate. Use gelatin-coated plates.*
4. After 12 to 24 hr, exchange the medium for pig iPSC culture medium (supplemented with doxycycline at a final concentration of 1 μ g/mL if using a TetO lentiviral system).
5. Change pig iPSC medium supplemented with doxycycline (final concentration, 1 μ g/mL if using a TetO lentiviral system) every 24 hr and check for colony formation. *Colonies should start becoming microscopically visible approximately 7 to 10 days post-infection.*
6. Let colonies grow into a reasonable size (approximately >50 cells/colony). *This should take until approximately day 21 post-infection.*

Picking and establishing pig iPSC clones

7. One hour before picking iPSC colonies, pre-feed the cells by replenishing with fresh pig iPSC medium. *This is especially important when the medium has turned acidic (indicated by yellow color), since pre-feeding will increase cell survival after dissociation.*
8. Prepare a microscope inside a laminar hood to maintain sterile conditions for picking colonies (*Figure 2*).
9. Before picking, select up to 40 good colonies by circling the colony with a marker pen on the bottom of the plate to be able to retrieve the selected colonies when the actual picking procedure is started. *Suitable colonies should appear translucent and circular. See Figure 7 for examples of suitable pig iPSC colonies.*
10. Add 50 μ L of 0.25% trypsin/0.53 mM EDTA into each of several 15-mL tubes.
11. Use a 20 μ L (P20) pipet tip for the picking procedure. Pick one individual colony by gently scratching with the pipet tip. Make sure not to touch any neighboring colonies.
12. Transfer each picked colony into an individual 15-mL tube containing 50 μ L of 0.25% trypsin/0.53 mM EDTA. Dissociate the colony by gentle pipetting and incubate at 37°C in a water bath for 4 min. *Pick up as many colonies as possible within 15 min to limit exposure of picked colonies to trypsin.*
13. Dissociate the colony by gentle mechanical dissociation with the pipet tip and pipetting up and down. *Ideally, colonies should be dissociated into small cell clusters instead of single-cell dissociation.*
14. Once the colony is properly dissociated, add in 1 mL of pig iPSC medium. Transfer the cell suspension from each picked colony into a single well of a 24-well plate that has been gelatin-coated and pre-seeded with growth-inactivated MEF cells as described in *Unit 23.2*. *Alternatively, use feeder-free conditions using Matrigel-coated plates with mTeSR1 medium. Incubate at 37°C with 5% CO₂.*
15. After 48 hr, replenish the medium every 24 hr until cells reach 80% to 90% confluency. *This should take about 7 to 10 days. Cells are now ready to be passaged into a 6-well plate.*

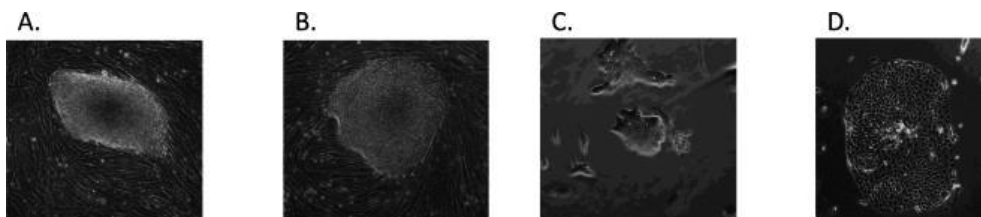


Figure 7. Examples of pig iPSC colonies. **(A)** A developing pig iPSC colony. **(B)** A good pig iPSC colony, cultured on MEFs. Note the translucent appearance and sharp borders. **(C)** A good pig iPSC colony grown on Matrigel. **(D)** A bad pig iPSC colony, grown on Matrigel. This colony looks heterogeneous and differentiated and should be removed from the culture dish.

In vitro culturing and expansion of pig iPSCs

If reprogramming cells using a doxycycline-inducible system, wean the cells off doxycycline gradually after picking colonies. As a guideline, use the following schedule: use 1/2 concentration of doxycycline and then lower the concentration with each passage, so 1/4 concentration, then no doxycycline. If cell morphology begins to degrade, slow the rate of weaning. Do not change medium conditions at the time of passaging; rather wait until the cells have attached (usually after 12 to 24 hr) before making changes to the doxycycline concentration.

16. Before splitting, remove differentiated colonies under a microscope under sterile conditions (i.e., via slow-vacuum aspiration or pipet scraping). Be careful not to leave the plate out too long and make sure cells do not dry out if using the vacuum method. See *Figure 7* for examples of good pig iPSC colonies as well as bad pig iPSC colonies that should be removed from the culture dish.
17. Wash cells with warm PBS (no Ca or Mg). Aspirate PBS and add 1 mL of 100 U/mL collagenase IV and incubate 4 min at 37°C with 5% CO₂ (for pig iPSCs grown on MEFs). *Alternatively, add 0.5 mL of 0.6 to 2.4 mg/mL Dispase or 0.5 mL of 1 × Accutase and incubate for 0.5 to 1 min at 37°C with 5% CO₂ (for pig iPSCs grown in feeder-free conditions). Collagenase IV is used for passaging cells grown on MEFs. For cells grown on Matrigel, use Dispase or Accutase instead of collagenase IV. Trypsinization is not recommended, since aggressive dissociation into single cells will not be well tolerated. Expect to see visible curling or thickening of colonies around the edges.*
18. Aspirate the enzyme and wash with 2 mL of PBS. After aspirating PBS, add 1 mL of pig iPSC medium supplemented with ROCK inhibitor (at 10 μM final concentration). Using a cell lifter, scrape the entire well to lift the colonies.
19. Transfer colonies into a 15-mL conical tube; wash the well with 1 mL of pig iPSC medium and transfer washings into the 15-mL tube. Centrifuge 4 min at 200 × g, at room temperature. Aspirate supernatant and leave the pellet undisturbed.
20. Resuspend the pellet in pig iPSC medium. Use 2 mL of medium per well of a 6-well plate that is going to be seeded. *The ratio depends on cell density prior to passaging. Usually a 1:3 ratio (1 nearly confluent well can be passaged into 3 new wells) serves as a good guideline. For this example, resuspend the cell pellet in 6 mL of medium.*
21. Triturate to obtain medium to small fragments (~50 to 200 cells per fragment). Avoid over-t triturating, since this may cause cell death, especially when colonies are broken down to single-cell suspensions.
22. Prewash wells of a gelatin-coated MEF-seeded 6-well plate (prepared as in *Unit 23.2*) or Matrigel-coated wells with 1 mL of warm pig iPSC medium, aspirate medium, and add 2 mL of suspended cell solution into each well.

23. Replenish the cells with 2 mL of fresh pig iPSC medium every 24 hr until cells reach confluency.

This usually takes about 7 to 10 days. Cells are now ready for passaging. It is advisable to prepare frozen stocks of newly reprogrammed iPSCs at low passage for future use. See below for freezing and thawing instructions. Cell death is a common problem when cells are transferred directly from serum-containing medium to serum-free medium, like mTeSR1 medium. This may appear quite dramatic initially as up to 50% of cells may fail to attach, but abundant viable and proliferative cells should become apparent upon medium change.

Freezing pig iPSCs

For cells grown on Matrigel/mTeSR1, a similar procedure can be followed, except for using 500 μ L of mFreSR per 6-well plate. mFreSR is a defined, serum-free cryopreservation medium designed for the cryopreservation of cells. It is very important to minimize the amount of pipetting to ensure later cell survival.

24. Before beginning the freezing procedure, label 2-mL cryovials with information on cell line, passage number, and date. *Generally one cryovial is used per well of a 6-well plate or five cryovials per 10-cm dish.*
25. Dissociate the cells of a nearly confluent well as described above in steps 16 to 19. Use collagenase IV for feeder/serum cultures and Dispase or Accutase for Matrigel/mTeSR1 cultures.
26. Add 500 μ L of freezing/cryopreservation medium to the cell pellet.
27. Carefully resuspend the pellet in the freezing medium, keeping cells in chunks that are as large as possible; generally pipetting two times should be enough.
28. Quickly transfer 500 μ L of the suspension into a pre-labeled 2-mL cryovial and place inside an isopropanol-containing freezing container. Store 24 to 48 hr at -80°C and then transfer to a liquid nitrogen storage tank. *When working with DMSO-containing freezing/cryopreservation medium, it is key to work as quickly as possible to transfer the freezing stock rapidly into a -80°C freezer to initiate the freezing procedure.*

Thawing pig iPSCs

Each vial should be thawed into 1 well of a 6-well plate. The passage number and the name of the cell line should be noted. Ideally cells should be kept in large clumps to increase survival efficiency, so vigorous pipetting should be avoided.

29. Add 9 mL of cold pig iPSC medium supplemented with 10 μ M ROCK inhibitor to a 15-mL tube.
30. Using cryogenic hand gloves and eye protectors remove the cryovial from the liquid nitrogen tank using forceps. *Caution: These safety precautions are required since cryovials stored in the liquid nitrogen tank may explode unexpectedly when exposed to rapid thawing.*

31. Remove the iPSC vial from the liquid nitrogen tank using forceps and immerse the vial in a 37°C water bath without submerging the cap. Thaw vial contents rapidly until just a few ice crystals are left.
32. Record the sample name and spray 70% ethanol on the outer surface of the vial then air dry quickly a few seconds in the sterile laminar hood.
33. Transfer the thawed cell mixture in the tube containing 9 mL of cold pig iPSC medium supplemented with ROCK inhibitor. Rinse the cryovial once with pig iPSC medium and transfer to tube.
34. Centrifuge 4 min at $200 \times g$, at room temperature.
35. Meanwhile, wash one well of a 6-well gelatin-coated and MEF-seeded (growth inhibited) with PBS. *Skip this step when using Matrigel plates.*
36. Add 2 mL of pig iPSC medium. *It is highly recommended that 10 μ M ROCK inhibitor Y-27632 be added for the first 24 hr to improve survival efficiency. Do not add ROCK inhibitor to medium replenishing steps that do not involve passaging or thawing.*
37. Aspirate the medium from the cell pellet and gently resuspend in 1 mL of pig iPSC medium supplemented with ROCK inhibitor. Pipet up and down slowly once or twice, avoiding disruption of the cell chunks. Transfer to one well of a 6-well plate.
38. Change the medium after 24 hr.
39. Feed cells daily with 2 mL medium. *Colonies may not develop the next day, but may emerge at any point from 3 to 10 days after plating.*
40. Perform the first passage mechanically, without the use of collagenase IV or Dispase. See steps 13 to 15 above for details. After this initial passage, cells can be cultured as described in steps 16 to 23. *It is highly recommended that a mycoplasma test (see Appendix 3F) be performed upon thawing.*

Alternative Protocol 3

Establishment and maintenance of human iPSCs

This protocol describes the establishment and maintenance of human iPSCs. See Basic Protocol 2 for the viral infection procedure. *Figure 8* is a schematic diagram showing the process of generating human iPSCs.

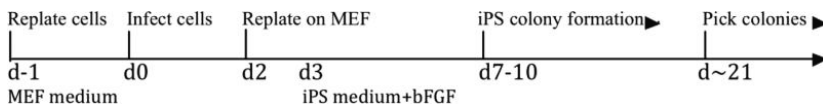


Figure 8. Schematic diagram of human iPSC generation.

Materials

Human fibroblasts infected with pluripotency factors (Basic Protocol 2); for timing, see *Figure 8*.

MEF medium (see recipe)

0.25% trypsin/0.53 mM EDTA (Invitrogen, cat. no. 25200-056)

24- and 6-well plates of inactivated mouse fibroblast feeder cells (*Unit 23.2*)

Human iPSC culture medium (see recipe)

Doxycycline (Sigma, cat. no. D9891; optional)

Matrigel-coated plates (see recipe; optional)

mTeSR1 medium (optional)

Phosphate-buffered saline (PBS) without CaCl₂ and MgCl₂ (Invitrogen 14190-250)

Collagenase IV

Accutase (optional)

Dispase (optional)

ROCK inhibitor Y27632 (Calbiochem, cat. no. 688000)

TeSR2 (STEMCELL Technologies, cat. no. 05860; optional)

mFreSR (STEMCELL Technologies, cat. no. 05855; optional) Freezing/

cryopreservation medium (see recipe)

Isopropanol

Liquid N₂

70% ethanol

15-mL conical tubes

Marker pen

Light microscope with camera

20- μ L (P20) and 1000- μ L (P1000) pipet tips

Cell lifter (Corning, cat. no. 3008)

Eppendorf Model 5810R benchtop centrifuge (or equivalent)

2.0-mL cryovials

Freezing chamber (e.g., Mr. Frosty; Thermo Scientific)

Liquid nitrogen storage tank

Cryogenic handling gloves and eye protectors

Forceps

Additional reagents and equipment for preparing inactivated mouse embryonic fibroblast feeder cells (*Unit 23.2*) and counting cells using a hemocytometer (*Appendix 3F*)

Post-infection culturing of infected fibroblasts

1. After 48 hr, or when cells reach confluency, aspirate the medium from the infected cells and dissociate by adding 0.5 mL of 0.25% trypsin-EDTA and incubating for 4 min at 37°C

with 5% CO₂. Add 2 mL of warm MEF medium, then pipet up and down to obtain a single-cell suspension. Transfer to a 15-mL tube containing 9 mL of warm MEF medium and centrifuge 4 min at 200 × g, at room temperature.

2. Discard the supernatant and resuspend the pellet in 8 mL of MEF cell culture medium.
3. Aspirate the medium from four single wells of a 6-wells plate that has been gelatin-coated and pre-seeded with growth-inhibited MEF cells as described in UNIT 23.2. Add 2 mL of the infected cell mixture per well onto the MEF feeder layer so that the infected cells are passaged in a 1:4 ratio. Incubate at 37°C with 5% CO₂. *It is recommended to culture human iPSCs on MEFs initially. Once stable colonies are established, the cells can be transferred to feeder-free conditions.*
4. After 12 to 24 hr, substitute the medium with human iPSC culture medium (supplemented with doxycycline if using a TetO lentiviral system).
5. Change human iPSC medium every 24 hr and check for colony formation. *Colonies should start becoming microscopically visible approximately 7 to 10 days post-infection.*
6. Let colonies grow to a reasonable size (approximately >50 cells/colony). *This should take until approximately day 21 post-infection.*

Picking and establishing human iPSC clones

7. One hour before picking iPSC colonies, pre-feed the cells by replenishing with fresh human iPSC medium. *This is especially important when the medium has turned acidic (indicated by yellow color), since pre-feeding will increase cell survival after dissociation.*
8. Prepare a microscope inside a laminar hood to maintain sterile conditions for picking colonies (Figure 2).
9. Before picking, select as many good colonies as necessary by circling the colony with a marker pen on the bottom of the plate to be able to retrieve the selected colonies when the actual picking procedure is started. *Suitable colonies should appear translucent and perfectly circular. See Figure 9 for examples of suitable human iPSC colonies.*
10. Place 50 µL of 0.25% trypsin/0.53 mM EDTA into each of several 15-mL tubes.
11. Use a 20-µL pipet tip for the picking procedure. Pick one individual colony by gently scratching with the pipet tip. Make sure not to touch any neighboring colonies.
12. Transfer each picked colony into an individual 15-mL tube containing 50 µL of 0.25% trypsin/0.53 mM EDTA. Dissociate the colony by gentle mechanical dissociation with the pipet tip and pipetting up and down. *Ideally, colonies should be dissociated into small cell clusters instead of single-cell dissociation.*
13. Once the colony is properly dissociated, add in 1 mL of human iPSC medium. Transfer the cell suspension from each picked colony into a single well of a 24-well plate that has been gelatin-coated and pre-seeded with growth-inactivated MEF cells as described in Unit

23.2. Incubate at 37°C with 5% CO₂. Alternatively, use feeder-free conditions using Matrigel-coated plates with mTeSR1 medium.

14. After 48 hr replenish human iPSC medium every 24 hr until cells reach 80% to 90% confluency. This should take about 7 to 10 days. Cells are now ready to be passaged into a 6-well plate.

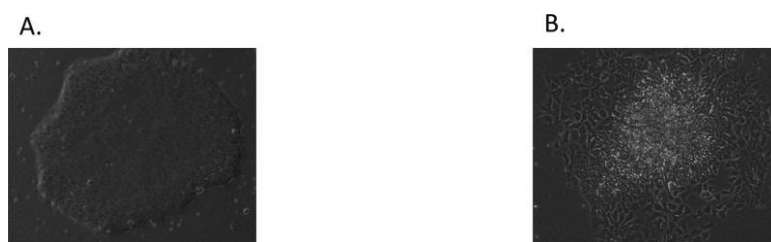


Figure 9. Examples of human iPSCs. (A) A good human iPSC colony grown on Matrigel. Note the translucent appearance and sharp borders. (B) A bad human iPSC colony grown on Matrigel. This colony looks heterogeneous and differentiated and should be removed from the culture dish. Images kindly provided by Dr. Emil M. Hansson at MGH Cardiovascular Research Center.

In vitro culture and expansion of human iPSCs

If reprogramming cells using a doxycycline-inducible system, wean the cells off doxycycline gradually after picking colonies. As a guideline, you can use the following schedule: use 1/2 concentration of doxycycline and then lower the concentration with each passage, so 1/4 concentration, then no doxycycline. If cell morphology begins to degrade, slow the rate of weaning. Do not change medium conditions at the time of passaging; rather wait until the cells have attached (usually after 12 to 24 hr) before making changes to the doxycycline concentration.

Note: If using MEFs plate 1 million MEFs per 10-cm plate or approximately 170,000 MEFs per well of a 6-well plate. Use gelatin-coated plates.

15. Before splitting, remove differentiated colonies under the microscope in sterile conditions (i.e., via slow-vacuum aspiration or pipet scraping). Be careful not to leave the plate out too long and make sure cells do not dry out if using the vacuum method. *See Figure 9 for examples of good human iPSC colonies as well as bad human iPSC colonies that should be removed from the culture dish.*
16. Wash cells with warm PBS (no Ca or Mg). Aspirate PBS and add 1 mL of 100 U/mL collagenase IV and incubate 4 min at 37°C with 5% CO₂ (for human iPSCs grown on MEFs). Alternatively, add 0.5 mL of 0.6 to 2.4 mg/mL Dispase or 0.5 mL of 1 × Accutase and incubate for 0.5 to 1 min at 37°C with 5% CO₂ (for human iPSCs grown in feeder-free conditions). Expect to see visible curling or thickening of colonies around the edges. *Collagenase IV is used for passaging cells grown on MEFs. For cells grown on Matrigel, use Dispase or Accutase in place of collagenase IV. Trypsinization is not recommended.*

17. Aspirate the enzyme and wash with 2 mL of PBS. After aspirating off PBS, add 1 mL of human iPSC medium supplemented with ROCK inhibitor (final concentration, 10 μ M). Using a cell lifter, scrape the entire well to lift the colonies.
18. Transfer colonies into a 15-mL conical tube; wash the well with 1 mL of human iPSC medium and transfer washings into the 15-mL tube. Centrifuge 4 min at 200 \times *g*, at room temperature. Aspirate supernatant and leave the pellet undisturbed.
19. Resuspend the pellet with human iPSC medium. Use 2 mL of medium per well of a 6-well plate that is going to be seeded. *The ratio depends on cell density prior to passaging. Usually a 1:3 ratio (1 nearly confluent well can be passaged into 3 new wells) serves as a good guideline. For this example, resuspend the cell pellet in 6 mL of medium.*
20. Triturate to obtain medium-to-small fragments (~50 to 200 cells per fragment). Avoid over-triturating since that will lead to cell death, especially when colonies are broken down to single-cell suspensions.
21. Pre-wash gelatin-coated and MEF-seeded wells or Matrigel-coated wells with 1 mL of warm human iPSC medium, aspirate medium, and add 2 mL of resuspended cell solution into each well.
22. Replenish the cells with 2 mL of fresh human iPSC medium every 24 hr until cells reach confluency. *This usually takes about 7 to 10 days. Cells are now ready for passaging. It is advisable to prepare frozen stocks of newly reprogrammed iPSCs at low passage for future use. Cell death is a common problem when cells are transferred directly from serum-containing medium to serum-free medium, like mTeSR1 medium. This may appear quite dramatic initially as up to 50% of cells may fail to attach, but abundant viable and proliferative cells should be able to become apparent upon medium change.*

Freezing human iPSCs

For cells grown on Matrigel/mTeSR1, a similar procedure can be followed as described below, except for using 500 μ L of mFreSR per 6-well. mFreSR is a defined, serum-free cryopreservation medium designed for the cryopreservation of human embryonic and induced pluripotent stem cells (hESCs and hiPSCs). Together with mTeSR1 or TeSR2, mFreSR eliminates the use of feeders and serum. hESCs cryopreserved in mFreSR have thawing efficiencies 5-to 10-fold higher than reported conventional thawing methods using serum.

Note: It is very important to minimize the amount of pipetting to ensure cell survival.

23. Before beginning the freezing procedure, label cryovials with information on cell line, passage number and date. Generally use one cryovial per well of a 6-well plate or five cryovials per 10-cm dish.
24. Dissociate the cells of a nearly confluent well as described above in steps 15-18 and use collagenase IV for feeder/serum cultures and Dispase or Accutase for Matrigel/mTeSR1 cultures.

25. Add 500 μL of freezing/cryopreservation medium to the cell pellet.
26. Carefully resuspend the pellet in the freezing medium, keeping cells in as large of chunks as possible; generally pipetting two times should be enough.
27. Quickly transfer 500 μL into a labeled cryovial, and place inside isopropanol-containing freezing container. Store 24 to 48 hr at -80°C , and then transfer to liquid nitrogen.

Thawing human iPSCs

Each vial should be thawed into 1 well of a 6-well plate. The passage number and the name of the cell line should be noted. Ideally, cells should be kept in large clumps to increase survival efficiency, so avoid vigorous pipetting.

28. Add 9 mL of cold human iPSC medium supplemented with 10 μM ROCK inhibitor into one 15-mL tube.
29. Using cryogenic hand gloves and eye protectors remove the cryovial from the liquid nitrogen tank using forceps
Safety precautions are required since cryovials stored in the liquid nitrogen tank may explode unexpectedly when exposed to rapid thawing.
30. Immerse the vial in a 37°C water bath without submerging the cap. Thaw vial rapidly until just a few ice crystals are left.
31. Record the sample name and spray 70% ethanol on the outer surface of the vial then air dry quickly a few seconds in the sterile laminar hood.
32. Transfer the thawed cell mixture in the tube containing 9 mL of cold human iPSC medium supplemented with ROCK inhibitor. Rinse the cryovial once with medium and transfer the rinse solution to the tube.
33. Centrifuge 4 min at $200 \times g$, at room temperature.
34. Meanwhile, wash one well of a 6-well plate that has been pre-coated with gelatin and seeded with irradiated or mitomycin C-treated MEF (prepared as in UNIT 23.2) with PBS. Skip this step when using Matrigel-only plates.
35. Aspirate the PBS and add 2 mL of human iPSC medium containing ROCK inhibitor (final concentration, 10 μM) to each well. *It is highly recommended to add 10 μM ROCK inhibitor Y-27632 for the first 24 hr to improve survival efficiency. ROCK inhibitor should not be added to any subsequent medium-replenishing steps that do not involve passaging or thawing. The ROCK Inhibitor Y-27632 enhances the survival rate of human embryonic stem cells following cryopreservation.⁴*
36. Aspirate the supernatant from the cell pellet after centrifugation and gently resuspend in 1 mL of human iPSC medium supplemented with ROCK inhibitor (at 10 μM final

- concentration). Pipet slowly once or twice, avoiding disruption of the cell chunks. Transfer to one well of a 6-well plate as prepared in step 34.
37. Change the medium after 24 hr.
 38. Feed cells daily with 2 mL medium. *Colonies may not develop the next day, but may emerge anywhere from 3 to 10 days.*
 39. Perform the first passage mechanically, without the use of collagenase IV or Dispase, as described in steps 7 to 14. After this initial passage, cells can be cultured as described in steps 15 to 22. *It is highly recommended to perform a mycoplasma test upon thawing.*

Reagents and solutions

Use deionized, distilled water in all recipes and protocol steps. For common stock solutions, see **Appendix 2**; for suppliers, see **Appendix 4**. Unless otherwise noted, all solutions and media are filter sterilized using a 0.22- μ M filter. All media must be stored at 4°C and should be used within 10 days of preparation, unless otherwise specified.

293FT Cell culture medium

450.00 mL DMEM (high glucose, Invitrogen, cat. no. 11965-092; 90% final)

50.00 mL fetal bovine serum (BenchMark FBS; Gemini Bioproducts, cat. no. 100-106; 10% final)

Store up to 1 month at 4°C

Cell culture dishes, pre-coated with 0.1% gelatin

Prepare 0.1% gelatin in sterile water. Incubate the culture dish (for 100-mm dish use Corning, cat. no. 430167) with the 0.1% gelatin for at least 30 min at room temperature. We recommend coating dishes right before use. Aspirate the excess gelatin and allow the plate to dry for 20 min.

Freezing/cryopreservation medium

900 μ L fetal bovine serum (BenchMark FBS; Gemini Bioproducts, cat. no. 100-106)

100 μ L dimethylsulfoxide (DMSO; Sigma D-2650)

Store up to 1 month at 4°C

For pig iPSCs or human iPSCs grown on Matrigel (BD Biosciences, cat. no. 354277) and mTeSR1 medium (STEMCELL Technologies 05850), it is advisable to use mFreSR medium (STEMCELL Technologies 05855) for cryopreservation.

Human iPSC medium

400 mL DMEM/F12 medium (Invitrogen, cat. no. 11330-057)
100 mL Knockout Serum Replacer (Invitrogen, cat. no. 10828-028)
5 mL L-glutamine (Invitrogen, cat. no. 25030-081)
5 mL MEM-NEAA (Invitrogen, cat. no. 11140-050)
5 mL penicillin/streptomycin solution (Invitrogen, cat. no. 15140-155)
3.5 μ L 2-mercaptoethanol (Sigma, cat. no. M7522)
5 to 10 μ g human bFGF (Invitrogen, cat. no. PHG0021)
Store up to 1 month at 4°C

Note: Knock-Out DMEM medium (Invitrogen, cat. no. 10829) can be used in place of DMEM/F12 medium. bFGF final concentration should be between 4 and 10 ng/mL. Addition of human bFGF will help maintain cells in an undifferentiated state.

Matrigel-coated culture dishes

Matrigel (BD Biosciences, cat. no. 354277) should be thawed and aliquoted on ice. Aliquots can be stored at -80°C . Mix the Matrigel and ice-cold Knock-Out DMEM medium (Invitrogen, cat. no. 10829) in a ratio of 1:100 on ice. Pipet to mix thoroughly and apply immediately to culture dishes, making sure to coat the entire bottom of the plate. Use 2 mL/well of a 6-well or 1 mL/well of a 24-well plate. Incubate the plate at 37°C for 1 hr. Plates can be used immediately or wrapped with Parafilm and stored at 4°C up to 15 days. Before use aspirate the Matrigel and wash once with cell culture medium.

Store up to 1 month at 4°C .

MEF medium

500.00 mL DMEM (high glucose; Invitrogen, cat. no. 11965-092; 81% final)
94.00 mL fetal bovine serum (BenchMark FBS; Gemini Bioproducts, cat. no. 100106; heat inactivated; 15% final)
12.50 mL pen/strep (5000 penicillin/5000 mg/mL streptomycin; Invitrogen, cat. no. 15070-063; 2% final)
6.25 mL 200 mM L-glutamine (Invitrogen, cat. no. 25030-081; 1% final)
6.25 mL 10 mM (100 \times MEM nonessential amino acids (Invitrogen, cat. no. 11140050; 1% final)
Store up to 1 month at 4°C

Mouse iPSC medium (CJ7 medium)

500.00 mL DMEM (high glucose; Invitrogen, cat. no. 11965-092; 81% final)

94.00 mL fetal bovine serum (BenchMark FBS; Gemini Bioproducts, cat. no. 100106; heat inactivated; 15% final)

12.50 mL penicillin/streptomycin solution (5000 penicillin/5000 mg/mL streptomycin; Invitrogen, cat. no. 15070-063; 2% final)

6.25 mL 200 mM L-glutamine (Invitrogen, cat. no. 25030-081; 1% final)

6.25 mL 10 mM (100× MEM nonessential amino acids (Invitrogen, cat. no. 11140050; 1% final)

4.4 μL 2-mercaptoethanol (2-ME; Sigma, cat. no. M-6250; $\sim 10^{-4}$ M final)

62.5 μL mouse LIF (10^7 U/mL stock; Chemicon, cat. no. ESG1107; 10^3 U/mL final)

Store up to 1 month at 4°C

Complete medium is stable for ~2 weeks. Medium older than this should be re-supplemented with fresh L-glutamine and mouse LIF.

Pig iPSC medium

400 mL DMEM/F12 Medium (Invitrogen, cat. no. 11330-057)

100 mL Knockout Serum Replacement (Invitrogen, cat. no. 10828-028)

5 mL L-glutamine (Invitrogen, cat. no. 25030-081)

5 mL of 10 mM (100×) MEM nonessential amino acids (Invitrogen, cat. no. 11140050)

5 mL penicillin/streptomycin solution (5000 penicillin/5000 mg/mL streptomycin; Invitrogen, cat. no. 15070-063)

3.5 μL 2-mercaptoethanol (Sigma, cat. no. M7522)

5 to 10 μg human bFGF (Invitrogen, cat. no. PHG0021)

Store up to 1 month at 4°C

Note: Knock-Out DMEM medium (Invitrogen, cat. no. 10829) can be used in place of DMEM/F12 medium. bFGF final concentration should be between 4 and 10 ng/mL. Addition of human bFGF will help maintain cells in an undifferentiated state.

Rat iPSC medium containing KOSR

400 mL Knockout DMEM (Invitrogen, cat. no. 10829)

100 mL Knockout Serum Replacer (Invitrogen, cat. no. 10828-028)

5 mL L-glutamine (Invitrogen, cat. no. 25030-081)

5 mL of 10 mM 100× MEM nonessential amino acids (Invitrogen, cat. no. 11140050)

5 mL penicillin/streptomycin solution (5000 penicillin/5000 mg/mL streptomycin; Invitrogen, cat. no. 15070-063)

3.5 μL 2-mercaptoethanol (2-ME; Sigma, cat. no. M7522)

Store up to 1 month at 4°C

Rat iPSC medium, serum-free

Prepare DMEM/F12-N2 medium: To 100 mL DMEM-F12 Medium (Invitrogen, cat. no. 11330-057), add 1 mL 100× N2 supplement (Invitrogen, cat. no. 17502048). Store at 4°C and use within 1 month.

Prepare neurobasal/B27 medium: To 100 mL Neurobasal Medium (Invitrogen, cat. no. 21103), add 2 mL B27 (Invitrogen, cat. no. 17504-044), and 0.5 to 1 mL of 200 mM L-glutamine (Invitrogen, cat. no. 25030-081). Store at 4°C and use within 1 month.

Prepare the serum-free rat iPSC medium: Mix DMEM/F12-N2 medium with Neurobasal/B27 medium in a ratio of 1:1. Add 2-mercaptoethanol (Sigma, cat. no. M7522) to a final concentration of 0.1 mM. Store at 4°C and use within 1 month.

For establishing and culturing Rat iPSCs, rat iPSC medium should always be supplemented with 0.5 μM MEK inhibitor (e.g., PD0325901, Stemgent, cat. no. 04-0006; <http://www.stemgent.com>), 3 μMGSK3β inhibitor (e.g., CHIR99021, Stemgent, cat. no. 04-0004), and 1000 U/mL of Rat LIF (Millipore, cat. no. LIF3005). Add freshly before use. These supplements help maintain rat iPSCs in an undifferentiated state.

Commentary

Background information

Regenerative medicine has gained significant promise in recent years for treating chronic and debilitating diseases.⁵ As the aging population increases in the U.S., it has become a medical and scientific imperative to find ways to alleviate the suffering of patients with some of the most challenging illnesses such as Alzheimer's disease, congestive heart failure, and emphysema. While the route to success in treating these diseases is far from clear at the moment, a number of scientific advances have enabled us to envision how cell replacement therapy may be accomplished. One such approach involves the use of pluripotent stem cells (PSCs), which exhibit both the ability to self-renew indefinitely and differentiate spontaneously into a wide variety of different cell types. Initial PSC studies in the 1970s employed a germline tumor called teratocarcinoma, which exhibits features of pluripotent stem cells but with the propensity for unchecked growth.⁶ Due to its cancer-like features, teratocarcinoma was relegated to nothing more than a developmental oddity. Then, in the early 1980s, with the isolation of mouse embryonic stem cells (ESCs),⁷ it became possible for investigators to engineer genome modifications that could be studied by *in vitro* differentiation or, when introduced into the germline, could even generate knock-out mice for *in vivo* studies. Since mouse ESCs were karyotypically normal, they contributed efficiently to all adult tissues when

injected into a developing blastocyst stage embryo. Furthermore, the creation of live-born animals exclusively from injected ESC in a tetraploid complementation assay validated the true developmental competency of these mouse ESCs.⁸⁻⁹ This has enabled the generation of countless numbers of genetic mouse models of human disease. However, despite these technical advances for deriving mouse ESCs, it took yet another 18 years for the generation of ESCs from discarded human embryos.¹⁰

Although mouse and human ESCs are now providing a platform for studies of early development, the use of human fetal-derived cells has been highly controversial. Furthermore, for a cell-based therapy to be successful, it would ideally involve immunohistocompatible donor cells with immunocompetent host individuals to avoid the need for immunosuppressants. In order to circumvent these issues, it would be desirable to have a source of pluripotent stem cell that can be derived easily from somatic cells. Early seminal work by Jon Gurdon and others demonstrated that the introduction of somatic cell nuclei from frogs into an enucleated oocyte can induce pluripotent gene expression in the nucleus of the injected somatic cell.¹¹ This principle was subsequently used to generate “cloned” animals such as Dolly the sheep.¹² Despite the success with nuclear cloning of multiple animal species, including primates,¹³⁻¹⁴ this approach has not led to successful human nuclear cloning thus far. The reason for this is likely due to the limited availability of donor human eggs. The challenging social climate for human embryo work has also not been conducive to significant progress in this area.

To overcome these challenges in human somatic cell nuclear transfer, Takahashi and Yamanaka set out to prove that direct reprogramming by means of transcription factor overexpression could be feasible.¹ In their seminal work, they systematically screened 24 transcription factors that are highly expressed in undifferentiated ESCs to find a combination of as few as four factors (Sox2, Oct4, Klf-4, and c-Myc) that could reprogram mouse embryonic fibroblasts into ESC-like cells. These induced pluripotent stem cells (iPSCs) express Nanog, Rex1, Oct4, and Sox2 from their endogenous loci and are able to silence the expression of exogenously supplied transcription factors to enable their differentiation *in vitro*. Following this groundbreaking work, many investigators from around the world have been able to reproduce these findings.¹⁵⁻¹⁷ Furthermore, the developmental competency of a subset of iPSCs lines were validated by their ability to generate “all-iPSC” mice in tetraploid complementation assays.¹⁸⁻²¹

Remarkable advances have since been made to improve the efficiency of iPSC generation. While the use of viral vectors has established the feasibility of transcription factor-based reprogramming, concerns regarding the potential tumorigenicity from viral-mediated genome modification have spurred the development of reprogramming strategies that are virus-free.

Such methods include non-integrating adenoviral vectors,²² naked plasmid transfection,²³ mini-circle plasmids,²⁴ proteins,²⁵ modified RNA,²⁶ and genome-editing enzymes such as Cre recombinase²⁷⁻²⁸ and transposases.²⁹⁻³⁰ While these non-integrating strategies induce minimal genome perturbation, their overall reprogramming efficiency is usually 100 to 1000 times lower than viral-based strategies. With the availability of lentiviruses carrying polycistronic cassettes encoding all four reprogramming factors, the efficiency of reprogramming has increased significantly.³¹⁻³²

Given the high degree of conservation of pluripotency gene function, iPSCs have been derived from a number of different popular species, including mouse,¹ rat,³³⁻³⁴ sheep,³⁵ pig,³⁶ rhesus monkey,³⁷ and human,³⁸⁻⁴⁰ as well as endangered species such as the drill and the nearly extinct northern white rhinoceros.⁴¹ This has been a remarkable feat, since the derivation of true ESC lines from some of these species (e.g., rat, sheep, pig) has been technically challenging. The availability of iPSCs from these species now allows creation of genetic models in large animals that may exhibit a more similar disease phenotype as human.

Critical parameters

The following guidelines should be followed to maximize reprogramming efficiency. Make sure to use fresh chemicals and unexpired media ingredients that have been handled and stored under recommended storage conditions. Fibroblasts should be of low passage number (ideally below p3) to avoid replicative senescence. Cells should never be allowed to become overconfluent, since this affects their reprogramming amenability. Similarly, do not let the feeder cells become overconfluent, or their abilities as feeder cells may decrease. When cells have been successfully reprogrammed into iPSCs, it is also important not to let cells become overconfluent since this will affect their pluripotent state and cells will start differentiating or die. To achieve this, cells should be cultured in fresh feeder and iPSC medium that should be replenished regularly (ideally every 24 hr), and cells should be passaged when reaching approximately 80% to 90% confluency.

At the virus-producing step, it is advisable to transfect the virus-producing cells with a suitable control to monitor the transfection efficiency. For this purpose, generally a lentiviral GFP or pMXs retroviral GFP vector can be used. This can be assessed by flow cytometry of the virus-producing cells. We routinely obtain 70% to 80% efficiency. High-efficiency transfection is crucial for iPSC induction.

For viral overexpression of transcription factors, it is important to use a high-titer virus with a high infection rate. Preferably use fresh virus and avoid multiple freeze/thaw cycles, as this

decreases the viral titer. When choosing a viral system, it is recommended to use a doxycycline-inducible lentiviral system, since this provides better control over transgene expression and silencing.

It is imperative for cell health and reprogramming efficiency to replenish with fresh medium regularly. If the cell medium color changes to yellow (indicator of medium acidity), change the medium immediately. It is always better to pre-feed 1 hr before passaging and/or freezing, since this reduces excessive cell death. For long-term storage, keep frozen cells in the gas phase of a liquid nitrogen tank. The recovery of iPSCs after freezing is about 50%.

Troubleshooting

This protocol has proven to have an extremely high success rate in our hands, generating good iPSC colonies almost 100% of the time. In case no or inefficient reprogramming is achieved, there are a few issues that need to be considered before repeating. First, make sure to use fresh fibroblasts of low passage number (passage <3). High-passage-number cells have significantly lower reprogramming efficiency. Second, it is of eminent importance that the virus used for reprogramming be of good quality in order for there to be a good viral infection rate. Only use fresh virus and limit freeze/thaw cycles to not more than one. It is worth considering checking whether the viral transfection rate in virus-producing cells is efficient by using a GFP control vector (see Critical Parameters for details). In case of small numbers of colonies after viral infection, one can also increase the MOI empirically to increase reprogramming efficiency.

If iPSCs are showing decreased survival or are not attaching to the feeder after passaging or colony picking, it may be due to excessive exposure to trypsin or vigorous pipetting. Make sure to pipet the cells gently when triturating and limit the exposure time to trypsin.

If the colonies are differentiating or disintegrating, this may be due to partial reprogramming or improper culturing conditions. Pick only iPSC clones of good morphology. Make sure to use freshly prepared medium at all times, with fresh reagents, to support the pluripotent conditions (especially LIF). Proof of pluripotency can be checked by analyzing the quantitative expression of pluripotent markers, teratoma assay in SCID mice and by chimeric mouse assays. It is advisable to do regular periodic mycoplasma testing (once a month) to rule out an underlying mycoplasma infection as the reason for unsuccessful reprogramming or culturing.

Anticipated results

The infection efficiency of fresh high titer virus in fibroblasts is more than 60%. Efficiency of iPSC clone derivation from infected (integrated) is approximately 1% for MEFs and 0.1% for TTFs.

After 24 hr of viral infection, many fibroblasts may die due to viral cytotoxicity, but a sufficiently large number of fibroblasts may proliferate abundantly and become confluent within 2 days. High-quality iPSC clones mimic the ESC-like proliferation and morphology (e.g., round shape, large nucleoli and translucent cytoplasm). Poor-quality iPSC clones do not exhibit ESC morphology and will not proliferate continuously when cultured in mouse iPSC medium.

Time considerations

Isolation and culture of embryonic fibroblasts generally takes up to 10 days.

Pause point: The mitomycin C-treated mouse feeder cells can be kept in the incubator for up to a week before use, but every 3 days fresh MEF medium should be replenished.

Virus can be harvested within 2 days after transfecting virus-producing cells with viral plasmids. It is recommended to do this in advance, since reprogramming virus can be stored at -80°C up to 1 year until ready for use. After successful infection, colonies start forming after 10 to 21 days, depending on the species. Picking and establishing iPSC colonies can take an additional 3 to 4 weeks.

It is recommended to freeze early-passage iPSCs (immediately after complete doxycycline weaning in case of using an inducible viral system). If necessary, cells can also be cultured and frozen at early passage for future use. For long-term storage, keep frozen cells in the gas phase of a liquid nitrogen tank. The recovery of iPSCs after freezing is about 50%.

Acknowledgments

This work was supported by grants from the Netherlands Organisation for Scientific Research (M.C.E.), NIH (OD004411, HL081086, HL100408 to S.M.W.) and the Harvard Stem Cell Institute (S.M.W.).

References

1. Takahashi K, Yamanaka S. Induction of pluripotent stem cells from mouse embryonic and adult fibroblast cultures by defined factors. *Cell*. 2006;126:663-676.
2. Donovan J, Brown P. Euthanasia. *Curr Protoc Immunol*. 2006;73:1.8.1-1.8.4.
3. Park IH, Lerou PH, Zhao R, Huo H, Daley GQ. Generation of human-induced pluripotent stem cells. *Nat Protoc*. 2008;3:1180-1186.
4. Li X, Meng G, Krawetz R, Liu S, Rancourt DE. The ROCK inhibitor Y-27632 enhances the survival rate of human embryonic stem cells following cryopreservation. *Stem Cells Dev*. 2008;17:1079-1085.
5. Wu SM, Hochedlinger K. Harnessing the potential of induced pluripotent stem cells for regenerative medicine. *Nat Cell Biol*. 2011;13:497-505.
6. Hogan BL. Changes in the behavior of teratocarcinoma cells cultivated in vitro. *Nature*. 1976;263:136-137.
7. Evans MJ, Kaufman MH. Establishment in culture of pluripotential cells from mouse embryos. *Nature*. 1981;292:154-156.
8. Nagy A, Góczy E, Diaz EM, Prideaux VR, Iványi E, Markkula M, Rossant J. Embryonic stem cells alone are able to support fetal development in the mouse. *Development*. 1990;110:815-821.
9. Eggen K, Akutsu H, Loring J, Jackson-Grusby L, Klemm M, Rideout WM 3rd, Yanagimachi R, Jaenisch R. Hybrid vigor, fetal overgrowth, and viability of mice derived by nuclear cloning and tetraploid embryo complementation. *Proc Natl Acad Sci U S A*. 2001;98:6209-6214.
10. Thomson JA, Itskovitz-Eldor J, Shapiro SS, Waknitz MA, Swiergiel JJ, Marshall VS, Jones JM. Embryonic stem cell lines derived from human blastocysts. *Science*. 1998;282:1145-1147.
11. Gurdon JB. The developmental capacity of nuclei taken from intestinal epithelium cells of feeding tadpoles. *J Embryol Exp Morphol*. 1962;10:622-640.
12. Campbell KH, McWhir J, Ritchie WA, Wilmut I. Sheep cloned by nuclear transfer from a cultured cell line. *Nature*. 1996;380:64-66.
13. Chan AW, Dominko T, Luetjens CM, Neuber E, Martinovich C, Hewitson L, Simerly CR, Schatten GP. Clonal propagation of primate offspring by embryo splitting. *Science*. 2000;287:317-319.
14. Byrne JA, Pedersen DA, Clepper LL, Nelson M, Sanger WG, Gokhale S, Wolf DP, Mitalipov SM. Producing primate embryonic stem cells by somatic cell nuclear transfer. *Nature*. 2007;2:497-502.
15. Maherali N, Sridharan R, Xie W, Utikal J, Eminli S, Arnold K, Stadtfeld M, Yachechko R, Tchieu J, Jaenisch R, Plath K, Hochedlinger K. Directly reprogrammed fibroblasts show global epigenetic remodeling and widespread tissue contribution. *Cell Stem Cell*. 2007;1:55-70.
16. Okita K, Ichisaka T, Yamanaka S. Generation of germline-competent induced pluripotent stem cells. *Nature*. 2007;448:313-317.
17. Wernig M, Meissner A, Foreman R, Brambrink T, Ku M, Hochedlinger K, Bernstein BE, Jaenisch R. In vitro reprogramming of fibroblasts into a pluripotent ES-cell-like state. *Nature*. 2007;448:318-324.
18. Boland MJ, Hazen JL, Nazor KL, Rodriguez AR, Gifford W, Martin G, Kupriyanov S, Baldwin KK. Adult mice generated from induced pluripotent stem cells. *Nature*. 2009;461:91-94.
19. Kang L, Wang J, Zhang Y, Kou Z, Gao S. iPS cells can support full-term development of tetraploid blastocyst-complemented embryos. *Cell Stem Cell*. 2009;5:135-138.
20. Zhao XY, Li W, Lv Z, Liu L, Tong M, Hai T, Hao J, Guo C.L., Ma, Q.W., Wang, L., Zeng, F., and Zhou, Q. iPS cells produce viable mice through tetraploid complementation. *Nature*. 2009;461:86-90.
21. Stadtfeld M, Apostolou E, Akutsu H, Fukuda A, Follett P, Natesan S, Kono T, Shioda T, Hochedlinger K. Aberrant silencing of imprinted genes on chromosome 12qF1 in mouse induced pluripotent stem cells. *Nature*. 2010;465:175-181.

22. Stadtfeld M, Nagaya M, Utikal J, Weir G, Hochedlinger K. Induced pluripotent stem cells generated without viral integration. *Science*. 2008;322:945-949.
23. Okita K, Nakagawa M, Hyenjong H, Ichisaka T, Yamanaka S. Generation of mouse induced pluripotent stem cells without viral vectors. *Science*. 2008;322:949-953.
24. Jia F, Wilson KD, Sun N, Gupta DM, Huang M, Li Z, Panetta NJ, Chen ZY, Robbins RC, Kay MA, Longaker MT, Wu JC. A nonviral minicircle vector for deriving human iPS cells. *Nat Methods*. 2010;7:197-199.
25. Zhou H, Wu S, Joo JY, Zhu S, Han DW, Lin T, Trauger S, Bien G, Yao S, Zhu Y, Siuzdak G, Schöler HR, Duan L, Ding, S. Generation of induced pluripotent stem cells using recombinant proteins. *Cell Stem Cell*. 2009;4:381-384.
26. Warren L, Manos PD, Ahfeldt T, Loh YH, Li H, Lau F, Ebina W, Mandal PK, Smith ZD, Meissner A, Daley GQ, Brack AS, Collins JJ, Cowan C, Schlaeger TM, Rossi DJ. Highly efficient reprogramming to pluripotency and directed differentiation of human cells with synthetic modified mRNA. *Cell Stem Cell*. 2010;7:618-630.
27. Kaji K, Norrby K, Paca A, Mileikovsky M, Mohseni P, Woltjen K. Virus-free induction of pluripotency and subsequent excision of reprogramming factors. *Nature*. 2009;458:771- 775.
28. Soldner F, Hockemeyer D, Beard C, Gao Q, Bell GW, Cook EG, Hargus G, Blak A, Cooper O, Mitalipova M, Isacson O, Jaenisch R. Parkinson's disease patient-derived induced pluripotent stem cells free of viral reprogramming factors. *Cell*. 2009;136:964-977.
29. Woltjen K, Michael IP, Mohseni P, Desai R, Mileikovsky M, Hämäläinen, R, Cowling R, Wang W, Liu P, Gertsenstein M, Kaji K, Sung HK, Nagy A. PiggyBac transposition reprograms fibroblasts to induced pluripotent stem cells. *Nature*. 2009;458:766- 770.
30. Yusa K, Rad R, Takeda J, Bradley A. Generation of transgene-free induced pluripotent mouse stem cells by the piggyBac transposon. *Nat Methods*. 2009;6:363-369.
31. Carey BW, Markoulaki S, Hanna J, Saha K, Gao Q, Mitalipova M, Jaenisch R. Reprogramming of murine and human somatic cells using a single polycistronic vector. *Proc Natl Acad Sci U S A*. 2009;106:157-162.
32. Sommer CA, Stadtfeld M, Murphy GJ, Hochedlinger K, Kotton DN, Mostoslavsky G. Induced pluripotent stem cell generation using a single lentiviral stem cell cassette. *Stem Cells*. 2009;27:543-549.
33. Li W, Wei W, Zhu S, Zhu J, Shi Y, Lin T, Hao E, Hayek A, Deng H, Ding S. Generation of rat and human induced pluripotent stem cells by combining genetic reprogramming and chemical inhibitors. *Cell Stem Cell*. 2009;4:16-19.
34. Kobayashi T, Yamaguchi T, Hamanaka S, Kato-Itoh M, Yamazaki Y, Ibata M, Sato H, Lee YS, Usui J, Knisely AS, Hirabayashi M, Nakauchi H. Generation of rat pancreas in mouse by interspecific blastocyst injection of pluripotent stem cells. *Cell*. 2010;142:787-799.
35. Li Y, Cang M, Lee AS, Zhang K, Liu D. Reprogramming of sheep fibroblasts into pluripotency under a drug-inducible expression of mouse-derived defined factors. *PLoS One*. 2011;6:e15947.
36. Ezashi T, Telugu BP, Alexenko AP, Sachdev S, Sinha S, Roberts RM. Derivation of induced pluripotent stem cells from pig somatic cells. *Proc Natl Acad Sci U S A*. 2009;106:10993-10998.
37. Liu H, Zhu F, Yong J, Zhang P, Hou P, Li H, Jiang W, Cai J, Liu M, Cui K, Qu X, Xiang T, Lu D, Chi X, Gao G, Ji W, Ding M, Deng H. Generation of induced pluripotent stem cells from adult rhesus monkey fibroblasts. *Cell Stem Cell*. 2008;3:587-590.
38. Takahashi K, Tanabe K, Ohnuki M, Narita M, Ichisaka T, Tomoda K, Yamanaka, S. Induction of pluripotent stem cells from adult human fibroblasts by defined factors. *Cell*. 2007;131:861-872.
39. Yu J, Vodyanik MA, Smuga-Otto K, Antosiewicz-Bourget J, Frane JL, Tian S, Nie J, Jonsdottir GA, Ruotti V, Stewart R, Slukvin II, Thomson JA. Induced pluripotent stem cell lines derived from human somatic cells. *Science*. 2007;318:1917- 1920.
40. Park IH, Zhao R, West JA, Yabuuchi A, Huo H, Ince TA, Lerou PH, Lensch MW, Daley, GQ. Reprogramming of human somatic cells to pluripotency with defined factors. *Nature*. 2008;451:141-146.

41. Friedrich Ben-Nun I, Montague SC, Houck ML, Tran HT, Garitaonandia I, Leonardo TR, Wang YC, Charter SJ, Laurent LC, Ryder OA, Loring JF. Induced pluripotent stem cells from highly endangered species. *Nat Methods*. 2011;8:829-831.

CHAPTER 3

Insulin-like growth factor promotes cardiac lineage induction *in vitro* by selective expansion of early mesoderm

Marc C. Engels^{1,2}, Kuppusamy Rajarajan¹, Rebecca Feistritz¹, Arun Sharma³, Ulrik B. Nielsen⁴, Martin J. Schalij², Antoine A.F. de Vries², Daniël A. Pijnappels², Sean M. Wu^{1,5}

¹Cardiovascular Research Center, Division of Cardiology, Department of Medicine, Massachusetts General Hospital, Boston, Massachusetts, USA

²Laboratory of Experimental Cardiology, Department of Cardiology, Heart Center Leiden, Leiden University Medical Center, Leiden, The Netherlands

³Department of Biology, Stanford University, Stanford, California, USA

⁴Silver Creek Pharmaceuticals Inc., San Francisco, California, USA

⁵Harvard Stem Cell Institute, Cambridge, Massachusetts, USA

Adapted from: Stem Cells. 2014;32:1493-1502.

Abstract

A thorough understanding of the developmental signals that direct pluripotent stem cells (PSCs) toward a cardiac fate is essential for translational applications in disease modeling and therapy. We screened a panel of 44 cytokines/signaling molecules for their ability to enhance Nkx2.5⁺ cardiac progenitor cell (CPC) formation during *in vitro* embryonic stem cell (ESC) differentiation. Treatment of murine ESCs with insulin or insulin-like growth factors (IGF1/2) during early differentiation increased mesodermal cell proliferation and, consequently, CPC formation. Furthermore, we show that downstream mediators of IGF signaling (e.g., phospho-Akt and mTOR) are required for this effect. These data support a novel role for IGF family ligands to expand the developing mesoderm and promote cardiac differentiation. Insulin or IGF treatment could provide an effective strategy to increase the PSC-based generation of CPCs and cardiomyocytes for applications in regenerative medicine.

Introduction

Despite the availability of many treatment options, heart disease remains the leading cause of death worldwide, prompting the need for more innovative therapeutic strategies such as cell-based therapy.¹ The ability to produce patient-specific induced pluripotent stem cells (iPSCs) holds great promise for such regenerative applications.^{2,3} A pivotal challenge in translating the potential of iPSCs into effective cardiac therapy is to generate sufficient quantities of functional cardiomyocytes to replace the large numbers of cells that are lost after myocardial injury.⁴ Although *in vitro* cardiac differentiation protocols for pluripotent stem cells (PSCs) are readily available, the yield for most PSC lines remains modest and highly variable.^{5,6} To improve the efficiency of cardiac differentiation, it is critical to understand the molecular mechanism of pluripotent cell commitment toward mesoderm during early development.⁷

In vitro differentiation of embryonic stem cells (ESCs) has been used to model early cardiac development due to the limited number of cells available when working with early stage embryos. When provided with appropriate cues, ESCs have been shown to faithfully recapitulate developmental gene expression patterns.⁸ During ESC differentiation, a gastrulation-like step takes place resulting in the commitment of some cells into ectodermal lineage and another set of cells into the mesendodermal lineage. A portion of the latter cells gives rise to the Brachyury⁺ mesodermal cell population. Some of these Brachyury⁺ cells become the first committed cardiac progenitor cells (CPCs) as defined by their expression of two key cardiac transcription factors, *Isl-1* and *Nkx2.5*.^{9,10} CPCs are multipotent at this stage and can give rise to cardiomyocytes, smooth muscle cells, and endothelial cells.^{11,12}

Cardiogenic commitment is driven by the activation of a number of highly conserved signaling pathways. For example, the transforming growth factor β superfamily members Activin A, bone morphogenetic protein 4 (BMP4), and Nodal as well as members of the fibroblast growth factor (i.e., FGF2) and Wnt (i.e., Wnt3a) families of signaling molecules have been shown to enhance or inhibit cardiac differentiation in a spatial- and temporal-specific fashion.^{5,13-19} To comprehensively evaluate signaling pathway activation during early cardiac lineage induction, we systematically screened a panel of 44 candidate cytokines/signaling molecules for their ability to enhance CPC formation. Consistent with previous findings, Wnt3a treatment during early differentiation enhanced mesodermal commitment leading to increased *Nkx2.5*⁺ CPC formation.^{20,21} Surprisingly, treatment with insulin and insulin-like growth factors (IGFs) positively regulated selective expansion of the mesendodermal cell population resulting in greater CPC formation. These ligands act through phosphorylation and activation of downstream targets such as Akt and mTOR and synergize with Wnt3a and FGF2.

Mechanistically, IGF induces selective expansion of the mesodermal cell population through increased proliferation. This study reveals a role for IGFs and insulin as regulators of *in vitro* mesodermal expansion and provides a strategy to significantly enhance the generation of PSC-derived CPCs.

Materials and methods

Growth factor screening

A previously described ESC line in which a cardiac-specific enhancer and base promoter of the murine Nkx2.5 locus drive enhanced green fluorescent protein (eGFP) gene expression was used for all experiments.¹¹ Nkx2.5-eGFP ESCs were cultured as previously described.¹¹ For the *in vitro* screening studies, cells were cultured in differentiation media containing 2% fetal bovine serum (FBS lot 894969; Life Technologies, Grand Island, NY, <http://www.lifetech.com>) and seeded at 4,000 cells per well in gelatin-coated 96-well plates (Corning Life Sciences, Tewksbury, MA, <http://www.corning.com/lifesciences>). Growth factors and signaling molecules were obtained from R&D Systems (Minneapolis, MN, <http://www.rndsystems.com>) as lyophilized powder and reconstituted as recommended by the manufacturer. A complete list of the compounds used for screening with the screening concentration range can be found in Supporting Information Table 1. Growth factors/signaling molecules were added to the cell culture at day 3 of differentiation at 1:2 dilutions in a dose range 4–1,000 µg/mL (i.e., 3.9, 7.8, 15.6, 31.3, 62.5, 125, 250, 500, 1000 µg/mL). The concentration with the greatest effect on GFP+ signal was considered for our screening results. Cells were assayed on day 6 of differentiation using a FACSCalibur high-throughput screening platform for 96-well plates (BD Biosciences, San Jose, CA, <http://www.bdbiosciences.com>). Data were analyzed with FlowJo software (Tree Star, Ashland, OR). The percentage of Nkx2.5-eGFP⁺ cells was assessed for each treatment group and compared to that of solvent-exposed control cells. Each experiment was performed in triplicate, and three independent experiments were performed for each condition. A hit was determined as having a *p* value <.05 using two-tailed Student's *t* test. For all subsequent experiments, optimized treatment timing and cytokine concentrations were used (*Figure 1D*; *Supporting Information Figure 1*).

Immunofluorescence microscopy

Nkx2.5-eGFP ESCs were differentiated as previously described¹¹ and treated with growth factors at day 1 or 2 of differentiation. Cells were cultured on 0.1%-gelatin-coated coverslips until assay or beating embryoid bodies (EBs) were manually collected and transferred to Nunc Lab-Tek II Chamber Slides (Thermo Fisher Scientific, Waltham, MA, <http://www.fishersci.com>). Cells were then fixed with 4% paraformaldehyde solution (Thermo Fisher Scientific) and permeabilized with Triton X-100 (Sigma-Aldrich, St. Louis, MO, <http://www.sigmaaldrich.com>). After washing three times with phosphate-buffered saline (PBS)/10%FBS/0.1% Tween-20 (Sigma-Aldrich), cells were incubated overnight at 4°C with mouse monoclonal antibodies directed against sarcomeric α -actinin (clone EA-53; Sigma-Aldrich; 1:250 dilution), affinity-purified goat-anti-Brachyury IgG (R&D Systems, Minneapolis, MN, <http://www.rndsystems.com/>; 1:100 dilution), rabbit anti-Ki67 IgG (clone D3B5; Cell Signaling Technology, Danvers, MA; 1:100 dilution), and rabbit anti-phospho-Akt (Thr308) IgG (clone C31E5E; Cell Signaling Technology, 1:1600 dilution). Next, cells were washed again and incubated for 60 minutes at RT (room temperature) with Alexa Fluor dye-conjugated secondary antibodies (Life Technologies;<http://www.lifetechnologies.com>, Grand Island, NY, diluted 1:500 in PBS/10%FBS/0.1% Tween-20). Immunostained samples were mounted using VECTASHIELD mounting medium with 4',6-diamidino-2-phenylindole (Vector Laboratories, Burlingame, CA,<http://www.vectorlabs.com>). For Draq5 labeling, Draq5 reagent (Cell Signaling Technology, Danvers, MA, <http://www.cellsignal.com/>, 1:5,000 dilution) was added to the culture media and incubated for 5 minutes at RT. Live cells were immediately imaged after staining. Images were acquired with an LSM 510 META inverted laser scanning confocal microscope (Carl Zeiss, Oberkochen, Germany, <http://microscopy.zeiss.com>) or a digital color camera-equipped fluorescence microscope (Nikon Eclipse 80i; Nikon Instruments Europe, Amstelveen, The Netherlands, <http://www.nikon.com/>) and processed using Fiji software (www.fiji.sc) and Adobe Photoshop version 5 (Adobe Systems, San Jose, CA, <http://www.adobe.com/>).

Quantitative reverse transcription-polymerase chain reaction

Nkx2.5-eGFP ESCs were seeded in 24-well plates (Corning Life Sciences) and treated with growth factors at day 1 or 2 of culture. At different time points after growth factor addition (i.e., day 0, 2, 4, 6, and 8), cells were lysed in TRIzol Reagent (Life Technologies) and total RNA was isolated using the RNeasy Mini Kit (Qiagen, Venlo, The Netherlands, <http://www1.qiagen.com>). Reverse transcription was done with iScript cDNA Synthesis Kit (Bio-Rad, Hercules CA, <http://www.bio-rad.com>). Gene expression levels were assayed using HotStart-IT SYBR Green quantitative polymerase chain reaction (qPCR) Master Mix (Affymetrix, Santa Clara, CA, <http://www.affymetrix.com>), and the primer pairs were specified in Supporting Information Table 2. PCR amplifications were performed in a CFX96 Touch Real-Time PCR Detection System (Bio-

Rad). Each condition was tested in three independent experiments using three samples per experiment.

Flow cytometry

Nkx2.5-eGFP ESCs were cultured in 24-well plates and treated at day 1 or 2 with growth factors. At the time point(s) of interest, cells were dissociated using trypsin/EDTA (Life Technologies) and 10 mg/mL collagenase A/B (Roche Applied Science, Indianapolis, IN, <http://www.roche-applied-science.com>) solutions in Hank's buffered salt solution (HBSS; Invitrogen)/20% FBS, fixed in 4% paraformaldehyde solution and permeabilized in ice-cold 100% methanol (Thermo Fisher Scientific). After washing two times with PBS, cells were incubated with primary antibodies for 1 hour at RT, washed again, and incubated for 1 hour at RT with appropriate Alexa Fluor dye-conjugated secondary antibodies. Following additional washings, cells were suspended in HBSS (Invitrogen) supplemented with 10% FBS and analyzed using a FACSCalibur flow cytometer (BD Biosciences). The following primary antibodies were used: cardiac troponin T (cTnT; clone 13-11; Thermo Fisher Scientific; 1:100 dilution in HBSS/10% FBS) and affinity-purified goat-anti-Brachyury IgG (R&D Systems; 1:100 dilution), mouse anti-GATA4 IgG₁ (clone L97-56; BD Biosciences; 1:200 dilution, San Jose, CA, <http://www.bdbiosciences.com>), mouse anti-Nestin IgG_{2a} (clone 307501; R&D Systems; 1:200 dilution), and rabbit anti-Ki67 IgG (clone D3B5; Cell Signaling Technology, Danvers, MA; 1:250 dilution). Appropriate dilutions were determined by comparison with undifferentiated ESCs and growth-inhibited mouse embryonic fibroblasts as negative controls. Data analysis was done using FlowJo software. Each condition was tested in three experiments using three independent samples per experiment.

Flow cytometric analysis of phospho-Akt

Nkx2.5-eGFP ESCs were differentiated as described previously.¹¹ EBs were collected at day 4. Next, the cells were dissociated, serum-starved for 2 hours, and exposed to growth factors for 15 minutes at 37°C in a humidified 5% CO₂ atmosphere. Cells were immediately fixed and stained with rabbit anti-phospho-Akt (Thr308) IgG (clone C31E5E; Cell Signaling Technology, diluted as specified by the manufacturer) as described previously.²² The presence of phospho-Akt was determined using a FACSCalibur flow cytometer and FlowJo software for data analysis.

Small-molecule inhibition studies

Validated small-molecule inhibitors of downstream IGF signaling pathway targets were added to Nkx2.5-eGFP ESCs simultaneously with insulin, IGF1, or IGF2 at day 1 or 2. Cells were analyzed by flow cytometry for eGFP expression as previously described. A dose titration was performed to determine the optimal concentration of each compound. The following small molecules were used: MK-2206 dihydrochloride (Selleckchem, Houston, TX, <http://www.selleckchem.com>).

com/), PI 103 hydrochloride (R&D Systems), PP 242 (R&D Systems), and KU-0063794 (Stemgent, Cambridge, MA, <https://www.stemgent.com/>).

Statistical methods

A two-tailed Student's *t* test was performed using GraphPad Prism software version 6 (GraphPad Software, La Jolla, CA) or Microsoft Excel (Microsoft, Redmond, WA). Results were considered significant at *p* values <.05.

Results

IGFs and insulin promote cardiac differentiation of murine ESCs

To identify novel signaling pathways involved in early cardiac lineage commitment, murine Nkx2.5-eGFP ESCs were differentiated *in vitro* by leukemia inhibitory factor (LIF) withdrawal and treated with cytokines/signaling molecules on day 3 of differentiation. On day 6 of differentiation, which coincides with the onset of Nkx2.5⁺ CPC formation,¹¹ the frequency of eGFP⁺ cells was quantified by automated flow cytometry (*Figure 1A*). Four of the 44 factors that were screened (i.e., IGF1, IGF2, insulin, and Wnt3a) significantly increased CPC formation (*Figure 1B and C*). Interestingly, treatment with Activin A, BMP2, or BMP4 at day 3 of differentiation decreased CPC formation. The remaining 37 factors showed no significant effect. We validated the effects of the positive hits by demonstrating a dose-dependent increase in eGFP⁺ cell formation following treatment with IGF1, IGF2, insulin or, as a positive control, Wnt3a, which had been previously implicated in early cardiogenesis (*Figure 1D*).²¹ Although FGF2 treatment did not reach statistical significance in our initial screening assay, it showed a clear dose-dependent increase in the number of eGFP⁺ cells when the timing of the treatment was optimized (*Supporting Information Figure S1*). Also the effect of IGFs and insulin on CPC formation is time/differentiation stage-specific (*Supporting Information Figure S1*). Accordingly, no increase in cell quantity was observed after treatment of FACS-sorted Nkx2.5-eGFP⁺ cells (CPCs) with IGF/insulin compared to untreated controls (*Supporting Information Figure S2*). Furthermore, a synergistic effect on CPC formation was observed between IGF1, IGF2 or insulin and either Wnt3a or FGF2. No synergy was seen between FGF2 and Wnt3a or between members of the IGF family of ligands (*Supporting Information Figure S3*).

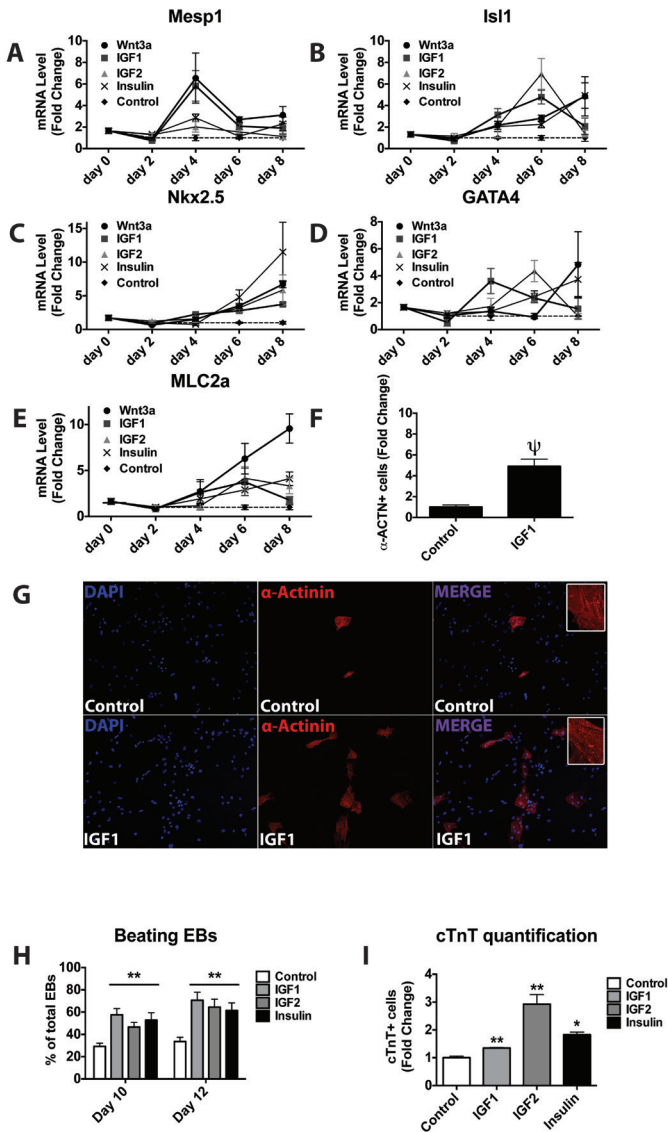


Figure 2. IGF/insulin treatment of murine embryonic stem cells enhances Nkx2.5⁺ cardiac progenitor cell (CPC) formation. Comparison by quantitative reverse transcriptase polymerase chain reaction of the expression levels of CPC genes in cells treated with 125 μ g/mL Wnt3a, 125 μ g/mL IGF1, 300 μ g/mL IGF2, or 10 mg/mL insulin (A) Mesp1 (B) Isl1 (C) Nkx2.5 (D) GATA4, and (E) MLC2a. (F) Quantification of sarcomeric α -actinin⁺ cells of untreated controls and IGF1-treated cells. (G) Representative microscopic images of untreated controls and of IGF1-treated cells (day 12) following immunostaining for sarcomeric α -actinin. DAPI-stained DNA (DAPI; blue), sarcomeric α -actinin (α -Actinin; red). (H) Quantification of beating EBs as % of total EBs (days 10 and 12 of differentiation). (I) Quantification of cTnT⁺ cells by flow cytometry (day 12). Mean \pm SEM of triplicate experiments is shown. NS, nonsignificant; *, $p < .05$; **, $p < .01$; ***, $p < .001$; ψ , $p < .0001$. Abbreviations: cTnT, cardiac troponin T; DAPI, 4',6-diamidino-2-phenylindole; EBs, embryoid bodies; IGF-1, insulin-like growth factor.

Confirmation of IGF/insulin-mediated increase in CPC formation in differentiating murine ESCs

To validate the ability of IGFs and insulin to enhance cardiogenesis, we measured the expression of cardiac lineage genes in growth factor-treated differentiating cells. Treatment with IGF1, IGF2, or insulin increased the expression of cardiac mesoderm- and CPC-specific genes such as *Mesp1*, *Isl-1*, *Nkx2.5*, *GATA4*, and *MLC2a* compared with that in untreated control cells (*Figure 2A–E*). The ability of IGF/insulin-induced CPCs to produce cardiomyocyte-like cells with sarcomeric architecture was demonstrated by immunocytological staining for and sarcomeric α -actinin (*Figure 2F*). Cells treated with IGF1 also were able to differentiate more readily into cardiomyocytes compared to untreated controls (*Figure 2G*). Accordingly, IGF-stimulated cells were able to differentiate into *Nkx2.5*-eGFP⁺ cells (*Supporting Information Figure S4*) and showed an increased frequency of beating EBs (*Figure 2H*). These findings were supported by flow cytometric quantification of the number of cTnT⁺ cells (*Figure 2I*).

IGF/insulin treatment induces mesendoderm formation

To investigate the mechanism involved in the stimulation of CPC formation by IGFs and insulin, we examined the expression of developmental stage- and lineage-specific genes. No significant difference in the expression of pluripotency markers such as *Pou5f1* (Oct 4) (*Figure 3A*) and *Nanog* (*Figure 3B*) was found between control and IGF/insulin-treated cells. This suggests that IGF/insulin treatment does not elicit a greater degree of overall differentiation from a pluripotent state. The expression levels of mesoderm- and endoderm-specific genes such as *Eomes*, *Brachyury*, *GATA4*, *Gooseoid*, α fetal protein, hepatocyte nuclear factor-1b, *HNF3b*, and *SOX17* were all significantly increased by IGF/insulin treatment (*Figure 3C–D*). On the other hand, the expression of ectoderm-specific genes, such as *Nestin*, *GBX2*, *FGF5*, and *Pax6* were unchanged or slightly decreased (*Figure 3E*). These results were corroborated by flow cytometric analysis of *Brachyury* (*Figure 4A–B*) and *GATA4* expression (*Figure 4C–D*). Consistently, the number of *Nestin*⁺ ectodermal cells decreased after IGF/insulin treatment (*Figure 4E–F*). Taken together, these data support the ability of IGF1, IGF2, and insulin to stimulate the formation of *Brachyury*⁺mesoderm or *GATA4*⁺ mesendoderm at the expense of ectoderm.

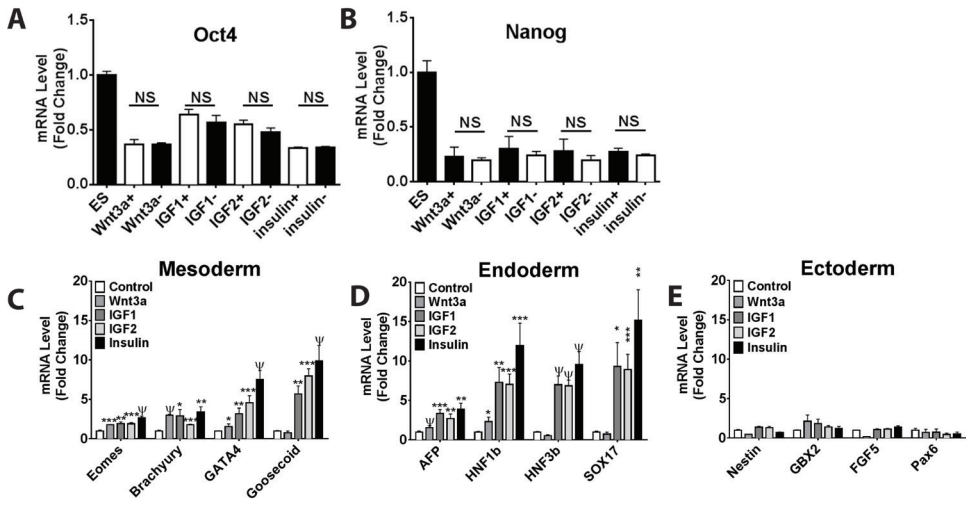


Figure 3. IGF/insulin stimulation of murine ESCs induces expression of mesendodermal genes. Comparison by reverse transcriptase polymerase chain reaction of the expression levels at day 4 of (A) Oct4, (B) Nanog, (C) mesodermal genes, (D) endodermal genes, and (E) ectodermal genes in untreated cells and in cells exposed to Wnt3a (125 μ g/mL), IGF1 (125 μ g/mL), IGF2 (300 μ g/mL), or insulin (10 mg/mL). Mean \pm SEM of triplicate experiments is shown. NS, nonsignificant; *, $p < .05$; **, $p < .01$; ***, $p < .001$; ψ , $p < .0001$. Abbreviations: ESC, embryonic stem cell; IGF, insulin-like growth factor.

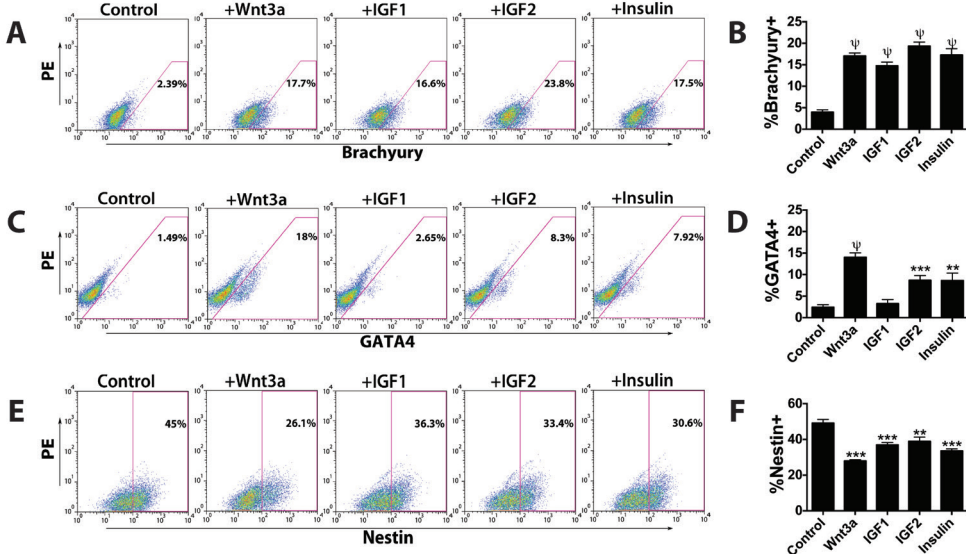


Figure 4. IGF/insulin treatment of murine embryonic stem cells gives rise to early mesodermal cells. Flow cytometric analysis of the expression at day 4 of the germ layer markers (A, B) Brachyury, (C, D) GATA4, and (E, F) Nestin in untreated cells and in cells exposed to Wnt3a (125 μ g/mL), IGF1 (125 μ g/mL), IGF2 (300 μ g/mL), or insulin (10 mg/mL). Mean \pm SEM of triplicate experiments is shown. **, $p < .01$; ***, $p < .001$; ψ , $p < .0001$. Abbreviations: IGF, insulin-like growth factor; PE, phycoerythrin.

IGFs and insulin stimulate proliferation of Brachyury⁺ mesodermal cells

Since IGFs have been implicated in cardiomyocyte proliferation,²³⁻²⁶ we studied the ability of IGFs and insulin to induce proliferation within the mesodermal Brachyury⁺ cell population. Coimmunostaining for Brachyury and the proliferation marker Ki-67 revealed a significant increase in the percentage of Brachyury⁺/Ki-67⁺-double-positive cells after IGF1/2 or insulin treatment, but not after Wnt3a or FGF2 treatment (Brachyury⁺/Ki-67⁺: 22.6±4.4%) (Figure 5A-B, E-F). Interestingly, there was no significant increase in Ki-67 staining within the Brachyury⁻ cell population after IGF/insulin treatment (Figure 5C-D). These data demonstrate that IGFs and insulin selectively promote mesodermal cell proliferation.

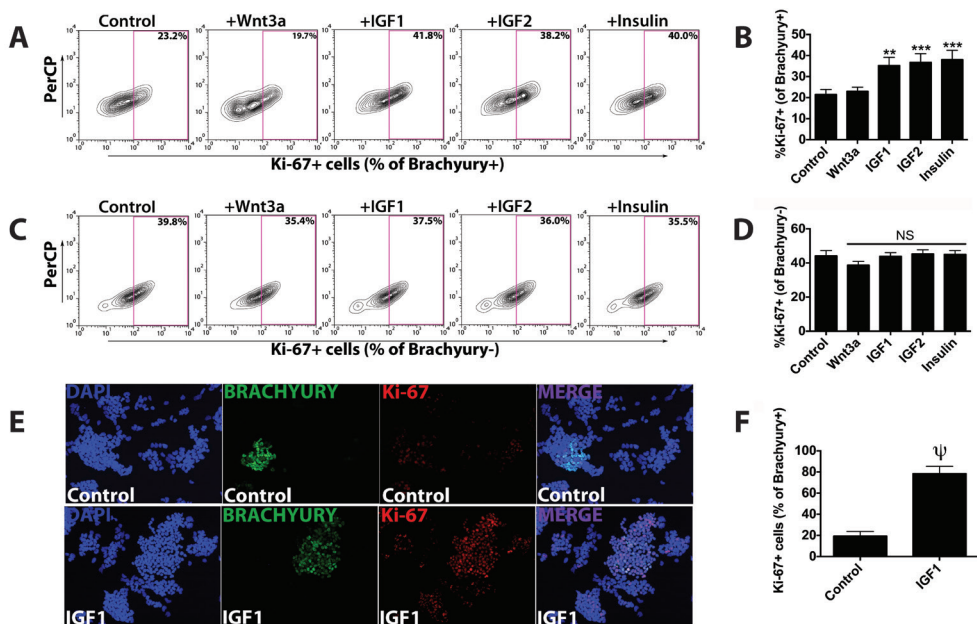


Figure 5. IGF/insulin treatment selectively increases proliferation within the Brachyury⁺ cell population during murine embryonic stem cell differentiation. Flow cytometry analysis of the expression at day 4 of the proliferation marker Ki-67 in Brachyury⁺ or Brachyury⁻ cells in untreated controls and in cells exposed to Wnt3a (125 µg/mL), IGF1 (125 µg/mL), IGF2 (300 µg/mL), or insulin (10 mg/mL). (A, B) Ki-67 expression in Brachyury⁺ cells. (C, D) Ki-67 expression in Brachyury⁻ cells. Mean ± SEM of triplicate experiments is shown. NS, nonsignificant; **, $p < .01$; ***, $p < .001$. (E) Representative microscopy images (×200) of untreated controls and IGF1-treated cells after immunostaining for DAPI (blue), Brachyury (green), Ki-67 (red). (F) Quantification of Ki-67⁺ cells in Brachyury⁺ cells of untreated controls and IGF1-treated cells. Abbreviation: IGF, insulin-like growth factor.

IGF/insulin treatment causes rapid Akt phosphorylation in Brachyury⁺ mesodermal cells

It has been established that Akt phosphorylation is one of the mediators of IGF signaling.²⁷ To examine whether Akt phosphorylation in mesodermal cells is involved in IGF/insulin-mediated induction of CPC formation, differentiating Nkx2.5-eGFP ESCs were treated with IGF1, IGF2 or insulin and subjected to flow cytometric analysis to investigate the occurrence of Akt phosphorylation in Brachyury⁺ cells. We found a significant increase in the percentage of Brachyury⁺/phospho-Akt⁺ cells following IGF/insulin treatment (Figure 6A-D). The effect of IGFs and insulin on Akt phosphorylation appears specific since treatment with FGF2 or Wnt3a showed no such effect (Supporting Information Figure S5). These data indicate that IGFs and insulin indeed signal through downstream Akt phosphorylation in the Brachyury⁺ cell population.

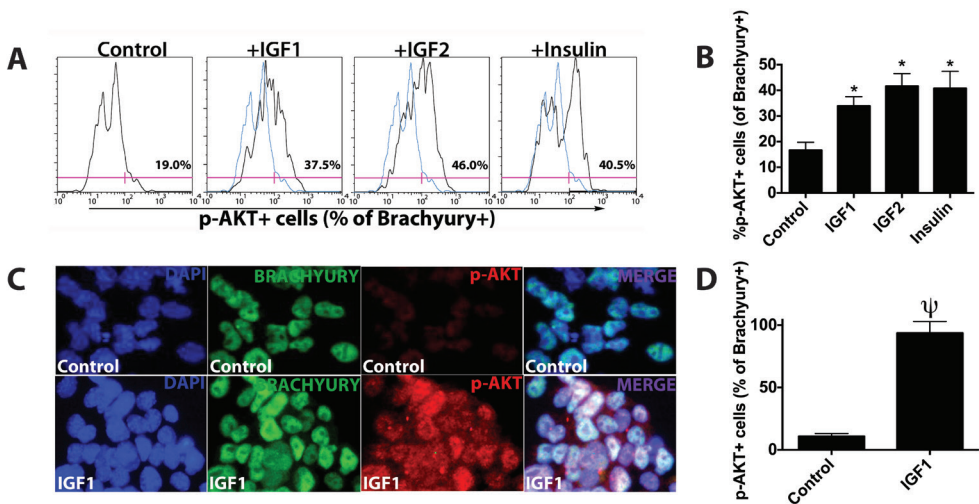


Figure 6. IGF/insulin treatment promotes Akt phosphorylation in murine embryonic stem cell (ESC)-derived Brachyury⁺ cells. (A) Flow cytometric analysis of p-AKT expression in Brachyury⁺ cells following treatment of Nkx2.5-eGFP ESCs with IGF1 (125 μ g/mL), IGF2 (300 μ g/mL), or insulin (10 mg/mL) and untreated control Nkx2.5-eGFP ESCs. (B) Quantification of p-AKT expression in Brachyury⁺ cells. Mean \pm SEM of triplicate experiments is shown. *, $p < .05$; ψ , $p < .0001$. (C) Representative microscopic images ($\times 1,000$) of untreated controls and IGF1-treated cells after immunostaining for DAPI (blue), Brachyury (green), and p-AKT (red). (D) Quantification of p-AKT⁺ cells in Brachyury⁺ cells of untreated controls and IGF1-treated cells. Abbreviations: DAPI, 4',6-diamidino-2-phenylindole; IGF, insulin-like growth factor; p-Akt, phospho-AKT.

Akt and mTOR signaling are required for IGF/insulin-mediated expansion of the CPC pool

To further examine downstream mediators of IGF signaling responsible for its enhancement of CPC formation, differentiating Nkx2.5-eGFP ESCs were coincubated with IGF1, IGF2, or insulin and selective small-molecule inhibitors of PI3K, Akt, and mTOR. IGF/insulin-induced formation of eGFP⁺ CPCs was dose-dependently reduced when differentiating Nkx2.5-eGFP ESCs were

treated with specific inhibitors of phosphoinositol-3 kinase (PI3K) (PI 103), Akt (MK-2206), and mammalian target of rapamycin (mTOR) (KU-0063794 and PP 242) (Figure 7A-D). Furthermore, after treatment of IGF/insulin-stimulated Nkx2.5-eGFP ESCs with MK-2206, the frequency of Brachyury⁺/Ki-67⁺-double-positive cells was significantly lower compared to mock-treated cells (Supporting Information Figure S6). These data demonstrate that IGF signaling through PI3K, Akt, and mTOR enhances proliferation of mesodermal cells resulting, ultimately, in increased CPC formation.

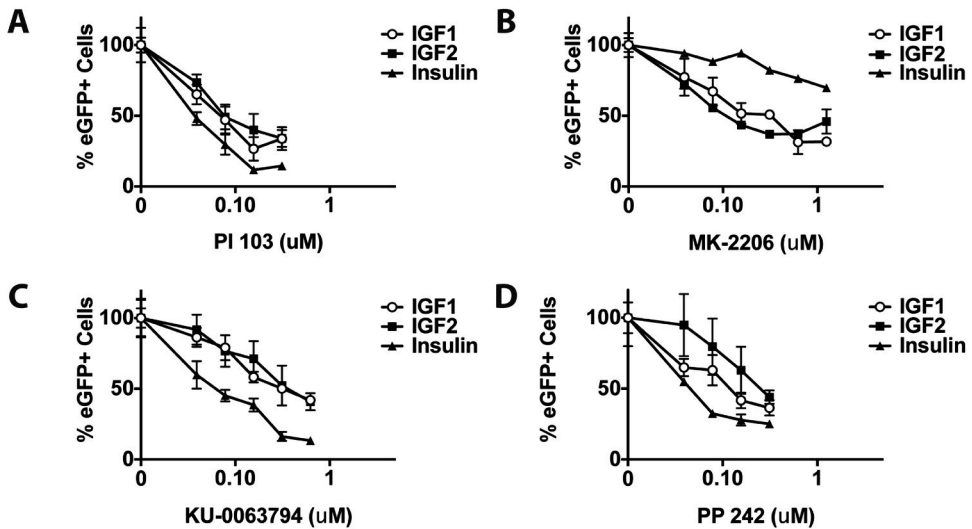


Figure 7. Selective inhibition of PI3K, Akt, or mTOR abolishes IGF-induced cardiac differentiation of murine embryonic stem cells (ESCs). Flow cytometric analysis of eGFP expression in IGF1- (125 μ g/mL), IGF2- (125 μ g/mL), or insulin (10 mg/mL)-treated Nkx2.5-eGFP ESCs in the presence of selective small molecule inhibitors of the PI3K/Akt/mTOR signaling pathway. Dose responses were determined for (A) PI 103 (inhibitor of PI3K), (B) MK-2206 (inhibitor of Akt), (C) KU-0063794 (inhibitor of mTOR), and (D) PP 242 (inhibitor of mTOR). Abbreviations: eGFP, enhanced green fluorescent protein; IGF, insulin-like growth factor.

Discussion

In this study, we performed a growth factor screen to identify mediators of early mesoderm induction that can give rise to cardiac lineage induction. The key findings of this study are: (a) IGF1, IGF2, insulin, Wnt3a, and FGF2 treatment of murine ESCs significantly increases Nkx2.5⁺ CPC formation, (b) IGF and insulin selectively promote Brachyury⁺ mesodermal cell proliferation, (c) IGF treatment leads to an increase in Akt phosphorylation within the Brachyury⁺ cell population, and (d) activation of PI3K, Akt, and mTOR signaling is required for

the ability of IGFs and insulin to enhance CPC formation. These data demonstrate a role for IGFs and insulin in early germ layer development *in vitro*, by their ability to selectively enhance the proliferation of mesodermal cells, leading to increased cardiac lineage differentiation.

Signaling pathways involved in cardiac differentiation

While our screen identified a novel role for IGFs and insulin to regulate early *in vitro* cardiogenesis, Activin A, BMP2, and BMP4 treatment at this stage of development inhibited cardiac differentiation. The latter ligands have been shown to play a context-dependent role in cardiac development in previous studies.²⁸⁻³⁰ For example, a recent small-molecule screening study revealed the ability of a BMP inhibitor, dorsomorphin, to activate cardiogenic differentiation.³⁰ Other studies have shown both a dose- and stage-specific requirement for BMP signaling to enhance cardiac differentiation.⁵ This context-dependent effect of BMP treatment has been previously reported.³¹ Consistent with this, the addition of Activin A or BMPs alone to differentiating ESC cultures has been shown to preferentially induce endodermal lineage development while combined Activin A and BMP treatment was shown to induce mesodermal cardiac lineage formation.³²

Role of IGF/insulin in early cardiomyogenesis

Some studies have revealed a negative modulatory effect of IGF and insulin expression on cardiomyocyte differentiation in human ESCs.³³⁻³⁵ Similarly, a recent study found differential effects of FGF signaling pathway activation in mouse and human ESCs.³⁶ The apparent discrepancy between these and our findings are most likely due to differences in the developmental stage in which IGF/insulin was added to cells. In this study, we examined the effect of IGF/insulin on mesodermal cells, whereas prior human ESC studies examined the effect of IGF/insulin on cardiomyocyte differentiation from postmesodermal cells. It has been well-recognized that developmental regulators such as Wnt and Notch exert a biphasic role on cardiac lineage differentiation. We believe this is likely to be the case for IGF/insulin as well. Indeed, our preliminary data showed that treatment of mouse CPCs with IGF results in decreased cardiomyocyte differentiation. This suggests that our findings in mouse ESC here are largely consistent with those from prior human ESC studies.

Our data showed that IGF signaling results in selective expansion of Brachyury⁺ mesodermal cells through induction of proliferation. As such, the mechanism by which IGFs and insulin stimulate CPC formation appears different from that of Wnt3a or FGF2, which showed no obvious proliferation rate changes in Brachyury⁺ mesodermal cells (*Figure 5*). Furthermore, combining either Wnt3a or FGF2 with IGF/insulin resulted in additive increases in Nkx2.5-eGFP⁺ cells, which are no greater than the increases when each factor was added singularly

(Supporting Information Figure S3). These data further support that IGF and insulin act through a different downstream signaling pathway than FGF2 or Wnt3a.

In support of our findings, Morali et al. found that IGF2^{-/-} ESC lines exhibit an impaired ability to differentiate into cardiogenic and myogenic lineages when differentiated *in vitro*. This phenotype could be partially rescued when differentiating cells were treated with exogenous IGF2.³⁷ A more recent study describes the ability of IGF to increase ESC-derived vascular cells as well, a finding that may also be related to the upregulation of Brachyury⁺ mesodermal cells.³⁸ Additionally, IGF and insulin treatment showed a marked induction of endodermal markers (Figure 3D), suggesting this pathway could also be active during endodermal lineage formation. A recent study showed IGF treatment directed hepatocyte differentiation from definitive endoderm.³⁹

Conclusion

To our knowledge, this is the first study demonstrating a direct role for IGFs and insulin to promote the *in vitro* differentiation of PSCs into mesoderm. We showed that IGF/insulin treatment of murine ESCs selectively expands the Brachyury⁺ mesodermal cell pool via activation of PI3K, Akt, and mTOR, leading to increased cell proliferation. These findings contribute to our understanding of early developmental events and provide a new strategy to enhance directed cardiac differentiation for regenerative applications.

Acknowledgements

Laura Prickett-Rice and Katherine Folz-Donahue at the Center for Regenerative Medicine Harvard Stem Cell Institute Flow Cytometry Core provided assistance with flow cytometry experiments. Andrew Olson at the Stanford Neuroscience Microscopy Service (supported by NIH NS069375) at Stanford School of Medicine provided technical assistance with confocal microscopy imaging. M.C.E. was supported by a Mosaic grant from the Netherlands Organization for Scientific Research (NWO 017.007.064). D.A.P. was supported by NWO (VENI grant 91611070) and S.M.W. was supported by NIH/Officer of the Director's New Innovator Award (OD004411), NIH/NHLBI U01 (HL099776) and K08 (HL081086) and by the Harvard Stem Cell Institute.

Author Contributions

M.C.E.: conception and design, collection and/or assembly of data, data analysis and interpretation, manuscript writing, and final approval of manuscript; K.R., R.F., and A.S.: collection and/or assembly of data, data analysis and interpretation, and final approval of manuscript; U.B.N.: provision of study material, financial support, and final approval of

manuscript; M.J.S.: financial support, data analysis and interpretation, and final approval of manuscript; A.A.F.V.: data analysis and interpretation, manuscript writing, and final approval of manuscript; D.A.P.: conception and design, data analysis and interpretation, manuscript writing, and final approval of manuscript; S.M.W.: conception and design, financial support, data analysis and interpretation, manuscript writing, and final approval of manuscript.

Disclosure of potential conflicts of interest

U.B.N. is the chief executive officer of Silver Creek Pharmaceuticals, Inc.

References

1. Fuster V, Voute J, Hunn M, Smith SC Jr. Low priority of cardiovascular and chronic diseases on the global agenda: A cause for concern. *Circulation*. 2007;23:1966–1970.
2. Takahashi K, Yamanaka S. Induction of pluripotent stem cells from mouse embryonic and adult fibroblast cultures by defined factors. *Cell*. 2006;126:663–676.
3. Wu SM, Hochedlinger K. Harnessing the potential of induced pluripotent stem cells for regenerative medicine. *Nat Cell Biol*. 2011;13:497–505.
4. Burridge PW, Keller G, Gold JD, Wu JC. Production of de novo cardiomyocytes: Human pluripotent stem cell differentiation and direct reprogramming. *Cell Stem Cell*. 2012;10:16–28.
5. Kattman SJ, Witty AD, Gagliardi M, Dubois NC, Niapour M, Hotta A, Ellis J, Keller G. Stage-specific optimization of activin/nodal and BMP signaling promotes cardiac differentiation of mouse and human pluripotent stem cell lines. *Cell Stem Cell*. 2011;8:228–240.
6. Burridge PW, Thompson S, Millrod MA, Weinberg S, Yuan X, Peters A, Mahairaki V, Koliatsos VE, Tung L, Zambidis ET. A universal system for highly efficient cardiac differentiation of human induced pluripotent stem cells that eliminates interline variability. *PLoS One*. 2011;6:e18293.
7. Van Vliet P, Wu SM, Zaffran S, Puc at M. Early cardiac development: A view from stem cells to embryos. *Cardiovasc Res*. 2012;96:352–362.
8. Murry CE, Keller G. Differentiation of embryonic stem cells to clinically relevant populations: Lessons from embryonic development. *Cell*. 2008;132:661–680.
9. Cai CL, Liang X, Shi Y, Chu PH, Pfaff SL, Chen J, Evans S. Isl1 identifies a cardiac progenitor population that proliferates prior to differentiation and contributes a majority of cells to the heart. *Dev Cell*. 2003;5:877–889.
10. Stanley EG, Biben C, Elefanty A, Barnett L, Koentgen F, Robb L, Harvey RP. Efficient cre-mediated deletion in cardiac progenitor cells conferred by a 3'UTR-ires-cre allele of the homeobox gene *Nkx2-5*. *Int J Dev Biol*. 2002;46:431–439.
11. Wu SM, Fujiwara Y, Cibulsky SM, Clapham DE, Lien CL, Schultheiss TM, Orkin SH. Developmental origin of a bipotential myocardial and smooth muscle cell precursor in the mammalian heart. *Cell*. 2006;127:1137–1150.
12. Moretti A, Caron L, Nakano A, Lam JT, Bernhausen A, Chen Y, Qyang Y, Bu L, Sasaki M, Martin-Puig S, Sun Y, Evans SM, Laugwitz KL, Chien KR. Multipotent embryonic *isl1+* progenitor cells lead to cardiac, smooth muscle, and endothelial cell diversification. *Cell*. 2006;127:1151–1165.
13. Willems E, Spiering S, Davidovics H, Lanier M, Xia Z, Dawson M, Cashman J, Mercola M. Small-molecule inhibitors of the Wnt pathway potently promote cardiomyocytes from human embryonic stem cell-derived mesoderm. *Circ Res*. 2011;109:360–364.
14. Zhang J, Klos M, Wilson GF, Herman AM, Lian X, Raval KK, Barron MR, Hou L, Soerens AG, Yu J, Palecek SP, Lyons GE, Thomson JA, Herron TJ, Jalife J, Kamp TJ. Extracellular matrix promotes highly efficient cardiac differentiation of human pluripotent stem cells: The matrix sandwich method. *Circ Res*. 2012;111:1125–1136.
15. Tran TH, Wang X, Browne C, Zhang Y, Schinke M, Izumo S, Burcin M. Wnt3a-induced mesoderm formation and cardiomyogenesis in human embryonic stem cells. *Stem Cells*. 2009;27:1869–1878.
16. Hao J, Daleo MA, Murphy CK, Yu PB, Ho JN, Hu J, Peterson RT, Hatzopoulos AK, Hong CC. Dorsomorphin, a selective small molecule inhibitor of BMP signaling, promotes cardiomyogenesis in embryonic stem cells. *PLoS One*. 2008;3:e2904.
17. Shimoji K, Yuasa S, Onizuka T, Hattori F, Tanaka T, Hara M, Ohno Y, Chen H, Egasgira T, Seki T, Yae K, Koshimizu U, Ogawa S, Fukuda K. G-CSF promotes the proliferation of developing cardiomyocytes in vivo and in derivation from ESCs and iPSCs. *Cell Stem Cell*. 2010;6:227–237.

18. Willems E, Cabral-Teixeira J, Schade D, Cai W, Reeves P, Bushway PJ, Lanier M, Walsh C, Kirchhausen T, Izpisua Belmonte JC, Cashman J, Mercola M. Small molecule-mediated TGF- β type II receptor degradation promotes cardiomyogenesis in embryonic stem cells. *Cell Stem Cell*. 2012;11:242–252.
19. Watanabe Y, Miyagawa-Tomita S, Vincent SD, Kelly RG, Moon AM, Buckingham ME. Role of mesodermal FGF8 and FGF10 overlaps in the development of the arterial pole of the heart and pharyngeal arch arteries. *Circ Res*. 2010;106:495–503.
20. Takada S, Stark KL, Shea MJ, Vassileva G, McMahon JA, McMahon AP. Wnt-3a regulates somite and tailbud formation in the mouse embryo. *Genes Dev*. 1994;8:174–189.
21. Ueno S, Weidinger G, Osugi T, Kohn AD, Golob JL, Pabon L, Reinecke H, Moon RT, Murry CE. Biphasic role for Wnt/beta-catenin signaling in cardiac specification in zebrafish and embryonic stem cells. *Proc Natl Acad Sci USA*. 2007;104:9685–9690.
22. Schulz KR, Danna EA, Krutzik PO, Nolan GP. Single-cell phospho-protein analysis by flow cytometry. *Curr Protoc Immunol*. 2012;Chapter 8:Unit 8.17:1–20.
23. Li P, Cavallero S, Gu Y, Chen TH, Hughes J, Hassan AB, Brüning JC, Pashmforoush M, Sucov HM. IGF signaling directs ventricular cardiomyocyte proliferation during embryonic heart development. *Development* 2011;138:1795–1805.
24. Oikonomopoulos A, Sereti KI, Conyers F, Bauer M, Liao A, Guan J, Crapps D, Han JK, Dong H, Bayomy AF, Fine GC, Westerman K, Biechele TL, Moon RT. Wnt signaling exerts an antiproliferative effect on adult cardiac progenitor cells through IGFBP3. *Circ Res*. 2011;109:1363–1374.
25. Xin M, Kim Y, Sutherland LB, Qi X, McAnally J, Schwartz RJ, Richardson JA, Bassel-Duby R, Olson EN. Regulation of insulin-like growth factor signaling by Yap governs cardiomyocyte proliferation and embryonic heart size. *Sci Signal*. 2011;4:ra70.
26. McDevitt TC, Laflamme MA, Murry CE. Proliferation of cardiomyocytes derived from human embryonic stem cells is mediated via the IGF/PI 3-kinase/Akt signaling pathway. *J Mol Cell Cardiol*. 2005;39:865–873.
27. Alessi DR, Andjelkovic M, Caudwell B, Cron P, Morrice N, Cohen P, Hemmings BA. Mechanism of activation of protein kinase B by insulin and IGF-1. *EMBO J*. 1996;15:6541–6551.
28. Sugi Y, Lough J. Activin-A and FGF-2 mimic the inductive effects of anterior endoderm on terminal cardiac myogenesis in vitro. *Dev Biol*. 1995;168:567–574.
29. Kruihof BP, van Wijk B, Somi S, Kruihof-de Julio M, Pérez Pomares JM, Weesels F, Wessels A, Moorman AF, van den Hoff MJ. BMP and FGF regulate the differentiation of multipotential pericardial mesoderm into the myocardial or epicardial lineage. *Dev Biol*. 2006;295:507–522.
30. Ao A, Hao J, Hopkins CR, Hong CC. DMH1, a novel BMP small molecule inhibitor, increases cardiomyocyte progenitors and promotes cardiac differentiation in mouse embryonic stem cells. *PLoS One*. 2012;7:e41627.
31. de Pater E, Ciampicotti M, Priller F, Veerkamp J, Strate I, Smith K, Legendijk AK, Schilling TF, Herzog W, Abdelilah-Seyfried S, Hammerschmidt M, Bakkers J. BMP signaling exerts opposite effects on cardiac differentiation. *Circ Res*. 2012;110:578–587.
32. Yao S, Chen S, Clark J, Hao E, Beattie GM, Hayek A, Ding S. Long-term self-renewal and directed differentiation of human embryonic stem cells in chemically defined conditions. *Proc Natl Acad Sci USA*. 2006;103:6907–6912.
33. Freund C, Ward-van Oostwaard D, Monshouwer-Kloots J, van den Brink S, van Rooijen M, Xu X, Zweigerdt R, Mummery C, Passier R. Insulin redirects differentiation from cardiogenic mesoderm and endoderm to neuroectoderm in differentiating human embryonic stem cells. *Stem Cells*. 2008;26:724–733.
34. Xu XQ, Graichen R, Soo SY, Balakrishnan T, Rahmat SN, Sieh S, Tham SC, Freund C, Moore J, Mummery C, Colman A, Zweigerdt R, Davidson BP. Chemically defined medium supporting cardiomyocyte differentiation of human embryonic stem cells. *Differentiation*. 2008;76:958–970.

35. Tran TH, Wang X, Browne C, Zhang Y, Schinke M, Izumo S, Burcin M. Wnt3a-induced mesoderm formation and cardiomyogenesis in human embryonic stem cells. *Stem Cells*. 2009;27:1869–1878.
36. Greber B, Wu G, Bernemann C, Joo JY, Han DW, Ko K, Tapia N, Sabour D, Sternecker J, Tesar P, Schöler HR. Conserved and divergent roles of FGF signaling in mouse epiblast stem cells and human embryonic stem cells. *Cell Stem Cell*. 2010;6:215–226.
37. Morali OG, Jouneau A, McLaughlin KJ, Thiery JP, Larue L. IGF-II promotes mesoderm formation. *Dev Biol*. 2000;227:133–145.
38. Piecewicz SM, Pandey A, Roy B, Xiang SH, Zetter BR, Sengupta S. Insulin-like growth factors promote vasculogenesis in embryonic stem cells. *PLoS One*. 2012;7:e32191.
39. Magner NL, Jung Y, Wu J, Nolte JA, Zern MA, Zhou P. Insulin and IGFs enhance hepatocyte differentiation from human embryonic stem cells via the PI3K/AKT pathway. *Stem Cells*. 2013;31:2095–2103.

Supporting information

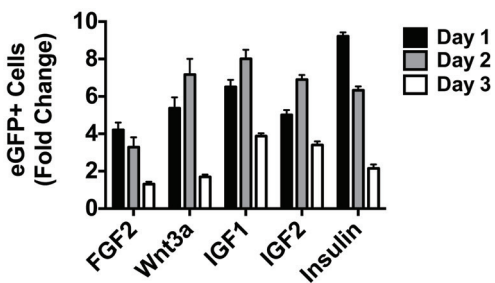


Figure S1. Flow cytometric assessment of the optimal timing of IGF/insulin stimulation-induced formation of CPCs from murine ESCs. The growth factors were added on the indicated day after LIF removal. Bars represent fold change in eGFP+ cell count by growth factor treatment. Mean \pm SEM of triplicate experiments is shown.

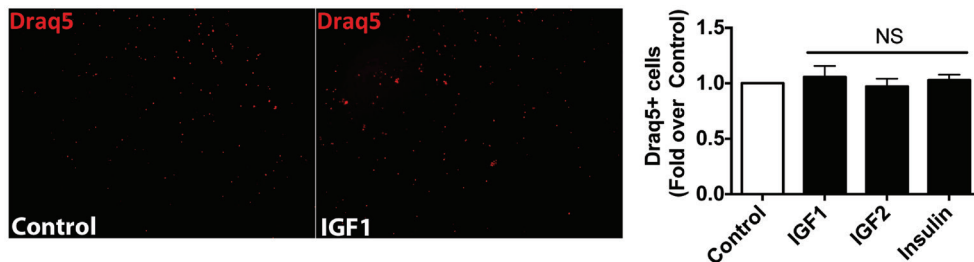


Figure S2. Representative microscopic images of Draq5-labeled untreated controls and IGF1-treated cells (day 11) after fluorescence-activated cell sorting of Nkx2.5-eGFP+ cells at day 6. Quantification of Draq5+ cells after treatment with IGF1 (125 μ g/mL), IGF2 (300 μ g/mL), insulin (10mg/mL) or untreated controls of sorted Nkx2.5-eGFP+ cells. NS, not significant.

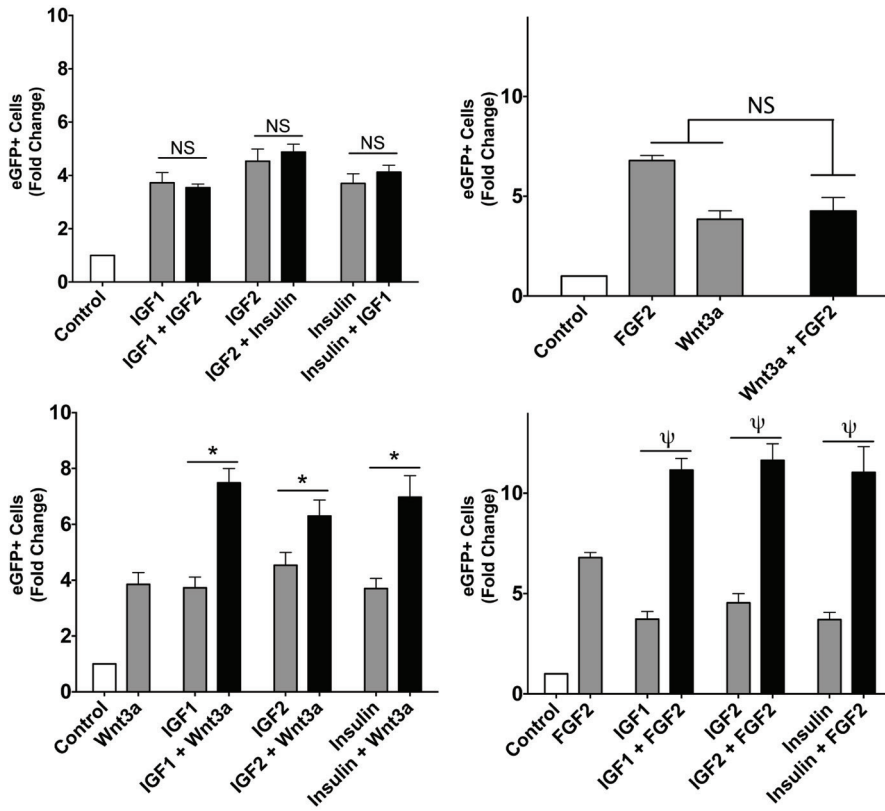


Figure S3. IGFs and insulin synergize with Wnt3a and FGF2 in stimulating the formation of CPCs from murine ESCs. Nkx2.5-eGFP ESCs were exposed to IGF1 (125 $\mu\text{g}/\text{mL}$), IGF2 (300 $\mu\text{g}/\text{mL}$), insulin (10 mg/mL), FGF2 (200 $\mu\text{g}/\text{mL}$) or Wnt3a (125 $\mu\text{g}/\text{mL}$) alone or in pairs as indicated below the graphs and the resulting number of eGFP+ CPCs was determined by flow cytometry. Bars represent mean of SEM in triplicate experiments. NS, non-significant; *, $p < 0.05$; ψ , $p < 0.0001$.

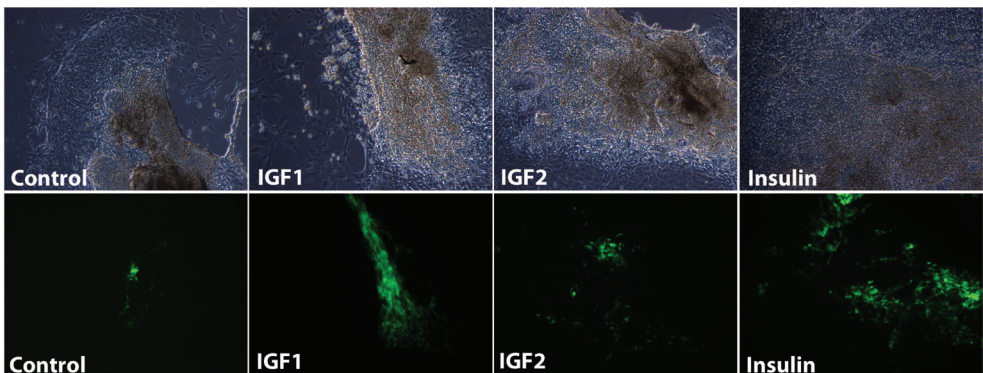


Figure S4. Representative phase contrast photomicroscopic images of differentiating murine Nkx2.5-eGFP ESCs as untreated control or following treatment with IGF1, IGF2 or insulin.

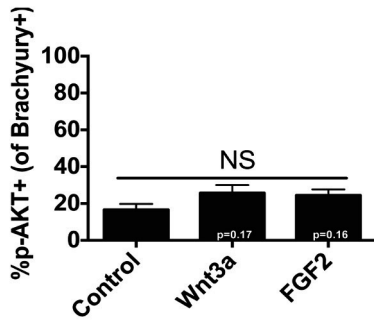


Figure S5. Treatment of Nkx2.5-eGFP ESCs with Wnt3a (125 $\mu\text{g}/\text{mL}$) or FGF2 (200 $\mu\text{g}/\text{mL}$) does not increase Akt phosphorylation in Brachyury+ cells. Flow cytometric analysis of phospho-AKT (pAkt) expression in Brachyury+ cells following treatment of Nkx2.5-eGFP ESCs with Wnt3a or FGF2. Control, untreated Nkx2.5-eGFP ESCs. Bars represent mean \pm SEM of triplicate experiments. NS, non-significant.

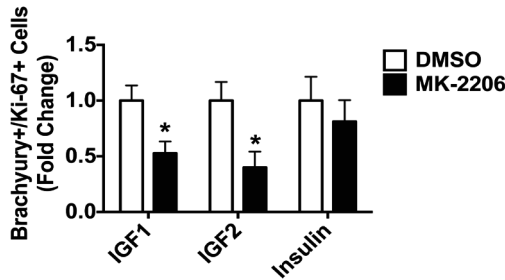


Figure S6. Selective inhibition of Akt signaling abolishes IGF/insulin-dependent proliferation of murine ESC-derived Brachyury+ cells. Flow cytometric quantification of Ki67 expression in Brachyury+ cells following treatment of 33 differentiating murine ESCs with IGF1, IGF2 or insulin in the presence of the Akt inhibitor ML-2206 or its solvent, DMSO. Mean \pm SEM of triplicate experiments is shown. *, $p < 0.05$.

Supplementary Table 1. Cytokines for screening assay.

Cytokine	Concentration Range ($\mu\text{g/mL}$)
Wnt3a	4-1000
IGF1	4-1000
IGF2	4-1000
Insulin	4-1000
FGF2	4-1000
LIF	4-1000
Wnt7a	4-1000
Wnt11	4-1000
SDF-1 α	4-1000
TGF α	4-1000
MCP1	4-1000
G-CSF	4-1000
IL-3	4-1000
IL-6	4-1000
EPO	4-1000
TNF α	4-1000
NRG EGF domain	4-1000
TGF β 1	4-1000
TGF β 2	4-1000
Betacellulin	4-1000
Wnt1	4-1000
Wnt2	4-1000
EGF	4-1000
FGF4	4-1000
HGF	4-1000
PDGF-AA	4-1000
PDGF-AB	4-1000
PDGF-BB	4-1000
SCF	4-1000
VEGF-A 121	4-1000
VEGF-A 165	4-1000
VEGF-B	4-1000
Thymosin β -4	4-1000
GLP-1	4-1000
Exenatide	4-1000
VEGF	4-1000
FGF10	4-1000
DKK-1	4-1000
A83	4-1000
Dorsomorphin	4-1000
Carbonoxolone	4-1000
BMP4	4-1000
Activin A	4-1000
BMP2	4-1000

Supplementary Table 2. Primers used for RT-qPCR.

Target Gene	Forward Primer (5'→3')	Reverse Primer (5'→3')
β-actin	GAAGGAGATTACTGCTCTGGCTCCTAGCAC	TCATCGTACTCCTGCTTGCTGATCC
Mesp1	GCTCGGTCCCGTTTAAAGC	ACGATGGGTCCCACGATTCT
Isl-1	ATGATGGTGGTTTACAGGCTAAC	TCGATGCTACTTCACTGCCAG
Nkx2.5	ACAAAGCCGAGACGGATGG	CTGTCGCTTGCACCTGTAGC
GATA4	CACCCCAATCTCGATATGTTTGA	GCACAGGTAGTGTCCTGTC
MLC2a	AAGGGAAGGGTCCCATCAACTTCA	AACAGTTGCTCTACCTCAGCAGGA
Oct4	CTGAGGGCCAGGCAGGAGCACGAG	CTGTAGGGAGGGCTTCGGGCACTT
Nanog	TCTTCTGGTCCCCACAGTTT	GCAAGAATAGTTCTCGGGATGAA
Eomes	GCAATAAGATGTACGTTACCCCA	GCAGAGACTGCAACACTATCAT
Brachyury	GCTGGATTACATGGTCCCAAG	GGCACTTCAGAAATCGGAGGG
GATA4	CACCCCAATCTCGATATGTTTGA	GCACAGGTAGTGTCCTGTC
Goosecoid	CAGATGCTGCCCTACATGAAC	TCTGGGTACTTCGTCTCCTGG
AFP	CCATCACCTTTACCCAGTTTGT	CCCATCGCCAGAGTTTTTCTT
HNF1b	AGGGAGGTGGTCGATGTCA	TCTGGACTGTCTGGTTGAACT
HNF3b	GGAGGCAAGAAGACCGCTC	CCTTTAGCTCGCTTAGGCCAC
SOX17	GATGCGGGATACGCCAGTG	CCACCTCGCCTTTCACCTTTA
Nestin	CCCTGAAGTCGAGGAGCTG	CTGCTGCACCTCTAAGCGA
GBX2	CAACTTCGACAAAGCCGAGG	ACTCGTCTTCCCTTGCCCT
FGF5	TGTGTCTCAGGGGATTGTAGG	AGCTGTTTTCTTGAATCTCTCC
Pax6	TACCAGTGCTACCAGCCAAT	TGCACGAGTATGAGGAGGTCT

CHAPTER 4

Forced fusion of human ventricular scar cells with cardiomyocytes suppresses arrhythmogenicity in a co-culture model

Marc C. Engels^{1,†}, Saïd F.A. Askar^{1,†}, Wanchana Jangsangthong¹; Brian O. Bingen¹, Iolanda Feola¹, Jia Liu¹, Rupamanjari Majumder¹, Michel I.M. Versteegh², Jerry Braun², Robert J.M. Klautz², Dirk L. Ypey¹, Antoine A.F. de Vries^{1,†}, Daniël A. Pijnappels^{1,†}

[†]These authors contributed equally to this work.

Laboratory of Experimental Cardiology¹, Department of Cardiology, and Department of Cardiothoracic Surgery², Heart Lung Center Leiden, Leiden University Medical Center, Leiden, the Netherlands.

Adapted from: Cardiovascular Research. 2015;107:601-612.

Abstract

Aims: Fibrosis increases arrhythmogenicity in myocardial tissue by causing structural and functional disruptions in the cardiac syncytium. Forced fusion of fibroblastic cells with adjacent cardiomyocytes may theoretically resolve these disruptions. Therefore, the electrophysiological effects of such electrical and structural integration of fibroblastic cells into a cardiac syncytium were studied.

Methods and results: Human ventricular scar cells (hVSCs) were transduced with lentiviral vectors encoding enhanced green fluorescent protein alone (eGFP \uparrow -hVSCs) or together with the fusogenic vesicular stomatitis virus-G protein (VSV-G/eGFP \uparrow -hVSCs) and subsequently co-cultured (1:4 ratio) with neonatal rat ventricular cardiomyocytes (NRVMs) in confluent monolayers yielding eGFP \uparrow - and VSV-G/eGFP \uparrow -co-cultures, respectively. Cellular fusion was induced by brief exposure to pH = 6.0 medium. Optical mapping experiments showed eGFP \uparrow -co-cultures to be highly arrhythmogenic (43.3% early afterdepolarization [EAD] incidence vs. 7.7% in control NRVM cultures, $P < 0.0001$), with heterogeneous prolongation of action potential (AP) duration (APD). Fused VSV-G/eGFP \uparrow -co-cultures displayed markedly lower EAD incidence (4.6%, $P < 0.001$) than unfused co-cultures, associated with decreases in APD, APD dispersion, and decay time of cytosolic Ca $^{2+}$ waves. Heterokaryons strongly expressed connexin43 (Cx43). Also, maximum diastolic potential in co-cultures was more negative after fusion, while heterokaryons exhibited diverse mixed NRVM/hVSC whole-cell current profiles, but consistently showed increased outward K_v currents compared with NRVMs or hVSCs. Inhibition of K_v channels by tetraethylammonium chloride abrogated the anti-arrhythmic effects of fusion in VSV-G/eGFP \uparrow -co-cultures raising EAD incidence from 7.9% to 34.2% ($P < 0.001$).

Conclusion: Forced fusion of cultured hVSCs with NRVMs yields electrically functional heterokaryons and reduces arrhythmogenicity by preventing EADs, which is, at least partly, attributable to increased repolarization force.

Introduction

While cardiomyocytes (CMCs) are responsible for the coordinated contraction of the heart by forming a functional syncytium of contractile cells via an extensive network of gap and adherent junctions, cardiac fibroblasts (CFBs) play a crucial supportive role.¹ Interactions between CMCs and CFBs are not only important for the optimal functioning of the healthy heart, but also play a major role in the adaptation to pathological conditions.^{2,3} For example, after myocardial infarction, the number of fibroblastic cells at the site of injury increases significantly, resulting in scar formation. While scar formation ensures cardiac integrity after damage, in the long run cardiac fibrosis negatively affects both the electrical and mechanical performance of the heart.⁴

Cardiac fibrosis is a process of adaptation and repair involving replacement of damaged CMCs by fibrous tissue in response to injury (e.g. myocardial infarction), disease, and aging, which creates an imbalance between parenchymal and interstitial cells. Moreover, cardiac fibrosis increases tissue heterogeneity as it causes local accumulation of fibroblastic cells (particularly myofibroblasts) and excessive deposition of extracellular matrix, potentially disrupting normal conduction pathways. Cardiac fibrosis may also affect cardiac ion transporters and Ca²⁺-handling proteins through crosstalk between CMCs and cardiac (myo)fibroblasts.⁵ As a result of the disruptive effects of scar fibroblasts on the cardiac syncytium, electrical impulse generation and propagation could become disturbed, leading to an increased pro-arrhythmic risk in fibrotic myocardium.⁶

Although several studies have focused on the mechanisms underlying arrhythmia initiation and dynamics in fibrotic substrates⁷⁻⁹, relatively few studies have been undertaken to restore the interrupted electrical syncytium.¹⁰ An obvious strategy to reduce the arrhythmogenicity associated with cardiac fibrosis, is to normalize as much as possible tissue composition, structure, and function and thereby reduce electrical heterogeneity. This goal may be achieved by increasing the number of excitable and/or well-coupled cells or by improving the electrophysiological properties of resident, non-excitable, poorly coupled fibroblastic cells. Both cell and gene therapy have been employed to reduce electrical heterogeneity at sites of cardiac injury.¹¹ Impaired electrical impulse generation and propagation in fibrotic myocardium can indeed be improved by transplantation of stem cell-derived CMCs, thereby lowering pro-arrhythmic risk,¹² although opposite findings have also been reported.¹³ More direct approaches to improve electrophysiological function of fibrotic myocardium through genetic modification of cardiac (myo)fibroblasts have also been pursued, such as manipulation of their ion channel and/or gap junction protein expression levels.^{10,14} Also, direct

cardiomyogenic transdifferentiation of (myo)fibroblasts via transcription factor- or microRNA-based reprogramming has been explored as a strategy to convert fibroblasts into CMCs.¹⁵ Although theoretically this approach may succeed in restoring the electrophysiological balance in fibrotic hearts, cardiomyogenic reprogramming of cardiac (myo)fibroblasts is still inefficient and incomplete.¹⁶

From a conceptual point of view, merging of myocardial scar cells into the cardiac syncytium may represent a mechanistically new approach to reduce fibrosis-related arrhythmogenicity. Therefore, in this study, the electrophysiological effects of integrating fibroblastic cells into the cardiac syncytium by forced heterocellular fusion were investigated. To this purpose, human ventricular scar cells (hVSCs) were endowed with controllable membrane fusion capacity by transduction with a lentivirus vector (LV) encoding the vesicular stomatitis virus G protein (VSV-G).¹⁷

Methods

Expanded methods descriptions are available in the Supplementary material online.

Human tissue was collected in accordance with guidelines posed by the Medical Ethics Committee of Leiden University Medical Center (LUMC), which follow the principles described in the Declaration of Helsinki. All animal experiments were approved by LUMC's Animal Experiments Committee and conformed to the Guide for the Care and Use of Laboratory Animals as stated by the US National Institutes of Health.

Isolation, culture, and transduction of hVSCs

hVSCs were isolated from surgical waste material consisting of myocardial scar tissue of patients undergoing left ventricular reconstructive surgery ($n = 10$) and cultured as described previously.^{10,18} Cells from all 10 patients were pooled and used at passage number 2-4 for further experiments. hVSCs were transduced with LVs encoding enhanced green fluorescent protein (eGFP) and the fusogenic VSV-G (LV.VSV-G/eGFP \uparrow) or eGFP alone (LV.eGFP \uparrow) to generate VSV-G/eGFP \uparrow -hVSCs and eGFP \uparrow -hVSCs, respectively.

Neonatal rat ventricular myocyte isolation and co-culture

Neonatal rat ventricular myocytes (NRVMs) were isolated as described previously.¹⁹ Briefly, neonatal Wistar rats (2 days *post-partum*) were anaesthetized by 5% isoflurane inhalation, and adequate anaesthesia was confirmed by the absence of reflexes. Next, hearts were rapidly excised, and ventricles were finely minced and dissociated with collagenase type 1 (450 U/

mL; Worthington, Lakewood, NJ, USA) and DNase I (18.75 Kunitz/mL; Sigma-Aldrich, St. Louis, MO, USA). After selective depletion of most fibroblastic cells by pre-plating, the remaining cells (mainly CMCs) were mixed with hVSCs in a ratio of 4:1 for all co-culture groups and seeded on fibronectin-coated (Sigma-Aldrich) coverslips in 24-well plates (Corning Life Sciences, Corning, NY, USA). Co-cultures were established with untransduced hVSCs (UT-co-cultures), VSV-G/eGFP \uparrow -hVSCs (VSV-G/eGFP \uparrow -co-cultures) or eGFP \uparrow -hVSCs (eGFP \uparrow -co-cultures). NRVM cultures without hVSCs (hereinafter referred to as NRVM cultures) were taken along as control whenever indicated. Cells were plated at a total density of $0.5\text{--}6 \times 10^5$ cells/well, depending on the assay. Twelve to 16 hours after plating, cultures were treated for 2 h with mitomycin-C (10 $\mu\text{g/mL}$; Sigma-Aldrich) to prevent proliferation of non-CMCs.¹⁹

Induction and assessment of cell-to-cell fusion

To induce intercellular fusion, cells were incubated with sodium 2-(4-morpholino-)ethanesulfonate-buffered (Sigma-Aldrich) NRVM culture medium of pH 6.0 for 3.5 min at 37°C in water vapour-saturated 95% air/5% CO₂ on Day 3 of co-culture. All co-cultures, including those containing untransduced hVSCs and eGFP \uparrow -hVSCs and NRVM cultures underwent the same treatment unless indicated otherwise. Fusion efficiency was assessed by immunocytological assay and by phase contrast microscopy. Phase contrast analysis was done on Day 4 of co-culture (*i.e.* 24 h after induction of intercellular fusion) using a Carl Zeiss Axiovert 40C microscope. For each culture, 10 random fields of view were analysed. The total number of nuclei in each field of view was counted, as well as the total number of nuclei in heterokaryons (*i.e.* cells containing > 2 nuclei). The percentage of heterokaryonic nuclei per field of view was calculated and averaged for the 10 fields of view inspected per experimental group. VSV-G/eGFP \uparrow -co-cultures were included for further assay when 40-60% of the nuclei were in heterokaryons.

Optical voltage mapping

Assessment of the electrophysiological effects of heterocellular fusion was performed by optical voltage mapping as described previously.²⁰ On Day 5 of co-culture, cells were loaded with potentiometric dye by incubation for 15 min at 37°C with colourless HEPES-buffered DMEM/F12 containing 8 μM di-4-ANEPPS (both from Life Technologies, Carlsbad, CA, USA), and optically mapped using a MiCAM ULTIMA-L imaging system (SciMedia USA, Costa Mesa, CA, USA). To study the effect of K_v current inhibition, cultures were optically mapped after a 10-min incubation with 40 mM tetraethylammonium chloride (TEA; Sigma-Aldrich) or 1 mM 4-aminopyridine (4-AP; Sigma-Aldrich) at 37°C.

Optical mapping of Ca²⁺ dynamics

Intracellular Ca²⁺ dynamics were assessed by optical mapping with the Ca²⁺-sensitive dye Rhod-2-AM (Life Technologies). Cells were labelled by incubation with 2.5 μM Rhod-2-AM in DMEM/F12 at 37°C for 30 min. Next, cells were incubated in fresh, unsupplemented DMEM/F12 for another 30 min in the incubator for de-esterification of internalized Rhod-2-AM. Optical signals were captured using the MiCAM ULTIMA-L imaging system. Cells were stimulated electrically at a frequency of 1-Hz. As a quantitative measure of Ca²⁺ dynamics, the time for the signal to decrease to 63% of the peak value was determined using BrainVision Analyzer 1101 software (Brainvision, Tokyo, Japan).

Transwell assays

The effects of paracrine signaling of hVSCs on the electrophysiological properties of NRVMs was assessed by transwell assays. NRVMs were cultured as described previously, plated at a density of 6×10^5 cells/well on fibronectin-coated, 15-mm diameter, round glass coverslips and placed at the bottom of 24-well transwell plates (Corning Life Sciences). The transwell inserts (0.4 μm pore size) were seeded with hVSCs (1.5×10^5 cells/insert) or were left unseeded to provide negative controls. Cells were cultured in NRVM culture medium, which was refreshed every 48 h to allow ample exposure to paracrine factors. At Day 5 of culture, optical mapping experiments were performed as described above. To investigate the possibility of acute paracrine effects during optical mapping experiments, hVSC-seeded or empty inserts were cultured in DMEM/F12 for 48 h, after which the culture medium was collected. This conditioned medium (CM) was subsequently used for potentiometric dye loading and during optical mapping.

Patch-clamp recordings

Patch-clamp measurements were conducted on Day 5 of (co-)culture with a conventional system consisting of a MultiClamp 700B amplifier and a Digidata 1440A A/D converter, controlled by Clampex 10 software (Axon CNS, Molecular Devices, Sunnyvale, CA, USA), as previously described.²¹ Current- and voltage-clamp recordings were performed on single NRVMs, single hVSCs, and solitary heterokaryons. In addition, perforated patch-clamp recordings on NRVMs in confluent NRVM cultures, NRVMs adjacent to eGFP⁺-hVSCs in confluent eGFP⁺-co-cultures and heterokaryons in confluent VSV-G/eGFP⁺-co-cultures were also performed to examine the AP characteristics in these cultures. Data sets were derived from ≥ 3 independent experiments.

Statistical analysis

Statistical analyses were performed using GraphPad Prism software version 6 (Graphpad Software, La Jolla, CA, USA). Unpaired Student's *t*-test, Fisher's exact test and one-way analysis of variance (ANOVA) with Bonferroni's multiple comparison test were used for comparisons

between experimental groups. Data were expressed as mean \pm standard error of mean (SEM) for a specified number (n) of observations with each observation representing an independent culture or cell. Results were considered statistically significant at P -values < 0.05 . Statistical significance was expressed as follows: $*P < 0.05$, $**P < 0.001$, NS: not significant.

Results

Co-culture of NRVMs with hVSCs is pro-arrhythmic

Immunocytological staining showed that all hVSCs were positive for collagen type 1 (COL1), but negative for smooth muscle myosin heavy chain (sm-MHC), sarcomeric alpha-actinin (ACTN), and platelet endothelial cell adhesion molecule (PECAM-1). Of the COL1⁺ cells, roughly 40% were alpha smooth muscle actin (α -SMA)-positive (see Supplementary material online, *Figure S1*). Phase contrast microscopy showed that NRVM cultures, as well as UT-co-cultures, formed confluent monolayers. Immunocytological analyses confirmed a 4:1 ratio of NRVMs (ACTN⁺ cells) and hVSCs (human lamin A/C [hLMNA⁺] cells) in UT-co-cultures (*Figure 1A*). Optical voltage mapping of 1-Hz electrically stimulated cultures indicated a significantly lower conduction velocity (CV) in UT-co-cultures than in NRVM cultures (*Figure 1B*). Both NRVM and UT-co-cultures typically displayed 1:1 uniform convex propagation originating from the bipolar pacing electrode (*Figure 1C*). UT-co-cultures typically featured increases in action potential (AP) duration (APD; *Figure 1D and E*) and APD₈₀ dispersion (*Figure 1F*). This was associated with a much higher early afterdepolarization (EAD) incidence upon 1-Hz stimulation in UT-co-cultures compared with NRVM cultures (*Figure 1G and H*). These data indicate that addition of hVSCs to NRVM cultures greatly increases their arrhythmogenicity.

To investigate whether paracrine signaling of hVSCs could render NRVM cultures pro-arrhythmic, hVSCs were cultured on a cell-impermeable membrane above NRVMs using transwell culture plates. These studies showed no significant difference in CV, APD₈₀, APD₈₀ dispersion, and EAD incidence between NRVM cultures that had, and NRVM cultures that had not been exposed to paracrine factors released by hVSCs (Supplementary material online, *Figure S2*). Paracrine signalling by hVSCs thus seems not to be a major contributor to the high arrhythmogenicity of NRVM-hVSC co-cultures.

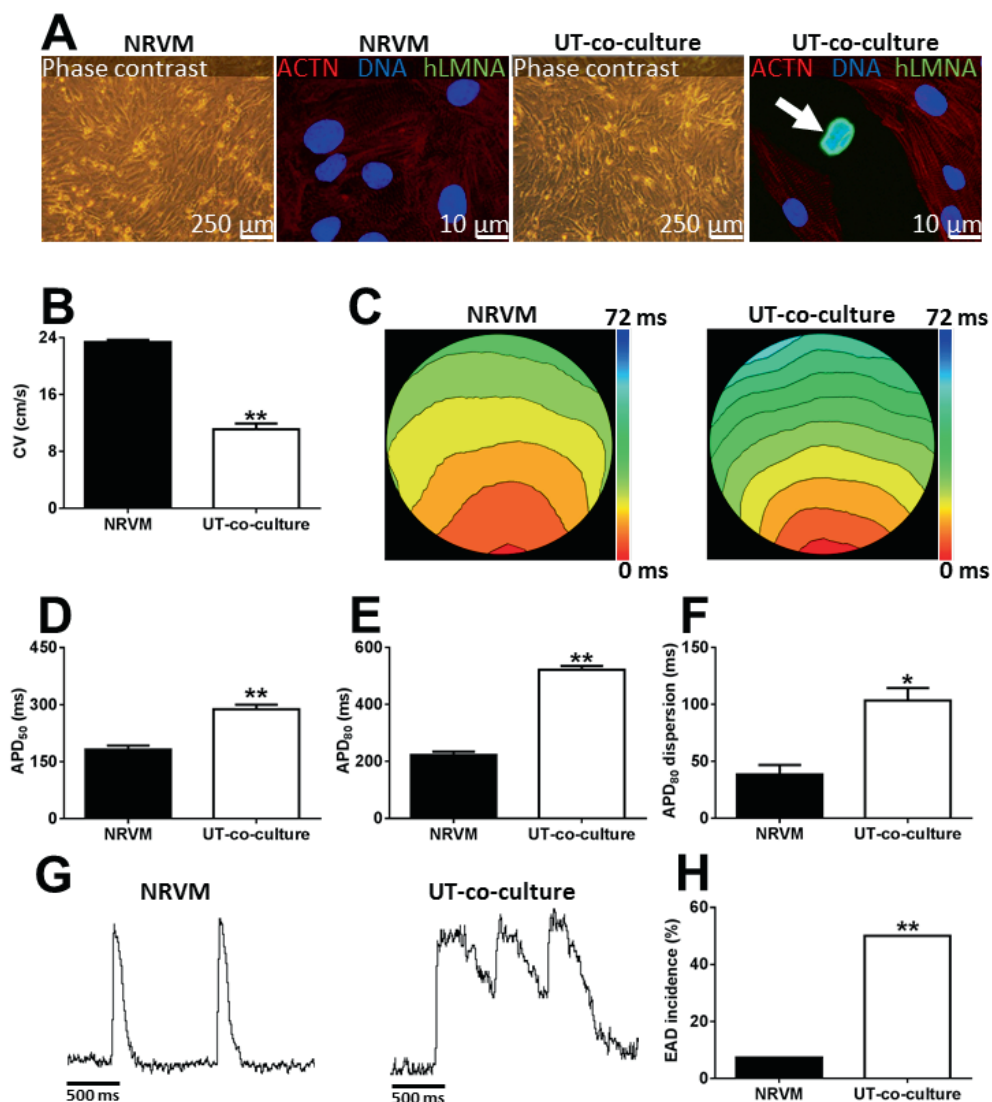


Figure 1. NRVM-hVSC-co-cultures display a pro-arrhythmic phenotype. (A) Typical examples of phase-contrast microscopic images and immunocytochemical stainings of NRVM cultures (left panels) and UT-co-cultures, which contained NRVMs and untransduced hVSCs (right panels) in a 4:1 ratio. Cells were stained for sarcomeric α -actinin (ACTN, red, NRVMs), human lamin A/C (hLMNA, green, hVSCs) and with Hoechst 33342 (DNA, blue, nuclei). The white arrow indicates an hLMNA⁺ hVSC nucleus. (B) Assessment of CV by optical mapping. (C) Representative activation maps (6-ms isochrone spacing) of NRVM culture (left) and UT-co-culture (right) paced at 1 Hz. Quantification of (D) APD₅₀, (E) APD₈₀ and (F) APD₈₀ dispersion. (G) Typical optical signal trace during 1-Hz electrical stimulation of an NRVM culture (left) and an EAD-displaying UT-co-culture (right). (H) Quantification of EAD incidence. Quantitative data were based on 41 NRVM cultures and 46 UT-co-cultures.

Characterization of heterokaryonic fusion products

hVSCs were transduced with LV.eGFP \uparrow (Figure 2A; control vector) to generate hVSCs that were only eGFP $^+$ (eGFP \uparrow -hVSCs; Supplementary material, Figure S3A), or with LV.VSV-G/eGFP \uparrow (Figure 2B) to generate hVSCs expressing both VSV-G and eGFP (VSV-G/eGFP \uparrow -hVSCs; Supplementary material, Figure S3B). The transduced cells were then co-cultured with NRVMs. Brief exposure of these co-cultures to pH= 6.0 medium caused the VSV-G/eGFP \uparrow -hVSCs, but not the eGFP \uparrow -hVSCs, to fuse with surrounding NRVMs (Figure 2C and D). Immunostaining of eGFP \uparrow -co-cultures showed the presence of ACTN $^+$ /hLMNA $^-$ cells (NRVMs) and of cells that were positive for COL1 and hLMNA (hVSCs; Figure 2C). However, after induction of fusion in VSV-G/eGFP \uparrow -co-cultures, large multinucleated cells were observed, which were positive for COL1 as well as for ACTN, confirming fusion of hVSCs with NRVMs into heterokaryons (Figure 2D). These cells contained on average 11.0 ± 0.8 nuclei, of which $22.5 \pm 1.3\%$ were positive for hLMNA (Figure 2E). The VSV-G/eGFP \uparrow -co-cultures did not show signs of apoptosis at 2, 4 or 6 after fusion induction, as assessed by annexin V live cell staining (Supplementary material, Figure S4).

To further study the electrophysiological characteristics of heterokaryons at a functional level, patch-clamp experiments were performed on single NRVMs, single hVSCs and isolated heterokaryons. As expected, short depolarizing current-clamp stimulations (5 ms, 100-300 pA) were sufficient to evoke APs in NRVMs (Figure 3A), but failed to initiate APs in hVSCs. The spiky response of hVSCs to the current stimulus reflects their inexcitability, as the response curve follows the discharge characteristics of a passive resistance-capacitance circuit (Figure 3B). Under our experimental conditions, 1 out of 2 heterokaryons (hereinafter referred to as responsive heterokaryons) readily elicited an AP upon stimulation (Figure 3C). Maximal upstroke velocity was 38.0 ± 5.9 mV/ms for responsive heterokaryons, compared to 88.0 ± 13.2 mV/ms for NRVMs (Figure 3D). AP amplitude did not significantly differ between these heterokaryons and NRVMs (Figure 3E), while the average APD $_{80}$ of responsive heterokaryons was considerably longer than that of NRVMs (480.6 ± 90.2 ms vs. 110.9 ± 8.0 ms, $P < 0.0022$, $N = 10$ and 8 , respectively). Furthermore, responsive heterokaryons had a resting membrane potential in between that of unfused hVSCs and NRVMs (Figure 3F). Being derived from multiple cells, heterokaryons possessed a larger cell membrane capacitance (C_m) than individual NRVMs or hVSCs (Figure 3G). These data indicate that forced heterocellular fusion yields electrically functional heterokaryons.

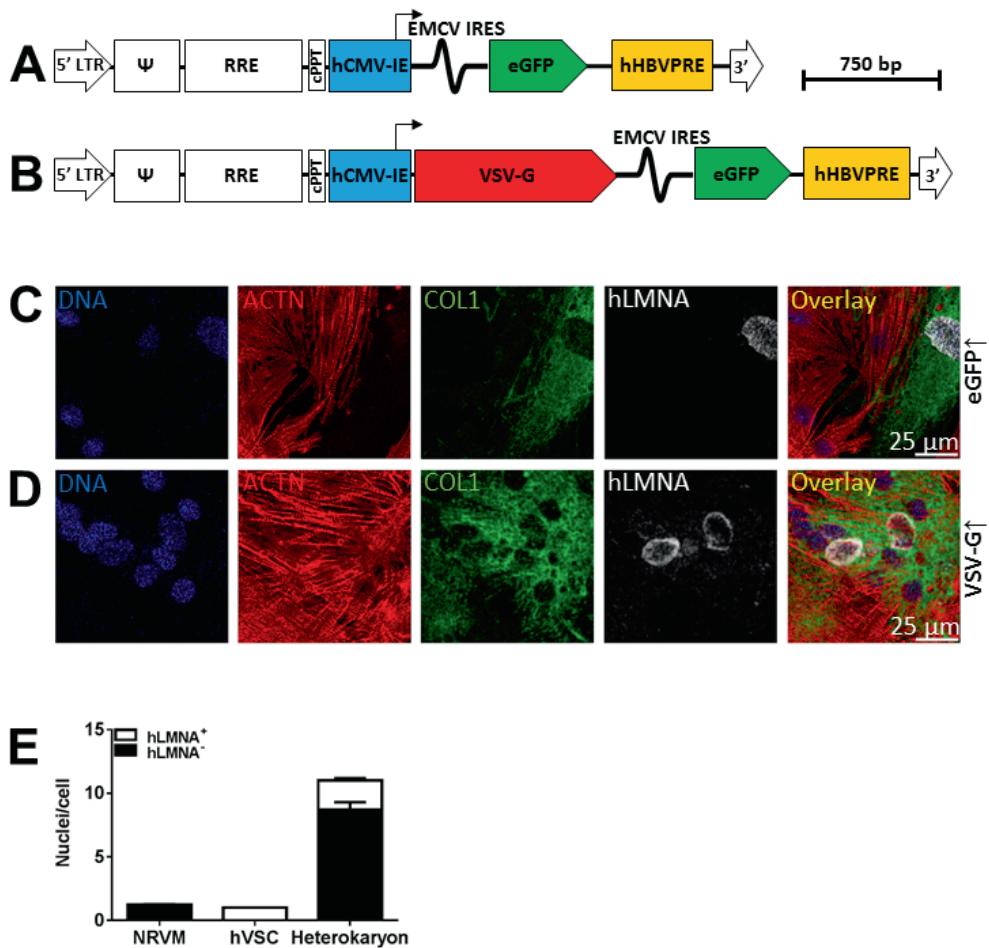


Figure 2. VSV-G-mediated heterocellular fusion of hvSCs with NRVMs. Proviral DNA structure of (A) LV.eGFP \uparrow and (B) LV.VSV-G/eGFP \uparrow . The different abbreviations are explained in the chapter designated “Construction of self-inactivating lentiviral vector (SIN-LV) shuttle plasmids” of the Supplementary material. Co-culture containing hvSCs transduced with either (C) LV.eGFP \uparrow (eGFP \uparrow -co-culture; eGFP \uparrow) or (D) LV.VSV-G/eGFP \uparrow (VSV-G/eGFP \uparrow -co-culture; VSV-G \uparrow) upon brief exposure to pH 6. Cells were stained for sarcomeric α -actinin (ACTN, red, NRVMs), collagen type I (COL1, green, hvSCs), human lamin A/C (hLMNA, white, hvSCs) and Hoechst 33342 (DNA, blue, nuclei). (E) Quantification of total number of nuclei and their origin per cell for NRVMs (N=31), hvSCs (N=28) and heterokaryons (N=53), as assessed by immunocytological staining. Human nuclei were distinguished from rat nuclei by their positive staining for hLMNA. Scale bar=25 μ m.

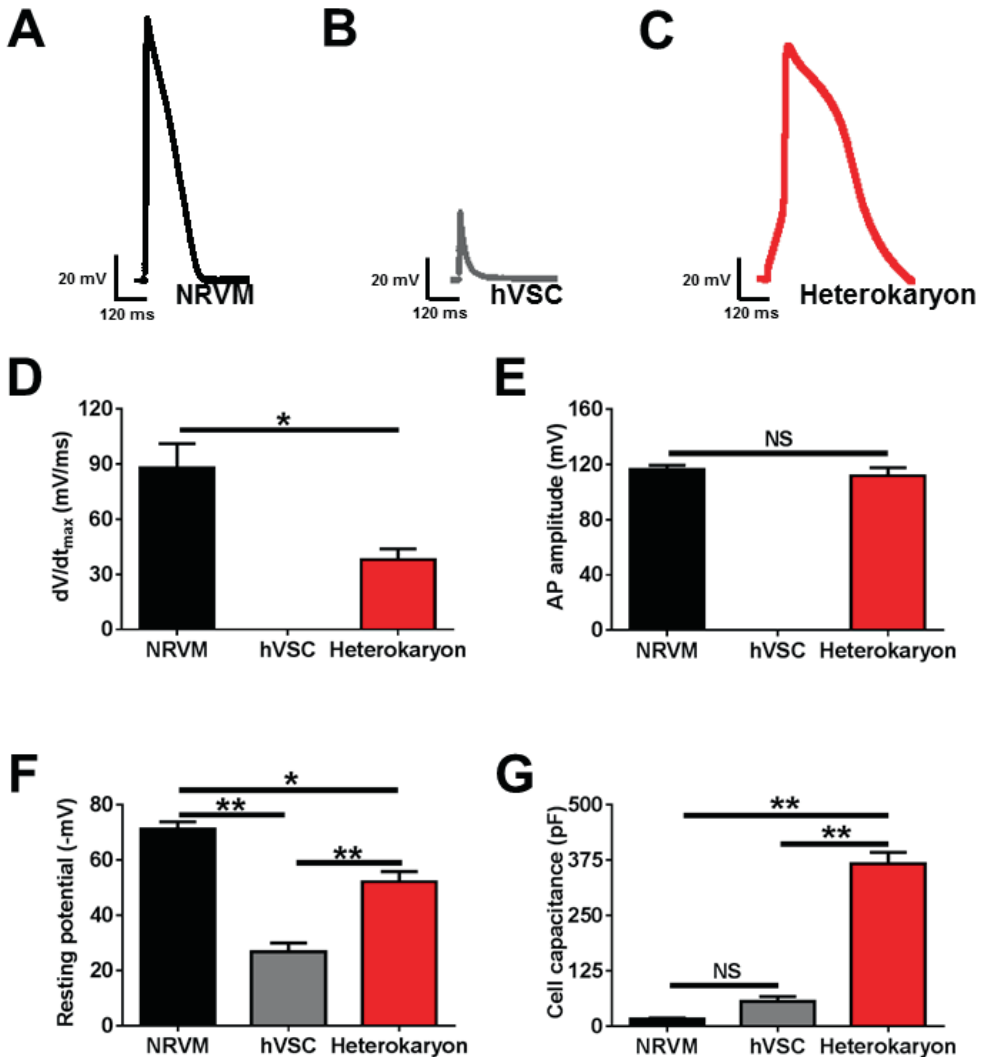


Figure 3. Fusion of hVSCs with NRVMs yields excitable heterokaryons. Typical current-clamp responses evoked by short current pulses in a single (A) NRVM, (B) hVSC and (C) responsive heterokaryon. Measurements from single NRVMs (N=8), single hVSCs (N=9) and isolated heterokaryons (N=9), comparing (D) maximum upstroke velocity (dV/dt_{max}), (E) AP amplitude and (F) resting membrane potential (RMP). To standardize the AP recording conditions, the cells were kept at a RMP of -80 mV by an appropriate holding current (G) C_m of isolated NRVMs, solitary hVSCs and isolated responsive and non-responsive heterokaryons.

Forced heterocellular fusion reduces arrhythmogenicity

To study the effects of heterocellular fusion in our fibrosis model, optical voltage mapping recordings were performed. Low pH-pretreated eGFP⁺- and VSV-G/eGFP⁺-co-cultures both showed convex 1:1 electrical propagation upon 1-Hz electrical stimulation (*Figure 4A*). However, EAD incidence in fused VSV-G/eGFP⁺-co-cultures was much lower than in eGFP⁺-co-cultures and similar to the EAD incidence in control NRVM cultures (*Figure 4B-D*). Furthermore, as compared to eGFP⁺-co-cultures, fused VSV-G/eGFP⁺-co-cultures displayed shorter APs, less APD dispersion and higher CVs (*Figure 4E-J*). Similar results were obtained for (co-)cultures subjected to 2-Hz electrical pacing. Patch-clamp experiments in monolayer cultures confirmed the beneficial effects of NRVM-hVSC fusion on APD, maximal upstroke velocity, AP amplitude and MDP (Supplementary material, *Figure S5*). Collectively, these data show that fusion of CMCs with hVSCs strongly reduces the arrhythmogenicity of fibrotic NRVM cultures.

Changes in cytosolic Ca²⁺ handling could be a possible mechanism contributing to the arrhythmogenic effect of fibrosis and of the beneficial effect of fibroblast-cardiomyocyte fusion in our co-cultures. To investigate this possibility, optical mapping experiments with the Ca²⁺ indicator Rhod-2-AM were carried out in NRVM cultures as non-fibrotic control cultures, eGFP⁺-co-cultures and fused VSV-G/eGFP⁺-co-cultures. For each culture type the duration of the Ca²⁺ waves (characterized by Ca²⁺ decay times) followed the APD (compare *Figure S6* with main manuscript, *Figure 4I*). This suggests that the arrhythmogenicity of unfused NRVM-hVSC co-cultures is not due to abnormalities in Ca²⁺ handling and that the beneficial effect of heterocellular fusion on fibrotic NRVM cultures does not result from the restoration of abnormalities in Ca²⁺.

Heterokaryons show abundant expression of gap junctional proteins

Immunocytological staining of eGFP⁺-co-cultures for connexin43 (Cx43) gave strong signals at CMC-CMC borders, but very weak signals at hVSC-CMC interfaces. In contrast, heterokaryons showed abundant Cx43 expression, predominantly at heterokaryon-CMC and heterokaryon-heterokaryon borders (*Figure 5A and B*). In line with these findings, mRNA levels for Cx43 were significantly higher in fused VSV-G/eGFP⁺-co-cultures than in eGFP⁺-co-cultures. Western blot analyses also showed protein levels of Cx43 to be significantly increased in fused as compared to non-fused NRVM-hVSC co-cultures (*Figure 5C*).

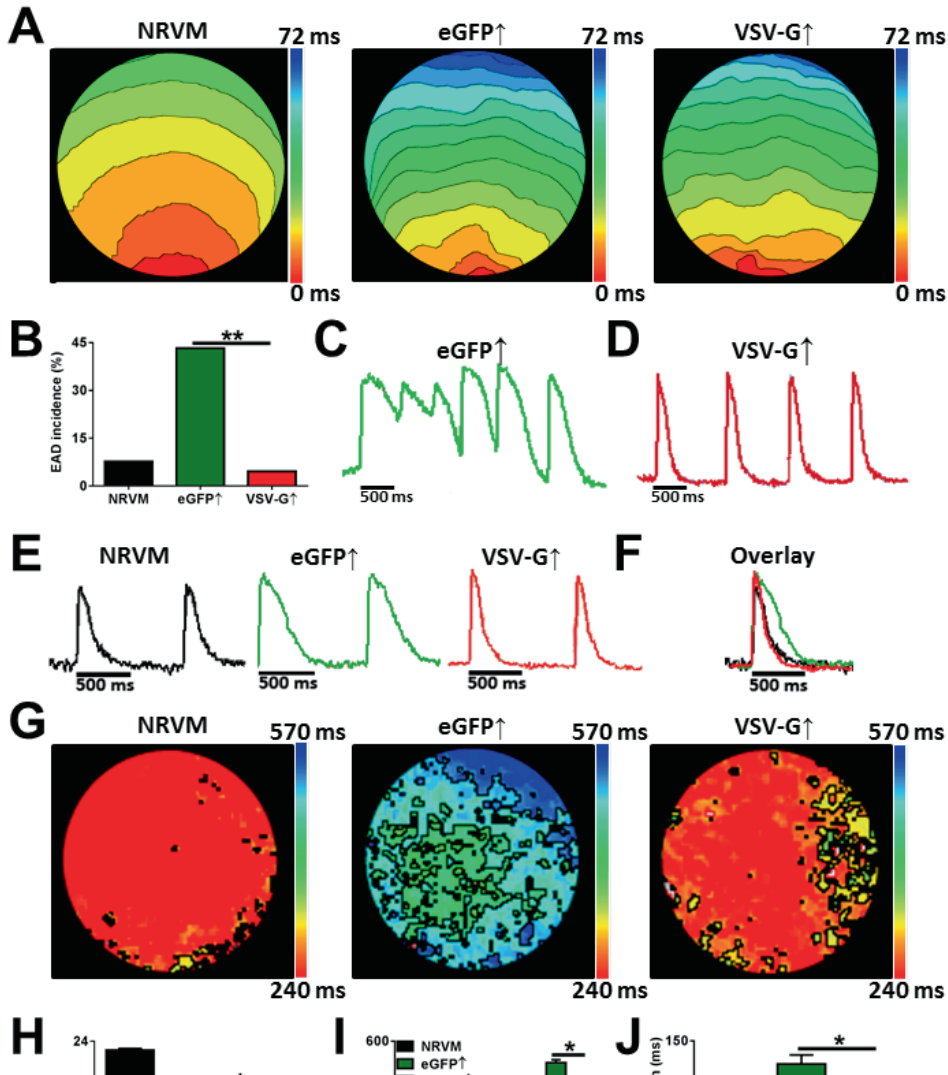


Figure 4. Heterocellular fusion reduces arrhythmogenicity in NRVM-hVSC co-cultures. Optical mapping of NRVM culture (NRVM; N=39), eGFP \uparrow -co-cultures (eGFP \uparrow ; N=60), and fused VSV-G/eGFP \uparrow -co-cultures (VSV-G \uparrow ; N=65). (A) Typical examples of activation maps (6-ms isochrone spacing) following 1-Hz pacing. (B) Quantification of EAD incidence. (C) Typical optical signal trace in an EAD-displaying eGFP \uparrow -co-culture. (D) Typical optical signal trace in a fused, non-arrhythmic VSV-G/eGFP \uparrow -co-culture. (E) Typical spatially and cubically filtered optical signal traces of NRVM culture (left), eGFP \uparrow -co-culture (middle) and -VSV-G/eGFP \uparrow -co-culture (right) following 1-Hz pacing, and (F) representative signal trace overlay. (G) Representative APD $_{80}$ maps. Quantification of (H) CV, (I) APD $_{50}$ and APD $_{80}$, and (J) APD $_{80}$ dispersion.

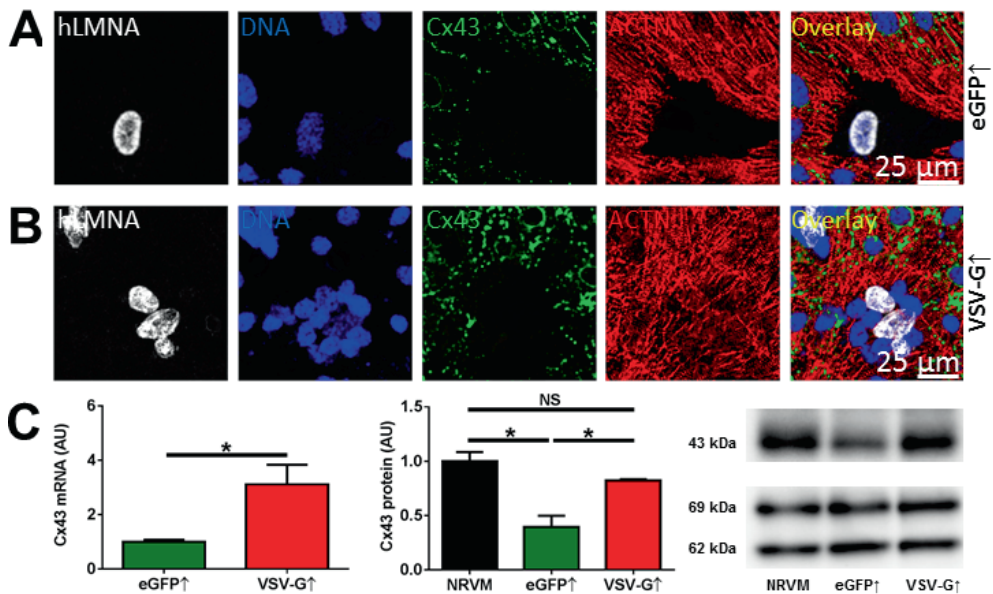


Figure 5. Heterocellular fusion increased gap junctional protein expression. Cells were stained for human lamin A/C (hLMNA, white), Hoechst 33342 (DNA, blue, nuclei), connexin43 (Cx43, green) and sarcomeric α -actinin (ACTN, red). (A) Representative eGFP[↑]-co-culture (eGFP[↑]) and (B) fused VSV-G/eGFP[↑]-co-culture (VSV-G[↑]). (C) Quantification of Cx43 mRNA (left panel) and protein (middle panel) and representative Western blot (right panel) showing the 43-kDa Cx43 protein as well lamin A/C protein species of 62 and 69 kDa, which served as loading controls. Quantitative data were based on 4 independent samples per group. AU, arbitrary units. Scale bar=25 μ m.

Heterocellular fusion is anti-arrhythmic, at least partly, by enhancing repolarization force

Voltage-clamp analysis of the ionic membrane currents in single NRVMs, hVSCs and heterokaryons (Supplementary material, *Figure S7* and *Figure 6A*) showed that the NRVMs and hVSCs share their currents in the heterokaryons to a variable degree, causing about half of the heterokaryons to readily produce APs upon stimulation. Significant in this analysis was the increased I_{Kv} when averaged over its time course in the total pool of heterokaryons (*Figure S7H*), which resulted from an overall slower inactivation rate (*Figure 6A-C*). This I_{Kv} was strongly reduced by 40 mM TEA (*Figure 6D-E*). This observation allowed us to investigate whether the anti-arrhythmic effects of forced heterocellular fusion are mechanistically linked to the observed increase in repolarization force by optical mapping experiments on low pH-pretreated monolayer cultures after incubation of the cells with 40 mM TEA to block outward K_v currents. Both TEA-treated eGFP[↑]- and VSV-G/eGFP[↑]-co-cultures showed 1:1 electrical convex propagation from the pacing electrode upon 1-Hz pacing (*Figure 7A*). TEA treatment had no significant effect on CV (*Figure 7B*), but significantly increased APD₈₀ and APD dispersion (*Figure 7C-F*). TEA treatment also significantly raised EAD incidence in VSV-G/eGFP[↑]-co-cultures, but not in eGFP[↑]-co-cultures where incidence was already high (*Figure 7G* and

H). On the other hand, exposure to 1 mM 4-AP, which inhibits average I_{Kv} by only ~30% (see Supplemental material), did not increase EAD incidence in fused VSV-G/eGFP \uparrow -co-cultures, despite its prolonging effect on APD₃₀ (Supplementary material, Figure S8). Collectively, these data demonstrate that upon TEA incubation, fused VSV-G/eGFP \uparrow -co-cultures displayed a similar electrophysiological phenotype as unfused eGFP \uparrow -co-cultures, in terms of APD, APD dispersion and EAD incidence. This strongly suggests that heterocellular fusion reduces the arrhythmogenicity of NRVM-hVSC co-cultures, at least partly, by enhancing repolarization force, consistent with the increased I_{Kv} found in the heterokaryons.

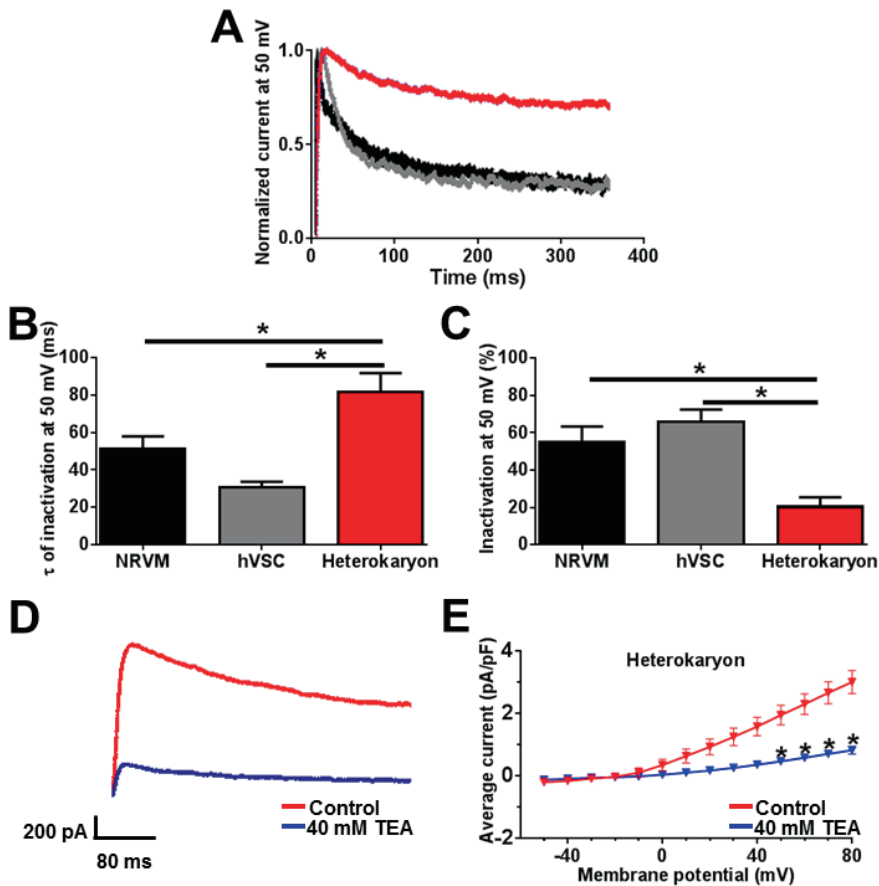


Figure 6. Heterokaryons possess outward K_v currents with slower inactivation kinetics than NRVMs or hVSCs and are TEA sensitive. (A) Typical outward current traces of the three cell types at 50 mV test potential, normalized for the initial peak amplitude. (B) Quantification of inactivation time constant (τ_{inact}) at 50 mV test potential. (C) Quantification of degree of current inactivation (I_{inact}) at 50 mV. (D) Superimposed typical records of whole-cell outward currents evoked at a test potential of 50 mV of a control (red) and TEA-treated (blue) heterokaryon. (E) Average current density-voltage plot of control (red) and TEA-treated (blue) heterokaryons shows a significant TEA-dependent decrease in current density at positive potentials.

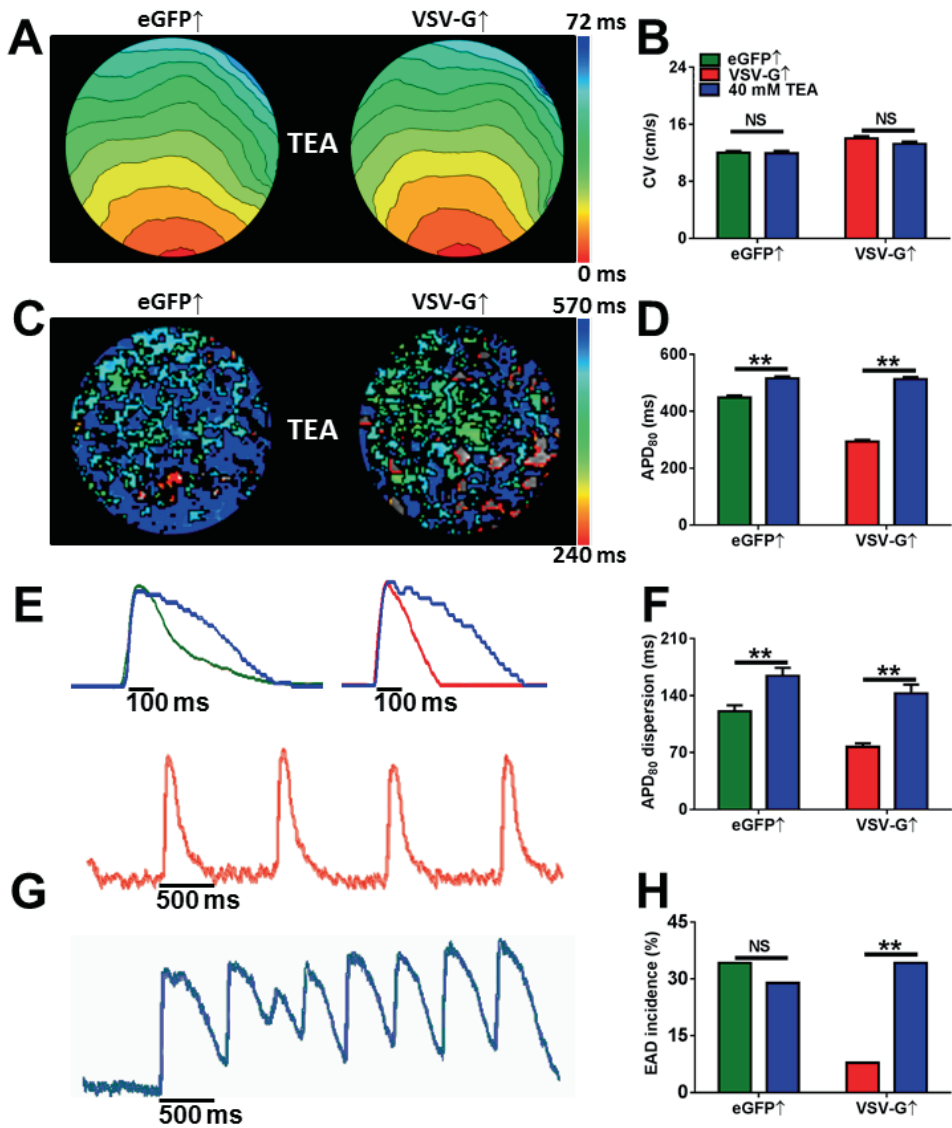


Figure 7. Inhibition of outward K_v currents abolishes the anti-arrhythmic effects of heterocellular fusion in VSVG/eGFP⁺-co-cultures. (A) Typical activation maps (6-ms isochrone spacing) of TEA-treated eGFP⁺-co-cultures (eGFP⁺) and fused VSV-G/eGFP⁺-co-cultures (VSV-G⁺). (B) Quantification of CV in TEA-treated and control eGFP⁺-co-cultures (N=38) and VSV-G/eGFP⁺-co-cultures (N=38). (C) Typical APD₈₀ maps of TEA-treated eGFP⁺- and VSV-G/eGFP⁺-co-cultures. (D) Effect of TEA on APD₈₀. (E) Typical spatially and cubically filtered optical signal trace overlays of a representative eGFP⁺-co-culture (left) before (green) and after (blue) treatment with 40 mM TEA, and of a VSV-G/eGFP⁺-co-culture (right) before (red) and after (blue) TEA treatment. (F) Effect of TEA on APD₈₀ dispersion. (G) Typical spatially and cubically filtered optical signal traces of a representative VSV-G/eGFP⁺-co-culture before (red) and after incubation with 40 mM TEA (blue). The blue signal trace shows the occurrence of multiple EADs. (H) Effect of TEA on EAD incidence.

Discussion

The key findings of this study are as follows: first, co-culture of hVSCs with NRVMs creates a pro-arrhythmic substrate by favoring EAD generation. Second, transduction of hVSCs with an LV encoding the fusogenic VSV-G endows these cells with controllable membrane fusion capacity, which enables them to fuse with surrounding NRVMs, resulting in formation of functional heterokaryons expressing high levels of Cx43 and showing strong outward K_v currents. Third, such forced cellular fusion of hVSCs with NRVMs reduces arrhythmogenicity in NRVM-hVSC co-cultures by preventing EADs. Finally, enhanced repolarization force is an important contributor to this anti-arrhythmic effect of heterocellular fusion.

Electrophysiological consequences of fibrosis

Intercellular communication between adjacent CMCs via gap junctions enables cardiac tissue to act as a functional syncytium and to ensure well-coordinated electrical and mechanical activation of the heart. In cardiac fibrosis, excessive deposition of extracellular matrix and local accumulation of inexcitable fibroblasts leads to disruptions of this syncytium.⁶ While *in vitro* models to specifically study the role of the extracellular matrix on arrhythmogenesis remain to be developed, cell culture models have provided detailed information on the potential pro-arrhythmic effects of fibroblast-CMC interactions.^{5,10} Consistent with these studies, our NRVM-hVSC co-cultures were slightly depolarized due to the (weak) electrical coupling of NRVMs to hVSCs.²² This slight depolarization and the consequential increases in Na_v and K_v channel inactivation could at least partly explain the lower CV, longer APD and slower repolarization in the UT-co-cultures compared with the NRVM cultures. However, electrical coupling of the inexcitable hVSCs to the surrounding NRVMs could also have contributed to the lower CV and increased APD in the fibrotic NRVM cultures, due to the resulting capacitive loading of the NRVMs and its prolonging effect on both depolarization and repolarization time. Finally, a decrease in contact area between NRVMs due to insertion of hVSCs in between NRVMs, resulting in less efficient electric coupling between CMCs, may also have reduced CV. Besides a lower CV, the slower repolarization rate (causing “triangulation” of the AP) in the $I_{Ca,L}$ window current region seems another important cause of the high arrhythmogenicity of the NRVM-hVSC co-cultures as it favours EADs.²³ Previous studies demonstrated that paracrine factors released by CFBs change the electrophysiological properties of CMCs.^{24,25} Transwell experiments showed that paracrine signaling from hVSCs did not have arrhythmogenic effects in our co-culture model. These disparate results may be explained by the fact that these previous studies were either carried out with CMCs and CFBs of neonatal rats or with CMCs and CFBs of adult rats using cell ratios and time points of assessment different from ours.^{24,25} Paracrine signaling by CFBs could, however, still modulate other processes in CMCs, which were not investigated in this study.

Electrophysiological consequences of heterocellular fusion

Forced cellular fusion of hVSCs with NRVMs in NRVM-hVSC co-cultures resulted in an increase in CV, decreases in APD and APD dispersion, and, ultimately, in a lower EAD incidence. Heterokaryons resulting from NRVM-hVSC fusion seem to primarily owe their negative MDP to I_{Kir} and their excitability to I_{Nav} and $I_{Ca,L}$ of the NRVMs incorporated into the heterokaryons. The overall excitability of the responsive heterokaryons was, however, lower than that of NRVMs due to the decreased $I_{Ca,L}$ density and increased C_m . Apparently, the decreased I_{Kir} density in individual heterokaryons was still strong enough to bring the MDP to a value between those of single hVSCs and NRVMs, which was favoured by the small leakage conductance in heterokaryons. However, the MDP of fused VSV-G/eGFP \uparrow -co-cultures did not significantly differ from that of NRVM cultures indicating that in our confluent monolayer cultures the heterokaryons were hyperpolarized by coupling with surrounding CMCs. Gap junctional coupling efficiency may be increased with heterocellular fusion considering the fusion-dependent increases in Cx43 transcript levels as well as in Cx43 protein levels and the abundant Cx43 expression at interfaces between adjacent heterokaryons and at borders between heterokaryons and NRVMs. In a previous study our research group showed that in confluent monolayer cultures hVSCs are electrically coupled with surrounding NRVMs albeit weakly,¹⁰ which corresponds to the low Cx43 expression at hVSC-NRVM interfaces in the eGFP \uparrow -co-cultures. Efficient electrical coupling of heterokaryons with surrounding non-fused NRVMs may explain why cardiac excitation waves are well conducted through heterokaryons, despite their reduced excitability in comparison to NRVMs. Efficient gap junctional coupling is also expected to increase CV by lowering intercellular resistance. An additional possible reason for the increase in CV in fibrotic NRVM cultures after fusion could be the presence of enlarged intracellular compartments allowing APs to traverse several NRVM diameters at once.

Another important aspect is the significant role for repolarizing currents in the anti-arrhythmic effects of forced heterocellular fusion, as indicated by patch-clamp measurements. After compensation for cell size, a significantly stronger transient outward K_v current with slower inactivation kinetics was observed in heterokaryons than in NRVMs. The resulting increase in repolarization force could explain the observed reduction of APD and EAD incidence. This notion was confirmed by our TEA experiments, which showed that I_{Kv} inhibition in fused VSV-G/eGFP \uparrow -co-cultures resulted in loss of the anti-arrhythmic effects of heterocellular fusion as manifested by an increase in EAD incidence to a value similar to that of non-fused NRVM-hVSC co-cultures. The exact mechanisms by which forced heterocellular fusion between hVSCs and NRVMs increases the outward K_v currents in fusion products warrants further investigation. One possibility is selective activation of K_v channel genes as a result of the fusion process due to the combinatorial effects of transcriptional regulators from two different cell types. Depending on

the specific epigenetic landscapes in the nuclei of NRVMs and hVSCs, transcription of certain genes may be more readily upregulated in heterokaryons than that of others. If there was a selection for K_v channels, this could have accounted for the enhanced K_v current seen after fusion. The mixed content of NRVMs and hVSCs in heterokaryons could also have increased the activity of individual K_v channels by altered posttranslational modifications or association with other regulatory proteins. The strong Cx43 expression at heterokaryon-CMC interfaces might also allow heterokaryonic I_{Kv} to facilitate repolarization of surrounding NRVMs and I_{Kir} from NRVMs to support repolarization of adjacent heterokaryons. This mutual sharing of two repolarizing channel types may cause an overall faster repolarization and, consequently, less AP triangulation. This, in turn, would have an anti-arrhythmic effect by reducing EAD risk.²³ However, furthering our understanding on the precise role of electrical coupling in cardiac impulse propagation after heterocellular fusion will depend on dedicated studies. These studies should also address to what extent heterokaryons are able to respond to subsequent pathological processes by gap junctional modulation, like normally occurs in damaged myocardium to prevent spread of death signals to surrounding healthy cardiac tissue.²⁶

Regarding the effect of heterocellular fusion on Ca^{2+} handling, our patch-clamp data show that the average Ca^{2+} peak current in heterokaryons is decreased compared with NRVMs, while Ca^{2+} transient decay times are smaller in fused VSV-G/eGFP- \uparrow -co-cultures than in eGFP \uparrow -co-cultures. The underlying molecular mechanisms of these findings warrant further investigation, but previous studies have shown that decreases in I_{CaL} and Ca^{2+} transient decay time are associated with a reduction in EAD incidence.²⁷ In our co-culture model, repolarizing K^+ currents and opposing Ca^{2+} currents seem to be the main determinants of EAD risk. Previously, APD prolongation associated with K^+ current downregulation was shown to be important in generating the I_{CaL} -mediated component of EADs.²⁸ This is in agreement with our data, since inhibition of I_{Kv} in fused VSV-G/eGFP- \uparrow -co-cultures by TEA completely annulled the suppressive effect of heterocellular fusion on EAD incidence in fibrotic NRVM cultures.

However, it is likely that additional mechanisms add to the anti-arrhythmic effects of forced heterocellular fusion. For example, cell-to-cell fusion increases C_{mr} , which impacts electrophysiological source-sink relationships and thereby reduces the likelihood of EAD propagation.²⁹ As the anti-arrhythmic effects of forced heterocellular fusion seems to be the resultant of multiple interacting factors, future studies should be directed at unraveling the individual contributions of each of them. For instance, *in silico* experiments could show the effect of selective downregulation of K_v currents (I_{Ks} , I_{Kr}) and thereby clarify their individual roles in increasing repolarization force and decreasing EAD incidence. Similarly, modulation of gap junctional protein (especially Cx43) expression could give insight into the contribution of electrical coupling to the anti-arrhythmic effects of NRVM-hVSC fusion.

Taken together, the present study presents proof-of-concept of heterocellular fusion as a novel means to modify electrophysiological properties on a multicellular level. Our findings may also trigger the exploration of new treatment options for fibrosis-mediated arrhythmias aimed at increasing electrical homogeneity by heterocellular fusion or other means.

Clinical perspectives and study limitations

The extent and functional relevance of heterocellular coupling in healthy and diseased myocardium, especially between (myo)fibroblasts and adjacent CMCs, is still unclear. Dedicated transgenic animal models and specialized techniques are probably needed to unravel the role of CMC-CFB coupling in the intact heart as a prerequisite for translation of our results to the *in vivo* setting.³⁰ In fact, before heterocellular fusion could be considered as a possible therapeutic modality, several important issues need to be resolved. Whether heterocellular fusion is safe would have to be addressed first by investigating its effect on myocardial integrity, stiffness and contractility. Furthermore, although our results in the 2D co-culture model suggest an anti-arrhythmic effect of heterocellular fusion, it is uncertain whether the same holds true in the 3D myocardium, with its complex anatomy and its different, disease-specific patterns of fibrosis.³¹ Since our model was limited to a diffuse pattern of fibrosis, the effects of heterocellular fusion on other types of cardiac fibrosis remain to be investigated. In addition, apart from lowering pro-arrhythmic risk by decreasing EAD incidence, the APD-shortening effect of heterocellular fusion in VSV-G/eGFP- \uparrow -co-cultures may also increase arrhythmogenic potential as it increases the risk for reentrant circuit formation due to a decrease in wavelength.³² Although we did not find any evidence of reentrant tachyarrhythmias in our model, whether the same is true *in vivo* remains to be studied.

Regarding the limitations of our model, CMCs from neonatal rats were used since human CMCs could not be obtained in amounts sufficient for the experiments with monolayers presented in this study. Although these monolayers provide a standardized and controllable 2D model of fibrosis-related arrhythmias, these disorders normally occur in the 3D myocardium of diseased hearts. Nevertheless, 2D models with NRVMs have proven their usefulness as a model system for studying key electrophysiological processes of the heart.³³ Furthermore, while the beginning and duration of heterocellular fusion could be tightly controlled by timed exposure of the VSV-G/eGFP- \uparrow -co-cultures to low pH medium, the quantitative aspects of fusion were less easy to control, but still allowed us to perform reproducible studies. This limitation resulted in heterokaryons of different composition and therefore with various degrees of excitability. Hence, it would be important for future studies to develop a fusion method with greater control over the final composition and electrical properties of the fusion products. Nonetheless, even with the current approach, a fusion-dependent decrease in arrhythmogenicity of fibrotic CMC cultures could be demonstrated.

Conclusions

In summary, forced cellular fusion of hVSCs with NRVMs in confluent monolayer cultures yields functional heterokaryons and reduces arrhythmogenicity by preventing the occurrence of EADs. This decrease in EAD incidence is, at least partly, attributable to an increase in repolarization force, but is also associated with increased intercellular Cx43 expression and reduced Ca^{2+} decay time. Forced heterocellular fusion could provide a novel basis for anti-arrhythmic engineering of cardiac tissue.

Funding

This work was supported by the Netherlands Organization for Scientific Research (NWO) [Mosaic grant 017007064 to M.C.E. and Veni grant 91611070 to D.A.P.], the Dutch Heart Foundation (2014T110 to S.F.A.A.), Ammodo (to D.A.P.) and by the Royal Netherlands Academy of Arts and Sciences (KNAW) [CEP project 10CDP007 to A.A.F.d.V.].

Acknowledgements

We thank our LUMC colleagues Margreet de Jong and Rebecca Feistritz from the Laboratory of Experimental Cardiology for excellent technical support, Martin Jan Schlij for critically reading the manuscript, and Annelies van der Laan and Joop Wiegant from the Department of Molecular Cell Biology for technical assistance with confocal microscopy.

Conflict of interest

None declared.

References

1. Kakkur R, Lee RT. Intramyocardial fibroblast myocyte communication. *Circ Res*. 2010;106:47-57.
2. Souders CA, Bowers SL, Baudino TA. Cardiac fibroblast: the renaissance cell. *Circ Res*. 2009;105:1164-1176.
3. Leask A. Getting to the Heart of the Matter: New Insights Into Cardiac Fibrosis. *Circ Res*. 2015;116:1269-1276.
4. Sun Y, Weber KT. Infarct scar: a dynamic tissue. *Cardiovasc Res*. 2000;46:250-256.
5. Rohr S. Arrhythmogenic implications of fibroblast-myocyte interactions. *Circ Arrhythm Electrophysiol*. 2012;5:442-452.
6. Nguyen TP, Qu Z, Weiss JN. Cardiac fibrosis and arrhythmogenesis: the road to repair is paved with perils. *J Mol Cell Cardiol*. 2014;70:83-91.
7. Kohl P, Camelliti P, Burton FL, Smith GL. Electrical coupling of fibroblasts and myocytes: relevance for cardiac propagation. *J Electrocardiol*. 2005;38:45-50.
8. McDowell KS, Arevalo HJ, Maleckar MM, Trayanova NA. Susceptibility to arrhythmia in the infarcted heart depends on myofibroblast density. *Biophys J*. 2011;101:1307-1315.
9. Xie Y, Garfinkel A, Camelliti P, Kohl P, Weiss JN, Qu Z. Effects of fibroblast-myocyte coupling on cardiac conduction and vulnerability to reentry: A computational study. *Heart Rhythm*. 2009;6:1641-1649.
10. Pijnappels DA, van Tuyn J, de Vries AA, Grauss RW, van der Laarse A, Ypey DL, Atsma DE, Schalij MJ. Resynchronization of separated rat cardiomyocyte fields with genetically modified human ventricular scar fibroblasts. *Circulation*. 2007;116:2018-2028.
11. Cho HC, Marban E. Biological therapies for cardiac arrhythmias: can genes and cells replace drugs and devices? *Circ Res*. 2010;106:674-685.
12. Shiba Y, Fernandes S, Zhu WZ, Filice D, Muskheli V, Kim J, Palpant NJ, Gantz J, Moyes KW, Reinecke H, Van BB, Dardas T, Mignone JL, Izawa A, Hanna R, Viswanathan M, Gold JD, Kotlikoff MI, Sarvazyan N, Kay MW, Murry CE, Laflamme MA. Human ES-cell-derived cardiomyocytes electrically couple and suppress arrhythmias in injured hearts. *Nature*. 2012;489:322-325.
13. Chong JJ, Yang X, Don CW, Minami E, Liu YW, Weyers JJ, Mahoney WM, Van BB, Cook SM, Palpant NJ, Gantz JA, Fugate JA, Muskheli V, Gough GM, Vogel KW, Astley CA, Hotchkiss CE, Baldessari A, Pabon L, Reinecke H, Gill EA, Nelson V, Kiem HP, Laflamme MA, Murry CE. Human embryonic-stem-cell-derived cardiomyocytes regenerate non-human primate hearts. *Nature*. 2014;510:273-277.
14. Kizana E, Ginn SL, Allen DG, Ross DL, Alexander IE. Fibroblasts can be genetically modified to produce excitable cells capable of electrical coupling. *Circulation*. 2005;111:394-398.
15. Ieda M, Fu JD, Delgado-Olguin P, Vedantham V, Hayashi Y, Bruneau BG, Srivastava D. Direct reprogramming of fibroblasts into functional cardiomyocytes by defined factors. *Cell*. 2010;142:375-386.
16. Chen JX, Krane M, Deutsch MA, Wang L, Rav-Acha M, Gregoire S, Engels MC, Rajarajan K, Karra R, Abel ED, Wu JC, Milan D, Wu SM. Inefficient reprogramming of fibroblasts into cardiomyocytes using Gata4, Mef2c, and Tbx5. *Circ Res*. 2012;111:50-55.
17. Gottesman A, Milazzo J, Lazebnik Y. V-fusion: a convenient, nontoxic method for cell fusion. *Biotechniques*. 2010;49:747-750.
18. van Tuyn J, Pijnappels DA, de Vries AA, de V, I, van der Velde-van Dijke, Knaan-Shanzer S, van der Laarse A, Schalij MJ, Atsma DE. Fibroblasts from human postmyocardial infarction scars acquire properties of cardiomyocytes after transduction with a recombinant myocardin gene. *FASEB J*. 2007;21:3369-3379.
19. Askar SF, Ramkisoensing AA, Schalij MJ, Bingen BO, Swildens J, van der Laarse A, Atsma DE, de Vries AA, Ypey DL, Pijnappels DA. Antiproliferative treatment of myofibroblasts prevents arrhythmias in vitro by limiting myofibroblast-induced depolarization. *Cardiovasc Res*. 2011;90:295-304.

20. Askar SF, Ramkisoensing AA, Atsma DE, Schalij MJ, de Vries AA, Pijnappels DA. Engraftment patterns of human adult mesenchymal stem cells expose electrotonic and paracrine proarrhythmic mechanisms in myocardial cell cultures. *Circ Arrhythm Electrophysiol.* 2013;6:380-391.
21. Bingen BO, Engels MC, Schalij MJ, Jangsangthong W, Neshati Z, Feola I, Ypey DL, Askar SF, Panfilov AV, Pijnappels DA, de Vries AA. Light-induced termination of spiral wave arrhythmias by optogenetic engineering of atrial cardiomyocytes. *Cardiovasc Res.* 2014;104:194-205.
22. Jacquemet V, Henriquez CS. Loading effect of fibroblast-myocyte coupling on resting potential, impulse propagation, and repolarization: insights from a microstructure model. *Am J Physiol Heart Circ Physiol.* 2008;294:H2040-H2052.
23. Weiss JN, Garfinkel A, Karagueuzian HS, Chen PS, Qu Z. Early afterdepolarizations and cardiac arrhythmias. *Heart Rhythm.* 2010;7:1891-1899.
24. Pedrotty DM, Klinger RY, Kirkton RD, Bursac N. Cardiac fibroblast paracrine factors alter impulse conduction and ion channel expression of neonatal rat cardiomyocytes. *Cardiovasc Res.* 2009;83:688-697.
25. Cartledge JE, Kane C, Dias P, Tesfom M, Clarke L, Mckee B, Al AS, Chester A, Yacoub MH, Camelliti P, Terracciano CM. Functional crosstalk between cardiac fibroblasts and adult cardiomyocytes by soluble mediators. *Cardiovasc Res.* 2015;105:260-270.
26. Garcia-Dorado D, Rodriguez-Sinovas A, Ruiz-Meana M. Gap junction-mediated spread of cell injury and death during myocardial ischemia-reperfusion. *Cardiovasc Res.* 2004;61:386-401.
27. January CT, Riddle JM. Early afterdepolarizations: mechanism of induction and block. A role for L-type Ca²⁺ current. *Circ Res.* 1989;64:977-990.
28. Zeng J, Rudy Y. Early afterdepolarizations in cardiac myocytes: mechanism and rate dependence. *Biophys J.* 1995;68:949-964.
29. Xie Y, Sato D, Garfinkel A, Qu Z, Weiss JN. So little source, so much sink: requirements for afterdepolarizations to propagate in tissue. *Biophys J.* 2010;99:1408-1415.
30. Quinn TA, Camelliti P, Siedlecka U, Poggioli T, Loew LM, Knöpfel T, Kohl P. Cell-specific expression of voltage-sensitive protein confirms cardiac myocyte to non-myocyte electrotonic coupling in healed murine infarct border tissue. *Circulation* 2014;130:A11749.
31. de Jong S, van Veen TA, van Rijen HV, de Bakker JM. Fibrosis and cardiac arrhythmias. *J Cardiovasc Pharmacol.* 2011;57:630-638.
32. Kleber AG, Rudy Y. Basic mechanisms of cardiac impulse propagation and associated arrhythmias. *Physiol Rev.* 2004;84:431-488.
33. Herron TJ, Lee P, Jalife J. Optical imaging of voltage and calcium in cardiac cells & tissues. *Circ Res.* 2012;110:609-623.

Supporting information

Methods

Animal studies

All animal experiments were approved by the Animal Experiments Committee of the Leiden University Medical Center (LUMC) and conformed to the Guide for the Care and Use of Laboratory Animals as stated by the US National Institutes of Health.

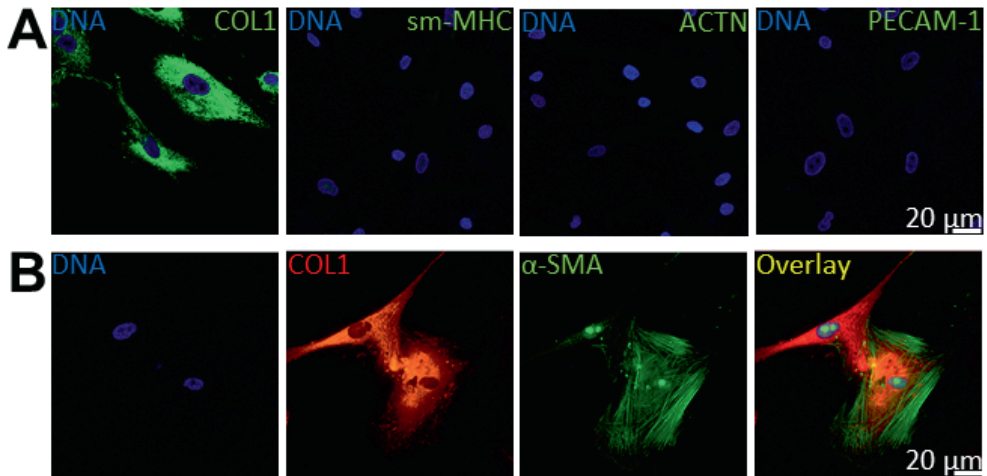
Human ventricular scar cell (hVSC) isolation and culture

Human tissue was collected in accordance with guidelines posed by the Medical Ethics Committee of the LUMC and adhered to the principles described in the Declaration of Helsinki. hVSCs were isolated as described previously.^{1,2} Surgical waste material consisting of human myocardial scar tissue was obtained from 10 patients undergoing left ventricle reconstructive surgery (Dor procedure). Samples were cut into small pieces (1-3 mm diameter), transferred to 6-well cell culture plates (Corning Life Sciences, Corning, NY) coated with porcine gelatin (Sigma-Aldrich, St. Louis, MO) and covered with round glass coverslips (30 mm in diameter) to prevent floating. Cells were cultured in a humidified 95% air/5% CO₂ environment at 37°C. hVSC culture medium, consisting of Dulbecco's modified Eagle's medium (DMEM; Life Technologies, Bleiswijk, the Netherlands) containing 10% fetal bovine serum (FBS), 100 U/mL penicillin, 100 µg/mL streptomycin, 2 mM GlutaMAX-I and 1 mM sodium pyruvate (all from Life Technologies), was refreshed every 3 days. The cells that grew out of the tissue pieces were trypsinized (0.05% trypsin-EDTA; Life Technologies), frozen in FBS/10% dimethyl sulfoxide (DMSO; Miltenyi Biotec, Leiden, the Netherlands) and stored in the vapor compartment of a liquid nitrogen tank at -175° C until use. Cells at passage numbers 2-4 were used for further experiments.

Construction of self-inactivating lentiviral vector (SIN-LV) shuttle plasmids

Plasmid construction was performed using standard techniques or following the instructions accompanying specific reagents.³ The construction of the monocistronic enhanced green fluorescent protein (eGFP)-encoding SIN-LV shuttle plasmid pLV.hCMV-IE.IRES.eGFP.hHBVPRE (main manuscript, *Figure 2A*) has been described elsewhere.⁴ The bicistronic SIN-LV shuttle plasmid pLV.hCMV-IE.VSV-G.IRES.eGFP.hHBVPRE (main manuscript, *Figure 2B*), which codes for eGFP and for the vesicular stomatitis virus G (VSV-G) protein, was generated by insertion of the 1.7-kb EcoRI fragment of pLP.VSV-G (Life Technologies) in the proper orientation in between the two EcoRI recognition sites of pLV.hCMV-IE.IRES.eGFP.hHBVPRE. The correctness of pLV.hCMV-IE.VSV-G.IRES.eGFP.hHBVPRE was verified by restriction mapping using 5 different enzymes. Restriction endonucleases and other DNA modifying enzymes were obtained from Thermo Fisher Scientific (Landsmeer, the Netherlands) or New England Biolabs (Bioké, Leiden,

the Netherlands). For large-scale purification of the SIN-LV shuttle and packaging plasmids the JETSTAR 2.0 Plasmid Maxiprep kit (Genomed, Löhne, Germany) was used following the instructions of the manufacturer.



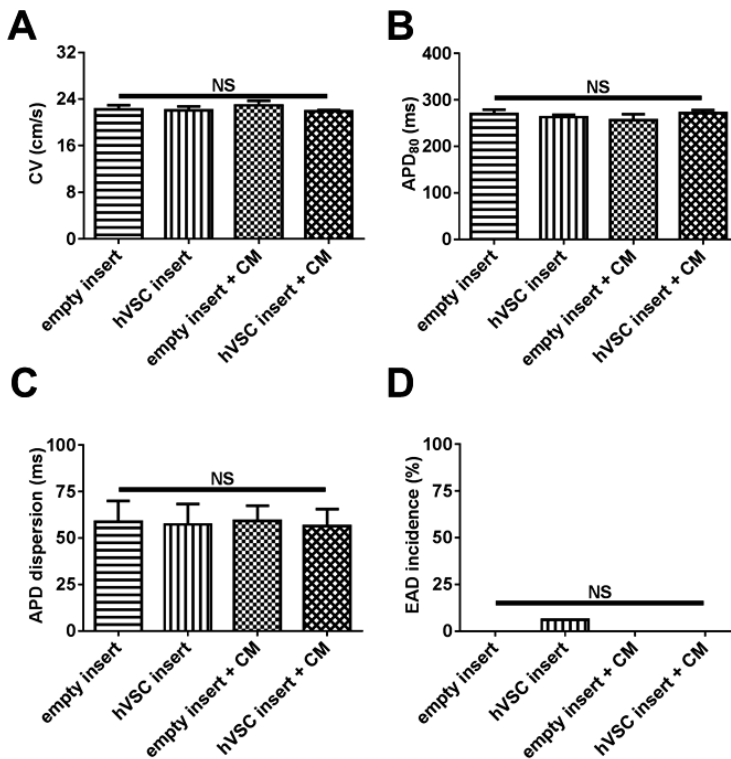
Supplementary Figure S1. Immunocytochemical characterization of hVSCs. (A) Cells were immunostained for collagen type I (COL1, green, fibroblastic cells), smooth muscle myosin heavy chain (sm-MHC, green, smooth muscle cells), sarcomeric α -actinin (ACTN, green, cardiomyocytes), CD31 (PECAM-1, green, endothelial cells) and Hoechst 33342 (DNA, blue, nuclei). (B) hVSCs were immunostained for collagen type I (COL1, red, fibroblastic cells) and α -smooth muscle actin (α -SMA, green, myofibroblastic cells and smooth muscle cells). Quantifications were based on 3 independent isolations and 25 images.

The abbreviations used in *Figure 2A* and *B* of the main manuscript are explained as follows: 5' LTR: chimeric 5' long terminal repeat containing enhancer and promoter elements of Rous sarcoma virus and the human immunodeficiency virus type 1 (HIV1) R and U5 regions. Ψ : HIV1 packaging signal. RRE: HIV1 Rev-responsive element. cPPT: HIV1 central polypurine tract and termination site. hCMV-IE: human cytomegalovirus *immediate early* promoter. VSV-G: vesicular stomatitis virus glycoprotein-coding sequence. EMCV IRES: encephalomyocarditis virus internal ribosome entry site. eGFP: *Aequorea victoria* enhanced green fluorescent protein-encoding sequence. hHBVPRE: human hepatitis B virus posttranscriptional regulatory element. 3': wildtype 3' HIV1 long terminal repeat with a large deletion in the U3 region.

SIN-LV production and transduction

LV.VSV-G/eGFP \uparrow and LV.eGFP \uparrow particles were produced in 293T cells from SIN-LV shuttle plasmids pLV.hCMV-IE.VSV-G.IRES.eGFP.hHBVPRE and pLV.hCMV-IE.IRES.eGFP.hHBVPRE, respectively, as described previously.⁵ SIN-LV particles were concentrated by ultracentrifugation and subsequently suspended in phosphate-buffered saline (PBS) containing 1% bovine serum albumin (BSA) fraction V (Sigma-Aldrich). SIN-LV suspensions were stored in 100 μ L portions at

-80°C until use. hVSCs were thawed freshly for each experiment 4 days before co-culture. At 1 day after culture initiation, hVSCs were transduced by adding SIN-LV suspension directly to culture medium containing 10 µg/mL diethylaminoethyl-dextran (Carl Roth, Karlsruhe, Germany). At 24 h after vector addition, the inoculum was removed. LV.VSV-G/eGFP⁺-transduced hVSCs (hereinafter referred to as VSV-G/eGFP⁺-hVSCs) and LV.eGFP⁺-transduced hVSCs (hereinafter referred to as eGFP⁺-hVSCs) were then washed 3 times with culture medium and kept in fresh culture medium for 2 additional days until establishment of co-cultures with neonatal rat ventricular myocytes (NRVMs). Transduction efficiency was determined by assessment of eGFP fluorescence with an Axiovert 200M inverse fluorescence microscope (Carl Zeiss, Sliedrecht, the Netherlands). SIN-LVs were applied at doses that resulted in transduction of nearly 100% of hVSCs, without microscopic signs of cytotoxicity.



Supplementary Figure S2. Investigation of the effects of paracrine factors released by hVSCs on the electrophysiological behavior of NRVMs using transwell assay and optical voltage mapping. NRVM cultures incubated with empty transwell inserts (empty insert; N=8), NRVM cultures incubated with hVSC-containing transwell inserts (hVSC insert; N=16), NRVM cultures incubated with empty inserts and conditioned hVSC medium (empty insert + CM; N=8) and NRVM cultures incubated with hVSC-containing inserts and conditioned medium (hVSC insert + CM; N=16) were analyzed for (A) CV, (B) APD_{90'}, (C) APD₉₀ dispersion and (D) EAD incidence.

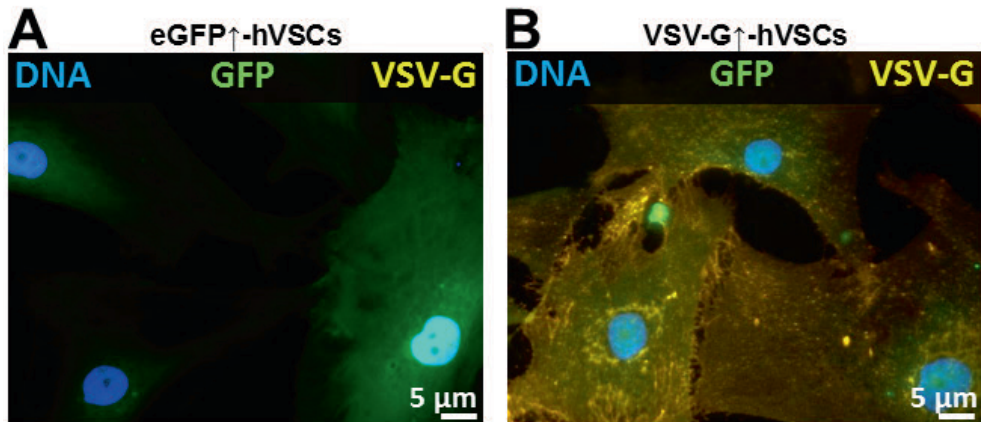
Neonatal rat ventricular cardiomyocyte (NRVM) isolation and co-culture

NRVMs were isolated as described previously.⁶ Briefly, neonatal Wistar rats (2 days *post-partum*) were anaesthetized by 5% isoflurane inhalation and adequate anaesthesia was confirmed by absence of reflexes. Hearts were rapidly excised and after removal of atrial tissue, the ventricles were finely minced and dissociated with collagenase type 1 (450 U/mL; Worthington, Lakewood, NJ) and DNase I (18.75 Kunitz/mL; Sigma-Aldrich). The resulting cell suspension was applied to Primaria cell culture dishes (BD Biosciences, Breda, the Netherlands) and incubated for 75 min at 37°C and 5% CO₂ to allow preferential attachment of non-myocytes (predominantly cardiac fibroblasts). Unattached cardiac cells (mainly NRVMs) were passed through a cell strainer (70 µm mesh pore size; BD Biosciences), to obtain a single cell suspension, and seeded in 24-well cell culture plates (Corning Life Sciences) onto bovine fibronectin (Sigma-Aldrich) -coated round glass coverslips (15 mm in diameter). For establishing NRVM-hVSC co-cultures, hVSCs were trypsinized and counted on the day of NRVM isolation and mixed with the NRVMs in a ratio of 4 NRVMs:1 hVSC before plating. Co-cultures were established with untransduced hVSCs (UT-co-cultures), eGFP⁺-hVSCs (eGFP⁺-co-cultures) or VSV-G/eGFP⁺-hVSCs (VSV-G/eGFP⁺-co-cultures). Cells were plated at a total density of 0.5-6×10⁵ cells/well, depending on the assay. At day 1 of culture, cells were incubated with mitomycin-C (10 µg/mL; Sigma-Aldrich) for 2 h to inhibit cell proliferation, as described previously.⁷ Culture medium (hereinafter referred to as NRVM culture medium) consisted of DMEM/Ham's F10 medium (1:1, v/v; Life Technologies) supplemented with 5% horse serum (Life Technologies), 2% BSA and sodium ascorbate to a final concentration of 0.4 mM and was refreshed daily.

Immunocytology

Cells were fixed with PBS/4% formaldehyde (Merck, Amsterdam, the Netherlands) for 15 min at room temperature (RT), washed 3 times with PBS and permeabilized by incubation for 10 min at RT with PBS/0.05% Triton-X100 (Sigma-Aldrich). After 3 washes with PBS/0.1% Tween-20 (Sigma-Aldrich), samples were incubated with primary antibodies diluted in PBS/10% FBS/1% BSA. Antibodies against the following antigens were used: human lamin A/C to detect cells of human origin (1:200; mouse IgG2b, clone 636; Vector Laboratories, Burlingame, CA), sarcomeric α-actinin to detect NRVMs (1:300; mouse IgG1, clone EA-53; Sigma-Aldrich), collagen type 1 to identify fibroblastic cell types (1:300; rabbit IgG, polyclonal; Abcam, Cambridge, United Kingdom), smooth muscle myosin heavy chain (MYH11 gene product) to detect smooth muscle cells (1:200; mouse IgG1, clone hSM-V; Sigma-Aldrich), CD31 (PECAM-1 gene product) to identify endothelial cells (1:200; rat IgG2a, clone MEC 13.3; BD Biosciences), α-smooth muscle actin (ACTA2 gene product) to detect myofibroblasts and smooth muscle cells (1:200; mouse IgG2a, clone 1A4; Sigma-Aldrich), GFP to detect LV.eGFP⁺- and LV.VSV-G/eGFP⁺-transduced cells (1:200, rabbit IgG, polyclonal; Life Technologies), VSV-G to detect LV.VSV-G/

eGFP \uparrow -transduced cells (1:200; mouse IgG1, clone P5D4, Cy3-conjugated; Sigma-Aldrich) and connexin43 (1:200; rabbit IgG, polyclonal; Sigma-Aldrich). After washing 3 times for 5 min with PBS/0.1% Tween-20, cells were incubated with appropriate Alexa Fluor 488/568-conjugated secondary antibodies (1:500; Life Technologies) or, for detecting human lamin A/C, with biotin-conjugated goat-anti mouse IgG_{2b} secondary antibodies (1:200; Santa Cruz Biotechnology, Santa Cruz, CA) and Qdot 655 streptavidin conjugates (1:200; Life Technologies). The VSV-G protein was detected without the use of secondary antibodies due to the covalent linkage of the primary antibodies to Cy3. Nuclear counterstaining was performed by incubating the cells for 10 min at RT with 10 μ g/mL Hoechst 33342 (Life Technologies). Coverslips were mounted in Vectashield mounting medium (Vector Laboratories). Images were acquired with a Leica TCS SP8 confocal laser scanning microscope (Leica Microsystems, Rijswijk, the Netherlands) or with a digital color camera-equipped fluorescence microscope (Nikon Eclipse 80i; Nikon Instruments Europe, Amstelveen, the Netherlands). Storage and quantification of immunofluorescence signals was done using dedicated software (Leica Application Suite [Leica Microsystems], NIS Elements [Nikon Instruments Europe] and Fiji [www.fiji.sc]). Each immunostaining was performed on at least 3 independent cell cultures.



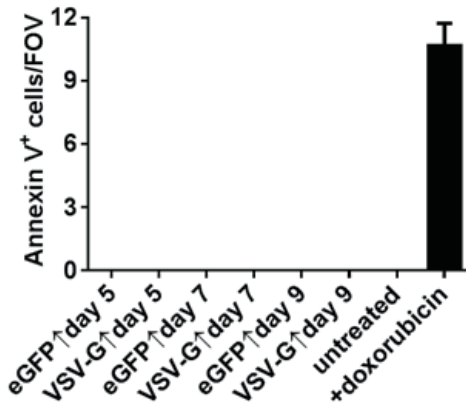
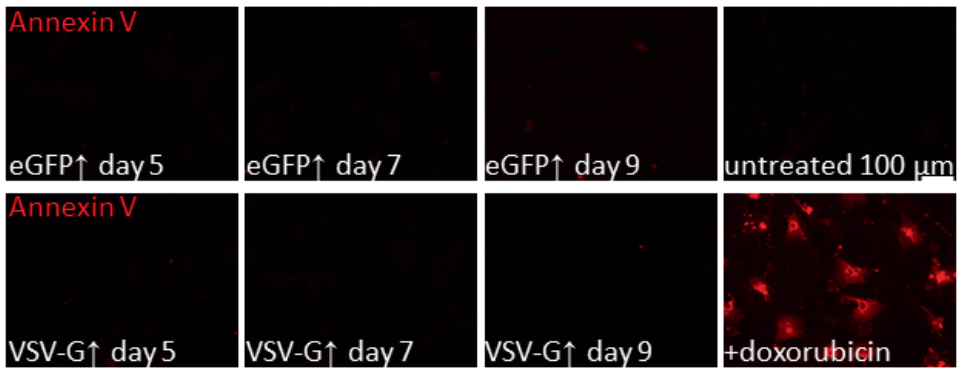
Supplementary Figure S3. Immunocytological confirmation of forced VSV-G expression following transduction of hVSCs with LV.VSV-G/eGFP \uparrow . Immunocytological staining of hVSC monocultures consisting of (A) eGFP \uparrow -hVSCs and (B) VSV-G/eGFP \uparrow -hVSCs for green fluorescent protein (GFP; green), vesicular stomatitis virus G protein (VSV-G; yellow) and DNA (blue). VSV-G $^+$ cells were only present in the LV.VSV-G/eGFP \uparrow -transduced hVSC cultures. Based on 3 independent transductions and 30 images.

Reverse transcription quantitative-polymerase chain reaction (RT-qPCR) analysis

Dedicated cell cultures samples were used for RT-qPCR experiments, which were performed as described previously.⁸ Briefly, cells were lysed using TRIzol reagent (Life Technologies) and total RNA was isolated with the RNeasy Mini Kit (Qiagen, Venlo, the Netherlands). Reverse transcription was performed using the iScript cDNA synthesis kit (Bio-Rad Laboratories, Veenendaal, the Netherlands). Connexin43 (Cx43) mRNA expression levels were quantified with the Biorad SensiFAST SYBR No-ROX kit (Meridian Biosciences, Singapore), using oligodeoxyribonucleotides: 5' GGGATAAGGGAGGTACACA 3' (rat Gja1-specific forward primer) and 5' CACTCAATTCATGTACACAGACT 3' (rat Gja1-specific reverse primer). For normalisation purposes, 18S rRNA sequences were amplified in parallel using primers: 5' GTAACCCGTTGAACCCATT 3' (rat Rn18S-specific forward primer) and 5' CCATCCAATCGGTAGTAGCG 3' (rat Rn18S-specific reverse primer). PCR amplifications were performed using a CFX96 Touch Real-Time PCR detection system (Bio-Rad Laboratories). For data analysis and analysis CFX Manager Software version 3.1 (Bio-Rad Laboratories) was used.

Western Blotting

Cells were washed 3 times with ice-cold PBS and lysed on ice in RIPA buffer (50 mM Tris-HCl [pH=8.0], 150 mM NaCl, 1% Triton X-100, 0.5% sodium deoxycholate, 0.1% sodium dodecyl sulfate supplemented with protease inhibitors [cOmplete, Mini Protease Inhibitor Cocktail Tablet; Roche Applied Science, Penzberg, Germany]). After centrifugation of the cell lysate for 15 min at $21,130 \times g$ and 4°C, the supernatant was collected, passed 3 times through a 29 Gauge needle (BD Biosciences), aliquoted and stored at -80°C until assay. Protein concentration was determined using the BCA protein assay kit (Thermo Fisher Scientific). Proteins were size-fractionated in Novex Bolt 8% Bis-Tris Plus gels (Life Technologies) and transferred to Amersham Hybond-N⁺ polyvinylidene difluoride membranes (GE Healthcare, Diegem, Belgium) by wet electroblotting using a Bolt Mini Blot Module (Life Technologies). After blocking for 1 h in 2% ECL Prime blocking reagent (GE healthcare) dissolved in Tris-based saline/0.1% Tween-20 (TBST), membranes were incubated for 1 h with primary antibodies directed against Cx43 (Gja1 gene product; 1:100,000; rabbit IgG, polyclonal; Sigma-Aldrich) or lamin A/C (Lmna gene product; 1:5,000; rabbit IgG, polyclonal; Santa Cruz Biotechnology) as an internal control. All antibodies were diluted in TBST/2% ECL Prime blocking reagent. After 3 washes with TBST, blots were incubated with corresponding horseradish peroxidase-conjugated secondary antibodies (1:25,000; donkey-anti-rabbit IgG-HRP, Santa Cruz Biotechnology) for 1 h at RT. After another 3 wash steps with TBST, membranes were immersed in SuperSignal West Femto Maximum Sensitivity substrate (Thermo Scientific) and chemiluminescence was measured with the ChemiDoc XRS imaging system (Bio-Rad Laboratories). Dedicated software was used for imaging and quantification.

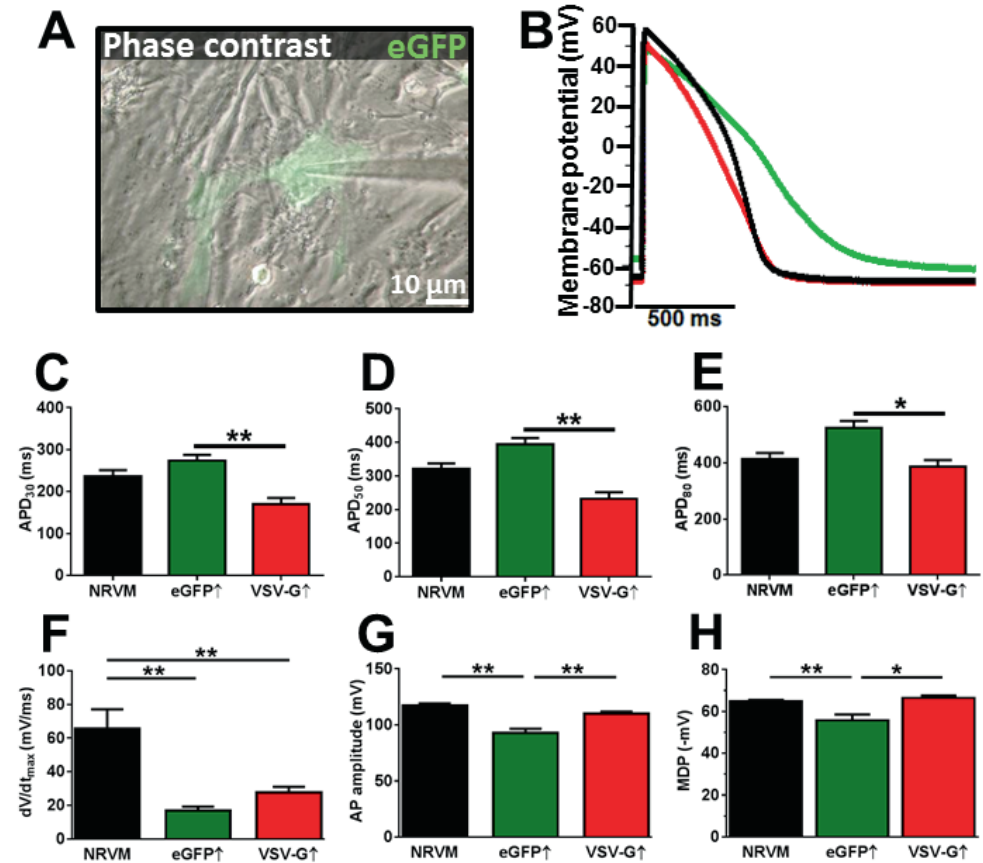


Supplementary Figure S4. Assessment of the viability of eGFP⁺-co-cultures (eGFP⁺) and fused VSV-G/eGFP⁺-co-cultures (VSV-G⁺) by live cell staining for externalized phosphatidylserine as early marker of apoptosis. On day 5, 7 and 9 of culture, *i.e.* at 2, 4 and 6 days after the induction of intercellular fusion, the cells were incubated with Alexa Fluor 568-conjugated annexin V and the number of fluorescently labelled cells per field of view (FOV) was determined. NRVM cultures that were incubated for 24 h with 1 mM doxorubicin (Sigma-Aldrich) or its solvent (untreated) served a positive and negative controls, respectively. The quantitative data are based on 3 independent experiments and 20 images.

Apoptosis assay

Apoptosis in our cell cultures was assessed by labeling with Alexa Fluor 568-conjugated annexin V (Life Technologies). Cells were cultured on glass coverslips in 24-well cell culture plates as described previously, and assays were performed on day 5, 7 and 9 of culture, *i.e.* at 2, 4 and 6 days after the induction of intercellular fusion. Cells were washed once with ice-cold PBS and immediately afterwards incubated for 15 min at RT and in the dark with Alexa Fluor 568-conjugated annexin V (diluted 1:20 in homemade binding buffer) as recommended by the manufacturer. The binding buffer consisted of 10 mM HEPES, 140 mM NaCl, and 2.5 mM CaCl₂ and was set at pH 7.4 with NaOH solution. Next, the cell cultures were washed once with ice-cold binding buffer, which was replaced by PBS for live cell imaging using a Leica

DMI6000 B inverted microscope (Leica Microsystems) equipped with a color camera and dedicated software. To generate positive control samples, NRVM cultures were treated with 1 mM doxorubicin (Sigma-Aldrich) during 24 h immediately prior to assay.



Supplementary Figure S5. Effect of heterocellular fusion on AP characteristics assessed in confluent monolayer cultures by the perforated-patch WC patch-clamp technique. (A) Typical example of a VSV-G/eGFP \uparrow -co-culture after induction of fusion showing an eGFP \uparrow (eGFP; green) heterokaryon with the patch-pipette attached to its surface. (B) Overlay of typical AP recordings of an NRVM in a NRVM culture (black), of a NRVM in a 4:1 configuration with hVSCs in an eGFP \uparrow -co-culture (green) and of a heterokaryon surrounded by NRVMs in a VSV-G/eGFP \uparrow -co-cultures (red). Quantification of APD at (C) 30% repolarization (APD₃₀), (D) 50% repolarization (APD₅₀) and (E) 80% repolarization (APD₈₀), (F) maximum upstroke velocity (dV/dt_{max}), (G) AP amplitude and (H) maximum diastolic potential (MDP), as measured by perforated patch recordings in NRVM cultures (black; N=8), eGFP \uparrow -co-cultures (green; N=7) and VSV-G/eGFP \uparrow -co-cultures (red; N=10).

Optical voltage mapping

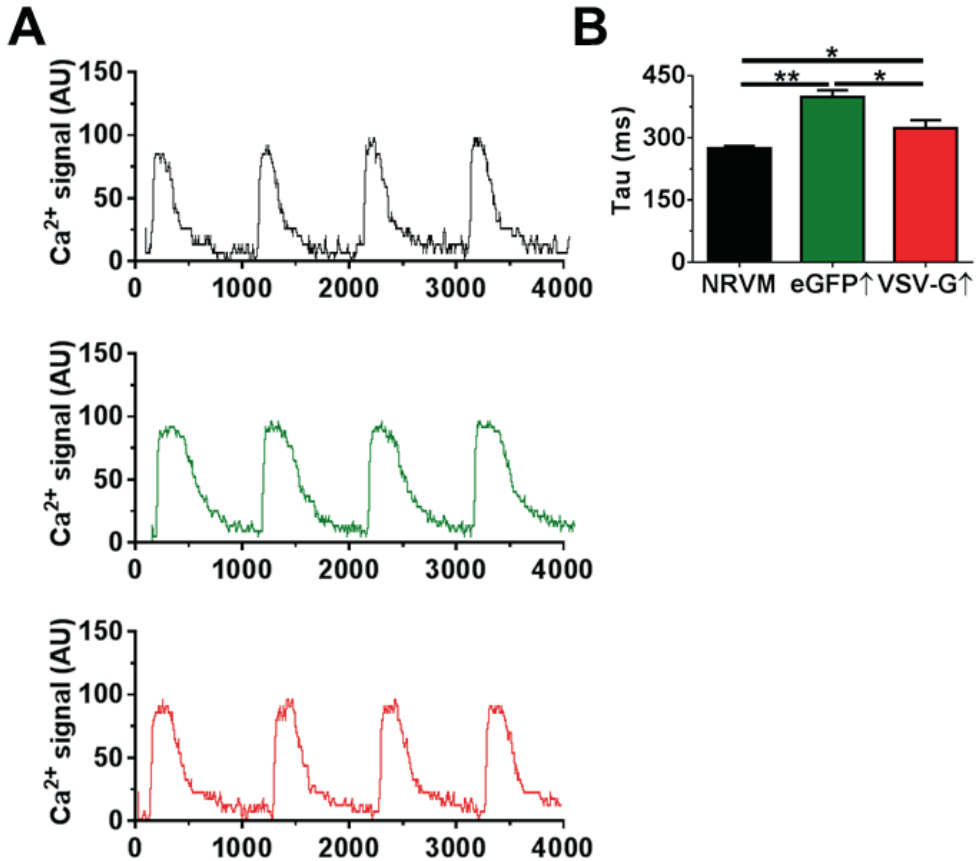
Assessment of the effects of heterocellular fusion on cardiac electrical impulse propagation in monolayers was done by optical mapping 48 h after fusion induction. Cells were loaded with voltage-sensitive dye by incubation for 15 min at 37°C in a humidified incubator (95% air/5% CO₂) with serum-free and phenol red-less DMEM/Ham's F12 medium (1:1, v/v; DMEM/F12; Life Technologies) containing 8 μM di-4-ANEPPS (Life Technologies). After replacement of the staining solution with fresh unsupplemented DMEM/F12, mapping experiments were performed with a MiCAM ULTIMA-L imaging system (SciMedia, Costa Mesa, CA). Cells were stimulated electrically with an epoxy-coated bipolar platinum electrode with square 10 ms, 8 V suprathreshold electrical stimuli using a STG 2004 stimulus generator and MC Stimulus II software (both from Multichannel Systems, Reutlingen, Germany). Optical signals were recorded at a 6-ms frame rate and analyzed using BrainVision Analyzer 13.04.20 software (Brainvision, Tokyo, Japan), after spatial and temporal filtering. Upon 1-Hz pacing, cell cultures were assessed for conduction velocity (CV), action potential (AP) duration (APD) at 50% and 80% of full repolarization (APD₅₀ and APD₈₀, respectively), APD dispersion of repolarization and early afterdepolarization (EAD) incidence. APD dispersion was calculated as the maximal temporal difference in APD₈₀ within one culture. EADs were defined as one or more abnormal depolarizations during phase 2 or 3 of the AP during 1-Hz electrical pacing. EADs were quantified by calculating the percentage of cultures that showed one or more EADs upon 1-Hz pacing during optical mapping assay. To study the effects of outward K_v current blockade, cultures were incubated for 10 min in NRVM culture medium containing 40 mM tetraethylammonium (TEA; Sigma-Aldrich) or 1 mM 4-aminopyridine (4-AP; Sigma-Aldrich) and subjected to electrophysiological measurements immediately afterwards.

Patch-clamp recordings

Patch-clamp measurements were conducted on day 5 of culture at 20-23°C with a conventional system consisting of a MultiClamp 700B amplifier and a Digidata 1440A A/D converter, controlled by Clampex 10 software (Axon CNS, Molecular Devices, Sunnyvale, CA).

To manufacture patch pipettes, borosilicate glass capillaries (1.5 mm outer diameter and 1.17 mm inner diameter; Harvard Apparatus, Kent, United Kingdom) were pulled by a model P-30 vertical micropipette puller (Sutter Instrument Company, Novato, CA). When filled with pipette solution, pipettes showed a typical resistance of 2-3 MΩ. Whole-cell (WC) current-clamp recordings were performed on single NRVMs, single hVSCs and isolated heterokaryons in cultures that had been previously subjected to a brief low pH treatment to induce VSV-G-dependent intercellular fusion. The pipette solution consisted of (in mM): 80 potassium DL-aspartate, 40 KCl, 8 NaCl, 5.5 glucose, 5 HEPES, 5 EGTA, 1 MgCl₂, 4 Mg-ATP, and 0.1 Na₃-

GTP (adjusted to pH 7.20 with KOH). Unless mentioned otherwise, cells were bathed in an extracellular solution composed of (in mM): 126 NaCl, 11 glucose, 10 HEPES, 5.4 KCl, 1 MgCl₂, and 1.8 CaCl₂ (adjusted to pH 7.40 with NaOH).



Supplementary Figure S6. Measurement of Ca²⁺ transient dynamics in confluent monolayer cultures by optical mapping using the Ca²⁺ indicator Rhod-2-AM. (A) Typical Ca²⁺ signal traces for a NRVM culture (upper panel; black), an eGFP[↑]-co-culture (middle panel: green) and a VSV-G/eGFP[↑]-co-culture (lower panel: red). (B) Comparison of the times at which the cytosolic Ca²⁺ concentration had decreased to 63% of its peak value ($\tau_{63\%}$). N=10 for the NRVM cultures, N=9 for the eGFP[↑]-co-cultures and N=9 for the VSV-G/eGFP[↑]-co-cultures.

To study the effects of Kv current inhibition, cells were perfused with extracellular solutions consisting of (in mM): 11 glucose, 10 HEPES, 5.4 KCl, 1 MgCl₂, 1.8 CaCl₂ and either 40 TEA plus 86 NaCl or 1 4-AP plus 126 NaCl. The pH of these solutions was adjusted to 7.40 with NaOH. Whole-cell capacitance (C_m) was calculated from capacitive transient currents evoked during 5 mV steps from a holding potential of -50 mV using the membrane test feature of pClamp 10

software. Subsequently, C_m and the series resistance (>75%) were compensated electronically. C_m was used as a measure of cell size for current normalization.

Monolayer recordings were performed in confluent cultures on spontaneously active cells using a perforated patch-clamp method.⁹ Recordings encompassed NRVMs in NRVM cultures, NRVMs adjacent to eGFP-expressing hVSCs in eGFP \uparrow -co-cultures and heterokaryons in VSV-G/eGFP \uparrow -co-cultures. Each of these cell cultures had been exposed for 3.5 min to culture medium of pH 6.0, 48 hours before patch clamping. An ATP- and GTP-free pipette solution was used to tip-fill patch pipettes, and an ATP- and GTP-free pipette solution containing nystatin (120-200 μ g/mL; Sigma-Aldrich) was used to back-fill the pipettes. Recordings were started after the series resistance had reached steady state and the AP amplitude was stable (*i.e.* after 20-30 min). The integrity of the perforated patch was checked during and after recording for every experiments to ensure reliability of recordings. Data were sampled at intervals of 100 μ s and low-pass filtered at 2-4 kHz with a four-pole Bessel filter. The calculated liquid junction potential (\sim 11 mV) between pipette and bath solution was only compensated for in the case of resting membrane potential measurements of single cells. Data analysis was carried out with Clampfit 10 software (Axon CNS, Molecular Devices).

Statistical analysis

Statistical analyses were performed using GraphPad Prism software version 6 (Graphpad Software, La Jolla, CA). Unpaired Student's t test, Fisher's exact test and the one-way ANOVA test were used for comparing different experimental groups. Data were expressed as mean \pm standard error of mean (SEM) for a specified number (N) of observations. Results were considered statistically significant at P values <0.05. Statistical significance was expressed as follows: *: P<0.05, **: P<0.01, ***: P<0.001, NS: not significant.

Results

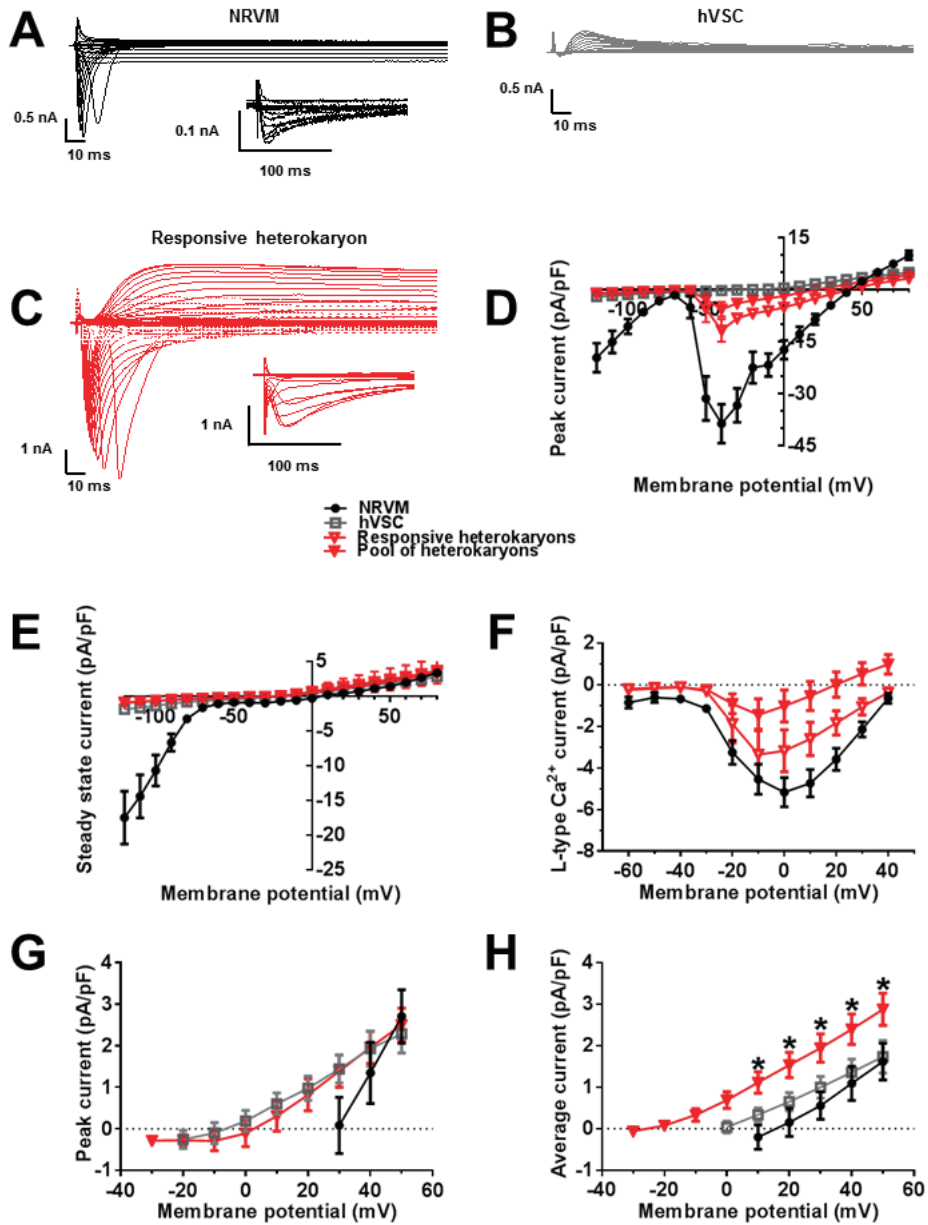
Ionic membrane currents in heterokaryons

In order to explore the anti-arrhythmic mechanisms of heterocellular fusion in more detail, patch-clamp experiments were conducted to compare whole-cell (WC) membrane current profiles of single NRVMs, single hVSCs and isolated heterokaryons. NRVMs showed voltage-step evoked WC-currents, typical for these excitable cells (*Figure S7A*).^{10,11} Inward rectifier currents (I_{Kir}) were observed upon hyperpolarizing voltage steps below -80 mV (*Figure S7A, D, E*). Fast transient inward currents were recorded upon depolarizing voltage steps from a holding voltage of -80 mV to voltages >-50 mV (*Figure S7A, D*). These currents were mainly voltage-

activated sodium currents (I_{Nav}), based on their fast time course, complete inhibition by 30 nM tetrodotoxin (TTX) (N=20, data not shown) and inactivation at -40 mV. The latter property was used to unmask the presence of voltage-activated L-type Ca^{2+} currents in the records (I_{CaL} ; *Figure S7A inset and F*). The complete inhibition of these currents by 10 μ M nitrendipine (N=8, data not shown) confirmed their identity. T-type Ca^{2+} currents were not investigated, because these currents are of minor importance in NRVMs.¹² Relatively small depolarization-activated outward currents (I_{ov}) could be evoked upon steps to voltages > 0mV. These currents are best recognized at voltages where the other currents are close to zero (main manuscript *Figure 6* and *Figure S7A, D and E*). The mean peak current-voltage (I-V) relationship of the total NRVM WC-current densities shows the typical I-V profile of these cells (*Figure S7D*).

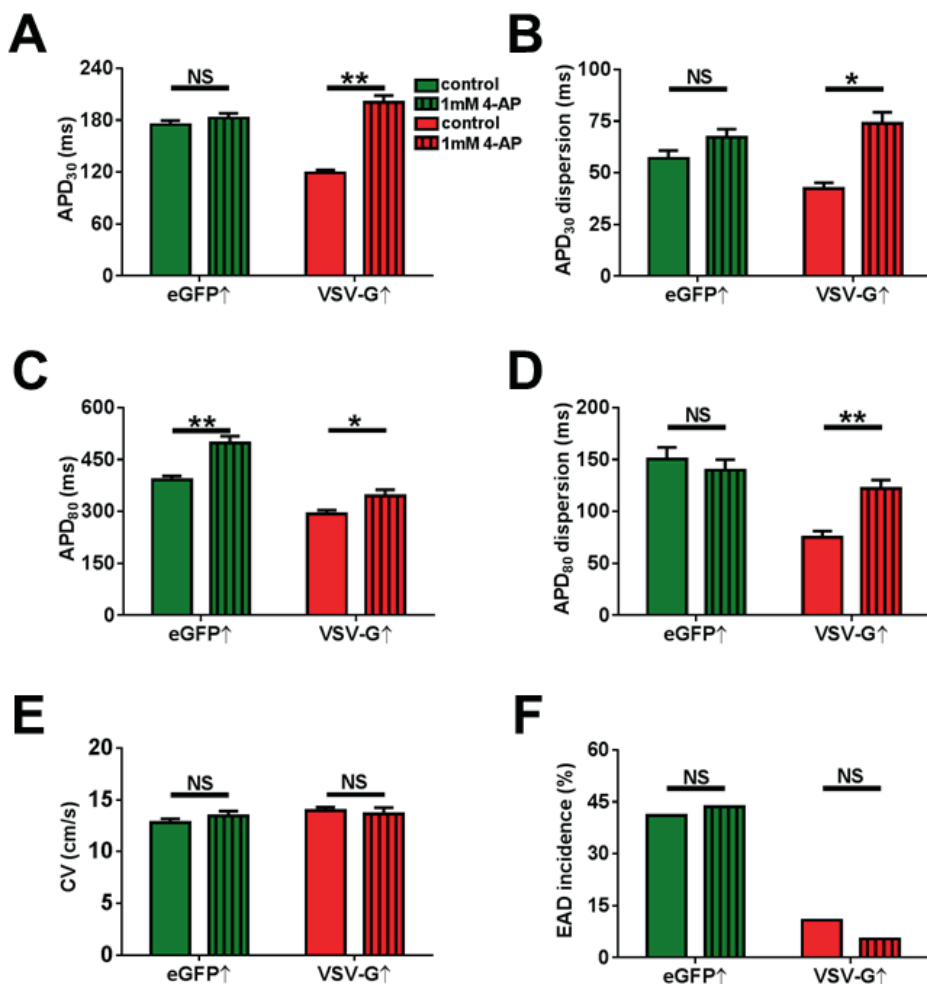
In contrast to NRVMs, WC-current records and I-V profiles of hVSCs showed absence of I_{Kir} , I_{Nav} and I_{CaL} , but presence of I_{ov} , consistent with inexcitable cell properties (*Figure S7B, D*).

The WC current-records of heterokaryons were not simple proportional additions of those of NRVMs and hVSCs. Upon stimulation with a defined current pulse, about half of the heterokaryons responded by eliciting an AP (main manuscript, *Figure 3C*). In current records of responsive heterokaryons, I_{Kir} , I_{Nav} , I_{CaL} and I_{ov} could be easily recognized (*Figure S7C with inset, D, F*). I_{Kir} was strongly diluted and I_{Nav} showed smaller current densities compared to NRVMs. This current could, however, not be evaluated quantitatively, because a reliable measurement of this current was not feasible in cells with such large C_m , as apparent from its slow time course. Peak I_{CaL} was much less diluted than I_{Kir} (*Figure S7F*). The peak I_{ov} density of the heterokaryons was similar to that of hVSCs at all positive potentials and to that of NRVMs around 50 mV (*Figure S7G*). The average I_{ov} density of heterokaryons was clearly increased at all positive potentials (*Figure S7H*) and showed an overall slower inactivation time course in comparison with NRVMs and hVSCs (main manuscript, *Figure 6B-C*). Pooled results show I-V curve profiles between that of responsive heterokaryons and hVSCs (*Figure S7D, F*). We concluded that I_{ov} was mainly K_v -current, as it was largely inhibited by 40 mM external TEA (main manuscript, *Figure 6D-E*), while inhibition by 1 mM 4-AP was ~30% (N=6, data not shown). Taken together, these data show that heterokaryons share cardiomyocytic and fibroblastic currents to a variable degree, with cardiomyocytic I_{Kir} density being most diluted by the heterocellular fusion, with I_{CaL} being upregulated for partial compensation of the dilution and with the average heterocellular I_{Kv} density being larger than I_{Kv} of hVSCs and of NRVMs. Thus, NRVMs contribute elements of excitability to the heterokaryons, while hVSCs contribute increased repolarization force to these fused cells.



Supplementary Figure S7. Membrane current profiles of single NRVMs, single hVSCs and solitary heterokaryons. Families of representative whole-cell current recordings of an (A) NRVM, (B) hVSC and (C) responsive heterokaryon. To obtain the recordings in A-C, 400-ms voltage pulses between -120 and +80 mV were applied in 10-mV increments every 5 s from the holding potential (V_h) = -80 mV. Calcium-current (I_{CaL}) traces in inset A and inset C were recorded at V_h = -40 mV to fully inactivate voltage dependent Na^+ current (I_{NaV}), and the test pulses were from -60 mV to 40 mV with 10 mV increases, separated by 5-s rest intervals. Voltage-current (I-V) relationship of the (D) total peak and (E) steady state current

density were expressed as the mean±SEM and measured from NRVMs (filled black circle; N=9), hVSCs (filled grey square; N=9), responsive heterokayons (open red triangle; N=7) and pool of heterokaryons (filled red triangle; N=15). *D* was obtained from the current amplitudes at the beginning of each voltage step, and *E* was obtained from steady state currents at the end of 400-ms test pulses. (*F*) I-V relationships of I_{CoL} are plotted at each test potential as mean±SEM obtained from NRVMs (filled black circle; N=7), responsive heterokayons (open red triangle; N=5) and the pool of heterokaryons (filled red triangle; N=11). I-V relationships of the (*G*) peak outward current were taken at 50-ms after depolarization and the (*H*) average outward current was calculated from 50-ms till 400-ms prior to repolarization from single NRVMs (filled black circle; N=9), single hVSCs (filled grey square; N=9) and isolated pooled responsive and non-responsive heterokaryons (filled red triangle; N=8 for each group).



Supplementary Figure S8. Evaluation of the effects of 4-AP on the electrophysiological properties of eGFP↑-co-cultures and fused VSV-G/eGFP↑-co-cultures by optical voltage mapping. Effect of 4-AP or vehicle (control) in unfused (eGFP↑; green, both N=8) and fused (VSV-G↑; red, both N=9) fibrotic NRVM cultures on (A) APD_{30r} (B) APD₃₀ dispersion, (C) APD_{80r} (D) APD₈₀ dispersion, (E) CV and (F) EAD incidence.

References

1. van Tuyn J, Pijnappels DA, de Vries AA, de Vries I, van der Velde-van Dijke I, Knaan-Shanzer S, van der Laarse A, Schalij MJ, Atsma DE. Fibroblasts from human postmyocardial infarction scars acquire properties of cardiomyocytes after transduction with a recombinant myocardin gene. *FASEB J*. 2007;21:3369-3379.
2. Pijnappels DA, van Tuyn J, de Vries AA, Grauss RW, van der Laarse A, Ypey DL, Atsma DE, Schalij MJ. Resynchronization of separated rat cardiomyocyte fields with genetically modified human ventricular scar fibroblasts. *Circulation*. 2007;116:2018-2028.
3. Green MR, Schaefer JA. Molecular Cloning: A Laboratory Manual. In: Cold Spring Harbor Laboratory Press, 2012.
4. Vellinga J, Uil TG, de Vries J, Rabelink MJ, Lindholm L, Hoeben RC. A system for efficient generation of adenovirus protein IX-producing helper cell lines. *J Gene Med*. 2006;8:147-154.
5. Bingen BO, Neshati Z, Askar SF, Kazbanov IV, Ypey DL, Panfilov AV, Schalij MJ, de Vries AA, Pijnappels DA. Atrium-specific Kir3.x determines inducibility, dynamics, and termination of fibrillation by regulating restitution-driven alternans. *Circulation*. 2013;128:2732-2744.
6. Askar SF, Ramkisoensing AA, Atsma DE, Schalij MJ, de Vries AA, Pijnappels DA. Engraftment patterns of human adult mesenchymal stem cells expose electrotonic and paracrine proarrhythmic mechanisms in myocardial cell cultures. *Circ Arrhythm Electrophysiol*. 2013;6:380-391.
7. Askar SF, Ramkisoensing AA, Schalij MJ, Bingen BO, Swildens J, van der Laarse A, Atsma DE, de Vries AA, Ypey DL, Pijnappels DA. Antiproliferative treatment of myofibroblasts prevents arrhythmias in vitro by limiting myofibroblast-induced depolarization. *Cardiovasc Res*. 2011;90:295-304.
8. Engels MC, Rajarajan K, Feistritz R, Sharma A, Nielsen UB, Schalij MJ, de Vries AA, Pijnappels DA, Wu SM. Insulin-like growth factor promotes cardiac lineage induction in vitro by selective expansion of early mesoderm. *Stem Cells*. 2014;32:1493-1502.
9. Akaike N, Harata N. Nystatin perforated patch recording and its applications to analyses of intracellular mechanisms. *Jpn J Physiol*. 1994;44:433-473.
10. Fermini B, Schanne OF. Determinants of action potential duration in neonatal rat ventricle cells. *Cardiovasc Res*. 1991;25:235-243.
11. Deschenes I, Armoundas AA, Jones SP, Tomaselli GF. Post-transcriptional gene silencing of KCHIP2 and Navbeta 1 in neonatal rat cardiac myocytes reveals a functional association between Na and Ito currents. *J Mol Cell Cardiol*. 2008;45:336-346.
12. Avila G, Medina IM, Jimenez E, Elizondo G, Aguilar CI. Transforming growth factor-beta1 decreases cardiac muscle L-type Ca²⁺ current and charge movement by acting on the Cav1.2 mRNA. *Am J Physiol Heart Circ Physiol*. 2007;292:H622-H631.

CHAPTER 5

Islands of spatially discordant APD alternans underlie arrhythmogenesis by promoting electrotonic dyssynchrony in models of fibrotic rat ventricular myocardium

Marc C. Engels^{1,†}, Rupamanjari Majumder^{1,†}, Antoine A.F. de Vries, PhD^{1,†},
Alexander V. Panfilov^{2,†}, Daniël A. Pijnappels, PhD^{1,†}

[†]These authors contributed equally to this work.

¹Laboratory of Experimental Cardiology, Department of Cardiology, Heart Lung Center Leiden,
Leiden University Medical Center, Leiden, the Netherlands.

²Department of Physics and Astronomy, Ghent University, Ghent, Belgium.

Adapted from: Scientific Reports. 2016;6:24334.

Abstract

Fibrosis and altered gap junctional coupling are key features of ventricular remodelling and are associated with abnormal electrical impulse generation and propagation. Such abnormalities predispose to reentrant electrical activity in the heart. In the absence of tissue heterogeneity, high-frequency impulse generation can also induce dynamic electrical instabilities leading to reentrant arrhythmias. However, because of the complexity and stochastic nature of such arrhythmias, the combined effects of tissue heterogeneity and dynamical instabilities in these arrhythmias have not been explored. Here, arrhythmogenesis was studied using *in vitro* and *in silico* monolayer models of neonatal rat ventricular tissue with 30% randomly distributed cardiac myofibroblasts and systematically lowered intercellular coupling achieved *in vitro* through graded knockdown of connexin43 expression. Arrhythmia incidence and complexity increased with decreasing intercellular coupling efficiency. This coincided with the onset of a specialized type of spatially discordant action potential duration alternans characterized by island-like areas of opposite alternans phase, which positively correlated with the degree of connexin43 knockdown and arrhythmia complexity. At higher myofibroblast densities, more of these islands were formed and reentrant arrhythmias were more easily induced. This is the first study exploring the combinatorial effects of myocardial fibrosis and dynamic electrical instabilities on reentrant arrhythmia initiation and complexity.

Introduction

Remodelling of ventricular tissue is an adaptive response to trauma, disease and ageing. It comprises structural and functional features, including changes in cardiac electrophysiology. Its structural aspects involve changes in cell size, cellular composition and tissue architecture. A key feature of this structural remodelling is cardiac fibrosis, which is characterized by increased numbers and activity of myofibroblasts. Such tissue heterogeneity as a consequence of fibrosis, could establish anatomical obstacles creating a substrate for irregular propagation of cardiac action potentials (APs), which promotes wavebreak and thereby predisposes to reentrant arrhythmias.¹⁻⁴ However, wavebreaks can also occur in structurally homogeneous cardiac tissue as a result of dynamically induced functional heterogeneity, such as AP duration (APD) alternans when such heterogeneity is large enough to cause electrotonic load imbalance, a feature promoted by electrical remodelling.⁵⁻⁹ Such imbalance is a well-established source of electrical instabilities.¹⁰

Electrical communication in cardiac tissue occurs via specialized protein channels called gap junctions, which are concentrated in intercalated discs at the longitudinal ends of cardiomyocytes.⁸ Gap junctions are formed when 'hemichannels' from neighbouring cardiomyocytes connect. Each hemichannel is composed of an assembly of six polypeptides called connexins. The most common and abundant connexin in the heart is connexin43 (Cx43).⁸⁻¹² Cx43 down-regulation and re-localization to the lateral surfaces of cardiomyocytes are prominent features of electrical remodelling in ventricular myocardium.¹³⁻¹⁵ Both redistribution of Cx43 and loss of Cx43 expression at the intercalated discs may result in conduction abnormalities like conduction slowing and block, thereby producing a substrate for the development of arrhythmias.¹⁶⁻²³

Early studies have investigated the role of anatomical obstacles in promoting conduction block²⁴⁻²⁵ as well as the occurrence of wavebreaks in a homogeneous tissue model with dynamically induced functional heterogeneity in electrophysiological properties.²⁶ Although the molecular mechanisms underlying arrhythmogenesis in heterogeneous cardiac tissue have been extensively theorized,^{5,21,24,26-35} the biophysical consequences of dynamically induced electrotonic imbalances in remodelled cardiac tissue remain poorly understood. One possible mechanism by which such heterogeneity may arise is through APD alternans. APD alternans can either occur as large spatially connected areas of tissue exhibiting consecutive APs of the same phase but with alternating durations (technically referred to as spatially concordant alternans or SCA) or as small connected regions of tissue displaying APs with alternating durations of opposite phase adjacent to one another (technically referred to as spatially discordant alternans

or SDA). As SDA promotes spatial dispersion of repolarization,^{29,36-41} it is mechanistically linked to conduction block and is believed to be more arrhythmogenic than SCA.⁴² In combination with tissue heterogeneity arising from mildly elevated levels of myofibroblasts, complex spatiotemporal interactions can be expected to occur prior to arrhythmogenesis. An in-depth biophysical study of these interactions could provide novel mechanistic insights that may help to understand the role of gap junctional remodelling and diffuse fibrosis in creating dynamic electrical instabilities in cardiac tissue.

Therefore, in this paper a head-to-head, synergistic *in silico-in vitro* approach was applied for studying the mechanisms underlying arrhythmias in remodelled ventricular tissue, focusing on the effects of Cx43 down-regulation and diffuse cardiac fibrosis. For this purpose, we used (i) freshly isolated neonatal rat ventricular cardiomyocytes (NRVMs), and (ii) a modified version of the mathematical model of these cells created by Korhonen *et al.*⁴³ including the adaptations made by Hou *et al.*⁴⁴ The NRVMs were used to establish confluent monolayers containing ~70% cardiomyocytes and ~30% neonatal rat cardiac myofibroblasts (MFBs) in a random distribution pattern. Intercellular coupling was systemically reduced *in vitro* via RNA interference (RNAi) by incubating the cells with increasing dosages of lentiviral vectors (LVs) encoding Gja1-specific short hairpin (sh) RNAs for selective Cx43 knockdown (Cx43↓) or *in silico* by gradually decreasing the intercellular coupling coefficient. In an earlier study from our group, the ability to inhibit Cx43 expression in cultured MFBs by lentiviral RNAi was proven structurally by immunohistological and western blot analyses and functionally by means of dye transfer assays.⁴⁵ In the current study, the same method was used to accomplish Cx43↓ in both NRVMs and MFBs. Programmed electrical stimulation and voltage mapping, together with an interactive data exchange strategy, were used to investigate whether and how these features of ventricular remodelling affected electrical impulse generation and propagation as well as arrhythmia initiation and complexity.

Our results demonstrate for the first time that Cx43↓ and increased myofibroblast density are responsible for a previously unexplored form of complex SDA, characterized by the spatiotemporal evolution of island-like areas of synchronized, oppositely phased APD alternans (designated as alternans phase islands or APIs). Our study not only reveals the presence of APIs in two-dimensional *in silico* and *in vitro* models of ventricular remodelling, but also demonstrates how these local disturbances could lead to the formation of reentrant tachyarrhythmias affecting the whole medium.

Results

Unless indicated otherwise, figure panels adjacent to a red vertical bar depict *in silico* results, whereas figure panels next to a blue vertical bar represent *in vitro* results.

Characterization of fibrotic NRVM monolayer cultures

Immunostaining for collagen type I, smooth muscle myosin heavy chain and CD31 (also known as platelet endothelial cell adhesion molecule 1) confirmed that the *in vitro* monolayer cultures consisted of ~70% NRVMs and ~30% MFBs in a random distribution pattern and did not contain vascular smooth muscle cells or endothelial cells (Supplementary Fig. S1). Exposure of these cultures to different dosages of LV.Cx43↓ resulted in a dose-dependent reduction in Cx43 RNA and protein levels (Supplementary Fig. S2), conduction velocity (CV) and wavelength (λ , defined as: $APD_{80} \times CV$; Supplementary Fig. S3). *In vitro* Cx43↓ was accompanied by an increase in reentry inducibility in the fibrotic NRVM cultures (Supplementary Fig. S3).

High-frequency pacing promotes arrhythmogenesis in fibrotic NRVM monolayer cultures

High-frequency electrical pacing (3.5 Hz) of our fibrotic NRVM monolayers with the highest degree of Cx43↓ *in vitro* led to complex arrhythmias, *i.e.*, reentrant arrhythmias with multiple phase singularities (PSs; points in the phase map where the phase is indeterminate, around which activation wave fronts hinge and progress through a complete cycle from $-\pi$ to $+\pi$; Fig. 1). In order to develop mechanistic insights into the underlying basis of these arrhythmias in a more subtle, precise, controllable and reproducible manner, we employed our *in silico* model. The first step involved validation of this model.

Validation of the *in silico* model of fibrotic NRVM monolayers

Fibrotic monolayer cultures with 4 different levels of Cx43↓ were studied *in vitro*. Based on the average CVs measured in these monolayers, the *in silico* intercellular coupling constant (see Methods for explanation) was adjusted so that the computer model produced CVs that closely matched the values measured *in vitro* (Fig. 1a). Next, the same pacing protocol was applied *in silico* as *in vitro*. The results from the *in silico* experiments resembled closely those of the *in vitro* studies, demonstrating CV-dependent threshold behaviour for arrhythmia incidence (Fig. 1b) and complexity (Fig. 1c). For both *in silico* and *in vitro* models, stable spiral wave reentry occurred only at $CV \sim 15$ cm/s (corresponding to $6\mu\text{L}$ LV.Cx43↓) and further CV lowering resulted in a similar gradual increase in the number of PSs. Arrhythmia complexity correlated negatively with CV and λ (Fig. 1d and 1e, respectively). Representative examples of the excitation patterns are shown in Fig. 1f. Thus, we not only developed a minimal *in silico* model for studying the electrophysiological consequences of cardiac remodelling, but also demonstrated its expedience to predict the outcome of *in vitro* experiments.

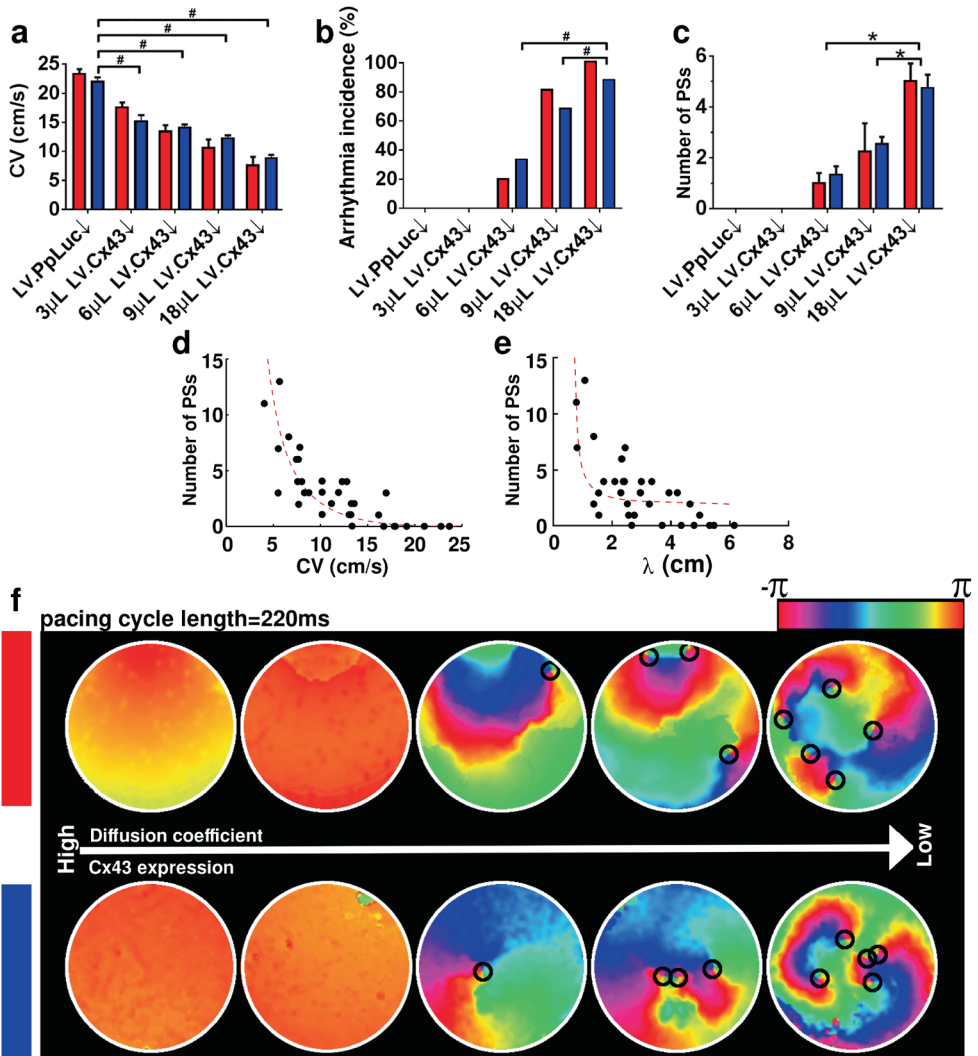


Figure 1. Complexity of electrical activation patterns increases with decreasing CV. Comparison of (a) CV, (b) arrhythmia incidence and (c) arrhythmia complexity (*i.e.*, number of PSs) in NRVM monolayers *in silico* (red bars) and *in vitro* (blue bars) at different levels of intercellular coupling and in the presence of 30% interspersed MFBs ($N > 9$). Statistical analysis was performed by comparing LV.PpLuc↓-transduced cell cultures (negative control) with cell cultures exposed to different amounts of LV.Cx43↓. Statistical significance was expressed as follows: *, $P < 0.05$, #, $P < 0.001$. Relationship between arrhythmia complexity and (d) CV or (e) wavelength (λ), defined as: $APD_{80} \times CV$. (f) Pseudocolor plots of phase maps from the *in silico* (top panel) and *in vitro* (bottom panel) datasets. The small black circles indicate the locations of PSs.

Arrhythmogenesis correlates with the development of complex patterns of SDA

Optical mapping recordings of arrhythmogenic *in vitro* cultures showed indications of localized APD alternans just prior to reentry initiation. Similar effects were observed *in silico*. Analysis of *in silico* synchronized APD distribution maps during rapid pacing revealed homogeneous APD distributions in substrates with a high CV (Fig. 2a), as opposed to the development of SDA in the substrates with the lowest CV considered (Fig. 2b). Substrates displaying SDA were characterized by the co-occurrence of three APD patterns: no alternans (NA), alternans with phase long-short (LS) and alternans with phase short-long (SL; Fig. 2c). While the type of SDA reported in previous studies^{36-39,46-47} was generally characterized by the development of open nodal lines separating regions of opposite alternans phase, in our model the nodal lines formed closed loops, enclosing regions of a particular alternans phase, which we designated APIs to stress their demarcated nature. To exclude random noise artefacts, we defined APIs as clusters of ≥ 10 connected data points exhibiting alternans of the same phase. APD maps from successive beats demonstrated that areas showing a long APD in beat n-1, displayed a short APD in beat n and again a long APD in beat n+1. Areas with a short APD in beat n-1, showed the inverse behaviour, *i.e.*, long and short APDs in beats n and n+1, respectively. There were also areas where the APD did not change substantially in consecutive beats, indicating absence of APD alternans in these areas. Following the predictions from our *in silico* model, we wrote customized software to generate synchronized APD maps from the optical mapping data generated *in vitro*. In perfect agreement with the *in silico* results, the *in vitro* cultures showed homogeneous synchronized APD maps at normal CVs (Fig. 2d), but complex alternans phase distribution patterns at low CV (Fig. 2e-f).

Role of APIs in arrhythmogenesis

In silico analysis revealed that rapid pacing induced wavebreaks along the borders between APIs of opposite alternans phase. This is illustrated at different CVs, by means of alternans phase maps (Fig. 3a1-a4). Superposition of these alternans phase maps with corresponding voltage maps (Fig. 3b1-b4) shows the position(s) of the wavebreak(s). At near normal CV (17.4 cm/s) neither APIs nor wavebreaks occurred. At CV of ~ 13.5 cm/s, a single large API arose and a wavebreak developed at the border of opposite alternans phase. Further conduction slowing led to higher numbers of (oppositely phased) APIs, thereby increasing wavebreak incidence. A similarly detailed analysis was not possible *in vitro* because of the limited resolution of the imaging setup used for optical voltage mapping. Nonetheless, the formation of APIs *in vitro*, generally also happened at CV < 15 cm/s and their number increased with further Cx43 \downarrow (Fig. 3c1-c4 and 3d1-d4). Moreover, in the fibrotic NRVM cultures wavebreaks always occurred in the vicinity of the borders between adjacent oppositely phased APIs, in consonance with our *in silico* predictions.

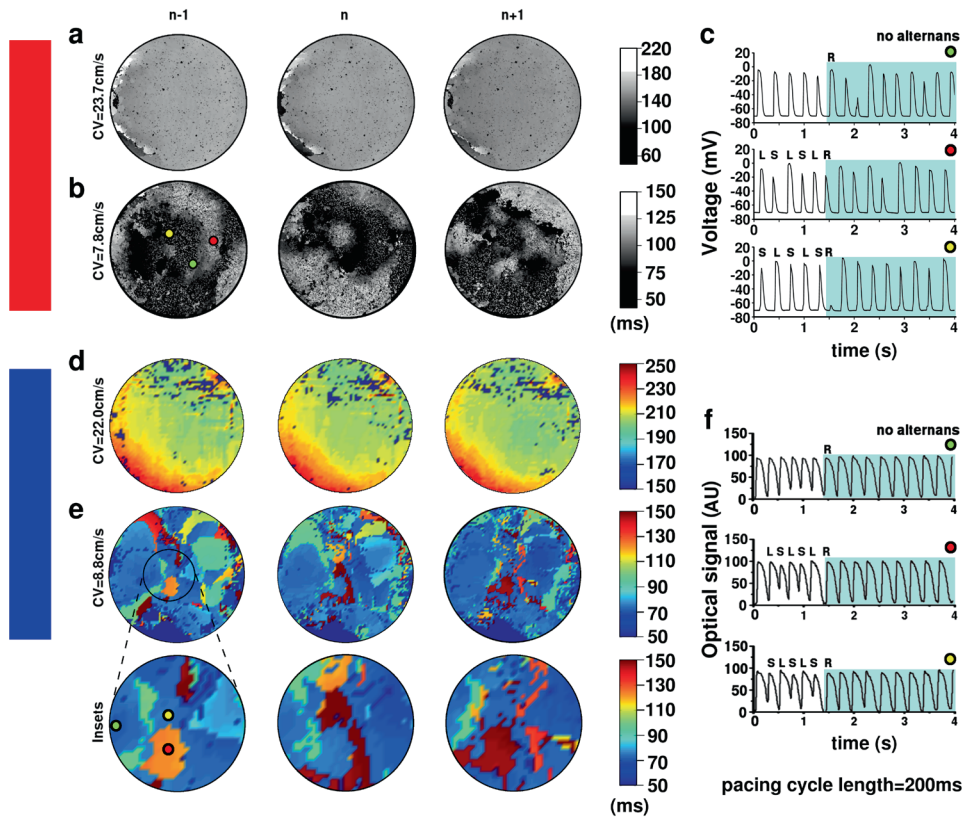


Figure 2. Reentry is preceded by API formation. APD_{80} maps of (a, b) *in silico* and (d, e) *in vitro* cocultures from 3 consecutive beats (n-1, n and n+1) at normal (a, d) and reduced (b, e) CV. The insets in (e) highlight an area showing local alternans phase reversal during successive beats. Time series of (c) voltage traces of the *in silico* monolayer shown in (b) and (f) optical signal traces of the *in vitro* monolayer shown in (e) at locations displaying no APD alternans (green dot) or APD alternans of opposite phase beginning either with a LS APD sequence (red dot) or a SL APD sequence (yellow dot). The light blue-colored area in (c) and (f) show signal recording after the onset of reentry. AU, arbitrary units.

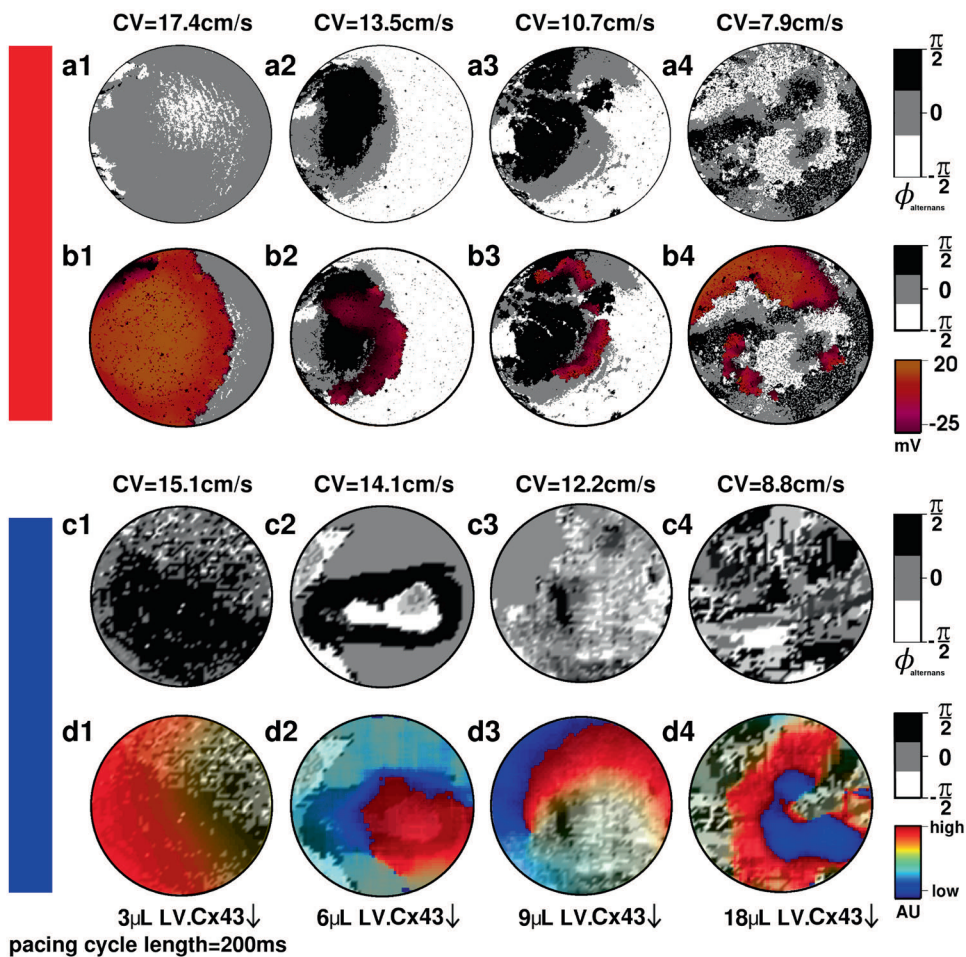


Figure 3. Wavebreaks occur along the borders of APis. Alternans phase maps of fibrotic (a, b) *in silico* or (c, d) *in vitro* NRVM cultures without (a, c) or with (b, d) superimposed activation maps just before the onset of reentrant conduction for the monolayers in which reentry could be induced by high-frequency pacing. Formation of APis and wavebreaks is promoted by CV lowering.

Time series recordings from different locations in arrhythmic *in vitro* NRVM cultures revealed a significantly higher probability of reentry induction in cultures showing APD alternans than in those without APD alternans ($P < 0.001$; Fig. 4a). Similarly, APD alternans occurred more frequently in cultures with successful stable reentry induction than in cultures that did not display stable reentry following high-frequency pacing ($P < 0.001$; Fig. 4b). Our *in vitro* data furthermore showed a positive correlation between the number of high frequency pacing-induced APis and reentry complexity (Fig. 4c).

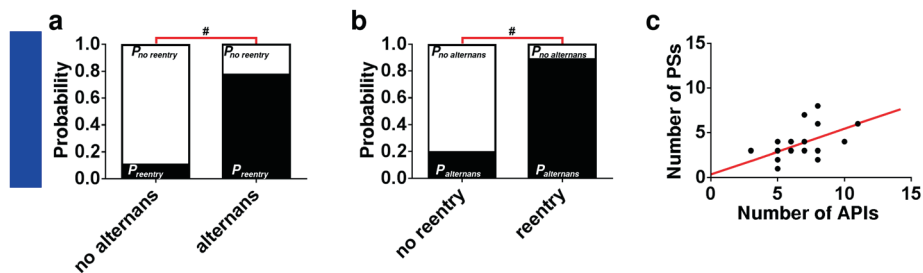


Figure 4. Close linkage between the occurrence of reentry and APD alternans in fibrotic *in vitro* NRVM cultures. (a) Probability of successful stable reentry induction in cultures showing APD alternans or no APD alternans. (b) Probability of occurrence of APD alternans during high-frequency pacing in cultures showing stable reentry or no reentry induction. (c) Relationship between the number of APIs and arrhythmia complexity (*i.e.*, the number of PSs).

Origin of APIs

Having made the association between reentry initiation, the complexity of reentry patterns and API formation, the origin of these APIs was investigated next. Specifically, the combinatorial effects of structural discontinuities (MFBs) and functional instabilities (high frequency pacing-induced alternans) on the onset of reentry were studied *in silico*. As shown in Fig. 5a-h, in monolayers with 30% randomly distributed MFBs, APIs only occurred at cycle lengths <333 ms and their number increased with a further decrease in cycle length. For investigations into the role of structural discontinuities in API formation, computer simulations of NRVM cultures containing different percentages of MFBs and a CV of ~ 7.9 cm/s (*i.e.*, the lowest CV analysed) were performed. High-frequency paced NRVM cultures without MFBs showed that APD alternans was practically absent (Fig. 6a1 and b1) and wavebreaks were not observed. In monolayers with 10% randomly distributed MFBs, APD alternans began to appear (Fig. 6a2 and b2). Large APIs emerged when $\sim 15\%$ of the cells were MFBs (Fig. 6a3 and b3). Stable API-mediated reentry was observed in monolayers containing $\geq 25\%$ MFBs (Fig. 6a4, b4, a5 and b5), and at $>40\%$ MFBs conduction block occurred. Thus, the presence of interspersed MFBs above a certain critical percentage could be recognized as a factor involved in the formation of APIs. Taken together, our data indicate the co-occurrence of (i) tissue heterogeneity (*e.g.*, diffuse fibrosis) and (ii) CV slowing below a certain threshold (*e.g.*, by Cx43 down-regulation) is required for successful API formation upon high-frequency pacing. Furthermore, increased numbers of MFBs lowers the threshold of CV reduction and decreased CV lowers the threshold of fibrosis necessary for API formation.

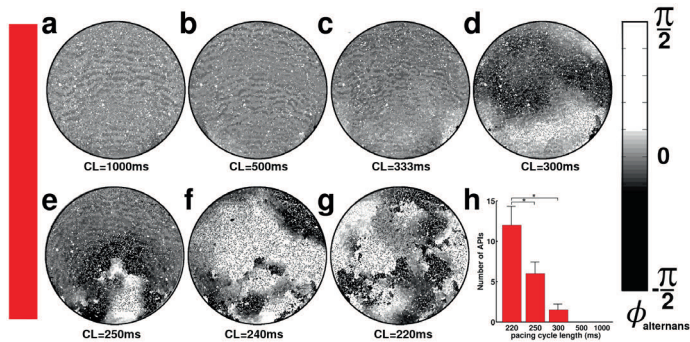


Figure 5. High-frequency pacing plays an essential role in API formation. Alternans phase maps of fibrotic *in silico* NRVM cultures corresponding to the experimental group with the lowest CV, paced at different cycle lengths (CLs) reveal a direct correlation between pacing frequency and API incidence.

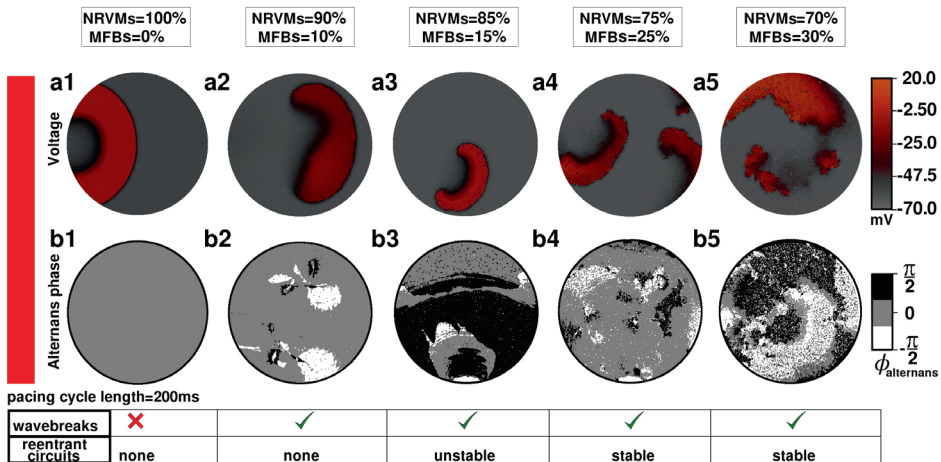


Figure 6. Role of MFBs in reentry initiation: insights from the *in silico* model. (a) Voltage and (b) alternans phase maps of *in silico* NRVM cultures corresponding to the experimental group with the lowest CV, containing different percentages of randomly distributed MFBs. Alternans was not observed in monolayers with 100% cardiomyocytes (a1 and b1); in the presence of 10% MFBs, some portions of the monolayer began to show unstable alternans (a2 and b2). In this scenario wavebreaks could occur, but these failed to develop into reentrant circuits. With 15% MFBs (a3 and b3) a limited number of large APIs began to form and; unstable reentry could be initiated. With 25% MFBs (a4 and b4), multiple APIs started to form, which evolved dynamically giving rise to stable reentrant circuits. Raising the percentage of MFBs to 30% further increased the pro-arrhythmicity of the substrate (a5 and b5).

Discussion

The key findings of this study are: (i) Rapid electrical pacing of fibrotic NRVM cultures showed a Cx43 expression-dependent threshold behaviour towards the development of stable reentrant arrhythmias in a model of ventricular remodelling-associated arrhythmogenesis; (ii) Arrhythmia complexity increased with decreasing Cx43 expression; (iii) The occurrence of complex arrhythmias was attributed to a decrease in electrotonic synchronization linked to the presence of MFBs; (iv) The increased dyssynchrony manifested itself as a special type of spatially discordant APD alternans characterized by APIs; (v) Reentrant arrhythmia incidence and complexity positively correlated with the number of APIs.

Ventricular remodelling is a dynamic process of alterations in size, shape and function of the ventricles in response to cardiac injury (e.g., myocardial infarction) and stress (e.g., pressure or volume overload). The contributing cellular events include cardiomyocyte death, cardiomyocyte hypertrophy, hyperplasia of cardiac fibroblasts (CFBs), CFB-MFB transformation, excessive extracellular matrix deposition and electrical remodelling.⁴⁸⁻⁴⁹ These events cause structural and functional disruptions of the cardiac syncytium, which contribute to a loss of force-generating capacity and the development of cardiac arrhythmias.

Several studies have shown that ventricular remodelling predisposes to the development of APD alternans following high-frequency pacing.⁵⁰⁻⁵¹ NRVM monolayers treated with Bay K8644⁴⁴ displayed high-frequency pacing-induced SDA, characterized by the co-occurrence of APD and $[Ca^{2+}]_i$ alternans with detectable nodal lines separating regions that alternated out of phase, suggesting that SDA is a dynamically generated phenomenon, predisposing to arrhythmias. A common aspect of electrical remodelling is Cx43 down-regulation and lateralization, which is associated with conduction slowing and arrhythmogenesis. Suppression of SDA in Langendorff-perfused guinea pig hearts by rotigaptide, which enhances gap junctional communication, suggests that intercellular uncoupling indeed plays an important role in the development of SDA.^{47,52}

Ventricular remodelling includes both structural and electrical changes, the independent consequences of which have been discussed above. However, the biophysical consequences of complex interactions between structural discontinuities and dynamically induced functional instabilities, and in particular their functional interdependencies (e.g., the influence on electrotonic balance, electrical signal propagation and synchronization as well as correlation with reentry complexity) remains poorly understood. This study aimed at addressing the role of these complex interactions in arrhythmogenesis using an interactive *in silico-in vitro* approach.

Our *in silico* monolayer studies revealed the existence of a direct relationship between the number of high frequency pacing-induced APIs and the percentage of interspersed MFBs (Fig. 6). This association is in line with findings by Woo *et al.*,⁵³ Kizana *et al.*⁵⁴ and Engelman *et al.*⁵⁵ In more detail, Woo *et al.*⁵³ showed that in NRVM monolayers, spatial heterogeneities related to the presence of CFBs can cause some nontrivial wave dynamics leading to complex reentrant conduction patterns. Kizana *et al.*⁵⁴ demonstrated that CFBs can modulate the excitability of cardiomyocytes in a Cx43-dependent manner. They explored the effect of Cx43-negative mouse fibroblasts on the intrinsic beat frequency of NRVMs cultured on top. NRVMs on top of wild-type fibroblasts (with native Cx43 levels) exhibited a significantly lower beating rate compared to those grown on fibroblasts lacking functional Cx43. Forced expression of Cx43 in fibroblasts from Cx43 knockout mice led to a near normalization of beating frequency, demonstrating that fibroblasts play an important role in modulating the excitability of NRVMs through gap junctional coupling. Furthermore, in an *in silico* study, Engelman *et al.*⁵⁵ found that SDA occurs at lower pacing frequencies and more often in fibrotic than in non-fibrotic cardiac tissue as a result of discontinuous conduction through the disrupted cardiac syncytium. Such abnormal AP propagation causes large local fluctuations in the diastolic intervals giving rise to regional electrotonic instability. These instabilities modulate the CV spatiotemporally and influence APD restitution.

We hypothesize that when such instabilities occur in close proximity of each other, the electrotonic balance of the system is perturbed. The propagating wavefront becomes fractionated, while island-like zones emerge, exhibiting synchronized electrophysiological behaviour (APD alternans of common phase). In this scenario, the size of an API is determined by the length scale of the influence of the localized instabilities. If the instabilities emerge distant from each other their mutual influence is small and an API may not form. However, if a region is highly fibrotic, it will sustain many synchronized instabilities and show a high propensity for API development. The dynamic state of the tissue prior to pacing,^{39,56-57} and short-term memory³⁷ are also likely to influence the development of APIs and their spatiotemporal distributions. Although previous studies mostly reported the occurrence of SDA characterized by open nodal lines, there are some studies that demonstrate island-like SDA patterns in explanted whole hearts.^{38,57} However, none of these studies, explored their relevance, origin or contribution to the development of arrhythmogenesis. Our work differs from earlier reports in that we made use of heterogeneous tissue models incorporating diffuse fibrosis. We found that diffuse fibrosis and Cx43 knockdown synergistically reduced the excitability of cardiac tissue, thereby causing fractionation of the propagating wavefront. This fractionation enhances localized electrical resynchronization leading to APIs. However, the exact mechanism by which such resynchronization results in APIs of specific shape is not

completely clear and requires special investigation that lies beyond the scope of this study. Additional research into the genesis and dynamics of APIs, including the relative abundance and distribution of each APD pattern and the role of short-term memory in API development is therefore warranted. Furthermore, it might be of interest to investigate $[Ca^{2+}]_i$ dynamics during API formation in future studies.

As shown in Fig. 3, a decrease in CV was associated with voltage alternans. The kind of alternans (spatially concordant or discordant) depended on the level of intercellular uncoupling. In NRVM cultures with modest Cx43↓, large connected areas without APD alternans co-existed with one or few large APIs. In cultures with a high degree of intercellular uncoupling, pacing above a critical frequency led to the development of more complex SDA patterns, characterized by multiple APIs of different size and phase. These APIs also appeared in the *in silico* model (Fig. 2). Once APIs are formed, the substrate is prone to develop wavebreaks. These wavebreaks formed along the boundaries between adjacent APIs of opposite phase (Fig. 3). At normal CVs the formation of APIs was inhibited. If the excitation wavelength is such that at any instant the substrate has enough recovered area to support one stable reentrant circuit, only the best positioned wavebreak gives rise to a sustained spiral wave. The optimal position seems to be determined by the degree of source-sink mismatch encountered by the wavebreak. Conduction slowing was associated with increased electrical dyssynchrony, exemplified by the formation of multiple APIs of opposite phase. During high-frequency pacing, APIs evolved dynamically, drifting towards one another until they appeared side-by-side. At maximal dyssynchrony (Fig. 7, stage 3), electrotonic interaction between adjacent APIs of opposite phase resulted in pacing-induced wavebreaks at the islands' borders. Higher dyssynchrony prior to reentry initiation correlated with more PSs.

Our data reveal that at higher MFB percentages a smaller reduction in Cx43 level suffices to induce APIs: with 30% MFBs, API induction is initiated at a CV of ~13.5 cm/s, while for 10% of MFBs APIs started to occur at a CV of ~7.9 cm/s (Fig. 3). Similarly, the level of fibrosis required for reentrant circuit formation is directly proportional to the Cx43 level. As seen from Fig. 6, at a CV of ~7.9 cm/s, stable API-mediated reentry requires at least 25% MFBs, whereas a monolayer with a CV of ~13.5 cm/s requires up to 30% MFBs for stable arrhythmias to occur. A monolayer with a CV as high as ~17.4 cm/s cannot support APIs even at 30% MFBs.

Electrotonic effects sometimes caused small APIs to merge, thereby decreasing the number of possible wavebreak initiation points. This could explain why in some cases although the substrate initially supported multiple spiral waves their number decreased over time with fewer stable reentrant circuits remaining. Stabilization of reentrant circuits via the onset of stable reentry resulted in disappearance of asynchronous APD alternans (Fig. 7). In our *in vitro* studies <1% of the co-cultures were excluded because they showed spontaneous activity. As

cardiomyocyte-fibroblast interaction can also result in the onset of oscillatory dynamics,⁵⁸⁻⁶⁰ it would be interesting to study the origin of arrhythmias in such co-cultures and their relation to fibrosis, as a future project.

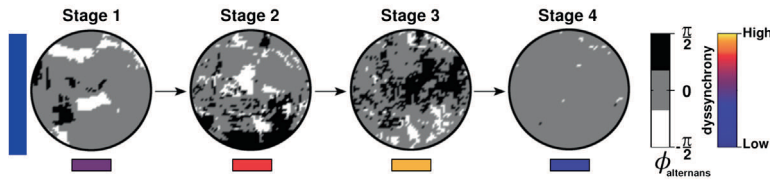


Figure 7. Conduction slowing causes progressive dyssynchrony leading to reentry initiation. In substrates with reduced CV, reentry initiation can be divided in 4 stages. In the first stage, high-frequency pacing induces patchy APD alternans leading to the formation of APIs and the substrate first begins to develop functional dyssynchrony. In the second stage, under the influence of electrotonic effects, these APIs evolve dynamically, drifting towards each other, such that APIs of opposite phases align side-by-side. The substrate thus develops SDA and dyssynchrony is increased. In the third phase, electrical interactions between adjacent APIs forces them to break up into smaller, disconnected API, thereby maximizing dyssynchrony within the substrate. This leads to wavebreaks, which, in the fourth and final stage of the process, mature into stable reentrant circuits in which spatial APD alternans disappears.

In extended systems (*i.e.*, cardiac monolayers, tissue preparations and whole hearts), alternans has been found to occur either synchronously (SCA) over large connected areas or asynchronously (SDA) over smaller regions separated from each other through nodal lines/surfaces. Although there is extensive literature attempting to correlate the dynamics of nodal lines to the underlying alternans mechanism,^{38-40,56-57,61-63} these studies mostly concerned the behaviour of nodal lines arising from SDA induced by CV restitution or tissue heterogeneity. In this study, we have been able to associate this unusual type of alternans with a pathological substrate and to identify a mechanism by which these APIs could increase pro-arrhythmic risk. This may provide relevance to our study from a clinical perspective.

Materials and Methods

Detailed technical information can be found in the Supplementary Information.

Numerical methods

The temporal electrophysiological behaviour of a single NRVM was described by using an ordinary differential equation:

$$\frac{dV}{dt} = \frac{-I_{ion} + I_{stim}}{C_m} (1)$$

where V is the transmembrane voltage in mV, t is time in ms, C_m is the capacitance per unit surface area of the cell in $\mu\text{F}/\text{cm}^2$, I_{stim} is the external current stimulus, and I_{ion} is the total ionic current flowing across the cell membrane. All currents are expressed in pA/pF. I_{ion} represents the sum of 12 major and minor ionic currents:

$$I_{ion} = I_{Na} + I_{K1} + I_{Kr} + I_{Ks} + I_t + I_{CaL} + I_{CaT} + I_{Nab} + I_{Cab} + I_f + I_{NCX} + I_{NaK} \quad (2)$$

where I_{Na} is the fast Na^+ current, I_{K1} is the time-independent K^+ current, I_{Kr} is the rapid delayed rectifier K^+ current, I_{Ks} is the slow delayed rectifier K^+ current, I_t is the transient outward K^+ current, I_{CaL} is the L-type Ca^{2+} current, I_{CaT} is the T-type Ca^{2+} current, I_{Nab} and I_{Cab} are the background Na^+ and Ca^{2+} currents, respectively, I_f is the hyperpolarization-activated current, I_{NCX} is the $\text{Na}^+/\text{Ca}^{2+}$ exchanger current, and I_{NaK} is the Na^+/K^+ ATPase current. The flow of currents in and out of the cells is controlled by ion channels, which were modelled as conductances. The opening and closing of these ion channels are controlled by gates with specific time constants. The formulation of these currents, as well as the model parameters and constants are listed in Hou *et al.*⁴⁴ Our new formulation of the Ca^{2+} dynamics of the cell is presented in the Supplementary Information.

The transmembrane potential of the NRVMs in the monolayer studies was governed by the following reaction-diffusion equation:

$$\frac{\partial V}{\partial t} = \nabla \cdot (\mathbf{D} \nabla V) - \frac{I_{ion} + I_{stim}}{C_m} \quad (3)$$

where \mathbf{D} is the symmetric tensor whose elements determine the degree of electrical conductance in each direction of propagation. In order to maintain consistency with our *in vitro* set up, anisotropy was disregarded. This reduced \mathbf{D} to a scalar coupling constant D multiplied by an identity matrix.⁶⁴ Thus in our monolayer simulations:

$$\frac{\partial V}{\partial t} = D \nabla^2 V - \frac{I_{ion} + I_{stim}}{C_m} \quad (4)$$

This equation was subject to Neumann zero-flux boundary conditions. The numerical details are provided in the Supplementary Information.

Thirty percent randomly distributed MFBs were introduced in the simulation domain. The MFBs were modelled using the passive formulation of MacCannell *et al.*⁶⁵ A gap junctional coupling coefficient (G_{gap}) of 0.5 nS/pF was used for intercellular coupling between NRVMs and MFBs.⁶⁶ The possible connections between NRVMs and MFBs in the *in silico* model are shown in Supplementary Fig. S4a. Details of the MFB model and the model for natural cellular

heterogeneity are also provided in the Supplementary Information. The AP characteristics were computed from a single mathematical cell and validated with existing literature (Supplementary Fig. S4b-c). The APD restitution curve derived from our *in silico* model lay in between those based on the *in vitro* and *in silico* data published by Hou *et al.*⁴⁴ (Supplementary Fig. S4d).

***In silico* pacing protocol**

The *in silico* monolayer was paced initially at 1000-ms cycle length for 3 s, with an electrical pulse strength of 100 pA and a duration of 2 ms. Next, the cycle length was gradually decreased in steps of 150 ms, taking care to pass 3-4 pulses at each cycle length until 1:1 capture was no longer observed or arrhythmia was initiated.

Experimental methods

All animal experiments were approved by the Animal Experiments Committee of Leiden University Medical Centre (LUMC) and conformed to the Guide for the Care and Use of Laboratory Animals as stated by the United States National Institutes of Health.

Cell isolation and culture

NRVMs and cardiac MFBs were isolated and cultured as described previously.⁶⁷ Briefly, hearts were excised from anaesthetized neonatal rats, and ventricular tissue was finely minced and dissociated with collagenase type 1 (450 U/mL; Worthington, Lakewood, NJ) and DNase I (18.75 Kunitz/mL; Sigma-Aldrich, St. Louis, MO). Our cell isolation protocol allowed us to obtain NRVMs with a baseline 15-20% contamination of MFBs. Therefore, after two consecutive pre-plating steps, the purified NRVMs were mixed with 10-15% neonatal rat MFBs, such that the final co-cultures had a ratio of 70 NRVMs:30 MFBs. The cells were seeded on fibronectin (Sigma-Aldrich)-coated glass coverslips in 24-well cell culture plates (Corning Life Sciences, Corning, NY). Cells were plated at a total density of $1-7 \times 10^5$ cells/well, depending on the assay, and treated for 2 hours with mitomycin-C (10 $\mu\text{g}/\text{mL}$; Sigma-Aldrich) to prevent proliferation of non-cardiomyocytes.⁶⁷

RNAi

Cx43 expression in NRVMs was selectively and dose-dependently inhibited using self-inactivating LV particles encoding two different rat Gja1 gene-specific shRNAs. The shuttle constructs used to generate the LVs are derivatives of plasmid clones TRCN0000348381 and TRCN0000068474 from the MISSION shRNA library (Sigma-Aldrich) in which the marker gene cassette consisting of the human phosphoglycerate kinase 1 gene promoter, the *Streptomyces alboniger* puromycin-N-acetyltransferase-coding sequence and, in case of TRCN0000348381,

the woodchuck hepatitis virus posttranscriptional regulatory element was substituted with the human eukaryotic translation elongation factor 1 alpha 1 gene promoter and the *Aequorea victoria* enhanced green fluorescent protein-coding sequence. The resulting LVs were designated LV.Cx43 \downarrow or LV.Cx43 $_1\downarrow$ and LV.Cx43 $_2\downarrow$, respectively. The negative control vector (LV.PpLuc \downarrow) had the same genetic makeup, except that it contained the *Photinus pyralis* luciferase (PpLuc)-specific shRNA-coding sequence of plasmid SHC007 (Sigma-Aldrich) instead of a rat Gja1-specific shRNA-coding sequence.

Optical voltage mapping

On day 9 of culture, assessment of AP propagation in cellular monolayers was performed by optical mapping using di-4-ANEPPS (Life Technologies) as potentiometric dye, as described previously.⁶⁷ Optical mapping was carried out with a MiCAM ULTIMA-L imaging system (SciMedia USA, Costa Mesa, CA). Optical signals were recorded at a 6-ms frame rate and analysed using BrainVision Analyzer 13.12.20 software (Brainvision, Tokyo, Japan). Based on the outcome of our *in silico* studies, the cultured monolayers were stimulated by electrical pacing with an epoxy-coated bipolar platinum electrode with square supra-threshold electrical stimuli, at a frequency predicted to induce arrhythmias.

Alternans phase maps

To construct alternans phase maps, we considered APD maps from 3 successive beats, designated n-1, n, and n+1. The alternans phase ($\phi_{alternans}$) at any point within the monolayer was calculated as:

$$\phi_{alternans} = \frac{APD_{n-1} + APD_{n+1} - 2APD_n}{APD_{long}} \quad (5)$$

$$APD_{long} = \begin{cases} \frac{APD_{n-1} + APD_{n+1}}{2} & \text{long - short alternans} \\ APD_n & \text{short - long alternans} \\ \frac{APD_{n-1} + APD_n + APD_{n+1}}{3} & \text{no alternans} \end{cases} \quad (6)$$

$\phi_{alternans}$ was then binned into 3 groups, with labels $\pi/2$ ($\phi_{alternans} \geq 0.6$), 0 ($-0.6 < \phi_{alternans} < 0.6$) and $-\pi/2$ ($\phi_{alternans} \leq -0.6$), to signify long-short, non-alternating and short-long APD sequences, respectively.

Statistics

Statistical analyses were performed using GraphPad Prism software version 6.02 (GraphPad Software, La Jolla, CA). Unpaired Student's *t* test and Fisher's exact test were used for comparisons between experimental groups, as appropriate. Data were expressed as mean±standard error of mean for a specified number (N) of observations. Results were considered statistically significant at *P* values <0.05. Statistical significance was expressed as follows: *: *P*<0.05, #: *P*<0.001 or NS: not significant. Non-linear regression curves were constructed by using robust exponential or hyperbolic 1-phase decay curve fits. Accuracy was expressed as coefficient of determination (*R*²). Arrhythmia complexity was defined as the number of PSs per monolayer culture (surface area 1.8 cm²). Phase maps were constructed with dedicated software using the phase space method, as described previously.⁶⁸

Acknowledgements

We thank Cindy Schutte-Bart, Margreet de Jong, Jia Liu, Iolanda Feola, Annemarie Kip and Alexander Teplenin from LUMC's Department of Cardiology for excellent technical support and help with LV production.

Author Contributions

R.M. and M.C.E.: conception and study design, collection and assembly of data, data analysis and interpretation, manuscript writing, and final approval of manuscript; A.A.F.V., A.V.P. and D.A.P.: study design, data analysis and interpretation, financial support, manuscript writing, and final approval of manuscript.

Additional Information

This work was supported by Ammodo (D.A. Pijnappels). Additional support was provided by the Netherlands Organization for Scientific Research (NWO) Mosaic grant 017007064 (M.C. Engels), the Royal Netherlands Academy of Arts and Sciences (KNAW) CEP project 10CDP007 (A.A.F. de Vries), the Netherlands Heart Institute (ICIN) project 230-148.04 (A.A.F. de Vries) and the Research Foundation - Flanders (FWO Vlaanderen, A.V. Panfilov).

Competing financial interests

The authors declare no competing financial interests.

References

1. Kohl P, Camelliti P, Burton FL, Smith GL. Electrical coupling of fibroblasts and myocytes: relevance for cardiac propagation. *J Electrocardiol.* 2005;38:45-50.
2. Miragoli M, Salvarani N, Rohr S. Myofibroblasts Induce Ectopic Activity in Cardiac Tissue. *Circ Res.* 2007;101:755-758.
3. Nguyen TP, Xie Y, Garfinkel A, Qu Z. Arrhythmogenic Consequences of Myofibroblast-Myocyte Coupling. *Cardiovasc Res.* 2012;93:242-251.
4. Ten Tusscher KH, Panfilov AV. Influence of diffuse fibrosis on wave propagation in human ventricular tissue. *Europace.* 2007;9:v138-v145.
5. Nakagami T, Tanaka H, Dai P, Lin SF, Tanabe T, Mani H, Fujiwara K, Matsubara H, Takamatsu T. Generation of reentrant arrhythmias by dominant-negative inhibition of connexin43 in rat cultured myocyte monolayers. *Cardiovasc Res.* 2008;79:70-79.
6. Joyner RW. Modulation of repolarization by electrotonic interactions. *Jpn Heart J.* 1986;27:167-183.
7. McSpadden LC, Kirkton RD, Bursac N. Electrotonic loading of anisotropic cardiac monolayers by unexcitable cells depends on connexin type and expression level. *Am J Physiol Cell Physiol.* 2009;297:C339-C351.
8. Nielsen MS, Axelsen LN, Sorgen PL, Verma V, Delmar M, Holstein-Rathlou NH. Gap junctions. *Compr Physiol.* 2012;2:1981-2035.
9. Gonzalez JP, Ramachandaran J, Xie LH, Contreras JE, Fraidenraich D. Selective Connexin43 Inhibition Prevents Isoproterenol-Induced Arrhythmias and Lethality in Muscular Dystrophy Mice. *Sci Rep.* 2015;5:1-11.
10. Sato D, Xie LH, Sovari AA, Tran DX, Morita N, Xie F, Karaqueuzian H, Garfinkel A, Weiss JN, Qu Z. Synchronization of chaotic early afterdepolarizations in the genesis of cardiac arrhythmias. *Proc Natl Acad Sci USA.* 2009;106:2983-2988.
11. Giepmans BN. Gap junctions and connexin-interacting proteins. *Cardiovasc Res.* 2004;62:233-245.
12. Jansen JA, Noorman M, Musa H, Stein M, de Jong S, van der Nagel R, Hund TJ, Mohler PJ, Vos MA, van Veen TA, de Bakker JM, Delmar M, van Rijen HV. Reduced heterogeneous expression of Cx43 results in decreased Nav1.5 expression and reduced sodium current that accounts for arrhythmia vulnerability in conditional Cx43 knockout mice. *Heart Rhythm.* 2012;9:600-607.
13. Akar FG, Spragg DD, Tunin RS, Kass DA, Tomaselli GF. Mechanisms underlying conduction slowing and arrhythmogenesis in nonischemic dilated cardiomyopathy. *Circ Res.* 2004;95:717-725.
14. Akar FG, Nass RD, Hahn S, Cingolani E, Shah M, Hesketh GG, DiSilvestre D, Tunin RS, Kass DA, Tomaselli GF. Dynamic changes in conduction velocity and gap junction properties during development of pacing-induced heart failure. *Am J Physiol Heart Circ Physiol.* 2007;293:H1223-H1230.
15. Van Norstrand DW, Asimaki A, Rubinos C, Dolmatova E, Srinivas M, Tester DJ, Saffitz JE, Duffy HS, Ackerman MJ. Connexin43 mutation causes heterogeneous gap junction loss and sudden infant death. *Circulation.* 2012;125:474-481.
16. Kieken F, Mutsaers N, Dolmatova E, Virgil K, Wit AL, Kellezi A. Structural and molecular mechanisms of gap junction remodelling in epicardial border zone myocytes following myocardial infarction. *Circ Res.* 2009;104:1103-1112.
17. Fontes MS, van Veen TA, de Bakker JM, van Rijen HV. Functional consequences of abnormal Cx43 expression in the heart. *Biochim Biophys Acta.* 2012;1818:2020-2029.
18. Osbourne A, Calway T, Broman M, McSharry S, Earley J, Kim GH. Downregulation of connexin43 by microRNA-130a in cardiomyocytes results in cardiac arrhythmias. *J Mol Cell Cardiol.* 2014;74:53-63.
19. Peters NS, Coromilas J, Severs NJ, Wit AL. Disturbed connexin43 gap junction distribution correlates with the location of reentrant circuits in the epicardial border zone of healing canine infarcts that cause ventricular tachycardia. *Circulation.* 1997;95:988-996.

20. Yao JA, Hussain W, Patel P, Peters NS, Boyden PA, Wit AL. Remodelling of gap junctional channel function in epicardial border zone of healing canine infarcts. *Circ Res.* 2003;92:437-443.
21. Remo BF, Qu J, Volpicelli FM, Giovannone S, Shin D, Lader J, Liu FY, Zhang J, Lent DS, Morley GE, Fishman GI. Phosphatase-resistant gap junctions inhibit pathological remodelling and prevent arrhythmias. *Circ Res.* 2011;108:1459-1466.
22. Beardslee MA, Lerner DL, Tadros PN, Laing JG, Beyer EC, Yamada KA, Kléber AG, Schuessler RB, Saffitz JE. Dephosphorylation and intracellular redistribution of ventricular connexin43 during electrical uncoupling induced by ischemia. *Circ Res.* 2000;87:656-662.
23. Gutstein DE, Morley GE, Tamaddon H, Vaidya D, Schneider MD, Chen J, Chien KR, Stuhlmann H, Fishman GI. Conduction slowing and sudden arrhythmic death in mice with cardiac-restricted inactivation of connexin43. *Circ Res.* 2001;88:333-339.
24. Sinha S, Christini DJ. Termination of re-entry in an inhomogeneous ring of model cardiac cells. *Phys Rev E Stat Nonlin Soft Matter Phys.* 2002;66:061903.
25. Sinha S, Stein KM, Christini DJ. Critical role of inhomogeneities in pacing termination of reentry. *Chaos.* 2002;12:893-902.
26. Breuer J, Sinha S. Death, dynamics and disorder: Terminating re-entry in excitable media by dynamically-induced heterogeneities. *Pramana.* 2005;64:553-562.
27. Chang MG, Zhang Y, Chang CY, Xu L, Emokpae R, Tung L, Marbán E, Abraham MR. Spiral waves and reentry dynamics in an in vitro model of the healed infarct border zone. *Circ Res.* 2009;105:1062-1071.
28. Thompson SA, Burridge PW, Lipke EA, Shambloft M, Zambidis ET, Tung L. Engraftment of human embryonic stem cell derived cardiomyocytes improves conduction in an arrhythmogenic in vitro model. *J Mol Cell Cardiol.* 2012;53:15-23.
29. Xie Y, Garfinkel A, Camelliti P, Kohl P, Weiss JN, Qu Z. Effects of fibroblast-myocyte coupling on cardiac conduction and vulnerability to reentry: a computational study. *Heart Rhythm.* 2009;6:1641-1649.
30. Danik SB, Liu F, Zhang J, Suk HJ, Morley GE, Fishman GI, Gutstein DE. Modulation of cardiac gap junction expression and arrhythmic susceptibility. *Circ Res.* 2004;95:1035-1041.
31. Ohara T, Ohara K, Cao JM, Lee MH, Fishbein MC, Mandel WJ, Chen PS, Karaqueuzian HS. Increased wave break during ventricular fibrillation in the epicardial border zone of hearts with healed myocardial infarction. *Circulation.* 2001;103:1465-1472.
32. Sovari AA, Iravanian S, Dolmatova E, Jiao Z, Liu H, Zandieh S, Kumar V, Wang K, Bernstein KE, Bonini MG, Duffy HS, Dudley SC. Inhibition of c-Src tyrosine kinase prevents angiotensin II-mediated connexin-43 remodelling and sudden cardiac death. *J Am Coll Cardiol.* 2011;58:2332-2339.
33. de Diego DC, Pai RK, Chen F, Xie LH, De Leeuw J, Weiss JN, Valderrábano M. Electrophysiological consequences of acute regional ischemia/reperfusion in neonatal rat ventricular myocyte monolayers. *Circulation.* 2008;118:2330-2337.
34. Rudenko AN, Panfilov AV. Drift and interaction of vortices in two-dimensional heterogeneous active medium. *Studia Biophysica.* 1983;98:183-188.
35. Panfilov AV, Vasiev BN. Vortex initiation in a heterogeneous excitable medium. *Physica D.* 1991;49:107-113.
36. Rosenbaum DS, Jackson LE, Smith JM, Garan H, Ruskin JN, Cohen RJ. Electrical alternans and vulnerability to ventricular arrhythmias. *N Engl J Med.* 1994;330:235-241.
37. Konta T, Ikeda K, Yamaki M, Nakamura K, Honma K, Kubota I, Yasui S. Significance of discordant ST alternans in ventricular fibrillation. *Circulation.* 1990;82:2185-2189.
38. Hayashi H, Shiferaw Y, Sato D, Nihei M, Lin SF, Chen PS, Garfinkel A, Weiss JN, Qu Z. Dynamic origin of spatially discordant alternans in cardiac tissue. *Biophys J.* 2007;92:448-460.
39. Mironov S, Jalife J, Tolkacheva EG. Role of conduction velocity restitution and short-term memory in the development of action potential duration alternans in isolated rabbit hearts. *Circulation.* 2008;118:17-25.

40. Qu Z, Garfinkel A, Chen PS, Weiss JN. Mechanisms of discordant alternans and induction of reentry in simulated cardiac tissue. *Circulation*. 2000;102:1664-1670.
41. Banville I, Gray RA. Effect of action potential duration and conduction velocity restitution and their spatial dispersion on alternans and the stability of arrhythmias. *J Cardiovasc Electrophysiol*. 2002;13:1141-1149.
42. Gaeta SA, Christini DJ. Non-linear dynamics of cardiac alternans: subcellular to tissue-level mechanisms of arrhythmia. *Front Physiol*. 2012;3:1-13.
43. Korhonen T, Hanninen SL, Tavi P. Model of excitation-contraction coupling of rat neonatal ventricular myocytes. *Biophys J*. 2009;96:1189-1209.
44. Hou L, Deo M, Furspan P, Pandit SV, Mironov S, Auerbach DS, Gong Q, Zhou Z, Berenfeld O, Jalife J. A major role for HERG in determining frequency of reentry in neonatal rat ventricular myocyte monolayer. *Circ Res*. 2010;107:1503-1511.
45. Askar SF, Bingen BO, Swildens J, Ypey DL, van der Laarse A, Atsma DE, Zeppenfeld K, Schalij MJ, de Vries AA, Pijnappels DA. Connexin43 silencing in myofibroblasts prevents arrhythmias in myocardial cultures: role of maximal diastolic potential. *Cardiovasc Res*. 2012;93:434-444.
46. de Diego C, Pai RK, Dave AS, Lynch A, Thu M, Chen F, Xie LH, Weiss JN, Valderrábano M. Spatially discordant alternans in cardiomyocyte monolayers. *Am J Physiol Heart Circ Physiol*. 2008;294:H1417-H1425.
47. Kjølbye AL, Dikshiteyn M, Eloff BC, Deschênes I, Rosenbaum DS. Maintenance of intercellular coupling by the antiarrhythmic peptide rotigaptide suppresses arrhythmogenic discordant alternans. *Am J Physiol Heart Circ Physiol*. 2008;294:H41-H49.
48. Burchfield JS, Xie M, Hill JA. Pathological ventricular remodelling mechanisms: part 1 of 2. *Circulation*. 2013;128:388-400.
49. Cutler MJ, Jeyaraj D, Rosenbaum DS. Cardiac electrical remodelling in health and disease. *Trends Pharmacol Sci*. 2011;32:174-180.
50. Girouard SD, Laurita KR, Rosenbaum DS. Unique properties of cardiac action potentials recorded with voltage-sensitive dyes. *J Cardiovasc Electrophysiol*. 1996;7:1024-1038.
51. Lou Q, Efimov IR. Enhanced susceptibility to alternans in a rabbit model of chronic myocardial infarction. *Conf Proc IEEE Eng Med Biol Soc*. 2009;2009:4527-4530.
52. Hsieh YC, Lin JC, Hung CY, Li CH, Lin SF, Yeh HI, Huang JL, Lo CP, Haugan K, Larsen BD, Wu TJ. Gap junction modifier rotigaptide decreases the susceptibility to ventricular arrhythmia by enhancing conduction velocity and suppressing discordant alternans during therapeutic hypothermia in isolated rabbit hearts. *Heart Rhythm*. 2016;13:251-261.
53. Woo SJ, Hong JH, Kim TY, Bae BW, Lee KJ. Spiral wave drift and complex-oscillatory spiral waves caused by heterogeneities in two-dimensional in vitro cardiac tissues. *New J Phys*. 2008;015005:10-18.
54. Kizana E, Ginn SL, Smyth CM, Boyd A, Thomas SP, Allen DG, Ross DL, Alexander IE. Fibroblasts modulate cardiomyocyte excitability: implications for cardiac gene therapy. *Gene Ther*. 2006;13:1611-1615.
55. Engelman ZJ, Trew ML, Smaill BH. Structural heterogeneity alone is a sufficient substrate for dynamic instability and altered restitution. *Circ Arrhythm Electrophysiol*. 2010;3:195-203.
56. Ziv O, Morales E, Song YK, Peng X, Odening KE, Buxton AE, Karma A, Koren G, Choi BR. Origin of complex behaviour of spatially discordant alternans in a transgenic rabbit model of type 2 long QT syndrome. *J Physiol*. 2008;587:4661-4680.
57. Gizzi A, Cherry EM, Gilmour RF Jr, Luther S, Filippi S, Fenton FH. Effects of pacing site and stimulation history on alternans dynamics and the development of complex spatiotemporal patterns in cardiac tissue. *Front Physiol*. 2013;4:71.1-71.12.
58. Jacquemet V. Pacemaker activity resulting from the coupling with nonexcitable cells. *Phys Rev E Stat Nonlin Soft Matter Phys*. 2006;74:011908.

59. Singh R, Xu J, Garnier NG, Pumir A, Sinha S. Self-organized transition to coherent activity in disordered media. *Phys Rev Lett*. 2012;108:068102.
60. Majumder R, Nayak AR, Pandit R. Nonequilibrium arrhythmic states and transitions in a mathematical model for diffuse fibrosis in human cardiac tissue. *PLoS One*. 2012;7:e45040.
61. Zhao X. Indeterminacy of spatiotemporal cardiac alternans. *Phys Rev E Stat Nonlin Soft Matter Phys*. 2008;78:011902.
62. Fox JJ, Riccio ML, Hua F, Bodenschatz E, Gilmour RF Jr. Spatiotemporal transition to conduction block in canine ventricle. *Circ Res*. 2002;90:289-296.
63. Ramshesh VK, Knisley SB. Use of light absorbers to alter optical interrogation with epi-illumination and transillumination in three-dimensional cardiac models. *J Biomed Opt*. 2006;11:24019-24012.
64. Panfilov AV, Holden AV. Computer simulation of re-entry sources in myocardium in two and three dimensions. *J Theor Biol*. 1993;161:271-285.
65. MacCannell KA, Bazzazi H, Chilton L, Shibukawa Y, Clark RB, Giles WR. A mathematical model of electrotonic interactions between ventricular myocytes and fibroblasts. *Biophys J*. 2007;92:4121-4132.
66. Henriquez AP, Vogel R, Muller-Borer BJ, Henriquez CS, Weingart R, Cascio WE. Influence of dynamic gap junction resistance on impulse propagation in ventricular myocardium: a computer simulation study. *Biophys J*. 2001;81:2112-2121.
67. Askar SF, Ramkisoensing AA, Schaliij MJ, Bingen BO, Swildens J, van der Laarse A, Atsma DE, de Vries AA, Ypey DL, Pijnappels DA. Antiproliferative treatment of myofibroblasts prevents arrhythmias in vitro by limiting myofibroblast-induced depolarization. *Cardiovasc Res*. 2011;90:295-304.
68. Bingen BO, Askar SF, Schaliij MJ, Kazbanov IV, Ypey DL, Panfilov AV, Pijnappels DA. Prolongation of minimal action potential duration in sustained fibrillation decreases complexity by transient destabilization. *Cardiovasc Res*. 2013;97:161-170.

Supporting information

Numerical methods

In our cardiomyocyte model, the Ca^{2+} core structure characteristic of the models by Korhonen *et al.*¹ and Hou *et al.*,² was replaced by a single chamber with a single Ca^{2+} component ($[\text{Ca}]_i$) that accounts for the cytosolic Ca^{2+} , the subsarcolemmal Ca^{2+} , the Ca^{2+} of the subsarcolemmal reticulum and the Ca^{2+} in between. For the study presented in this paper, cell contraction via excitation is neither a feature of interest, nor does it have, as we have checked, any significant influence on the qualitative results. Thus, this modification enabled us to increase the computational speed of the model while preserving the essential electrophysiological behavior of its predecessors.

Ca^{2+} related equations:

L-type Ca^{2+} current:

$$I_{\text{CaL}} = 4 G_{\text{CaL}} \text{dff}_{\text{Ca}} V \frac{F^2}{RT} \frac{\left(\text{Ca}_i e^{\left(\frac{2VF}{RT} \right)} - 0.341 \text{Ca}_o \right)}{e^{\left(\frac{2VF}{RT} \right)} - 1.0}, (1)$$

$$d_\infty = \frac{1.0}{1.0 + e^{\frac{-11.1 - V}{7.2}}}, (2)$$

$$\alpha_d = 0.25 + \frac{1.4}{1 + e^{\left(\frac{-(35+V)}{13} \right)}}, (3)$$

$$\beta_d = \frac{1.4}{1 + e^{\left(\frac{V+5.0}{5.0} \right)}}, (4)$$

$$\gamma_d = \frac{1.0}{1 + e^{\left(\frac{50.0 - V}{20} \right)}}, (5)$$

$$\tau_d = \alpha_d \beta_d + \gamma_d, (6)$$

$$\frac{dd}{dt} = \frac{d_{\infty} - d}{\tau_d}, (7)$$

$$f_{\infty} = \frac{1.0}{1.0 + e^{\left(\frac{23.3+V}{5.4}\right)}}, (8)$$

$$\tau_f = 1125 e^{\left(\frac{-|V+27.0|^2}{240}\right)} + \frac{165}{1 + e^{\left(\frac{25-V}{10}\right)}} + 120, (9)$$

$$\frac{df}{dt} = \frac{f_{\infty} - f}{\tau_f}, (10)$$

$$\alpha_{fCa} = \frac{1.0}{1 + \left(\frac{Ca_i}{0.325}\right)^8}, (11)$$

$$\beta_{fCa} = \frac{0.1}{1 + e^{\left(\frac{Ca_i - 0.5}{0.1}\right)}}, (12)$$

$$y_{fCa} = \frac{0.2}{1 + e^{\left(\frac{Ca_i - 0.75}{0.8}\right)}}, (13)$$

$$f_{Ca\infty} = \frac{\alpha_{fCa} + \beta_{fCa} + y_{fCa} + 0.23}{1.46}, (14)$$

$$\tau_{fCa} = 10 \text{ ms}, (15)$$

$$\frac{df_{Ca}}{dt} = k \frac{f_{Ca\infty} - f_{Ca}}{\tau_{fCa}}, (16)$$

where,

$$k = \begin{cases} 0 & f_{Ca\infty} > f_{Ca}, V > -60 \text{ mV} \\ 1 & \text{otherwise} \end{cases} (17)$$

Ca²⁺ fluxes:

$$J_{rel} = v_1 P_{o1} (Ca_{JSR} - Ca_i), (18)$$

$$J_{leak} = k_{leak} (Ca_{NSR} - Ca_i), (19)$$

$$J_{tr} = \frac{(Ca_{NSR} - Ca_{JSR})}{\tau_{tr}}, (20)$$

Ca²⁺ buffering:

$$\beta_{SR} = \frac{1.0}{1.0 + \frac{[CSQN]_{tot} K_{mCSQN}}{(Ca_{JSR} + K_{mCSQN})^2}}, (21)$$

Ryanodine receptor gating:

$$K_{mRyR} = \frac{3.51}{1.0 + e^{\frac{(Ca_{iSR} - 530.0)}{200.0}}} + 0.25, (22)$$

$$P_{C1} = 1 - P_{o1}, (23)$$

$$\frac{dP_{o1}}{dt} = k^+ \frac{Ca_{i^N}}{Ca_{i^N} + K_{mRyR}^N} P_{C1} - k^- P_{o1}, (24)$$

Sarcoplasmic/Endoplasmic Reticulum Ca²⁺ ATPase (SERCA):

$$J_{up} = \frac{V_{maxf} \left(\frac{Ca_i}{K_{mf}} \right)^{H_f} - V_{maxr} \left(\frac{Ca_{NSR}}{K_{mr}} \right)^{H_r}}{1.0 + \left(\frac{Ca_i}{K_{mf}} \right)^{H_f} + \left(\frac{Ca_{NSR}}{K_{mr}} \right)^{H_r}}, (25)$$

$$J_{CaSR} = J_{rel} - J_{up} + J_{leak}, (26)$$

$$J_{CaSL} = (2I_{NCX} - I_{CaL} - I_{CaT} - I_{Cab}) \frac{A_{cap} C_m}{2F \times 10^{-6}}, (27)$$

Ca²⁺ release and uptake:

$$\frac{dCa_{NSR}}{dt} = \frac{(J_{up} - J_{leak} - J_{tr})}{V_{NSR}}, (28)$$

$$\frac{dCa_{JSR}}{dt} = \beta_{SR} \frac{(-J_{rel} + J_{tr})}{V_{JSR}}, (29)$$

$$\beta_{Cai} = \frac{1.0}{1 + \frac{[TRPN]_{tot} K_{mTRPN}}{(Ca_i + K_{mTRPN})^2} + \frac{[CMDN]_{tot} K_{mCMDN}}{(Ca_i + K_{mCMDN})^2}}, (30)$$

$$\frac{dCa_i}{dt} = \beta_{Cai} \frac{(J_{CaSR} + J_{CaSL})}{V_{myo}}, (31)$$

All concentrations were measured in micromolar (μM) and all time constants in milliseconds (ms).

Simulation details:

A simulation domain containing 576 x 576 grid points was used with spatial resolution $\delta x = 0.003125$ cm and time step $\delta t = 0.002$ ms, 0.005 ms, 0.01 ms or 0.02 ms depending on the conduction velocities (CVs). The simulations were performed on a circular domain, with a diameter of 1.56 cm, in keeping with the diameter of a well from a 24-well cell culture plate.

Modeling myofibroblasts (MFBs):

The formulation for the myocyte-MFB coupling was as follows:

$$\frac{\partial V_m}{\partial t} = \frac{-I_{\text{ion}}}{C_m} + \text{Diff}_m, \quad (32),$$

$$\frac{\partial V_f}{\partial t} = \text{Diff}_f, \quad (33),$$

where V_m is the transmembrane voltage across myocytes, V_f is the transmembrane voltage across MFBs, Diff_m is the diffusion term for myocytes and Diff_f is the diffusion term for MFBs. The resting membrane potential of the MFBs was chosen to be -20 mV. The diffusion term for myocytes was computed (see Fig. S1a) as $\text{Diff}_m = \sum_{n=1}^4 a_n$. Here a_n is the term for electrical coupling to the n^{th} neighboring cell; ($n=1$ for the neighbor $(i-1, j)$, $n=2$ for the neighbor $(i+1, j)$, $n=3$ for the neighbor $(i, j-1)$, and $n=4$ for the neighbor $(i, j+1)$). Table I lists the values of a_n when the central cell was a myocyte and the n^{th} neighboring cell was a myocyte or an MFB.

Table I: Computing the diffusion term for Eq.32

a_n	neighbor: NRVM	neighbor: MFB
a_1	$\frac{D_{\text{mm}}}{(\delta x)^2} (V_m[i-1][j] - V_m[i][j])$	$\frac{G_{\text{gap}} C_f}{C_m} (V_f[i-1][j] - V_m[i][j])$
a_2	$\frac{D_{\text{mm}}}{(\delta x)^2} (V_m[i+1][j] - V_m[i][j])$	$\frac{G_{\text{gap}} C_f}{C_m} (V_f[i+1][j] - V_m[i][j])$
a_3	$\frac{D_{\text{mm}}}{(\delta x)^2} (V_m[i][j-1] - V_m[i][j])$	$\frac{G_{\text{gap}} C_f}{C_m} (V_f[i][j-1] - V_m[i][j])$
a_4	$\frac{D_{\text{mm}}}{(\delta x)^2} (V_m[i][j+1] - V_m[i][j])$	$\frac{G_{\text{gap}} C_f}{C_m} (V_f[i][j+1] - V_m[i][j])$

Similarly, when the central cell was an MFB, the diffusion term for Eq.33 was computed with a_n as listed in Table II.

Table II: Computing the diffusion term for Eq.33

a_n	neighbor: MFB	neighbor: NRVM
a_1	$\frac{D_{ff}}{(\delta x)^2} (V_f[i-1][j] - V_f[i][j])$	$G_{gap} (V_m[i-1][j] - V_f[i][j])$
a_2	$\frac{D_{ff}}{(\delta x)^2} (V_f[i+1][j] - V_f[i][j])$	$G_{gap} (V_m[i+1][j] - V_f[i][j])$
a_3	$\frac{D_{ff}}{(\delta x)^2} (V_f[i][j-1] - V_f[i][j])$	$G_{gap} (V_m[i][j-1] - V_f[i][j])$
a_4	$\frac{D_{ff}}{(\delta x)^2} (V_f[i][j+1] - V_f[i][j])$	$G_{gap} (V_m[i][j+1] - V_f[i][j])$

Modeling cellular variability:

To incorporate cellular variability, the following protocol was used: In our model, there are 10 ionic conductances, corresponding to the 10 major and minor ionic currents. A random number generator was used to generate 10 random numbers in the range 0.5-1.5, for each grid point location. Thus, if N be the number of grid points outside the circle of interest, $10 \times (576 \times 576 - N)$ random numbers were generated in the given range. At each grid point of the simulation domain, within the circle of interest, the 10 ionic conductances were multiplied with 10 of these random numbers. This heterogeneous configuration of the system was saved and used as initial condition for the actual simulations to follow. Thus in our simulations, the electrophysiological properties at every grid point location, were made different from each other, as in the in vitro situation, where cells display a natural heterogeneity in their ionic properties.

Experimental methods

Animal studies

All animal experiments were approved by the Animal Experiments Committee of Leiden University Medical Center and conformed to the Guide for the Care and Use of Laboratory Animals as stated by the United States National Institutes of Health.

Cell isolation and culture

Neonatal rat ventricular cardiomyocytes (NRVMs) were isolated as previously described.³ 2-Day old neonatal Wistar rat pups were anesthetized by inhalation of 5% isoflurane gas, after which adequate anesthesia was confirmed by the absence of reflexes. Hearts were rapidly excised, atria and annuli fibrosi cordis were removed, and the remaining ventricles were finely minced and dissociated with collagenase type 1 (450 U/mL; Worthington, Lakewood, NJ) and DNase I (18.75 Kunitz/mL; Sigma-Aldrich, St. Louis, MO). The cell suspension was transferred to Primaria cell culture dishes (Becton Dickinson, Breda, the Netherlands), which were incubated for 75 minutes at 37°C and 5% CO₂ to allow for preferential attachment of non-myocytes (predominantly cardiac fibroblasts [CFBs]). Unattached cardiac cells (mainly NRVMs) were collected and passed through a cell strainer (70- μ m mesh pore size; BD Biosciences, Breda, the Netherlands) to obtain a single cell suspension. The attached cells (mainly CFBs) were cultured for one week before establishing co-cultures of these cells, which by this time had obtained characteristics of MFBs,⁴ with freshly isolated NRVMs (*i.e.*, NRVMs from a subsequent round of isolation). To establish co-cultures, the MFBs were dissociated with 0.05% trypsin/EDTA (Life Technologies Europe, Bleiswijk, the Netherlands) and subsequently passed through a 70- μ m mesh pore size cell strainer. Single cell counting for both NRVM and MFB suspensions was performed using a BD Accuri C6 flow cytometer (BD Biosciences). NRVM and MF suspensions were mixed in ratios to obtain a 70% NRVMs and 30% MFBs and the resulting mixtures were seeded in 24-well cell culture plates (Corning Life Sciences, Amsterdam, the Netherlands) onto bovine fibronectin (Sigma-Aldrich)-coated round glass coverslips (15 mm diameter). Plating density was $1-7 \times 10^5$ cells/well, depending on the assay. After 24 hours, cells were incubated with mitomycin-C (10 μ g/mL; Sigma-Aldrich) for 2 hours to inhibit cell proliferation, as described previously.⁴ Culture medium consisted of Dulbecco's modified Eagle's medium (DMEM)/Ham's F10 medium (1:1, v/v; Life Technologies Europe) supplemented with 5% horse serum (Life Technologies Europe), 2% bovine serum albumin (BSA) and sodium ascorbate to a final concentration of 0.4 mM and was refreshed daily.

Construction of self-inactivating lentiviral vector (SIN-LV) shuttle plasmids

Selective knock-down of rat connexin43 (Cx43) expression was accomplished by RNA interference using SIN-LVs encoding rat Gja1 (rGja1) gene-specific short hairpin (sh) RNAs. To this end, the 1.9-kb SphIxEcoRI fragments of SIN-LV shuttle plasmid clones TRCN0000348381 and TRCN0000068474 from the MISSION shRNA library (Sigma-Aldrich) were ligated to the 5.7-kb SphIxEcoRI fragment of pLKO.1-PpLuc-shRNA.hEEF1A1.eGFP⁵ to generate pLKO.1-rGja1-shRNA348381.hEEF1A1.eGFP and pLKO.1-rGja1-shRNA068474.hEEF1A1.eGFP, respectively. pLKO.1-PpLuc-shRNA.hEEF1A1.eGFP, pLKO.1-rGja1-shRNA348381.hEEF1A1.eGFP and pLKO.1-rGja1-shRNA068474.hEEF1A1.eGFP were subsequently used to generate particles of the SIN-

LVs LV-Ppluc_↓, LV-Cx43_↓ (occasionally also named LV.Cx43_↓) and LV-Cx43_{2↓}, respectively. The correctness of the SIN-LV shuttle plasmids was verified by restriction mapping using 5 different enzymes and by partial nucleotide sequence analysis using the Quick Shot sequencing services of BaseClear (Leiden, the Netherlands) and the human *RNU6-1* gene-specific primer 5' GACTATCATATGCTTACCGT 3'. Restriction endonucleases and other DNA modifying enzymes were obtained from Thermo Fisher Scientific (Landsmeer, the Netherlands) or New England Biolabs (Bioké, Leiden, the Netherlands). For large-scale purification of the SIN-LV shuttle and packaging plasmids the JETSTAR 2.0 Plasmid Maxiprep kit (Genomed, Löhne, Germany) was used following the instructions of the manufacturer.

SIN-LV production and transduction

LV-Cx43_{1↓}, LV-Cx43_{2↓} and LV-PpLuc_↓ particles were produced in 293T cells from SIN-LV shuttle plasmids pLKO.1-rGja1-shRNA348381.hEEF1A1.eGFP, pLKO.1-rGja1-shRNA068474.hEEF1A1.eGFP and pLKO.1-PpLuc-shRNA.hEEF1A1.eGFP, respectively, as described previously.⁵ SIN-LV particles were concentrated by ultracentrifugation and subsequently suspended in phosphate-buffered saline (PBS) containing 1% BSA fraction V (Sigma-Aldrich). SIN-LV suspensions were stored in 100 µL portions at -80°C until use. Four days after culture initiation, cells were transduced by adding different volumes of SIN-LV suspension directly to culture medium. At 24 hours after vector addition, the inoculum was removed, the monolayers were washed 3 times with culture medium and kept in fresh culture medium until structural or functional analysis at day 9 of culture. Transduction efficiency was determined by assessment of enhanced green fluorescent protein (eGFP) fluorescence with an Axiovert 200M inverse fluorescence microscope (Carl Zeiss, Sliedrecht, the Netherlands). SIN-LVs were applied in a dose range that resulted in transduction of nearly 100% of cells at the lowest vector dose and did not cause microscopic signs of cytotoxicity at the highest vector dose.

Immunocytology

Cells were washed with PBS before fixing with PBS/4% formaldehyde (Merck, Amsterdam, the Netherlands) for 15 minutes at room temperature (RT) followed by 3 washes with PBS. For transduction efficiency assessment, cells immediately underwent nuclear counterstaining by incubation with 10 µg/mL Hoechst 33342 (Life Technologies Europe) for 10 minutes at RT. Coverslips were mounted in Vectashield mounting medium (Vector Laboratories, Burlingame, CA). For all other experiments, cells were permeabilized by incubation with PBS/0.05% Triton-X100 (Sigma-Aldrich) for 10 minutes at RT. After 3 washes with PBS/0.1% Tween-20, samples were incubated with primary antibodies diluted in PBS/1% donkey serum (DS)/1% BSA. Antibodies against the following antigens were used: sarcomeric α -actinin (Actn2 gene product) to detect NRVMs (1:200; mouse IgG1, clone EA-53; Sigma-Aldrich), collagen type I (Col1a1 gene

product) to identify fibroblastic cell types (1:200; rabbit IgG, polyclonal; Abcam, Cambridge, United Kingdom), CD31 (Pecam1 gene product) to identify endothelial cells (1:200; rat IgG2a, clone MEC 13.3; BD Biosciences), smooth muscle myosin heavy chain (Myh11 gene product) to detect smooth muscle cells (1:200; mouse IgG1, clone hSM-V; Sigma-Aldrich), and the gap junctional protein Cx43 (Gja1 gene product; 1:200; rabbit IgG, polyclonal; Sigma-Aldrich). After washing 3 times for 5 minutes with PBS/0.1% Tween-20, cells were incubated with appropriate Alexa Fluor 488/568-conjugated secondary antibodies (1:500; Life Technologies Europe) or, for detecting CD31, with biotinylated rabbit-anti rat IgG secondary antibodies (1:200; Vector Laboratories) and Alexa Fluor 488 streptavidin conjugates (1:200; Life Technologies). Nuclear counterstaining and mounting of the coverslips in Vectashield were performed as described before. Images were acquired with a Leica TCS SP8 confocal laser scanning microscope (Leica, Solms, Germany). Storage and quantification of immunofluorescence signals was done using dedicated software (Leica Application Suite [Leica], NIS Elements [Nikon Instruments Europe] and Fiji [www.fiji.sc]). Each experiment was performed on at least 3 independent cultures.

Reverse transcription-quantitative polymerase chain reaction (RT-qPCR) analysis

Dedicated cell cultures were used for RT-qPCR experiments, which were performed essentially as described previously.⁶ In brief, cells were lysed using TRIzol reagent (Life Technologies Europe) and total RNA was isolated with the RNeasy Mini kit (Qiagen, Venlo, the Netherlands). Reverse transcription was performed with the iScript cDNA synthesis kit (Bio-Rad Laboratories, Veenendaal, the Netherlands). cDNA amplification was carried out with the Biorline SensiFAST SYBR No-ROX kit (GC biotech, Alphen aan den Rijn, the Netherlands), using the following oligonucleotides: 5' GGGATAAGGGAGGTACACA 3' (rGja1 forward primer) and 5' CACTCAATTCATGTACACAGACT 3' (rGja1 reverse primer). For normalization purposes, rat 18S rRNA (Rn18s)-specific cDNA was amplified in parallel using the following primers: 5' GTAACCCGTTGAACCCCAT 3' (18S rRNA forward primer) and 5' CCATCCAATCGGTAGTAGCG 3' (18S rRNA reverse primer). PCR amplifications were performed using a CFX96 Touch Real-Time PCR detection system (Bio-Rad Laboratories). For data analysis, dedicated software was used for data storage and analysis (CFX Manager Software version 3.1 [Bio-Rad Laboratories]).

Western blotting

Western blotting was performed as previously described.⁷ Cells were washed 3 times with ice-cold PBS and lysed in 150 mM NaCl, 1% Triton X-100, 0.5% sodium deoxycholate, 0.1% sodium dodecyl sulfate, 50 mM Tris-HCl (pH 8.0) supplemented with protease inhibitors (cComplete, Mini Protease Inhibitor Cocktail Tablet; Roche Applied Science, Penzberg, Germany). After centrifugation for 15 minutes at 21,130×g and 4°C, the supernatant was collected, passed 3 times through a sterile syringe with 29G needle (BD Biosciences), aliquoted and stored

at -80°C until assay. Protein concentration was determined using the BCA protein assay kit (Thermo Fisher Scientific). Proteins were size-fractionated in Novex Bolt 8% Bis-Tris Plus gels (Life Technologies Europe) and transferred to Amersham Hybond-N⁺ polyvinylidene difluoride membranes (GE Healthcare, Diegem, Belgium) by wet electroblotting using a Bolt Mini blot module (Life Technologies Europe). After blocking for 1 hour in 2% ECL Prime blocking agent (GE healthcare) dissolved in Tris-based saline/0.1% Tween-20 (TBST), membranes were incubated for 1 hour with primary antibodies directed against Cx43 (1:100,000; rabbit IgG, polyclonal; Sigma-Aldrich) or lamin A/C (Lmna gene product; 1:5,000; rabbit IgG, polyclonal; Santa Cruz Biotechnology, Dallas, TX) as an internal control. All antibodies were diluted in TBST/2% ECL Prime blocking agent. After 3 times washing with TBST, blots were incubated with corresponding horseradish peroxidase-conjugated secondary antibodies (1:25,000; donkey-anti-rabbit IgG-HRP; Santa Cruz Biotechnology) for 1 hour at RT. After 3 wash steps with TBST, membranes were immersed in SuperSignal West Femto maximum sensitivity substrate (Thermo Fisher Scientific). Chemiluminescence was measured with the ChemiDoc Touch imaging system (Bio-Rad Laboratories), whose software was used for data storage and quantitative analysis.

Optical voltage mapping

Assessment of the effects of Cx43 knockdown on cardiac electrical impulse generation and propagation in monolayers was done by optical mapping on day 9 of culture. Cells were loaded with the potentiometric dye di-4-ANEPPS (8 μM final dye concentration; Life Technologies) in serum-free and phenol red-less DMEM/Ham's F12 medium (1:1, v/v; Life Technologies) by incubation for 15 minutes at 37°C in a humidified incubator (95% air/5% CO₂). Optical mapping experiments were performed in fresh unsupplemented DMEM/Ham's F12 medium at 37°C, using a MiCAM ULTIMA-L imaging system (SciMedia, Costa Mesa, CA). Cells were stimulated electrically with an epoxy-coated bipolar platinum electrode with square 10- ms, 8-V suprathreshold electrical stimuli using a STG 2004 stimulus generator and MC Stimulus II software (both from Multichannel Systems, Reutlingen, Germany). Optical signals were recorded at a 6-ms frame rate and analyzed using BrainVision Analyzer 13.12.20 software (Brainvision, Tokyo, Japan), after spatial and temporal filtering. Cultures were stimulated at pacing frequencies of 0.5, 1, 2, 3, 4 and 5 Hz, and assessed for CV, CV dispersion, action potential duration (APD) at 80% of full repolarization (APD₈₀) and APD₈₀ dispersion of repolarization. Fibrillation was induced by burst pacing at cycle lengths of 70-350 ms. Wavelength was calculated by multiplying average CV with APD₈₀ (for paced propagation) or with reentrant cycle length. Complexity was determined by quantifying phase singularities (PSs) per culture. Phase maps were constructed with dedicated software using the phase space method, as described previously.⁸

Statistical analysis

Statistical analyses were performed using GraphPad Prism software version 6 (Graphpad Software, La Jolla, CA). Unpaired Student's t test, Fisher's exact test and the one-way ANOVA test were used for comparing different experimental groups. Data were expressed as mean±standard error of mean (SEM) for a specified number (N) of observations. Results were considered statistically significant at p values<0.05. Statistical significance was expressed as follows: *: $P<0.05$, **: $P<0.001$ and NS: not significant.

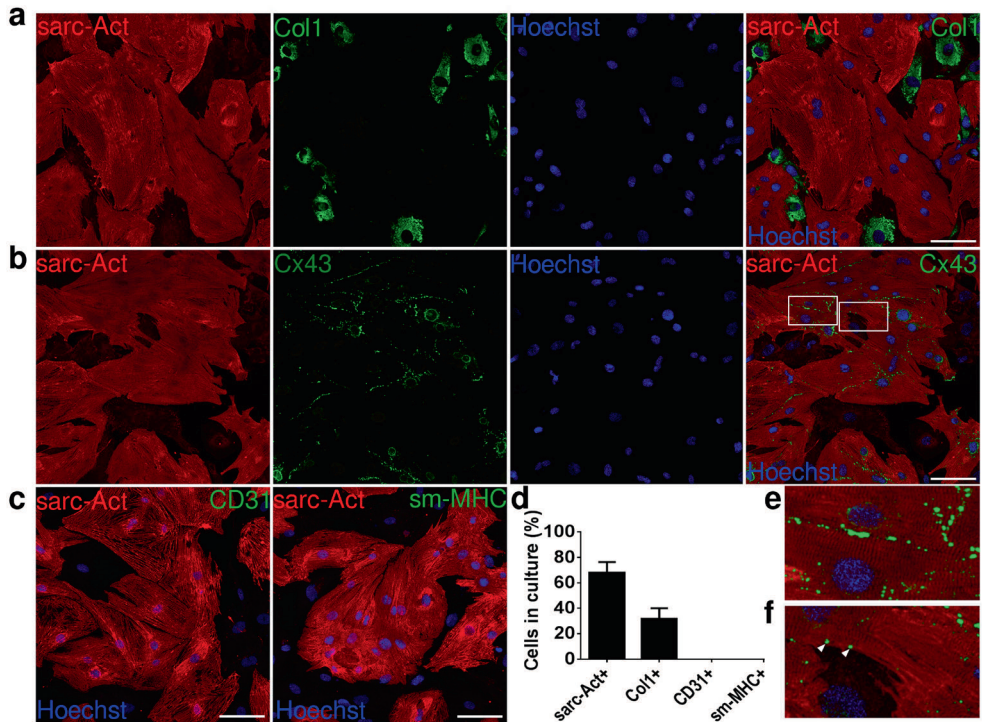


Figure S1. Immunocytochemical characterization of the *in vitro* model. **A**, Confocal microscopy images of immunocytochemical staining for sarcomeric alpha actinin (sarc-Act; red) and collagen type I (Col1; green) combined with Hoechst 33342 (nuclei, blue) show that the co-cultures contain ~70% sarc-Act⁺ cells (*i.e.*, NRVMs) and ~30% fibroblastic cells (*i.e.*, Col1⁺ cells). **B**, Confocal microscopy images of immunocytochemical staining for sarc-Act (red), Cx43 (green) combined with Hoechst 33342 (nuclei, blue) demonstrate the presence of Cx43 at cell-cell junctions, especially those between NRVMs. **C**, Confocal microscopy images of immunocytochemical staining for sarc-Act (red), CD31 (left panel; green) or smooth muscle myosin heavy chain (sm-MHC; right panel; green) combined with Hoechst 33342 (nuclei, blue) show the absence of endothelial cells (*i.e.*, CD31⁺ cells) and smooth muscle cells (sm-MHC⁺ cells). **D**, Quantification of immunological data. **E,F** High magnification images of the white boxes in subfigure B, showing Cx43 (**E**) between 2 NRVMs, and (**F**) between an NRVM and a MFB. White scale bars represent 100 μ m.

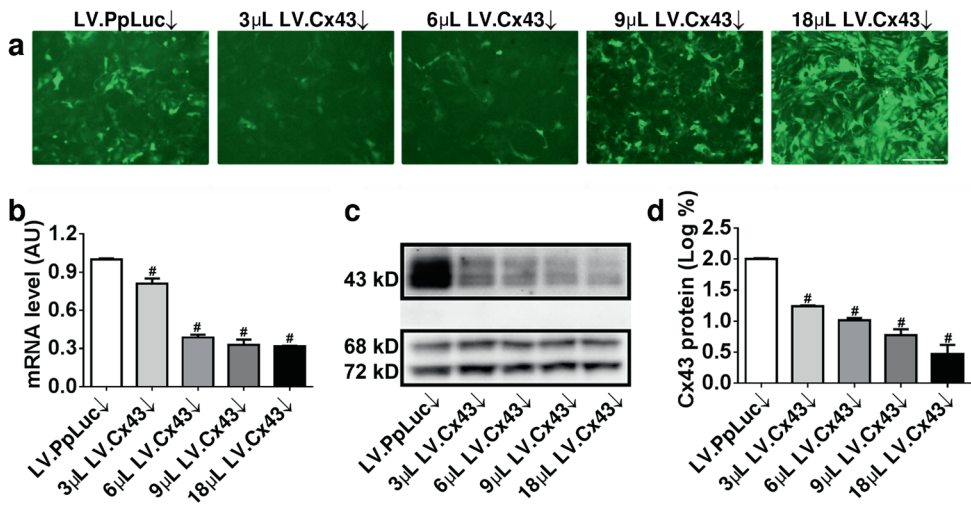


Figure S2. Effect of LV.Cx43↓ dose on Cx43 levels. **A**, Fluorographs of NRVM-MFB co-cultures transduced with different doses of LV.Cx43↓ or a single dose of the control vector LV.PpLuc↓. Increasing vector doses result in an increase of eGFP signal intensity. **B**, Relationship between vector dose and rGja1 mRNA level as measured by RT-qPCR in fibrotic NRVM cultures exposed to different amounts of LV.Cx43↓. **C**, Relationship between vector dose and Cx43 protein (43 kDa) level as determined by western blotting using lamin A/C as internal control (68 and 72 kDa protein species). **D**, Quantification of western blot data. #: $P < 0.001$. White scale bar represents 100 μm.

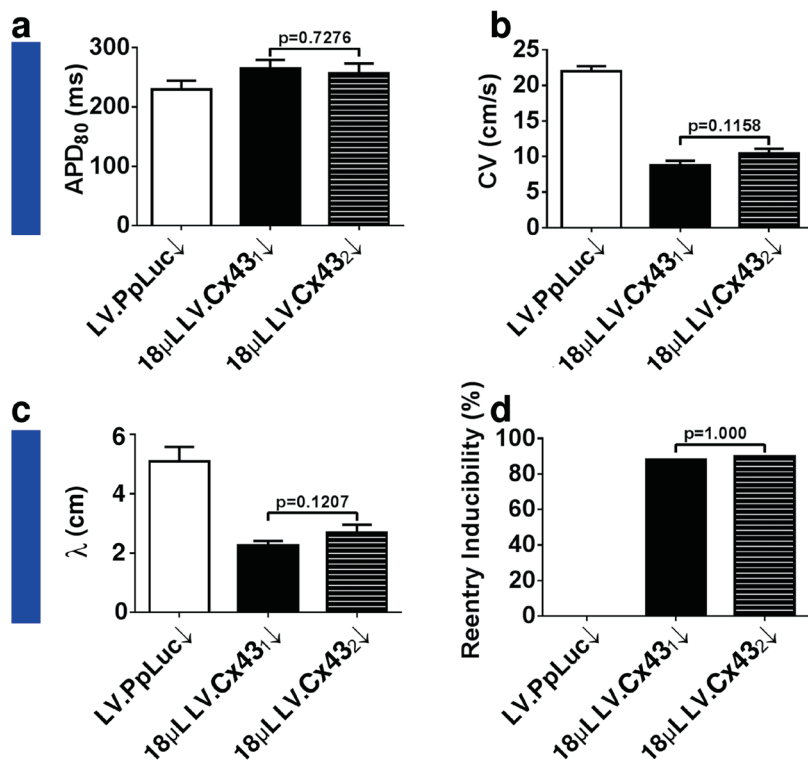


Figure S3. Comparison of the electrophysiological effects of SIN-LVs coding for two different rGja1-specific shRNAs. Transduction of fibrotic NRVM cultures with equal volumes of LV.Cx43₁↓ or LV.Cx43₂↓ did not result in significant differences in (A) APD₈₀, (B) CV, (C) wavelength (λ) and (D) reentry inducibility upon rapid pacing. However, CV and λ were considerably smaller and reentry inducibility was much larger than in LV.PpLuc↓-transduced NRVM-MFB co-cultures.

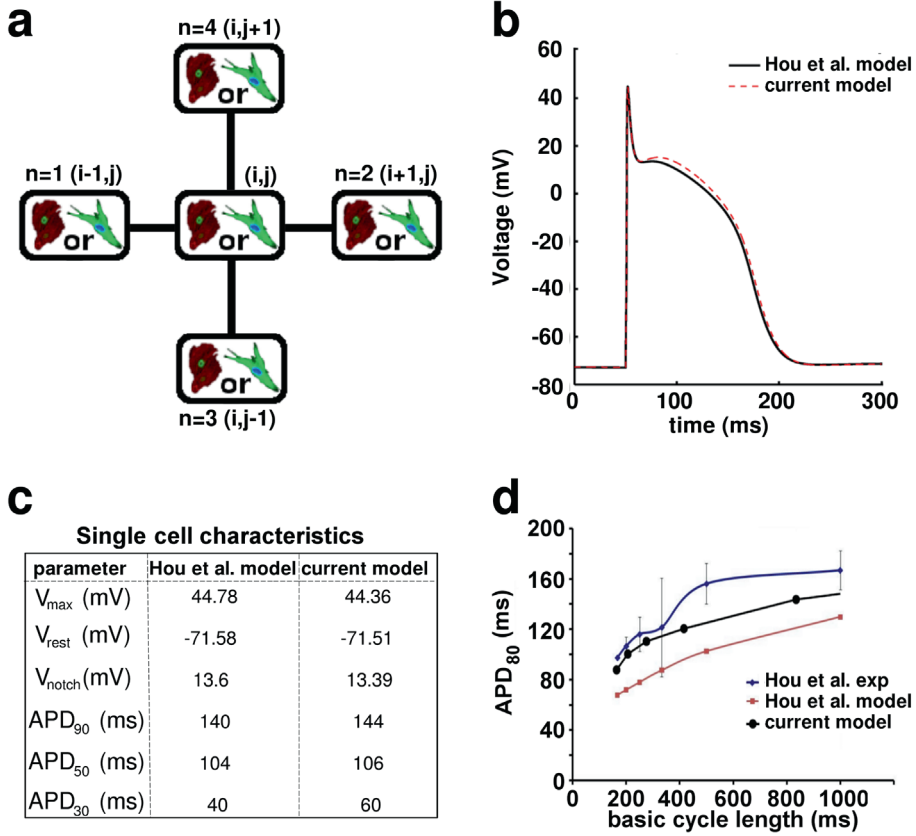


Figure S4. Mathematical model of NRVM. **A**, The connectivity of cells in the mathematical monolayer was modeled as a 5-point stencil, with each cell site being occupied by either a cardiomyocyte or a MFB, but not both. The central cell is labeled with index (i,j) ; neighboring cells are indexed as shown in the figure. **B**, Comparison of the action potential morphology and **(C)** action potential characteristics in the present model and in the model by Hou *et al.*² **D**, APD_{80} restitution curve of present model, compared with the *in silico* (model) and *in vitro* (exp) results obtained by Hou *et al.*²

References

1. Korhonen T, Hanninen SL, Tavi P. Model of excitation-contraction coupling of rat neonatal ventricular myocytes. *Biophys J*. 2009;96:1189-1209.
2. Hou L, Deo M, Furspan P, Pandit SV, Mironov S, Auerbach DS, Gong Q, Zhou Z, Berenfeld O, Jalife J. A major role for HERG in determining frequency of reentry in neonatal rat ventricular myocyte monolayer. *Circ Res*. 2010;107:1503-1511.
3. Askar SF, Ramkisoensing AA, Atsma DE, Schalij MJ, de Vries AA, Pijnappels DA. Engraftment patterns of human adult mesenchymal stem cells expose electrotonic and paracrine proarrhythmic mechanisms in myocardial cell cultures. *Circ Arrhythm Electrophysiol*. 2013;6:380-391.
4. Askar SF, Ramkisoensing AA, Schalij MJ, Bingen BO, Swildens J, van der Laarse A, Atsma DE, de Vries AA, Ypey DL, Pijnappels DA. Antiproliferative treatment of myofibroblasts prevents arrhythmias in vitro by limiting myofibroblast-induced depolarization. *Cardiovasc Res*. 2011;90:295-304.
5. Bingen BO, Neshati Z, Askar SF, Kazbanov IV, Ypey DL, Panfilov AV, Schalij MJ, de Vries AA, Pijnappels DA. Atrium-specific Kir3.x determines inducibility, dynamics, and termination of fibrillation by regulating restitution-driven alternans. *Circulation*. 2013;128:2732-2744.
6. Engels MC, Rajarajan K, Feistritz R, Sharma A, Nielsen UB, Schalij MJ, de Vries AA, Pijnappels DA, Wu SM. Insulin-like growth factor promotes cardiac lineage induction in vitro by selective expansion of early mesoderm. *Stem Cells*. 2014;32:1493-1502.
7. Engels MC, Askar SF, Jangsangthong W, Bingen BO, Feola I, Liu J, Majumder R, Versteegh MI, Braun J, Klautz RJ, Ypey DL, De Vries AA, Pijnappels DA. Forced fusion of human ventricular scar cells with cardiomyocytes suppresses arrhythmogenicity in a co-culture model. *Cardiovasc Res*. 2015;107:601-612.
8. Bingen BO, Askar SF, Schalij MJ, Kazbanov IV, Ypey DL, Panfilov AV, Pijnappels DA. Prolongation of minimal action potential duration in sustained fibrillation decreases complexity by transient destabilization. *Cardiovasc Res*. 2013;97:161-170.

CHAPTER 6

Light-induced termination of spiral wave arrhythmias by optogenetic engineering of atrial cardiomyocytes

Brian O. Bingen, MD^{1,†}; Marc C. Engels, MD^{1,†}; Martin J. Schalij, MD, PhD¹;
Wanchana Jangsangthong, PhD¹; Zeinab Neshati, MSc¹; Iolanda Feola, MSc¹;
Dirk L. Ypey, PhD¹; Saïd F.A. Askar, PhD¹; Alexander V. Panfilov, PhD²;
Daniël A. Pijnappels, PhD^{1,†}; Antoine A.F. de Vries, PhD^{1,†}

[†]These authors contributed equally to this work.

¹Laboratory of Experimental Cardiology, Department of Cardiology, Heart Lung Center Leiden, Leiden University Medical Center, Leiden, the Netherlands.

²Department of Physics and Astronomy, Ghent University, Ghent, Belgium.

Adapted from: Cardiovascular Research. 2014;104:194-205.

Abstract

Aims Atrial fibrillation (AF) is the most common cardiac arrhythmia and often involves reentrant electrical activation (e.g. spiral waves). Drug therapy for AF can have serious side effects including proarrhythmia, while electrical shock therapy is associated with discomfort and tissue damage. Hypothetically, forced expression and subsequent activation of light-gated cation channels in cardiomyocytes might deliver a depolarizing force sufficient for defibrillation, thereby circumventing the aforementioned drawbacks. We therefore investigated the feasibility of light-induced spiral wave termination through cardiac optogenetics.

Methods and results Neonatal rat atrial cardiomyocyte monolayers were transduced with lentiviral vectors encoding light-activated Ca^{2+} -translocating channelrhodopsin (CatCh; LV.CatCh~eYFP \uparrow) or eYFP (LV.eYFP \uparrow) as control, and burst-paced to induce spiral waves rotating around functional cores. Effects of CatCh activation on reentry were investigated by optical and multi-electrode array (MEA) mapping. Western blot analyses and immunocytology confirmed transgene expression. Brief blue light pulses (10 ms/470 nm) triggered action potentials only in LV.CatCh~eYFP \uparrow -transduced cultures, confirming functional CatCh-mediated current. Prolonged light pulses (500 ms) resulted in reentry termination in 100% of LV.CatCh~eYFP \uparrow -transduced cultures ($n = 31$) vs. 0% of LV.eYFP \uparrow -transduced cultures ($n = 11$). Here, CatCh activation caused uniform depolarization, thereby decreasing overall excitability (MEA peak-to-peak amplitude decreased 251.3 ± 217.1 vs. 9.2 ± 9.5 μV in controls). Consequently, functional core size increased and phase singularities (PSs) drifted, leading to reentry termination by PS–PS or PS–boundary collisions.

Conclusion This study shows that spiral waves in atrial cardiomyocyte monolayers can be terminated effectively by a light-induced depolarizing current, produced by the arrhythmogenic substrate itself, upon optogenetic engineering. These results provide proof-of-concept for shockless defibrillation.

Introduction

Atrial fibrillation (AF) is the most common cardiac rhythm disorder in clinical practice, substantially contributing to morbidity and mortality, especially in the elderly.¹ Yet, knowledge about its underlying mechanisms remains far from complete, although reentrant conduction is widely accepted to play a prominent role in AF. Still, current treatment of AF is suboptimal.¹⁻³ To convert AF to normal cardiac rhythm, drug treatment and/or electrical cardioversion are being employed. Drug treatment is rather ineffective and may have dangerous side effects such as the occurrence of ventricular arrhythmias, while electrical cardioversion is associated with tissue damage and serious discomfort. This makes the use of external or implantable cardioverter/defibrillator devices in AF treatment undesirable, as most patients would require multiple shocks per day causing electrical cardioversion to serve as a last resort treatment modality only.⁴ Hence, a search for an effective, but less painful and shockless method of cardioversion is warranted.

Electrical cardioversion relies on synchronous depolarization of large areas of the atrial myocardium, in order to terminate the reentrant conduction underlying fibrillation.⁵ In theory, shockfree cardioversion might be elicited by genetically modifying the atrial cardiomyocytes to express depolarizing cation channels that are activated through other means than electroshock, granted that the endogenous electrochemical gradients provide sufficient depolarizing force. Recently, optogenetics has been introduced as a method combining genetic engineering with light stimulation to control, with very high spatial and temporal resolution, specific cellular properties,⁶ including the membrane potential of excitable cells.⁷⁻⁹ To this end, light-gated ion channels from the microbial opsin family are expressed in target cells like cardiomyocytes or neurons, and subsequently activated by light of defined wavelengths to generate a controllable ion current. This strategy has previously been proved to be effective for light-induced pacing of ventricular cardiomyocytes following the forced expression of depolarizing light-gated channels in these cells.⁸ Hence, optogenetics might provide a feasible combination of cation channels and mode of activation to achieve shock-free cardioversion. Still, it is unknown whether optogenetic engineering of atrial cardiomyocytes (aCMCs) allows for light-induced termination of fibrillation maintained by reentrant spiral waves.

Therefore, we investigated whether by optogenetic modification of aCMCs, a depolarizing photocurrent (i.e. an ion current elicited by light) could be generated sufficiently strong to terminate reentrant conduction in monolayer cultures of these cells. To this purpose, we employed Ca^{2+} -translocating channelrhodopsin (CatCh),¹⁰ an ultra-sensitive light-gated cation channel, and a blue (470 nm) light-emitting diode (LED)-based light source for its activation. The effects of CatCh activation on reentrant conduction were investigated by voltage-sensitive dye and multi-electrode array (MEA) mapping in a 2D monolayer model of spiral wave reentry using neonatal rat aCMCs.¹¹

Methods

Animal studies

All animal experiments were approved by the Animal Experiments Committee of the Leiden University Medical Center and conformed to the Guide for the Care and Use of Laboratory Animals as stated by the US National Institutes of Health.

Cell isolation and culture

Neonatal rat aCMCs were isolated as described previously.¹¹ Briefly, 2-day-old Wistar rats were anaesthetized by 5% isoflurane inhalation and adequate anaesthesia was confirmed by the absence of reflexes. Hearts were rapidly excised and atria were carefully separated from the ventricles. Next, atrial tissue was minced and dissociated with collagenase type 1 (450 U/mL; Worthington, Lakewood, NJ, USA) and DNase I (18.75 Kunitz/mL; Sigma-Aldrich, St Louis, MO, USA) and pre-plated on Primaria-coated cell-culture dishes (Becton Dickinson, Breda, the Netherlands) for 120 min to allow selective attachment of non-myocytes (mainly cardiac fibroblasts). Unattached cells (mainly aCMCs) were seeded in 24-well cell-culture plates (Corning Life Sciences, Amsterdam, the Netherlands) containing fibronectin (Sigma-Aldrich)-coated, round glass coverslips (15 mm diameter). Cell densities of $0.5\text{--}8 \times 10^5$ cells/well were used depending on the assay. At Day 1 of culture, cells were incubated with Mitomycin-C (10 $\mu\text{g/mL}$; Sigma-Aldrich) for 2 h, as described previously.¹² The culture medium, which consisted of Dulbecco's modified Eagle's medium/HAM's F10 (1: 1, v/v; Life Technologies, Bleiswijk, the Netherlands) supplemented with 5% horse serum (Life Technologies), was refreshed daily and cells were cultured in a humidified incubator at 37°C and 5% CO₂.

Construction of self-inactivating lentiviral vector shuttle plasmids

The CatCh-encoding self-inactivating lentiviral vector (SIN-LV) shuttle plasmid pLV-CaMKIIa-hChr2(L132C)-eYFP.WPRE was kindly provided by the Stanford Optogenetics Resource Center (<http://www.stanford.edu/group/dlab/optogenetics>). To allow generation of SIN-LVs directing high-level *CatCh* expression in aCMCs, the murine *calcium/calmodulin-dependent protein kinase II alpha* promoter in pLV-CaMKIIa-hChr2(L132C)-eYFP.WPRE was replaced by a polymerase chain reaction (PCR) fragment encoding the striated muscle-specific MHCK7 promoter.¹³ The MHCK7 promoter was amplified with VELOCITY DNA polymerase (GC Biotech, Alphen aan den Rijn, the Netherlands) from a derivative of plasmid LV. Δ PRE.pA+.MHCK7. Luc¹⁴ using deoxyribonucleotides A117 (5' CCTTAATTAACCCCTTCAGATTAATAACTGA 3') and A118 (5' TTACCGGTGCTGGCTGGCTCTGA 3'; Sigma-Aldrich) as forward and reverse primer, respectively. Subcloning was done using the restriction enzymes PacI and AgeI-HF (both from New England Biolabs, Ipswich, MA, USA), recognition sequences of which were

introduced at both ends of the MHCK7 promoter fragment by the PCR procedure. This yielded the SIN-LV shuttle plasmid pLV.MHCK7.CatCh~eYFP.WHVPRE. For making a negative control vector, pLV.MHCK7.CatCh~eYFP.WHVPRE was incubated with AgeI-HF and BoxI (Thermo Fisher Scientific, Waltham, MA, USA), treated with Klenow polymerase (Thermo Fisher Scientific) and the resulting 10.0 kb DNA fragment was self-ligated yielding pLV.MHCK7.eYFP.WHVPRE. The correctness of the SIN-LV shuttle constructs was verified by restriction mapping with five different enzymes and by partial nucleotide sequence analysis using the Quick Shot sequencing services of BaseClear (Leiden, the Netherlands). For large-scale purification of the SIN-LV shuttle and packaging plasmids, the JETSTAR 2.0 Plasmid Maxiprep kit (Genomed, Löhne, Germany) was used following the instructions of the manufacturer.

SIN-LV production

LV.CatCh~eYFP \uparrow and LV.eYFP \uparrow particles were produced from the SIN-LV shuttle plasmids pLV.MHCK7.CatCh~eYFP.WHVPRE and pLV.MHCK7.eYFP.WHVPRE, respectively, using a previously described method.¹¹ The concentrated vector suspensions were aliquoted in 100 μ L portions and stored at -80°C until use. aCMCs were transduced at Day 4 of culture by adding vector suspension directly to the culture medium. After 18 h, cells were washed once with phosphate-buffered saline (PBS) and given fresh culture medium. The SIN-LVs were applied at doses that resulted in the transduction of essentially all aCMCs. Transduction level was assessed by enhanced yellow fluorescent protein (eYFP) visualization with an Axiovert 200 M inverse fluorescence microscope (Carl Zeiss, Sliedrecht, the Netherlands).

Immunocytology

Cultures were stained with antibodies directed against α -actinin (mouse IgG1, clone EA-53; Sigma-Aldrich), collagen type 1 (rabbit IgG; Abcam, Cambridge, MA, USA, ab292), connexin 43 (Cx43; rabbit Ig; Sigma-Aldrich, C6219), and atrial myosin light chain 2 (MLC2a; a gift from Dr. S.W. Kubalak, Charleston, SC, USA)¹⁵ after fixation in PBS/4% formaldehyde and permeabilization with PBS/0.1% Triton X-100. Incubation with primary antibodies [1: 200 dilution in PBS/5% foetal bovine serum (FBS; Life Technologies)] and corresponding Alexa Fluor 488/568-conjugated secondary antibodies (Life Technologies; 1:400 dilution in PBS/5% FBS) was done at 4°C . Nuclear counterstaining was performed at room temperature with 10 $\mu\text{g}/\text{mL}$ Hoechst 33342 (Life Technologies) in PBS/5% FBS. Coverslips were mounted in Vectashield mounting medium (Vector Laboratories, Burlingame, CA, USA). Images were acquired with a digital colour camera-equipped fluorescence microscope (Nikon Eclipse 80i; Nikon Instruments Europe, Amstelveen, the Netherlands). Storage and quantification of immunofluorescence signals was done using dedicated software [NIS Elements (Nikon Instruments Europe) and ImageJ (version 1.43; National Institutes of Health, Bethesda, MD, USA)]. Each immunostaining was performed on ≥ 3 independent aCMC cultures.

Western blotting

Cells were lysed in RIPA buffer [50 mM Tris-HCl (pH 8.0), 150 mM NaCl, 1% Triton X-100, 0.5% sodium deoxycholate, 0.1% sodium dodecyl sulfate supplemented with protease inhibitors (cOmplete, Mini Protease Inhibitor Cocktail Tablet; Roche Applied Science, Penzberg, Germany)]. Protein concentration was determined with the BCA Protein Assay Reagent (Thermo Fisher Scientific). Proteins were size-fractionated in NuPage Novex 12% Bis-Tris gels (Life Technologies) and transferred to Hybond polyvinylidene difluoride membranes (GE Healthcare, Diegem, Belgium) by wet electroblotting. After blocking for 1 h in Tris-based saline/0.1% Tween-20 (TBS-T)/5% bovine serum albumin (BSA; Sigma-Aldrich), membranes were incubated for 1 h with primary antibodies directed against green fluorescent protein (rabbit IgG; 1:1000; Life Technologies, A-11122) to detect eYFP or the CatCh~eYFP fusion protein or against glyceraldehyde 3-phosphate dehydrogenase (GAPDH; mouse IgG1, clone 6C5; 1:100 000; Merck Millipore, Billerica, MA, USA) as loading control. Next, blots were incubated with corresponding horseradish peroxidase-conjugated secondary antibodies (1:1000 in TBST/5% BSA; Santa Cruz Biotechnology, Dallas, TX, USA) again for 1 h. Blots were then immersed in ECL Prime Western blot detection reagent (GE Healthcare) and chemiluminescence was measured with the ChemiDoc XRS imaging system (Bio-Rad Laboratories, Veenendaal, the Netherlands).

Optical mapping

To analyse the electrophysiological effect of CatCh-generated photocurrents on aCMC cultures, cells were assayed by optical mapping on Day 7 or 8 of culture. Action potential (AP) propagation was visualized using the voltage-sensitive dye di-4-ANEPPS (Life Technologies). Cells were stimulated either electrically with an epoxy-coated bipolar platinum electrode with square suprathreshold electrical stimuli at 1–2 Hz or optically with light pulses from a 470 nm light-emitting diode (LED; SR-01-B0040 Rebel Star LED assembly; 70 Lm at 700 mA; Luxeonstar, Brantford, Ontario, Canada) mounted 10 mm below the centre of the wells of a 24-well cell-culture plate. A specialized stimulus generator (STG 2004) with corresponding software (MC Stimulus II; both from Multichannel Systems, Reutlingen, Germany) was used to perform both electrical and optical stimulation (see also Supplementary material online, *Figure S1*). Irradiance was measured using a PM100D optical power meter (Thorlabs, Munich, Germany) equipped with a S130C slim dual range sensor with the range set at 5 nW–5 mW and the wavelength set at 470 nm. Optical images were captured using a MiCAM ULTIMA-L imaging system (SciMedia, Costa Mesa, CA, USA). Optical pacing was performed by exposure for 10 ms to blue LED light at the maximal irradiance achievable with our setup (0.038 mW/mm²). Strength–duration curves of optical pacing threshold were constructed by varying pulse duration (5–25 ms) and irradiance (0.0050–0.038 mW/mm²). Reentry was induced by electrical burst pacing with a cycle length of 20–100 ms. After confirmation of the presence of reentrant arrhythmias, cultures

were exposed to blue LED light for 500 ms (at 0.038 mW/mm²). Specialized software was used for data analysis and construction of activation maps (BrainVision Analyzer 1101; Brainvision, Tokyo, Japan). For baseline shift adjustment during blue LED light exposure, several filters were applied allowing data interpretation during the LED-on period (see Supplementary material online, *Figure S1*). The phase-space method was used to identify and track phase singularities (PSs) of spiral waves as described previously.¹⁶ As measure of wavefront curvature, the straight distance between the spiral wave tip and the point of the first (or second) half winding of the wavefront was determined.¹⁷ To this purpose, a tangent line was drawn along the wavefront in the direct vicinity of the PS (Supplementary material online, *Figure S3*, dashed white lines). Next, the length of the normal line from its intersection with the tangent line to its intersection with the wavefront at half of the spiral wave's full winding was measured (Supplementary material online, *Figure S3*).

MEA mapping

To provide additional mechanistic insight into CatCh-mediated effects on spiral waves and to avoid potential complexities associated with the combined application of light-activated potentiometric dyes and ion channels (see also Supplementary material online, *Figure S1*), MEA mapping of extracellular potentials was performed in parallel to optical mapping as a matching non-optical control.

For MEA mapping, aCMCs were cultured in fibronectin-coated MEA culture dishes containing 60 30 μ m-diameter electrodes with an interelectrode spacing of 200 μ m (Multi Channel Systems). Next, reentry was induced by electrical burst pacing as described earlier. During recording, cultures were exposed to blue LED light pulses (10 ms for optical pacing or 500 ms for reentry termination). Electrograms were analysed using MC-Rack software (Multi Channel Systems).¹⁸

Whole-cell patch-clamp recordings

Voltage-clamp recordings in single LV.CatCh~eYFP \uparrow -transduced aCMCs were carried out in parallel to optical mapping experiments. Transduced cells (identified by their green-yellow fluorescence) were exposed to 10 or 500 ms blue LED light pulses to study CatCh-mediated photocurrents, after reaching G Ω seal, establishing whole-cell configuration, and setting holding potential at -45 mV. Experiments were performed at 19–23°C using a MultiClamp 700B amplifier, a Digidata 1440A A/D converter, Clampex 10.3 software (all from Axon CNS, Molecular Devices, Sunnyvale, CA, USA), the STG 2004 pulse generator with corresponding computer software, and an Axiovert 35 inverted phase-contrast and fluorescence microscope (Carl Zeiss). Cells were bathed in an extracellular solution composed of (in mmol/L) 137 NaCl, 5 KCl, 1 MgCl₂, 1.8 CaCl₂, 10 HEPES, and 11 glucose (pH 7.4 adjusted with NaOH). Patch pipettes

manufactured from borosilicate glass with capillary 1.5 mm outer diameter and 1.17 mm inner diameter (Harvard Apparatus, Kent, UK) were pulled by a model P-30 vertical micropipette puller (Sutter Instrument Company, Novato, CA, USA). The internal pipette solution contained (in mmol/L) 20 NaCl, 120 KCl, 1 MgCl₂, 5 EGTA, and 10 HEPES (pH 7.4 adjusted with KOH). Pipettes showed a typical resistance of 2–3 MΩ and liquid junction potentials (~5 mV) were corrected. Data were digitized at 10 kHz, filtered at 10 kHz (4-pole Bessel low-pass filter, 24 dB/octave, –3 dB at cut off) and analysed off-line using pClamp 10 electrophysiology data acquisition and analysis software (Axon CNS, Molecular Devices).

Statistical analysis

Statistical analyses were performed using SPSS11.0 for Windows (SPSS, Chicago, IL, USA). The Mann–Whitney *U* test or the Wilcoxon signed rank test was used for comparison between groups as indicated. Data were expressed as mean ± standard deviation (SD) for a number (*n*) of observations. Differences were considered statistically significant at *P* < 0.05.

Results

Characterization of 2D AF model

Immunocytological analysis at Day 8 showed that 100% of the α-actinin⁺ cells in monolayer cultures of neonatal rat atrial cells were positive for MLC2a, i.e. no MLC2a⁻/α-actinin⁺ cells were detected, confirming that all cardiomyocytes in these cultures were of atrial origin (*Figure 1A*). Cultures contained 18.3 ± 4.8% fibroblasts as judged by collagen type 1 immunostaining (*Figure 1B*). At Day 8 of culture, cells showed abundant Cx43 expression at intercellular junctions (*Figure 1C*) forming a dense ‘syncytial’ monolayer (*Figure 1D*), which could be assessed for conduction patterns by optical mapping and by MEA analysis. Typically, no spontaneous activity was observed in the atrial cell cultures. Upon 1 Hz electrical stimulation cultures showed 1:1 uniform convex activation originating from the bipolar pacing electrode, while no PSs were observed (*Figure 1E and G*), resembling normal atrial activation as occurs during sinus rhythm. However, after burst pacing, multiple spiral wave reentry circuits and corresponding PSs arose maintaining high-frequency activation (mean 13.8 ± 7.0 Hz) independent of any subsequent electrical stimulation (*Figure 1F and H*), resembling activation patterns found in AF.

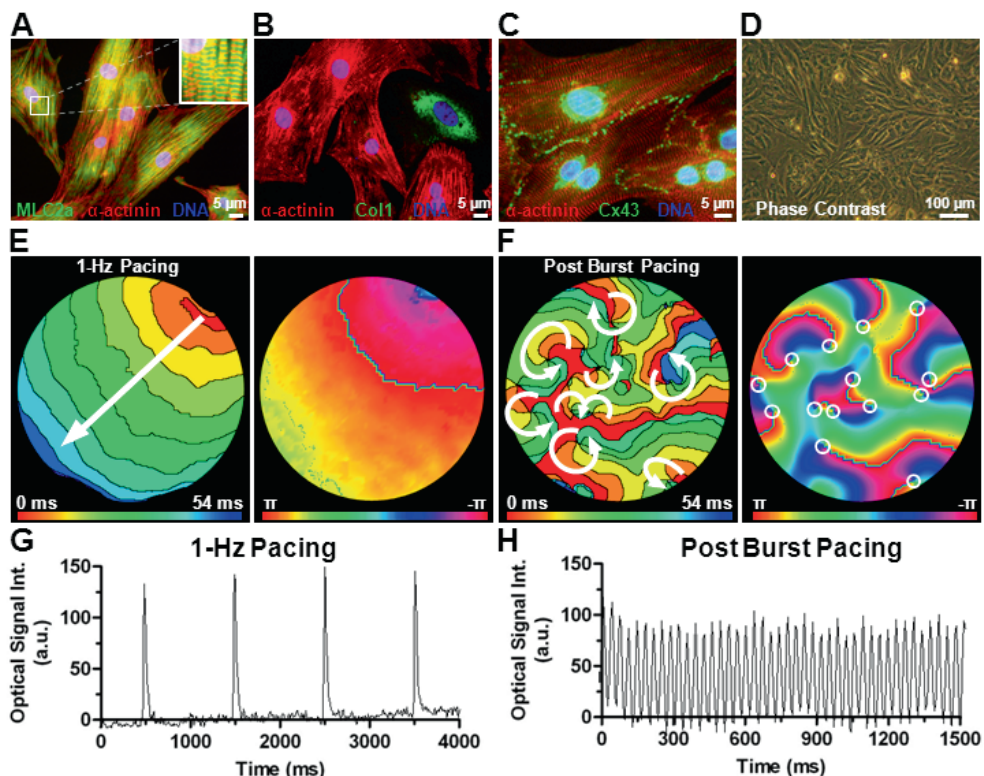


Figure 1. Characterization of 2D AF model. Typical examples of immunocytological double stainings for (A) MLC2a (aCMCs, green) and α -actinin (cardiomyocytes, red), (B) α -actinin (cardiomyocytes, red) and collagen type 1 (Col1; fibroblasts, green), and (C) α -actinin (cardiomyocytes, red) and Cx43 (gap junctions, green) in atrial cell cultures. The white inset in A (top right) shows a magnification of the boxed area (left). (D) Phase contrast image of a confluent atrial cell monolayer. (E) Typical activation map (6 ms isochrone spacing) and corresponding phase map of an atrial culture during 1 Hz electrical pacing, showing uniform convex propagation originating from the electrode (in the direction of the white arrow; left panel) and absence of PSs (right panel). (F) Typical activation map (6 ms isochrone spacing) and corresponding phase map of an atrial culture after electrical burst pacing. Multiple reentrant circuits are evident in the activation map, following the directions of the white arrows. The phase map shows multiple PSs indicated by white circles. Typical spatially filtered optical (i.e. di-4-ANEPPS-derived) signal traces in an atrial culture (G) during 1 Hz pacing and (H) after fibrillation is established by electrical burst pacing. a.u., arbitrary units.

Confirmation of functional CatCh expression

Atrial cell cultures were transduced with either the lentiviral vector LV.CatCh~eYFP \uparrow encoding a fusion protein between CatCh and eYFP, or the eYFP-encoding lentiviral vector LV.eYFP \uparrow as a control, to study the effects of CatCh activation on spiral waves (for vector maps, see Figure 2A). Because transgene expression is driven by a striated muscle-specific promoter, lentiviral vector-transduced atrial cultures showed eYFP signals almost exclusively in the α -actinin $^+$ cells (100 ± 38.6 vs. 8.7 ± 1.7 arbitrary units in non-myocytes and 100 ± 37.0 vs. 4.2 ± 1.6 arbitrary units in non-myocytes for the LV.eYFP \uparrow - and LV.CatCh~eYFP \uparrow -transduced cultures, respectively; $P <$

0.05). As expected, in the LV.eYFP \uparrow -transduced aCMCs, eYFP localized to the cytoplasm, while in the LV.CatCh~eYFP \uparrow -modified cells, eYFP fluorescence was membrane-associated (Figure 2B–D). Western blot analysis confirmed eYFP expression in atrial cell cultures after transduction with both LV.eYFP \uparrow and LV.CatCh~eYFP \uparrow , showing immunoreactive protein species of ~27 kDa (the predicted molecular weight of eYFP) and of around 60 kDa (due to fusion of CatCh to the N terminus of eYFP), respectively (Figure 2E). Optical and MEA mapping experiments showed that APs could be elicited by optical pacing through exposure to 10 ms light pulses (at 0.038 mW/mm²) in LV.CatCh~eYFP \uparrow - but not in LV.eYFP \uparrow -transduced cultures (see also Supplementary material online, Figure S2 for a strength–duration analysis of the pacing threshold in LV.CatCh~eYFP \uparrow -transduced cultures), while both culture types could be paced electrically (Figure 3A and B; $n = 12$ and $n = 9$, respectively). The maximum change in fluorescence intensity occurred within 12.0 ± 8.5 ms ($n = 5$) throughout the culture (Figure 3C), indicating synchronous depolarization of the monolayer by CatCh activation. The functionality of the generated photocurrent was further confirmed in patch-clamp experiments on single aCMCs (Figure 3D), which revealed inward currents with a peak current density of 5.31 ± 1.13 pA/pF upon exposure to 10 ms blue light pulses ($n = 6$).

Light-induced spiral wave termination

Exposure to prolonged light pulses (500 ms at 0.038 mW/mm²), producing a sustained current with a peak density of 12.01 ± 2.54 pA/pF in single aCMCs ($n = 6$; Figure 3D), led to spiral wave termination in all of the LV.CatCh~eYFP \uparrow - (31 out of 31), but none of the LV.eYFP \uparrow -transduced (0 out of 11) cultures, as judged by optical mapping analyses and confirmed by MEA recordings (Figure 4A–F). Importantly, LV.CatCh~eYFP \uparrow -transduced cultures that had been subjected to repeated optogenetic spiral wave termination displayed normal uniform conduction upon subsequent electrical activation implying retained excitability (Figure 4E).

No significant persisting electrophysiological or pro-arrhythmic changes were observed in LV.CatCh.eYFP \uparrow -transduced cultures following prolonged exposure (i.e. 500 ms) to blue light (see Supplementary material online, Figure S4). Also, contractility, as judged by phase-contrast microscopy, was retained after expression of CatCh~eYFP and its subsequent activation by a 500 ms blue light pulse. During exposure to a 500 ms light pulse, reentry was terminated within 163.1 ± 105.8 ms (range 36–444 ms, $n = 22$) suggesting that reentry could be terminated using pulses shorter than 500 ms. Hence, to find the pulse duration necessary for termination, we induced reentry in LV.CatCh.eYFP \uparrow -transduced cultures and attempted spiral wave termination by exposure to subsequent blue light pulses of 10, 20, 50, 100, 200, and 500 ms at 0.038 mW/mm². This showed that the average pulse duration necessary for arrhythmia termination was 133.3 ± 180.7 ms ($n = 6$).

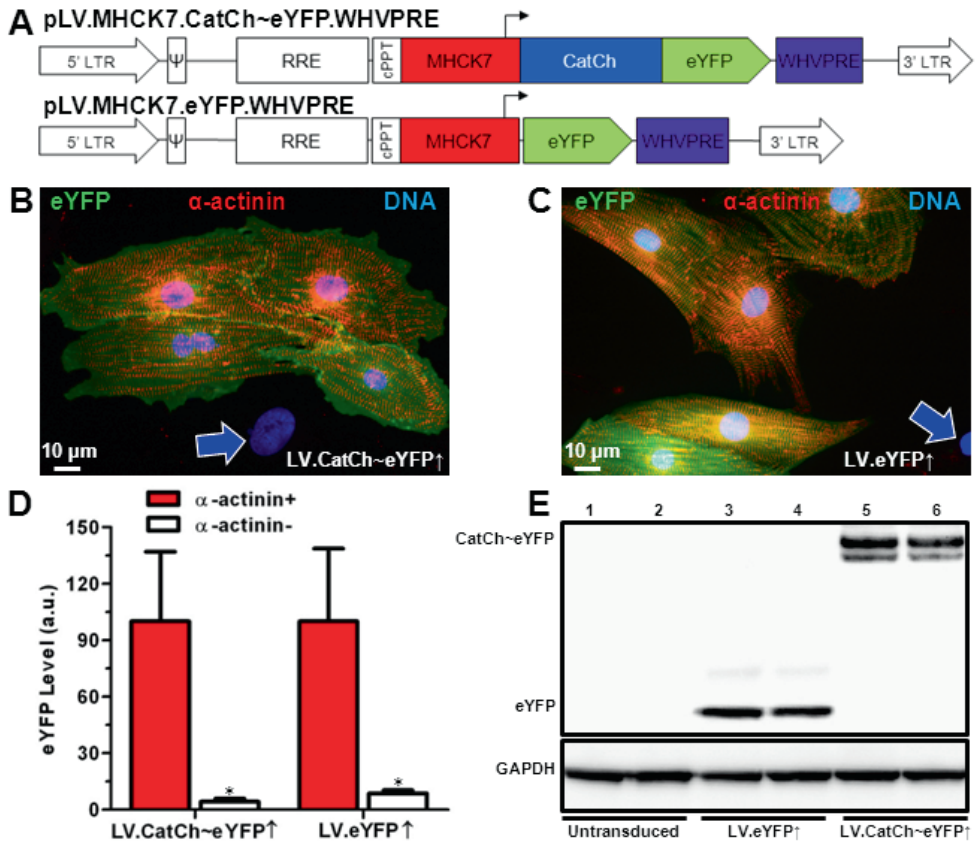


Figure 2. Immunocytological and western blot confirmation of forced CatCh expression. (A) Structure of the lentiviral vector DNA in plasmids pLV.MHCK7.CatCh~eYFP.WHVPRE (for generating LV.CatCh~eYFP⁺) and pLV.MHCK7.eYFP.WHVPRE (to produce LV.eYFP⁺). 5' LTR: chimeric 5' long terminal repeat containing enhancer and promoter elements of the human cytomegalovirus *immediate-early* gene and the human immunodeficiency virus type 1 (HIV1) R and U5 regions. Ψ: HIV1 packaging signal. RRE: HIV1 Rev-responsive element. cPPT: HIV1 central polyurine tract and termination site. MHCK7: chimeric striated muscle-specific promoter.¹³ CatCh: coding sequence of an ultra-light-sensitive and highly Ca²⁺-permeable mutant of the *Chlamydomonas reinhardtii* chlamyopsin 4 light-gated ion channel, also known as ChR2.¹⁰ eYFP: *Aequorea victoria* enhanced yellow fluorescent protein-coding sequence. WHVPRE: woodchuck hepatitis virus posttranscriptional regulatory element. 3' LTR: wild-type 3' HIV1 LTR. (B and C) Immunocytological staining of (B) LV.CatCh~eYFP⁺- and (C) LV.eYFP⁺-transduced atrial cultures for α-actinin (red; cardiomyocyte marker), showing membrane-associated and cytoplasmic eYFP signals (green), respectively. Blue arrows indicate nuclei of eYFP⁺/α-actinin⁻ cells (mainly cardiac fibroblasts). (D) Quantification of the eYFP signal in α-actinin⁺ (red bars) and α-actinin⁻ (white bars) cells in atrial cultures after transduction with LV.CatCh~eYFP⁺ or with LV.eYFP⁺. (E) Western blot analysis of eYFP/CatCh~eYFP levels in untransduced (lanes 1 and 2) atrial cultures and cultures transduced with LV.eYFP⁺ (lanes 3 and 4) or with LV.CatCh~eYFP⁺ (lanes 5 and 6) using glyceraldehyde 3-phosphate dehydrogenase (GAPDH) as loading control. **P* < 0.05 vs. α-actinin⁺ using the Mann–Whitney *U* test. a.u., arbitrary units.

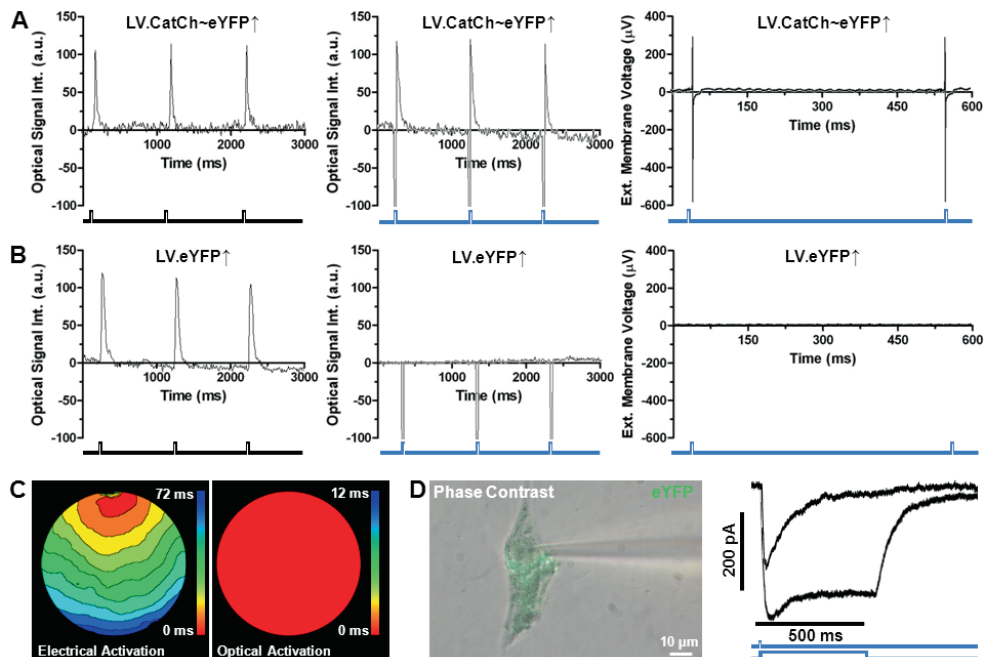


Figure 3. Confirmation of functional CatCh expression. (A and B) Typical optical signal traces (left and middle panels) and MEA recordings (right panels) in aCMC cultures transduced with (A) LV.CatCh~eYFP[↑] or with (B) LV.eYFP[↑] during 1 Hz electrical activation (left panels) or exposure to 10 ms blue light pulses at 1 Hz (middle panels) and 2 Hz (right panels). (C) Activation map of an LV.CatCh~eYFP[↑]-transduced atrial culture during 1 Hz electrical pacing (left) and exposure to a 10 ms blue light pulse of 1 Hz (right). (D) Typical example of a *CatCh~eYFP*-expressing aCMC used for patch-clamping (left) and two superimposed records of whole-cell inward currents from the same aCMC evoked at a holding potential of -45 mV by a 10 and 500 ms blue light pulse of equal intensity (see bottom traces) (right). As expected, non-transduced aCMCs did not show light-dependent currents. a.u., arbitrary units.

Next, we investigated the anti-arrhythmic mechanism underlying arrhythmia termination by CatCh activation. During reentry, a gradient in conduction velocity and AP amplitude was observed. Both parameters decreased near the spiral wave core (Figure 5A) while wavefront curvature was significantly higher near the core than in the periphery (the second vs. the doubled first half winding distance of the wavefront was 7.2 ± 1.9 vs. 4.1 ± 1.1 mm; $P < 0.05$, $n = 6$) (Figure 5B).

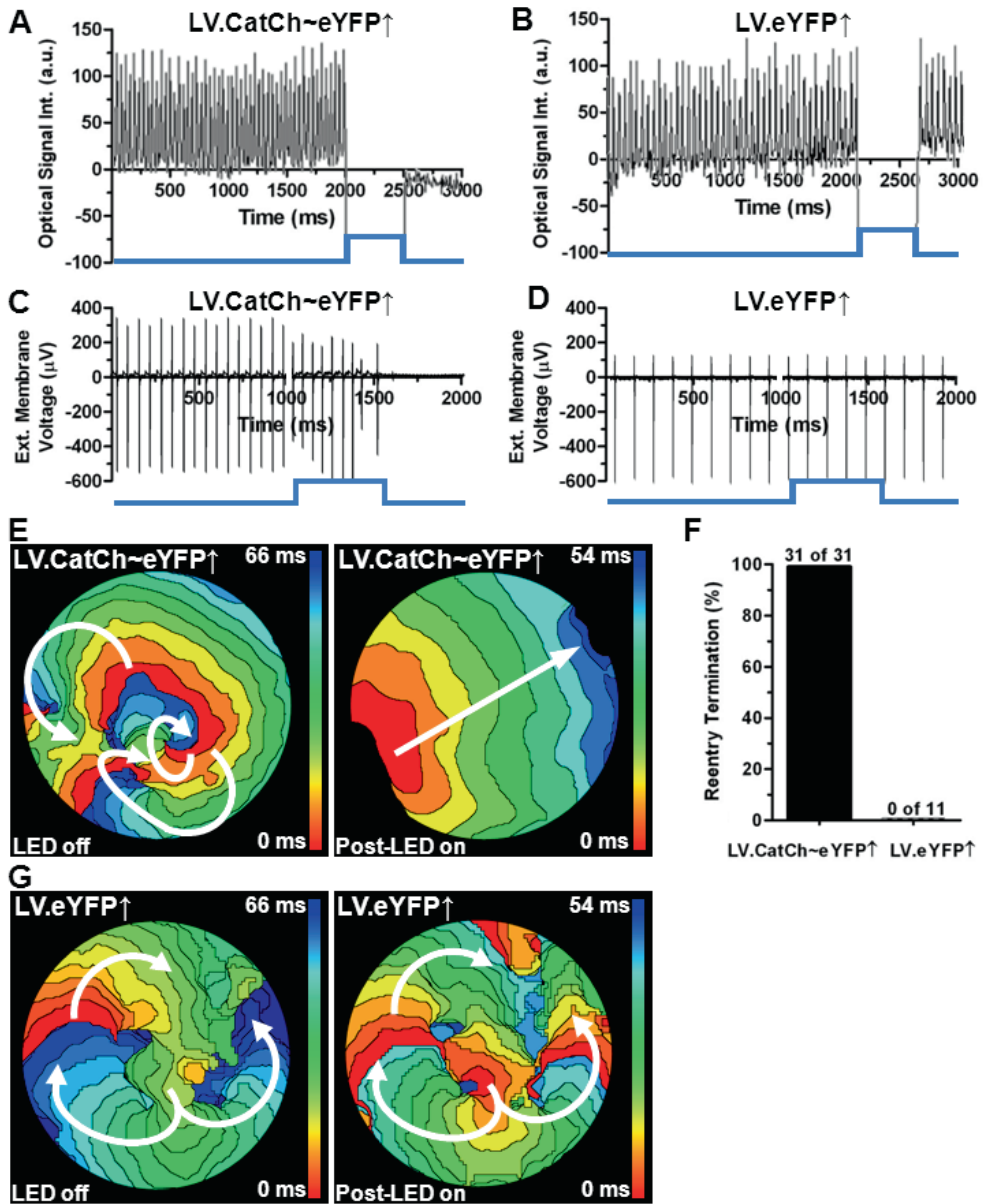


Figure 4. Effective light-induced spiral wave termination by CatCh expression. Typical signal traces in reentrant tachyarrhythmic atrial cultures transduced with (A and C) LV.CatCh~eYFP↑ or with (B and D) LV.eYFP↑ during (A and B) optical mapping or (C and D) MEA recordings, showing termination of tachyarrhythmic activity after exposure to blue light (500 ms duration) in LV.CatCh~eYFP↑ cultures only. Typical activation map of (E) LV.CatCh~eYFP↑- and (G) LV.eYFP↑-transduced atrial cultures before (left panel) and after (right panel) exposure to a 500 ms blue light pulse, showing light-induced termination of reentrant activity. (F) Quantification of the success rate of light-induced spiral wave termination in LV.CatCh~eYFP↑- and LV.eYFP↑-transduced cultures. a.u., arbitrary units.

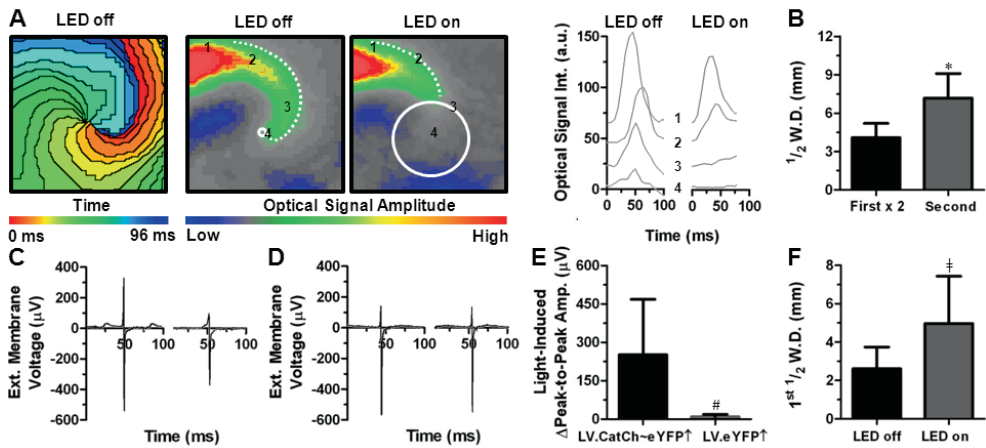


Figure 5. Light-induced increase in functional core size. (A) Activation map (left panel) and snapshots (two middle panels) after spatial and high-pass filtering of optical signals of an LV.CatCh~eYFP⁺-transduced atrial culture before and during exposure to a 500 ms blue light pulse (6 ms isochrone spacing). The optical signal traces (non-high-pass-filtered) are shown on the right. Numbers 1–4 correspond to the positions in the snapshots. White circles indicate estimated functional core sizes. (B) Quantification of the doubled first half winding distance ($\frac{1}{2}$ W.D.) of the wavefront and the second half winding distance as a measure of wavefront curvature during reentry in LV.CatCh~eYFP⁺-transduced atrial cultures. (C) Typical MEA recordings of LV.CatCh~eYFP⁺- or (D) LV.eYFP⁺-transduced atrial cultures during reentrant activity before (left) and at the beginning (right) of a 500 ms blue light pulse. (E) Quantification of MEA peak-to-peak amplitude changes upon exposure to blue light in LV.CatCh~eYFP⁺- and LV.eYFP⁺-transduced cultures. (F) Quantification of the first half-winding distance in LV.CatCh~eYFP⁺-transduced cultures prior to (LED off) and during (LED on) exposure to a 500 ms blue light pulse as a measure of wavefront curvature. * $P < 0.05$ vs. doubled first half-winding distance using a Wilcoxon signed rank test. † $P < 0.05$ vs. LV.CatCh~eYFP⁺-transduced cultures using a Mann–Whitney U test. # $P < 0.05$ vs. LED on using a Wilcoxon signed rank test. a.u., arbitrary units.

Depolarization by activation of CatCh led to a reduction in overall excitability. The reduction in excitability caused by light-induced depolarization was confirmed by MEA mapping showing a strong decrease in peak-to-peak amplitude [Δ peak-to-peak amplitude $251.3 \pm 217.1 \mu\text{V}$ in LV.CatCh~eYFP⁺-transduced cultures ($n = 6$) vs. $9.2 \pm 9.5 \mu\text{V}$ in LV.eYFP⁺-transduced cultures ($n = 5$) (Figure 5C and E), likely attributable to inactivation of the fast Na⁺ current. As a consequence, the critical wavefront curvature (the curvature at which the conduction velocity becomes zero, i.e. the curvature near the spiral wave core) was decreased (first half-winding distance was 2.6 ± 1.1 before light exposure vs. 5.0 ± 2.5 mm during light exposure, $n = 6$) (Figure 5F and Supplementary material online, Figure S3). Hence, during light exposure, the critical wavefront curvature is reached at a more peripheral point in the wavefront compared with the point of PS (i.e. the point of critical wavefront curvature) before light exposure. Since the source–sink relationship for impulse propagation in cardiac tissue does not allow wavefront curvature to exceed a critical value, spiral wave core size increased after the decrease in excitability during light exposure. This was evinced by a reduction in AP amplitude and inhibition of excitation near the functional core (Figure 5A).

As a consequence of the lowered critical curvature, culture-wide expansion of the PS trajectory around the growing functional core occurred, which increased the probability of critical collisions of PSs with culture boundaries (Figure 6A and Supplementary material online, Movie S1) or with PSs of opposite chirality (Figure 6B and Supplementary material online, Movie S2), ultimately causing spiral wave termination.

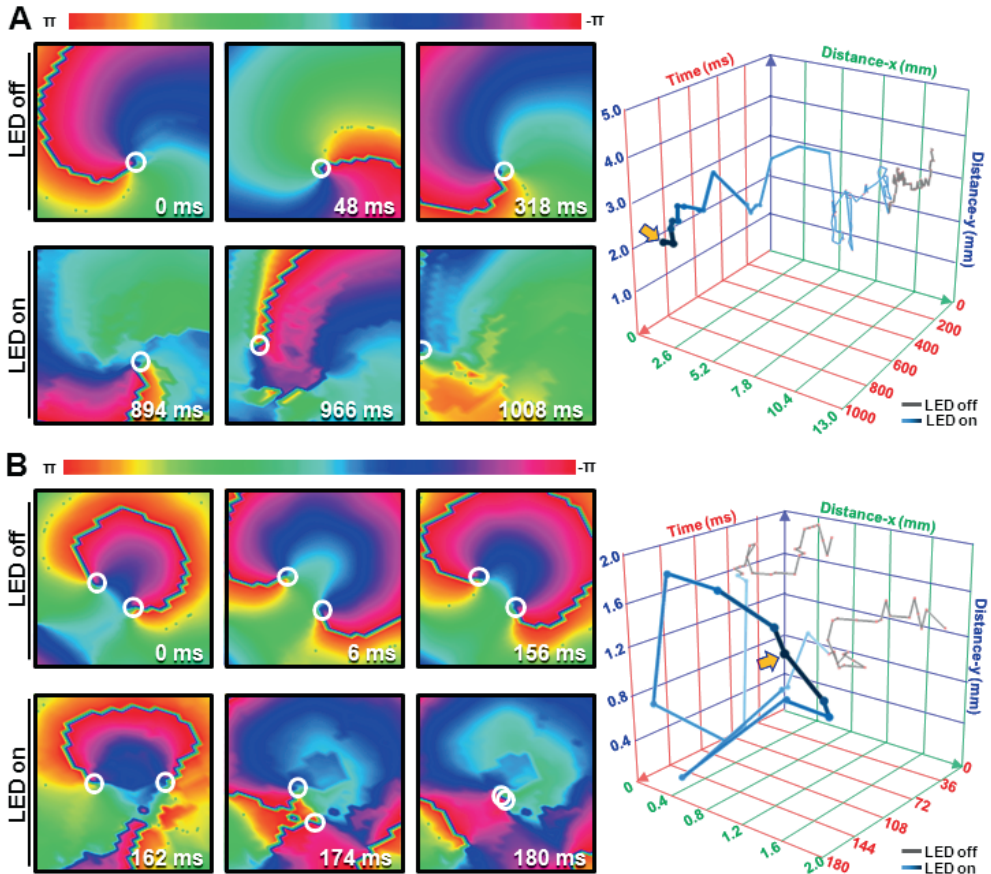


Figure 6. Light-induced alteration of PS trajectory and arrhythmia termination. Typical phase map sequence of an LV.CatCh~eYFP \uparrow -transduced atrial culture showing spiral wave phase progression before (upper sequences) and during (lower sequences) exposure to blue light leading to spiral wave termination by (A) PS–boundary collision and (B) PS–PS collision. White circles indicate PS positions. 3D graphs show the PS positions before (grey) and during (blue gradient) exposure to blue light, exemplifying PS drift leading to wave termination (yellow arrow).

Discussion

The key findings of this study are the following: first, neonatal rat aCMCs can be endowed with functional light-gated cation channels (i.e. CatCh) by lentiviral transduction without evident alterations in the characteristics of the AP or calcium transient. Secondly, activation of these channels by brief light pulses (10 ms/470 nm) provides a depolarizing current strong enough to serve as suprathreshold stimulus for instant and synchronous electrical activation of CatCh-expressing cardiomyocytes in atrial monolayer cultures. Thirdly, in such monolayers, stable rotors with PSs rotating around functional cores and maintaining fibrillatory activation can be terminated effectively and repeatedly by prolonged activation of CatCh (500 ms light exposure). Fourthly, mechanistically, prolonged CatCh activation reduces overall excitability of the fibrillating monolayers, followed by an increase in functional core size, resulting in PS drift, which ultimately leads to termination of the spiral wave arrhythmias. Finally, this is the first study to show that optogenetic engineering of neonatal rat aCMCs, by means of forced CatCh expression and subsequent photoactivation, allows fibrillating aCMC monolayers to generate themselves the electrical current needed for defibrillation. This proof-of-concept may give a strong impetus towards the design of shockless treatment strategies for AF.

Optogenetic control of cardiac excitability

In the past, most studies that aimed to unravel the mechanisms underlying cardiac arrhythmias and to identify new anti-arrhythmic targets relied exclusively on the use of pharmacological and/or electrical interventions to modulate electrophysiological processes in cardiomyocytes, like de- and hyperpolarization.^{12,16,18} More recently, genetic interventions including site-directed mutagenesis, gene knockdown/knockout and forced (trans)gene expression have been added to the repertoire of techniques to modulate cardiac ion channel activity and excitability in a more refined manner.¹¹ Nevertheless, even today's most sophisticated genetic interventions allow for only modest spatiotemporal, as well as, quantitative control of the target's functionality. Such constraints hamper further progress in our mechanistic understanding and treatment of cardiac arrhythmias. Optogenetic engineering, however, allows modulation of cellular electrophysiological properties with superb spatiotemporal and quantitative control in a non-voltage-gated fashion by combining the favourable properties of photoactivatable ion channels and light.⁶ As a result, optogenetics has become an indispensable tool in neuroscience to modulate the activity of neurons by light and thereby study the functional roles of specific neural pathways in the brain.⁶

More recently, optogenetics was introduced in the field of cardiovascular research by showing that channelrhodopsin-2 (ChR2)-expressing cardiomyocytes, either cultured *in vitro* or present in the intact heart, could be electrically excited by brief light pulses without obvious adverse

effects on cardiac function.⁷⁻⁹ These pulses caused depolarization of cardiomyocytes at the site of illumination, thereby triggering APs that were rapidly propagated across the cardiac tissue via gap junctions and merged into a spread of uniform electrical activation. Prolonged activation of light-gated cation channels in cardiomyocytes led to sustained depolarization of all cardiomyocytes without causing noticeable adverse effects.⁷ However, thus far, the potential of optogenetics to counteract cardiac tachyarrhythmias has not been investigated.

Optogenetic termination of spiral waves

Based on current evidence, reentrant spiral waves play a major role in the maintenance of fibrillation in both atria and ventricles.¹⁹ Hence, most strategies aiming to prevent or terminate AF involve the inhibition of reentry formation and the elimination of existing reentrant circuits, respectively. Previous studies have shown that during reentry, conduction velocity and excitability gradually increase from the rotor core towards the periphery. Paramount to the establishment of these gradients seem to be the inward rectifier K⁺ current (I_{K1}) and the fast Na⁺ current (I_{Na}), of which the amplitudes decrease towards the rotor core. The interplay between I_{K1} and I_{Na} determines reentry frequency and rotor stability as a decrease of either current slows and destabilizes the rotor, possibly leading to spiral wave termination.^{16,20,21} The present study is consistent with this concept, as a light-induced decrease in overall excitability increased the functional core size and terminated reentry. Due to the existing gradient in excitability, decreasing overall excitability will first prevent excitation near the core leading to its expansion thereby causing PS drift from a relatively stable position. Consequently, the chance for PSs to collide with each other or with physical boundaries will increase. Following light-triggered annihilation of all PSs in a culture, as found in our experiments, no spiral waves are generated anymore, allowing reestablishment of a regular cardiac activation pattern. Still, as optogenetic defibrillation is a new field of research, various aspects of this method need to be investigated in further detail in order to fully appraise its value as a research tool and to gain more insight into its therapeutic potential.

Potential advantages over established defibrillation strategies

While pharmacological blockade of I_{K1} and I_{Na} are well-accepted strategies to terminate reentry, they are associated with proarrhythmia, since the resulting chronic slowing of repolarization and conduction promote afterdepolarizations and reentry, respectively.^{16,22} Optogenetic therapy would, however, decrease excitability only during photostimulation, leaving important electrophysiological parameters unaltered after spiral wave termination.

Several advantages of optogenetic therapy over electrical cardiac therapy have been previously postulated in the light of cardiac pacing, including a higher level of spatial control^{7,8} and, more importantly, higher energy efficiency resulting in less tissue damage. For CatCh, the

enhanced energy efficiency might be even more pronounced than for earlier ChR2 variants due to its improved light sensitivity. While optical pacing might prove an interesting option for treatment of bradyarrhythmias, energy efficiency could be of even greater importance when trying to normalize heart rhythm during tachyarrhythmia. The possible applicability of optogenetics in the field of tachyarrhythmias was already hinted at in a study showing the ability to cause light-induced conduction block by overexpression of the hyperpolarizing light-sensitive Cl^- channel NpHR in zebrafish cardiomyocytes.⁷ Moreover, using ChR2(H134R), Bruegmann *et al.*⁸ showed that through a depolarizing photocurrent spontaneous beating of embryonic stem cell-derived cardiomyocytes could be depressed, most likely as a result of fast Na^+ channel inactivation upon prolonged local illumination. In the present study, the possibility to optogenetically suppress cardiac excitability was confirmed by prolonged light exposure of aCMCs expressing the Ca^{2+} -permeable and ultra-light-sensitive ChR2 mutant CatCh. The CatCh-dependent photocurrent was used to show that uniform light-induced depolarization can terminate spiral wave reentry, exemplifying the possibility to broaden the field of optogenetic control of myocardial function towards arrhythmia termination. In sharp contrast, traditional defibrillation is based on the delivery of high-energy electrical shocks to cause uniform depolarization. The use of high-energy electrical shocks is associated with severe discomfort in patients as well as tissue damage, increasing with stimulus strength and duration. A major improvement in electrical defibrillation has been the introduction of the biphasic waveform²³ and further technical refinements like multistage electrotherapy²⁴ are arising. Still, stimulus duration in traditional defibrillation must be confined to several milliseconds, whereas the optogenetic approach might enable the use of longer stimuli, such as applied in this study, without inducing tissue damage.

During traditional electrical defibrillation, reentry can be re-initiated at critical points in local electrical field strength, when shock strength is below the upper limit of vulnerability or when the shock causes the occurrence of virtual electrodes from which new fibrillatory waves can emanate.^{5,25–27} Since optogenetic defibrillation, as presented in this study, does not use an electric field to induce depolarization, it should not result in re-initiation of fibrillation by the formation of virtual electrodes. Under conditions of homogeneous transduction and illumination also re-initiation as a consequence of aforementioned critical points may be prevented by optogenetic arrhythmia termination. Concordantly, after light-induced spiral wave termination, no proarrhythmic reexcitations were found in our model. Thus, as shown in the present study, optogenetic therapy to control cardiac function and to terminate arrhythmias might provide several advantages over the traditional means of treating heart rhythm disorders.

Translational considerations and study limitations

This study shows that the endogenous electrochemical gradients present in cardiac tissue can be exploited for defibrillation by optogenetics, as an alternative to the external electrical current applied to interrupt reentrant circuits during conventional electrical defibrillation.⁵ However, we acknowledge that translating this principle to the *in vivo* situation comes with some hurdles that need to be overcome before considering any clinical applications.

First, in the present study, a 2D model of AF was used to demonstrate proof-of-principle for the optogenetic termination of fibrillatory conduction. This *in vitro* model lacks the complexity found in the intact 3D atrium and thus does not suffer from factors such as a low transduction efficiency of the target cell population and poor light penetration into the target tissue that might limit the effectiveness of optogenetic arrhythmia termination *in vivo*. Moreover, as we found termination of reentry by light to depend on the collision of PSs with boundaries or with PSs of opposite chirality, at least an area including the PS and its nearest physical boundary or a counteracting PS has to be illuminated for successful arrhythmia termination. However, because in our model the position of the PSs causing reentrant activation cannot be predetermined and their trajectories cannot be controlled, homogeneous illumination of the entire aCMC cultures is required for consistent reentry termination by light. Still, earlier work in the field of ventricular fibrillation has shown that effective defibrillation does not require every cell in the myocardium to be depolarized,⁵ hinting at the possibility that successful defibrillation may also be achieved in the case of incomplete light penetration and/or patchy transgene expression. This might even be more pronounced in AF, as rotors or drivers of AF usually localize to specific areas of the atrium such as the direct surroundings of pulmonary vein ostia. Hence, future studies testing the possibility of AF termination using local instead of global cation channel activation may provide an important next step in the realization of shockfree defibrillation *in vivo*.

Nevertheless, in tackling the possibility of insufficient light penetration *in vivo*, it may be critical to expand the optogenetic toolbox with improved/mutated light-gated cation channels displaying greater light sensitivity or increased ion conductance. In addition, due to the absorption of especially short-wavelength visible light by tissue constituents like blood, it might be of interest to look into (optogenetic) tools that are excited by light of higher wavelength (i.e. near-infrared) or by other energy sources (radio waves/ultrasound) and therefore allow deeper tissue penetration. These improvements are likely to arise in the near future through the ongoing research and advances in (opto)genetic technology.^{5,28}

Secondly, it should be noted that the physical boundaries of culture dishes (necessary for extinguishing PSs by collision, in addition to the collision to PSs of opposite chirality) differ from the anatomical boundaries in the intact atrium. Nonetheless, in several clinical studies, PS–boundary collisions have been identified as a mechanism of rotor termination in both

atrial and ventricular fibrillation.^{29,30} Hence, while in the intact atrium, the likelihood of a PS meeting a PS of opposite chirality may be diminished compared with that in our 2D model, light-induced rotor termination *in vivo* might be facilitated by the numerous anatomical boundaries contained within the atrium, such as the many walls of the microvasculature, the mitral/tricuspid valve rings, the ostia of the pulmonary veins, and the epi- and endocardium. Thirdly, in the present study, transgene expression was achieved by lentiviral vector-based gene transfer. Although lentiviral vectors are very efficient in inducing stable transgene expression *in vitro*, they are of limited use for *in vivo* cardiac gene therapy mainly because of their poor dissemination through myocardial tissue and their potential to cause insertional oncogenesis. These hurdles may be overcome by using adeno-associated virus (AAV) vectors for *in vivo channelrhodopsin* gene delivery to the heart as these vectors (i) can mediate long-term transgene expression in post-mitotic cells including cardiomyocytes without the need to integrate their DNA into the target cell genome, (ii) do not contain viral genes encoding potentially cytotoxic and/or immunogenic proteins, (iii) readily spread through myocardial tissue, and (iv) are well known for their excellent *in vivo* safety. The utility of AAV vectors for *in vivo* gene transfer to the human heart has been illustrated by a recent clinical study in which heart failure patients received AAV vector particles encoding sarco/endoplasmic reticulum Ca^{2+} -ATPase 2a,³¹ paving the way for the clinical application of optogenetic and other gene-based therapies in the field of cardiology.

Finally, also the delivery method of the necessary light (or any other excitatory energy source) *in vivo* needs to be perfected. In the field of neurology, solutions to this problem have already been postulated, and lie in the use of, for example, fiberoptics.^{32,33} Hence, the future might hold painfree implantable cardioverter defibrillator device therapy for AF, based on optogenetics and fibreoptic delivery of light, instead of electrical shocks applied via platinum leads, in specific areas of the atrial myocardium.

Without the intention to detract from this prospect, it should be noted that the conclusions drawn from the present study are only conceptual in relation to human AF and therefore cannot be readily extrapolated to the clinical setting. Hence, there is still a considerable amount of work to be done before optogenetic therapy (or any other therapy exploiting the electrochemical gradients that are endogenously present in myocardial tissue) becomes a realistic treatment option for patients with cardiac rhythm disorders.

Conclusions

In summary, forced expression of the light-gated cation channel CatCh in aCMCs allows for effective and repeated termination of reentrant conduction by photocurrent-induced functional core expansion. These results indicate that optogenetic control of cardiac electrical function could serve as a novel anti-arrhythmic strategy, in which the arrhythmogenic substrate

itself provides the defibrillating current. This may trigger the exploration of a previously uninvestigated principle to develop safe and effective new therapies for cardiac arrhythmias.

Funding

This work was supported by the Dutch Heart Foundation [E. Dekker grant (2012/T023 to B.O.B.)] and the Netherlands Organization for Scientific Research [Mosaic grant (017007064 to M.C.E.)]. D.A.P. is a recipient of a Vidi grant (91714336) of the Netherlands Organization for Scientific Research.

Acknowledgements

We thank Karl Deisseroth and Charu Ramakrishnan (Stanford University, Stanford, CA, USA) for providing the lentiviral vector shuttle plasmid pLenti-CaMKIIa-hChr2(L132C)-EYFP-WPRE, Ivan Kazbanov (Ghent University, Ghent, Belgium) for writing analysis software, and Huybert van der Stadt for excellent technical support.

Conflict of interest: none declared.

References

1. Lip GY, Tse HF, Lane DA. Atrial fibrillation. *Lancet* 2012;379:648-661.
2. Iwasaki YK, Nishida K, Kato T, Nattel S. Atrial fibrillation pathophysiology: implications for management. *Circulation* 2011;124:2264-2274.
3. Schotten U, Verheule S, Kirchhof P, Goette A. Pathophysiological mechanisms of atrial fibrillation: a translational appraisal. *Physiol Rev* 2011;91:265-325.
4. Wellens HJ, Lau CP, Luderitz B, Akhtar M, Waldo AL, Camm AJ, Timmermans C, Tse HF, Jung W, Jordaens L, Ayers G. Atrioverter: an implantable device for the treatment of atrial fibrillation. *Circulation* 1998;98:1651-1656.
5. Dossdall DJ, Fast VG, Ideker RE. Mechanisms of defibrillation. *Annu Rev Biomed Eng* 2010;12:233-258.
6. Deisseroth K. Optogenetics. *Nat Methods* 2011;8:26-29.
7. Arrenberg AB, Stainier DY, Baier H, Huiskens J. Optogenetic control of cardiac function. *Science* 2010;330:971-974.
8. Bruegmann T, Malan D, Hesse M, Beiert T, Fuegemann CJ, Fleischmann BK, Sasse P. Optogenetic control of heart muscle in vitro and in vivo. *Nat Methods* 2010;7:897-900.
9. Jia Z, Valiunas V, Lu Z, Bien H, Liu H, Wang HZ, Rosati B, Brink PR, Cohen IS. Stimulating cardiac muscle by light: cardiac optogenetics by cell delivery. *Circ Arrhythm Electrophysiol* 2011;4:753-760.
10. Kleinlogel S, Feldbauer K, Dempski RE, Fotis H, Wood PG, Bamann C, Bamberg E. Ultra light-sensitive and fast neuronal activation with the Ca(2+)--permeable channelrhodopsin CatCh. *Nat Neurosci* 2011;14:513-518.
11. Bingen BO, Neshati Z, Askar SF, Kazbanov IV, Ypey DL, Panfilov AV, Schaliy MJ, de Vries AA, Pijnappels DA. Atrium-Specific Kir3.x Determines Inducibility, Dynamics and Termination of Fibrillation by Regulating Restitution-Driven Alternans. *Circulation* 2013;128:2732-2744.
12. Askar SF, Ramkisoensing AA, Schaliy MJ, Bingen BO, Swildens J, van der Laarse A, de Vries AA, Ypey DL, Pijnappels DA. Antiproliferative treatment of myofibroblasts prevents arrhythmias in vitro by limiting myofibroblast-induced depolarization. *Cardiovasc Res* 2011;90:295-304.
13. Salva MZ, Himeda CL, Tai PW, Nishiuchi E, Gregorevic P, Allen JM, Finn EE, Meuse L. Design of tissue-specific regulatory cassettes for high-level rAAV-mediated expression in skeletal and cardiac muscle. *Mol Ther* 2007;15:320-329.
14. Goncalves MA, Janssen JM, Nguyen QG, Athanasopoulos T, Hauschka SD, Dickson G, de Vries AA. Transcription factor rational design improves directed differentiation of human mesenchymal stem cells into skeletal myocytes. *Mol Ther* 2011;19:1331-1341.
15. Kubalak SW, Miller-Hance WC, O'Brien TX, Dyson E, Chien KR. Chamber specification of atrial myosin light chain-2 expression precedes septation during murine cardiogenesis. *J Biol Chem* 1994;269:16961-16970.
16. Bingen BO, Askar SF, Schaliy MJ, Kazbanov IV, Ypey DL, Panfilov AV, Pijnappels DA. Prolongation of minimal action potential duration in sustained fibrillation decreases complexity by transient destabilization. *Cardiovasc Res* 2013;97:161-170.
17. Hou L, Deo M, Furspan P, Pandit SV, Mironov S, Auerbach DS, Gong Q, Zhou Z, Berenfeld O, Jalife J. A major role for HERG in determining frequency of reentry in neonatal rat ventricular myocyte monolayer. *Circ Res*. 2010;107:1503-1511.
18. Pijnappels DA, Schaliy MJ, Ramkisoensing AA, van TJ, de Vries AA, van der Laarse A, Ypey DL, Atsma DE. Forced alignment of mesenchymal stem cells undergoing cardiomyogenic differentiation affects functional integration with cardiomyocyte cultures. *Circ Res* 2008;103:167-176.
19. Jalife J. Inward rectifier potassium channels control rotor frequency in ventricular fibrillation. *Heart Rhythm* 2009;6:S44-S48.

20. Jalife J. Deja vu in the theories of atrial fibrillation dynamics. *Cardiovasc Res* 2011;89:766-775.
21. Pandit SV, Berenfeld O, Anumonwo JM, Zaritski RM, Kneller J, Nattel S, Jalife J. Ionic determinants of functional reentry in a 2-D model of human atrial cells during simulated chronic atrial fibrillation. *Biophys J* 2005;88:3806-3821.
22. Weiss JN, Garfinkel A, Karagueuzian HS, Chen PS, Qu Z. Early afterdepolarizations and cardiac arrhythmias. *Heart Rhythm* 2010;7:1891-1899.
23. Schneider T, Martens PR, Paschen H, Kuisma M, Wolcke B, Gliner BE, Russell JK, Weaver WD, Bossaert L, Chamberlain D. Multicenter, randomized, controlled trial of 150-J biphasic shocks compared with 200- to 360-J monophasic shocks in the resuscitation of out-of-hospital cardiac arrest victims. Optimized Response to Cardiac Arrest (ORCA) Investigators. *Circulation*. 2000;102:1780-1787.
24. Janardhan AH, Gutbrod SR, Li W, Lang D, Schuessler RB, Efimov IR. Multistage electrotherapy delivered through chronically-implanted leads terminates atrial fibrillation with lower energy than a single biphasic shock. *J Am Coll Cardiol*. 2014;63:40-48
25. Chen PS, Feld GK, Kriett JM, Mower MM, Tarazi RY, Fleck RP, Swerdlow CD, Gang ES, Kass RM. Relation between upper limit of vulnerability and defibrillation threshold in humans. *Circulation* 1993;88:186-192.
26. Efimov IR, Cheng YN, Biermann M, Van Wagoner DR, Mazgalev TN, Tchou PJ. Transmembrane voltage changes produced by real and virtual electrodes during monophasic defibrillation shock delivered by an implantable electrode. *J Cardiovasc Electrophysiol* 1997;8:1031-1045.
27. Frazier DW, Wolf PD, Wharton JM, Tang AS, Smith WM, Ideker RE. Stimulus-induced critical point. Mechanism for electrical initiation of reentry in normal canine myocardium. *J Clin Invest* 1989;83:1039-1052.
28. Entcheva E. Cardiac optogenetics. *Am J Physiol Heart Circ Physiol* 2013;304:H1179-H1191.
29. Ikeda T, Uchida T, Hough D, Lee JJ, Fishbein MC, Mandel WJ, Chen PS, Karagueuzian HS. Mechanism of spontaneous termination of functional reentry in isolated canine right atrium. Evidence for the presence of an excitable but nonexcited core. *Circulation* 1996;94:1962-1973.
30. Yamazaki M, Honjo H, Ashihara T, Harada M, Sakuma I, Nakazawa K, Trayanova N, Horie M, Kalifa J, Jalife J, Kamiya K, Kodama I. Regional cooling facilitates termination of spiral-wave reentry through unpinning of rotors in rabbit hearts. *Heart Rhythm* 2012;9:107-114.
31. Zsebo KM, Yaroshinsky A, Rudy JJ, Wagner K, Greenberg B, Jessup M, Hajjar RJ. Long Term Effects of AAV1/SERCA2a Gene Transfer in Patients with Severe Heart Failure: Analysis of Recurrent Cardiovascular Events and Mortality. *Circ Res* 2014;114:101-108.
32. Ahmari SE, Spellman T, Douglass NL, Kheirbek MA, Simpson HB, Deisseroth K, Gordon JA, Hen R. Repeated cortico-striatal stimulation generates persistent OCD-like behavior. *Science* 2013;340:1234-1239.
33. Tye KM, Prakash R, Kim SY, Fenno LE, Grosenick L, Zarabi H, Thompson KR, Gradinaru V, Ramakrishnan C, Deisseroth K. Amygdala circuitry mediating reversible and bidirectional control of anxiety. *Nature* 2011;471:358-362.

Supporting information

Methods

Optical mapping of intracellular $[Ca^{2+}]$

The effects of Catch activation on intracellular Ca^{2+} concentrations and dynamics were assessed by optical mapping using Rhod-2-AM (Life Technologies, Bleiswijk, the Netherlands) as calcium-sensitive dye. To this purpose, neonatal rat atrial cardiomyocyte (aCMC) cultures were incubated with 2.5 μ M Rhod-2-AM in Dulbecco's modified Eagle's medium/HAM's F12 (DMEM/F12; 1:1, v/v; Life Technologies at 37°C for 30 minutes, after which cells were rinsed with DMEM/F12 to remove excess dye. Subsequently, cells were kept in the incubator for another 30 minutes to allow de-esterification of internalized AM esters after which optical signals were captured using the MiCAM ULTIMA-L imaging system (SciMedia, Costa Mesa, CA). During optical mapping of $[Ca^{2+}]$, cells were stimulated electrically with an epoxy-coated bipolar platinum electrode by delivery of 3 square suprathreshold electrical stimuli at 1000-ms intervals (1 Hz) prior to exposure to a 500-ms blue light pulse. Electrical pacing at 1 Hz was re-initiated 10, 20, 50, 100, 200, 500 and 1000 ms after the blue light had been switched off. The amplitude of the calcium transient, the basal Ca^{2+} signal and the occurrence of propagated calcium waves were analyzed using BrainVision Analyzer 1101 software (Brainvision, Tokyo, Japan).

Results

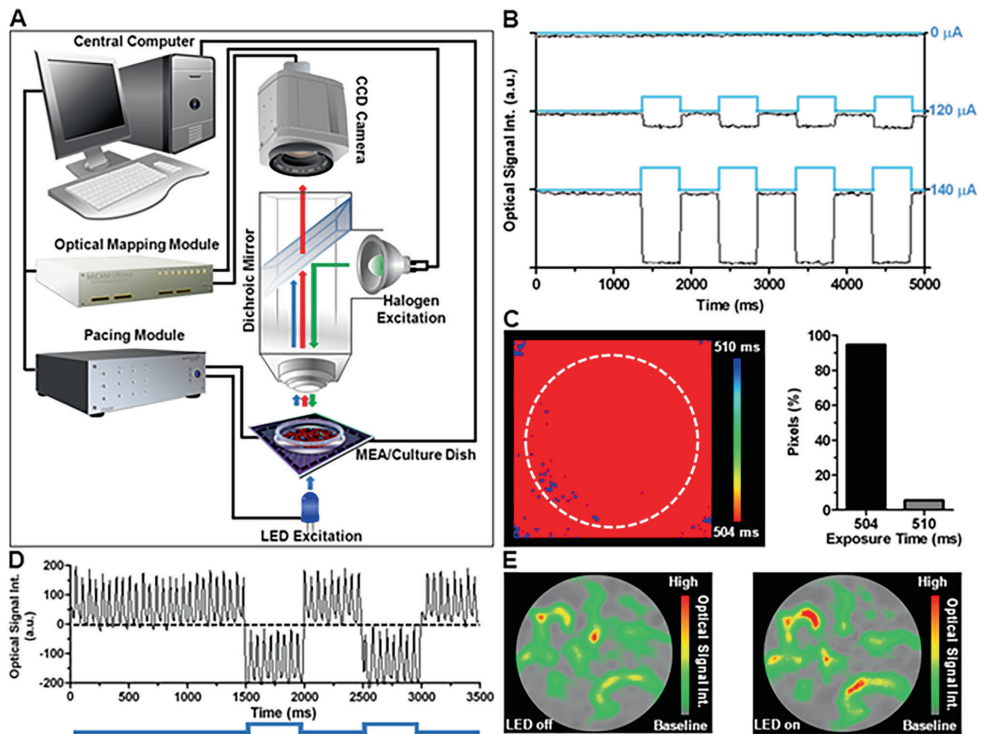
Optical mapping setup and light-emitting diode (LED)-induced shift in optical signal baseline

Using the setup depicted in Supplementary material online, *Figure S1A*, exposure of untransduced and unstimulated neonatal rat atrial cell cultures to blue light LED caused an immediate vertical drop in baseline optical signal (Supplementary material online, *Figure S1B*). The amplitude of the decrease in baseline optical signal depended on the light intensity. The temporal precision of the LED control by the pacing module was checked by calculating the exposure times detected by the charge-coupled device (CCD) camera. Upon a 500-ms blue light pulse, 94% of pixels showed an exposure time of 504 ms while for the remainder of the pixels the exposure time was 510 ms, exemplifying the tight control of the LED by the pacing module (Supplementary material online, *Figure S1C*). During reentry, optical signal baseline showed a similar downward shift as seen in the absence of activation. Importantly,

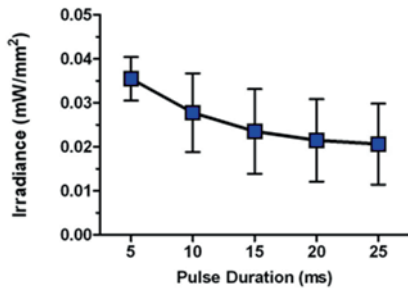
during the downward shift (LED-on period) the action potential (AP) morphology remained unchanged (Supplementary material online, *Figure S1D*). Offline adjustment of the baseline during the LED-on period did not principally alter optical signal distribution through the culture (Supplementary material online, *Figure S1E*). Thus, the optical mapping setup allowed direct correlation of events during the LED-on period with changes in electrophysiological parameters.

Electrophysiological effects of 500-ms light pulses on LV.CatCh~eYFP \uparrow -transduced aCMC cultures

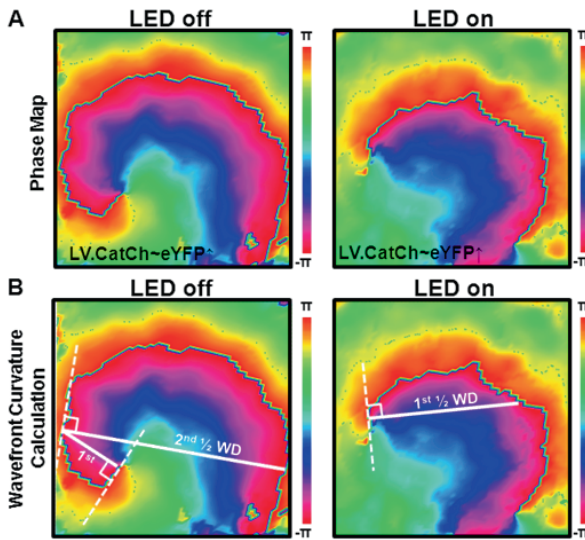
Because CatCh is permeable to Ca²⁺, prolonged light exposure could lead to perturbations in intracellular Ca²⁺ in LV.CatCh~eYFP \uparrow -transduced cultures, while the Na⁺ permeability of CatCh could lead to a decrease in excitability. As both effects, if persisting after turning off the LED, could be proarrhythmic, we tested the electrophysiological effects of the 500-ms blue light pulse used for termination of spiral wave reentry. To this purpose, aCMC cultures were paced electrically at 1 Hz prior to exposure to a 500-ms blue light pulse, during optical mapping using Rhod-2AM as Ca²⁺-binding dye (n=10) or di-4-ANEPPS (n=10) as a voltage-sensitive dye. Electrical pacing at 1 Hz was resumed 10, 20, 50, 100, 200, 500 and 1000 ms after turning off the blue LED. Comparison of the calcium transients prior to and after exposure to blue light did not reveal significant differences irrespective of the length of the LED off-to-electrical pacing interval (*Figure S4A,B*). Calcium transient amplitude after exposure to blue light was not significantly different from that before CatCh activation (100% vs 100.2 \pm 4.6% after light exposure) (*Figure S4C*). In addition, no propagated Ca²⁺ waves were found after the LED-on period. In 1 culture, reentry was induced by electrical pacing starting at 10 ms after the LED was turned off. In this particular case, pacing most likely occurred in the vulnerable window after repolarization from the LED-induced depolarizing current instead of being caused by perturbations in intracellular Ca²⁺ as no (propagated) calcium waves or reexcitations were found after exposure to a 500-ms blue light pulse (*Figure S4A,B,D*). In addition, conduction velocity, AP duration at 80% repolarization (APD₈₀) and AP amplitude in LV.CatCh~eYFP \uparrow -transduced aCMC cultures prior to light exposure did not significantly differ from those after exposure to blue light (conduction velocity: 100 vs 101.7 \pm 19.5% post LED-on, APD₈₀: 100 vs 103.4 \pm 10.5% after light exposure and AP amplitude: 100 vs 102.0 \pm 11.1% post LED-on) (*Figure S4E,F,G*). Together, these results indicate that prolonged (*i.e.* 500 ms) light exposure of LV.CatCh~eYFP transduced \uparrow -cultures, at the given conditions, does not cause pro-arrhythmicity due to persistent electrophysiological disturbances.



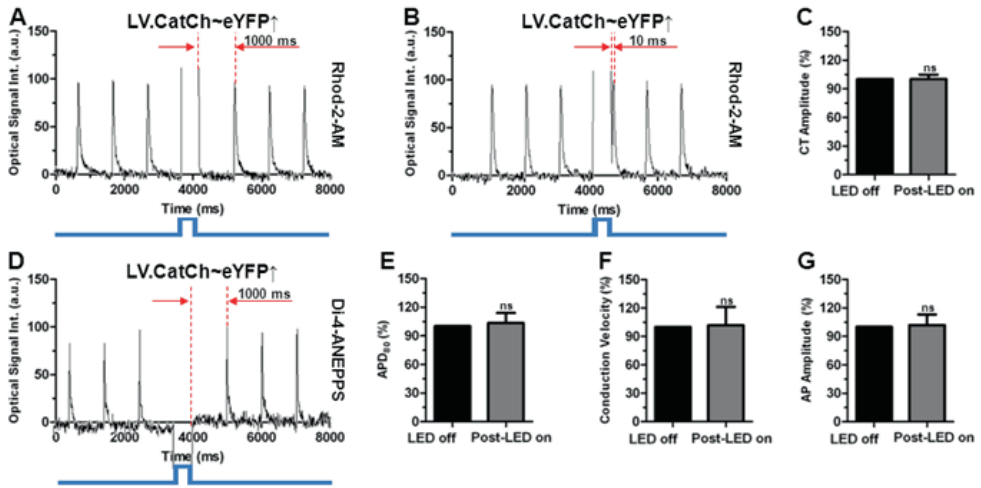
Supplementary Figure S1. Mapping setup and LED-induced shift in optical signal baseline. (A) Schematic representation of the mapping setup. (B) Examples of optical signal traces during exposure of an atrial culture to 500-ms blue LED light pulses of different intensities by changing the current input generated by the pacing module from 0 (upper lines) to 120 (middle lines) and 140 (lower lines) μA , showing that the magnitude of the decrease in baseline optical signal depends on the intensity of the blue light. (C) Exposure map and quantification of the exposure time per pixel of the charge-coupled device (CCD) camera measured at 6-ms intervals, showing exposure times of 504 and 510 ms for 94 and 4% of the pixels, respectively. (D) Typical example of an optical signal trace of an atrial culture during reentry induced by electrical burst pacing followed by exposure to two subsequent 500-ms blue LED light pulses, demonstrating that the drop in the baseline of the optical signal coincides with the exposure to blue light. The signal morphology remains unchanged, enabling direct read-out of the LED-on period in the optical mapping trace. (E) Snap shots of the optical signal in an atrial culture during reentry without exposure to blue light (left panel), and during exposure to blue light after correction of the baseline-drop artifact (right panel), showing similar optical signal distributions immediately before and 250 ms after the LED was turned on. MEA, multi-electrode array; a.u., arbitrary units.



Supplementary Figure S2. *Strength-duration analysis of optical pacing threshold.* Quantification of the average minimal irradiance necessary to elicit an AP at pulse durations of 5, 10, 15, 20 and 25 ms in LV.CatCh~eYFP⁺-transduced aCMC cultures (n=8).



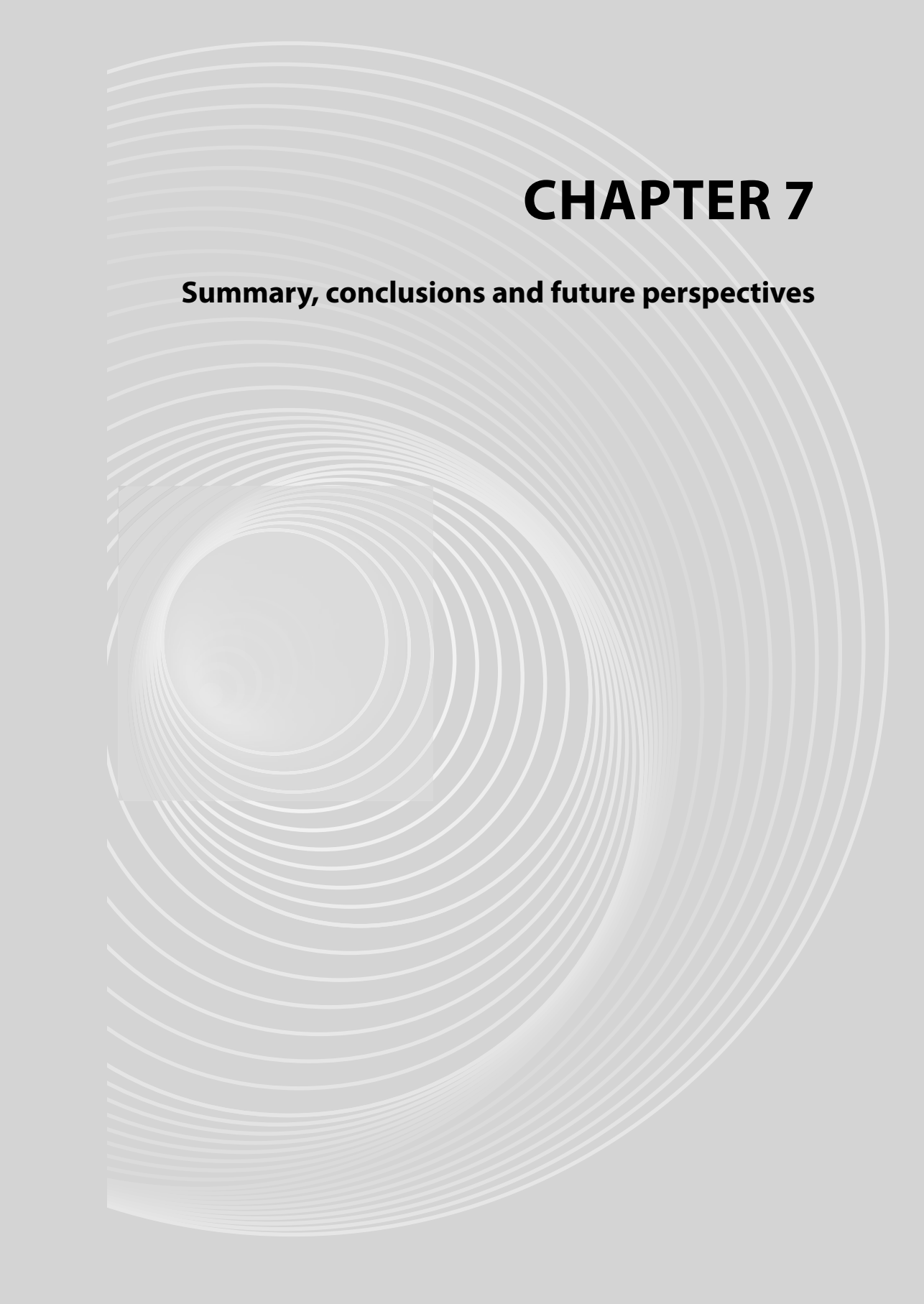
Supplementary Figure S3. *Wavefront curvature analysis.* (A) Typical examples of phase maps of an LV.CatCh~eYFP⁺-transduced aCMC culture before (left panel) and during (right panel) exposure to blue light. (B) The same phase maps as depicted in subfigure A including the lines used to measure the wavefront curvature. Dashed white lines represent tangent lines along the wavefront near the phase singularity. Uninterrupted white lines, perpendicular to the tangent line, represent the distance between the spiral wave tip and the wavefront at half winding (1st ½ WD). This shows that the 1st ½ WD is typically less than half of the second half winding distance, indicating an increase in wavefront curvature towards the phase singularity (left panel). The 1st ½ WD is increased during light exposure (right panel) indicating a decrease in wavefront curvature near the core.



Supplementary Figure S4. Electrophysiological effects of 500-ms light pulses on LV.CatCh~eYFP \uparrow -transduced aCMC cultures. (A,B) Typical examples of the Rhod-2-AM optical signals in 1-Hz electrically paced LV-CatCh~eYFP \uparrow -transduced aCMC cultures before and after exposure to a 500-ms blue light pulse. Electrical stimulation was resumed 1000 ms (A) or 10 ms (B) after turning off the LED. (C) Quantification of calcium transient (CT) amplitude based on Rhod-2-AM mapping. (D) Example of the di-4-ANEPPS optical signal in an LV.CatCh~eYFP \uparrow -transduced aCMC culture before and after exposure to a 500-ms blue light pulse. Electrical stimulation was resumed 1000 ms after turning off the LED. Quantification of (E) AP duration at 80% repolarization (APD₈₀), (F) conduction velocity and (G) action potential (AP) amplitude, based on voltage-sensitive dye mapping, after exposure to blue light as a percentage of these characteristics prior to exposure to light. ns: non-significant vs LED off using a Wilcoxon signed rank test.

Supplementary Movie 1 Typical example from an optical mapping experiment in a neonatal rat aCMC culture transduced with LV.CatCh~eYFP \uparrow during light-induced termination of spiral wave reentry. The upper part shows the high-pass-filtered optical signal in a 5-mm² square in the culture during spiral wave reentry induced by burst pacing, followed by a 500-ms blue light pulse causing spiral wave termination by a phase singularity-boundary collision. Note: High-pass-filtering caused the blue light-dependent downward shift in optical signal baseline to change into two short (± 18 ms duration) artifacts occurring when the LED is turned on and when the LED is turned off only. The lower part displays the corresponding spatially filtered optical AP progression prior to, during and after light-induced spiral wave termination.

Supplementary Movie 2 Typical example from an optical mapping experiment in a neonatal rat aCMC culture transduced with LV. CatCh~eYFP \uparrow during light-induced termination of spiral wave reentry. The upper part shows the high-pass-filtered optical signal in a 5-mm² square in the culture during spiral wave reentry induced by burst pacing, followed by a 500-ms blue light pulse causing spiral wave termination by a phase singularity-phase singularity collision. Note: High-pass-filtering caused the blue light-dependent downward shift in optical signal baseline to change into two short (± 18 ms duration) artifacts occurring when the LED is turned on and when the LED is turned off only. The lower part displays the corresponding spatially filtered optical AP progression prior to, during and after light-induced spiral wave termination.



CHAPTER 7

Summary, conclusions and future perspectives

Summary and conclusions

The general introduction of this thesis, **Chapter 1**, describes normal cardiac function and in more detail, the mechanisms of action potential initiation and propagation in the healthy heart. Furthermore, the effects of ischemic heart disease are discussed, the current treatment options and their limitations, followed by the potentials of regenerative medicine for cardiac disease, and the current status and problems that need to be overcome in order to bring these therapies a step closer to clinical practice. The aim of this thesis was to explore from a mechanistic point of view, cellular modification processes associated with heart disease, as well as harnessing cellular modification for treatment and prevention of detrimental electrophysiological consequences of heart disease.

Chapter 2 provides a comprehensive description for the generation of iPSCs from fibroblasts derived from four different species, namely mouse, rat, pig and human. In order to capitalize on the potential of pluripotent stem cell-based applications, such as patient-specific disease modelling or regenerative medicine, it is of vital importance to be able to create iPSCs with high quality and efficiency. We therefore selected four widely used model species and described an efficient method for generating iPSC lines of high quality.

Chapter 3 describes the result of a high throughput screen for cytokines and signalling molecules to induce cardiac lineage specification. To this end, a transgenic mouse embryonic stem cell (ESC) reporter line with the base promoter and cardiac enhancer region for Nkx2.5 coupled with eGFP, was used. A panel of 44 cytokines, growth factors and signalling molecules were tested by exposure of cells in a dose-response curve. Cardiac differentiation was assessed by flow cytometry quantification of eGFP⁺ cells, representing Nkx2.5⁺ cardiac progenitor cells (CPCs). This screen identified insulin-like growth factors (IGF1, IGF2 and insulin) as positive regulators of cardiac differentiation. Further analysis revealed that temporal stimulation with IGF resulted in selective proliferation in the Brachyury⁺ early mesodermal cell population, thereby selectively expanding cardiac precursor cells. This effect was not seen during simultaneous inhibition of Akt or mTOR, known downstream signalling molecules in the IGF pathway. Elucidating the intricate steps of signalling pathway activation and inhibition can be mimicked during the dynamic process of cell lineage specification. Early timed IGF pathway activation was shown to direct cells toward a cardiac lineage, and could ultimately lead to more efficient cardiac differentiation. Robust cardiomyocyte differentiation is a prerequisite to meet the large demand for transplanted cells in regenerative therapies.

In **Chapter 4** the electrophysiological effects of forced cellular fusion of human ventricular scar cells (hVSCs) with neonatal rat ventricular myocytes (NRVMs) was investigated. Scar cells were isolated from post-myocardial infarction scars of human left ventricles and characterized by immunological assay. Cultured hVSCs were predominantly (myo-)fibroblasts and approximately 40% of cells showed characteristic α -SMA striation. Upon co-culturing hVSCs with NRVMs (20%/80%), cultures showed action potential duration (APD) prolongation, increased APD dispersion and a markedly greater number of early after-depolarizations at 1 Hz pacing compared to non-hVSC containing NRVM cultures. Transduction of hVSCs with fusogenic *vesicular stomatitis virus-G* (VSV-G) allowed partially controllable cell membrane fusion with surrounding cells. This resulted in heterokaryonic cell clusters, which retained electrophysiological properties from hVSCs as well as NRVMs, but mostly resembled NRVMs. Importantly, in contrast to hVSCs, heterokaryons were electrically excitable and had large repolarization reserve. Patch clamp measurements confirmed presence of greater outward K_v current in heterokaryons compared to NRVMs and hVSCs. Fused co-cultures showed increased Cx43 expression, indicating better coupling, as well as a more negative membrane diastolic potential compared to unfused cultures. Fused hVSC/NRVM co-cultures showed an electrophysiologically favourable phenotype (cancellation of APD prolongation and dispersion, decreased incidence of EADs). This study provides proof of principle that forced cellular fusion is able to undo detrimental arrhythmogenic effects resulting from the presence of fibroblastic cells as occurs in diffuse fibrosis. Whether forced cellular fusion could ever become a therapeutic modality remains unlikely. However, fusion of electrophysiologically distinct cell types, and thereby removing their intercellular barriers, creates a less arrhythmogenic substrate and is therefore an interesting model to gain new insights into fibrosis-mediated arrhythmia.

In **Chapter 5** the results of complimentary *in silico* and *in vitro* models are presented in order to study the mechanisms underlying re-entry initiation and dynamics in remodelled cardiac tissue, characterized by fibrosis and conduction slowing. A common effect of cardiac injury is (local areas of) conduction slowing, usually due to tissue remodelling, such as fibrosis and decreased Cx43 expression. Therefore, NRVMs were cultured with 30% fibroblasts and cells were transduced with lentiviral vectors encoding short-hairpin RNAs directed against Cx43 in different dosages. Degree of Cx43 knock-down inversely correlated with culture conduction velocity. Upon rapid pacing, spatially discordant APD alternans was observed. Discrete areas of APD alternans were organized throughout the culture, and termed alternans phase islands (APIs), given their island-like patterns on culture maps. Wavebreaks occurred at borders between APIs of opposite polarity (APIs with long-short conformation APD alternans; L-S, lying adjacent to APIs with short-long alternans conformation; S-L). Extent of conduction slowing correlated with API formation, and ultimately re-entry complexity. This study provides

mechanistic insight into arrhythmia initiation and dynamics in a model of conduction slowing and fibrosis, representing remodelled ventricular tissue.

Chapter 6 describes a new approach to terminate re-entry once it has been established. To this purpose, atrial cardiomyocytes isolated from neonatal rats were cultured and transduced with lentiviral vectors encoding CatCh, a light-sensitive ion channel. These channelrhodopsins were originally isolated from algae and have recently become widely used in the optogenetics field, where protein behaviour can be modulated with high spatiotemporal control by exposure to light stimulation. Brief light pulses (10 ms blue light, 470 nm wavelength) were able to generate enough depolarizing current to evoke action potentials. After stable re-entry induction by rapid electrical pacing was established, cells were exposed to a brief 500 ms blue light pulse, which resulted in rapid re-entry termination in 100% of cases in CatCh-transduced cultures compared to 0% termination in eGFP-transduced control cultures. Mechanistically, rotor core size was shown to increase, thereby destabilizing the phase singularity which caused it to drift and collide with culture boundaries or phase singularities of opposite chirality. These results demonstrate the feasibility of arrhythmia termination by optogenetic engineering of cardiomyocytes, which equips cells with highly controllable ion channels, which, upon an external cue are able to intrinsically generate a defibrillating current.

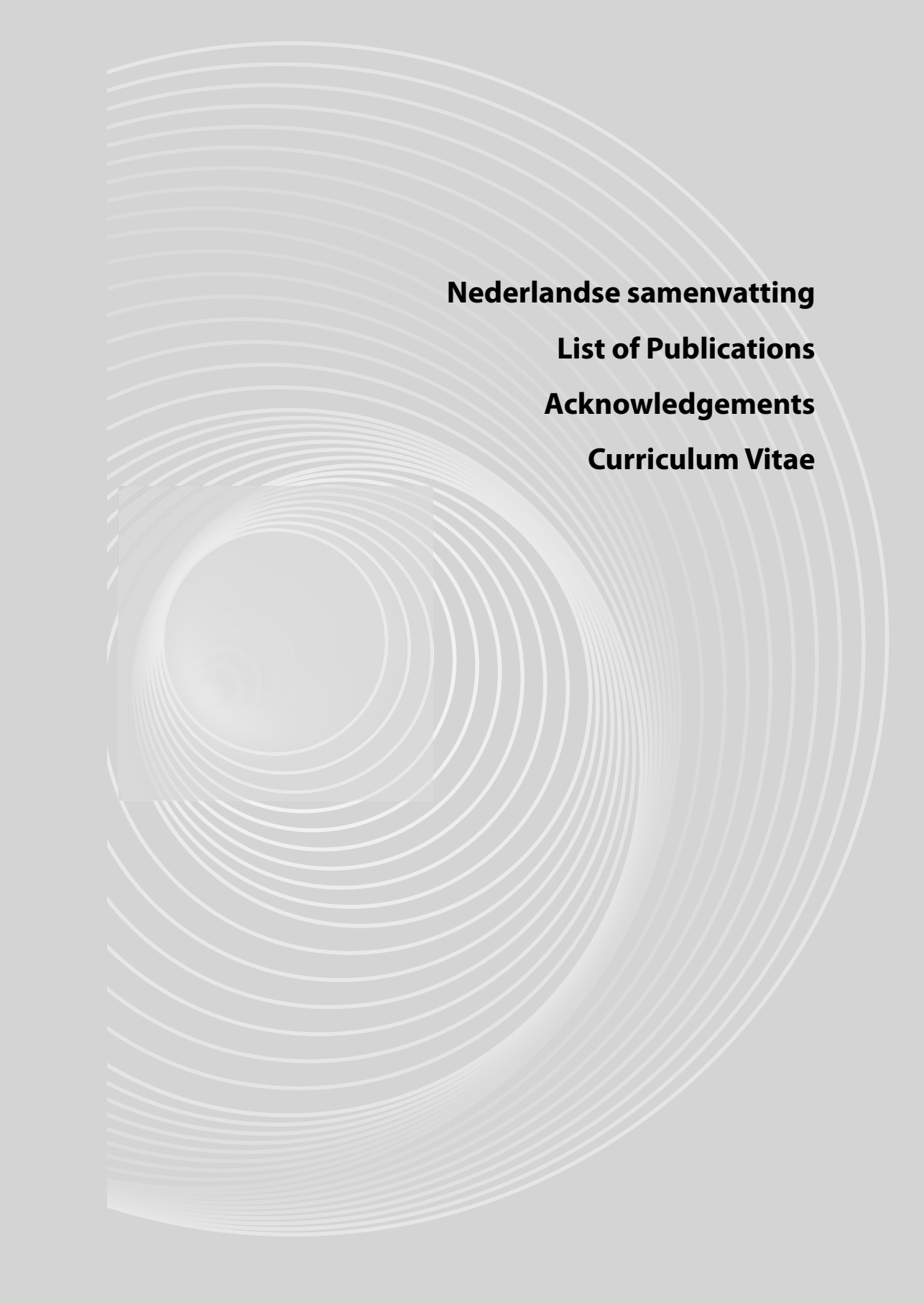
Future perspectives

Tremendous efforts have been made so far in order to bring regenerative therapies such as cellular or genetic interventions a step closer to clinical practice. These studies have shown that a lot more hurdles need to be overcome in order to achieve this important goal. First, differentiation protocols need to be further refined for efficient and reproducible cardiomyocyte generation from pluripotent stem cells. Many lessons can be learned from cardiac lineage specification and maturation in the developing embryo. Heart development is a complex multistage process, where cells are rapidly being exposed to molecular cues. This results in precisely timed activation of specific signalling pathways, which induce a specific set of transcription factors. Unravelling the spatiotemporal sequence of activation and inhibition of the signalling pathways and downstream transcription factors can give much insight into cardiac lineage specification, which can be mimicked *in vitro* by precise exposure of differentiating stem cells to signalling molecules in order to direct cardiac development. Given the complex nature of this process, a simpler, but laborious approach would be to conduct detailed screening for signalling molecules associated with cardiac development. Since signalling pathways can be active during very brief developmental steps, it will be important to identify at higher resolution cell lineage markers of intermediate developmental stages. This

can aid the molecular guidance of cells towards mature cardiomyocytes. These studies could potentially also lead to an improved set of factors that need to be overexpressed in order to achieve direct reprogramming into reprogrammed cardiomyocytes that are indistinguishable from native cells. This will also be important in order to attain cardiac cells that are mature, both electrophysiologically as well as in terms of contractility. In addition, improved cellular transplant homing and graft survival will be necessary to achieve sustained transplantation effects. Cellular guidance and alignment into the existing cardiac syncytium would allow for optimal graft function and simultaneously reduce arrhythmic activity associated with the graft. Further studies should give more insight into cellular integration into the host tissue, a process that is also disturbed in cardiac fibrosis. The arrhythmogenic substrate of cardiac fibrosis likely shares characteristics of transplanted cells, which are also poorly aligned and not integrated within the host tissue. Control over guided cellular alignment could be achieved by molecular gradients, such as in the developing embryo, or using a tissue patch of extracellular matrix containing scaffold, on which the cells are aligned by micro-patterning. Exact host tissue architecture can be visualized through advanced 3-dimensional imaging techniques. These images can subsequently be reconstructed in the lab by 3-dimensional printing of scaffolds to create an exact fit of transplantable cells. Micro-surgery could then be performed to create a perfectly aligned tissue patch.

Transplanted cells need to be well connected to surrounding host cells, a process that would likely benefit from cellular alignment. Suboptimal connection could lead to conduction slowing, thereby creating a vulnerable substrate for re-entry initiation through occurrence of action potential duration alternans phase islands (APIs). Future research should focus on the molecular mechanisms related to API formation. If, for example, APIs are related to alterations in an ionic current, this could become a promising drug target in order to prevent re-entry-based arrhythmia.

Lastly, cell grafts could be protected from the detrimental effects of arrhythmia by equipping them with an intrinsic defibrillator. The most elegant solution would be if cells could sense arrhythmic activity and activate an ion channel, thereby creating a defibrillating current. Although our studies provide proof of principle for cells to be able to generate an intrinsic defibrillating current, still many more steps are still to overcome in order to achieve cells with artificial intelligence that is able to self-defibrillate in case of arrhythmia. It is likely that an intricate molecular engineering process would lie at the basis of this solution, where an existing or transgenic ion channel would sense rapid membrane potential fluctuations and thereby activate itself or another ion channel, which could provide a current sufficiently strong to overcome the arrhythmic activity. Cellular and genetic interventions for heart disease have met many drawbacks which have so far prevented swift translation to clinical practice. Recent efforts have provided many clues that need to be resolved, but simultaneously give new hope for tailored therapies at the cellular and molecular level.



Nederlandse samenvatting

List of Publications

Acknowledgements

Curriculum Vitae

Nederlandse samenvatting

De algemene introductie van dit proefschrift, **Hoofdstuk 1**, beschrijft de normale hartfunctie en in meer detail, de mechanismen van actie potentiaal initiatie en propagatie in het gezonde hart. Verder worden de effecten van ischemische hartziekten beschreven, de huidige behandelopties en hun beperkingen, gevolgd door de mogelijkheden van regeneratieve therapieën voor hartziekten, alsmede de huidige status en problemen die dienen te worden opgelost om deze behandelingsmogelijkheden een stap dichterbij de klinische praktijk te brengen. Het doel van dit proefschrift was het vanuit een mechanistisch oogpunt onderzoeken van celmodificatieprocessen die betrokken zijn bij hartziekten, alsmede de toepassing van celmodificatie voor de behandeling en preventie van schadelijke ziekteprocessen op het electrofysiologisch functioneren van het hart.

Hoofdstuk 2 geeft een uitgebreide beschrijving van het genereren van geïnduceerde pluripotente stam cellen (iPSCs) met fibroblasten (bindweefselcellen) als uitgangscellen, voor vier verschillende soorten, namelijk muis, rat, varken en mens. Om gebruik te kunnen maken van het potentieel die applicaties met pluripotente stamcellen bieden, zoals patiënt-specifieke ziektemodellen of regeneratieve therapieën, is het van cruciaal belang om iPSCs te kunnen generen van hoge kwaliteit en efficiëntie. We kozen daarom vier veelgebruikte diermodellen en beschreven een efficiënte methode voor het ontwikkelen van iPSC lijnen van hoge kwaliteit.

In **Hoofdstuk 3** worden de resultaten beschreven van een systematische studie naar cytokines en signaleringsmoleculen die betrokken zijn bij de specificatie van de cardiale cellijn. Hiervoor werd een transgene embryonale stam cel (ESC) lijn uit muizen gebruikt. Deze ESC lijn was genetisch gemodificeerd met een basepromotor en cardiale enhancer regio van de Nkx2.5 transcriptie factor gekoppeld aan eGFP, zodat de cellijn kon worden gebruikt als reporterlijn. Een serie van 44 cytokines, groeifactoren en signaleringsmoleculen werden onderzocht door de cellen systematisch te behandelen met verschillende doses. Cardiale differentiatie werd onderzocht door kwantificatie van eGFP⁺ cellen middels flow cytometrische techniek. Deze cellen waren Nkx2.5⁺ cardiale voorlopercellen (cardiac progenitor cells; CPCs). Deze studie identificeerde insulin-like growth factors (IGF1, IGF2, insuline) als regulatoreiwitten die betrokken zijn bij cardiale differentiatie. Verdere analyse toonde dat tijdelijke stimulatie met IGF resulteerde in selectieve proliferatie van de Brachyury⁺ vroege mesodermale celpopulatie, waardoor selectief cardiale voorlopercelpopulatie werd vermeerderd. Dit effect was niet aanwezig bij gelijktijdige inhibitie van Akt of mTOR, bekende signaleringsmoleculen die actief zijn in de latere IGF signaleringscascade. Het ophelderen van de complexe processen van de activatie en inactivatie van signaleringscascades is belangrijk, omdat het kan worden

nagebootst tijdens het dynamische proces van cellijnspecificatie. Vroege tijdelijke activatie van de IGF signaleringscascade dirigeert cellen richting een cardiaal fenotype, en kan uiteindelijk leiden tot efficiëntere cardiale differentiatie. Het kunnen controleren van robuuste differentiatie van pluripotente stamcellen tot hartspiercellen is, gezien de grote vraag naar transplantiecellen, een vereiste voor regeneratieve therapieën.

In **Hoofdstuk 4** worden de electrofysiologische effecten van gedirigeerde celfusie onderzocht van humane ventriculaire littekencellen (human ventricular scar cells; hVSCs) met neonatale rat-hartspiercellen (neonatal rat ventricular myocytes; NRVMs). Littekencellen werden geïsoleerd uit post-myocard infarct littekens van humane linker ventrikels en gekarakteriseerd middels immunocytologische onderzoeken. Gekweekte hVSCs waren voornamelijk (myo-)fibroblasten en ongeveer 40% toonden karakteristieke α -SMA striatie patronen. Co-kweken bestaande uit hVSCs en NRVMs (20%/80%) toonden actie potentiaal duur (APD) verlenging, toename van APD dispersie en significant meer vroege na-depolarisaties (early after-depolarisations; EADs) tijdens 1 Hz elektrische stimulatie, vergeleken met kweken bestaande uit NRVMs, maar geen hVSCs. Genetische transductie van hVSCs met fusogeen *vesicular stomatitis virus-G* (VSV-G) faciliteerde een deels controleerbare celmembraanfusie van de hVSCs met omliggende cellen. Dit resulteerde in fusie producten bestaande uit celclusters die waren ontstaan uit hVSCs en NRVMs (heterokaryons). Heterokaryons toonden meer expressie van Connexine 43 (Cx43) dan ongefuseerde hVSCs, wat kan duiden op betere elektrische koppeling met omliggende cellen. Heterokaryons waren electrofysiologisch verschillend van zowel NRVMs als hVSCs en toonden verminderde exciteerbaarheid vergeleken met NRVMs. Patch-clamp metingen lieten een grote repolarisatie capaciteit zien, alsmede een grotere K_v stroom in heterokaryons vergeleken met NRVMs en hVSCs. Gefuseerde hVSC/NRVM co-kweken hadden een electrofysiologisch gunstiger fenotype dan niet-gefuseerd hVSC/NRVM co-kweken (vermindering van APD prolongatie en dispersie en verminderd aantal EADs). Deze studie biedt een nieuw concept, namelijk dat gedirigeerde celfusie in staat is om de schadelijke arrhythmogene condities tegen te gaan, die het gevolg zijn van de aanwezigheid van fibroblastische cellen, zoals tijdens fibrose. Of gedirigeerde celfusie ooit een therapeutische entiteit wordt blijft onwaarschijnlijk. Echter, fusie van electrofysiologisch verschillende celtypes, leidt tot verschillende processen die het arrhythmogene substraat tegengaan, zoals verbeterde cellulaire koppeling, afname van de intercellulaire weerstanden, en toename van exciteerbaarheid en repolariserend vermogen. Hierdoor is het een interessant model voor het verkrijgen van nieuwe inzichten in hartritmestoornissen op basis van fibrotische processen.

In **Hoofdstuk 5** worden de resultaten van complementaire *in silico* en *in vitro* modellen gepresenteerd voor het bestuderen van de mechanismen die ten grondslag liggen aan

het ontstaan en de ontwikkeling en dynamiek van een bepaalde ritmestoornis (re-entry) in geremodelleerd hartweefsel. Een veelvoorkomend gevolg van hartspierschade is remodellering van het weefsel, met name (lokale) geleidingsvertraging (b.v. door afregulatie van Cx43) en fibrose. Om dit te onderzoeken werden er co-kweken gemaakt bestaande uit NRVMs met 30% fibroblasten en cellen werden genetisch gemodificeerd middels transductie met lentivirale vectoren die coderen voor inhibitoire RNAs (short-hairpin RNAs), gericht tegen Cx43 in verschillende doseringen. De mate van Cx43 inhibitie was omgekeerd gecorreleerd met de geleidingsnelheid. Middels snelle stimulatie werd APD alternans waargenomen, wat discordant was in ruimte (ruimte-discordante APD alternans). Deze ruimte-discordante APD alternans organiseerde zich als discrete gebieden in het weefsel, zogenaamde alternans fase eilanden (alternans phase islands; APIs). Golfbreuken ontstonden op de grens tussen APIs van tegengestelde polariteit (APIs met lang-kort conformatie; L-K, die direct naast APIs met kort-lang conformatie; K-L lagen. De mate van geleidingsvertraging correleerde met API formatie en uiteindelijk re-entry complexiteit. Deze studie biedt mechanistische inzicht in het ontstaan van ritmestoornissen, alsmede hun dynamiek, in een model van geleidingsvertraging en fibrose.

In **Hoofdstuk 6** wordt een nieuwe benadering beschreven voor het termineren van re-entry als het eenmaal ontstaan is. Hiervoor werden atriale hartspiercellen geïsoleerd uit neonatale ratten en gekweekt en getransduceerd met lentivirale vectoren die coderen voor CatCh, een licht-gevoelig ion-kanaal. Deze licht-gevoelige ion-kanalen waren oorspronkelijk geïsoleerd uit algen en zijn recent veel toegepast in de optogenetica, wat zich toelegt op het moduleren van eiwitkarakteristieken middels stimulatie met licht. Dit biedt grote controle in tijd en ruimte. Korte lichtpuls (10 ms blauw licht, 470 nm golflengte) waren in staat om genoeg depolariserende stroom te genereren zodat actie potentialen konden worden opgewekt. Nadat stabiele re-entry inductie werd bewerkstelligd middels snelle elektrische stimulatie, werden cellen gestimuleerd met een korte 500 ms-durende blauwe lichtpuls, welke resulteerde in snelle re-entry terminatie in 100% van de gevallen in CatCh-getransduceerde kweken, maar in 0% van de gevallen in eGFP-getransduceerde controle kweken. Mechanistisch gezien was er sprake van expansie van de rotor kerngrootte, waardoor de fase singulariteit werd gedestabiliseerd, wat leidde tot driften en collisie met de kweekgrenzen of fase singulariteiten van tegengestelde chiraliteit. Deze resultaten demonstreren de mogelijkheid van ritmestoornis terminatie middels optogenetische modificatie van hartspiercellen, waardoor deze cellen worden uitgerust met ion-kanalen die goed controleerbaar zijn, en waardoor ze na toediening van een extern signaal, in staat zijn een intrinsieke stroom op te wekken die in staat is om een ritmestoornis te doen eindigen.

Toekomstperspectieven

Enorme inspanningen zijn tot nu toe geleverd voor het dichterbij brengen van regeneratieve therapieën, zoals cellulaire en genetische interventies naar de klinische praktijk. Deze studies hebben aangetoond dat veel hindernissen dienen te worden genomen alvorens dit belangrijke doel nagestreefd kan worden. Op de eerste plaats moeten differentiatietechnieken en –protocollen verder worden uitgewerkt voor het bereiken van hartspiercelgeneratie uit pluripotente stamcellen, die efficiënt en reproduceerbaar is. Veel kan hierbij geleerd worden van cardiale cellijn specificatie en maturatie in het ontwikkelende embryo. Hartontwikkeling is een complex proces, bestaande uit verschillende stadia, waarin cellen afwisselend worden blootgesteld aan moleculaire signalen. Dit resulteert in een precies getimede activatie van specifieke signaleringscascades, die leiden tot de inductie van een specifieke combinatie van transcriptie factoren. Het ontrafelen van de exacte volgorde in plaats en tijd van de activatie en inhibitie van de signaleringscascades en latere latere transcriptie factoren, kan inzicht geven in cardiale cellijn specificatie, welke kan worden nagebootst *in vitro* door precieze toediening van signaleringsmoleculen aan stamcellen die aan het differentiëren zijn, zodat cardiale ontwikkeling gereguleerd kan worden. Gezien de complexiteit van dit proces, is een simpelere, maar bewerkelijke benadering het uitvoeren van een gedetailleerde systematisch screenend onderzoek voor het identificeren van signaleringmoleculen die betrokken zijn bij cardiale differentiatie. Aangezien signaleringscascades kunnen worden geactiveerd tijdens kortdurende ontwikkelingsstappen, is het belangrijk om met hoge resolutie cellijn-specifieke markereiwitten te identificeren, die specifiek zijn voor intermediaire ontwikkelingsstadia. Dit kan de moleculaire begeleiding van cellen naar mature hartspiercellen verbeteren. Deze studies kunnen mogelijk ook leiden tot een verbeterde combinatie van factoren die tot overexpressie dienen te worden gebracht voor het bereiken van directe reprogramming naar hartspiercellen, die niet te onderscheiden zijn van native cellen uit het werkende hart. Dit is ook belangrijk voor het verkrijgen van cardiale cellen die matuur zijn, zowel uit electrofysiologisch als uit mecanisch oogpunt (in termen van contractiliteit). Voorts zijn verbeterde lokalisatie van getransplanteerde cellen in het zieke substraat, alsmede verbeterde overleving van de graft noodzakelijk voor het bereiken van langdurige transplantatie effecten. Cellulaire begeleiding en organisatie en inbedding in het bestaande cardiale syncytium zorgt voor optimale graft functie en leidt tegelijkertijd tot verminderde ritmestoornissen geassocieerd met het implantaat. Verdere studies moeten meer inzicht geven in cel-integratie in het ontvangende weefsel, een proces dat ook verstoord is in cardiale fibrose. Het arrhythmogene substraat van cardiale fibrose heeft waarschijnlijk overeenkomstige kenmerken met getransplanteerde cellen, aangezien deze ook slecht ingebed en niet optimaal geïntegreerd zijn. Controle over begeleide cellulaire inbedding zou kunnen worden bereikt middels moleculaire gradiënten,

gelijkaan in het ontwikkelende embryo, of door gebruik van een weefsel met een steunstructuur van extracellulaire matrix. Hierop kunnen cellen worden ingebed in de juiste richting middels micro-patronen. Gedetailleerde weefselarchitectuur van het ontvangende orgaan kan worden gevisualiseerd middels 3-dimensionale afbeeldingstechnieken. Deze afbeeldingen kunnen vervolgens worden gereconstrueerd in het laboratorium door middel van 3-dimensionale print-technieken van steunstructuren, om hiermee een exacte pas maat te vinden voor de getransplanteerde cellen. Micro-chirurgische technieken kunnen worden gebruikt voor het transplanteren van een optimaal geïntegreerd transplantatie-weefsel.

Getransplanteerde cellen dienen goed verbonden te zijn met omliggende cellen, een proces dat waarschijnlijk wordt verbeterd door optimale inbedding. Suboptimale verbinding en koppeling kan leiden tot geleidingsvertraging in het geval van de voortgeleiding van het elektrische signaal door het hart, waardoor er een kwetsbaar substraat ontstaat voor re-entry initiatie, bijvoorbeeld door het ontstaan van APD alternans fase eilanden (APIs). Toekomstig onderzoek zou zich moeten richten op de moleculaire mechanismen die zijn gerelateerd aan het ontstaan van APIs. Als, bijvoorbeeld, het ontstaan van APIs zijn gerelateerd aan veranderingen in ion-stromen, dan zouden de betrokken ion-kanalen een mogelijk doelwit kunnen zijn voor het ontwikkelen van nieuwe medicijnen voor de voorkoming van hartritmestoornissen die gebaseerd zijn op re-entry.

Tot slot, celtransplantaten zouden kunnen worden beschermd tegen de schadelijke gevolgen van ritmestoornissen door ze uit te rusten met een intrinsieke defibrillator. De meest elegante oplossing hiervoor zou zijn als de cellen in staat zouden zijn om zelf op te kunnen ontdekken wanneer er een ritmestoornis optreedt, en hierop kunnen reageren door activatie van een ion-kanaal, waardoor een defibrillerende stroom geactiveerd wordt. Hoewel er studies zijn die een bewijs van het concept leveren voor het principe dat cellen een intrinsieke defibrillerende stroom kunnen opwekken, zijn er nog veel stappen die genomen dienen te worden om te komen tot een hartcel met de kunstmatige intelligentie voor zelf-terminatie van hartritmestoornissen. Het is waarschijnlijk dat een complex moleculaire uitrusting van cellen een oplossing kan vormen. Hierbij zou een bestaand of transgeen ingebouwd ion-kanaal in staat zijn om waar te nemen dat er een ritmestoornis is ontstaan (bijvoorbeeld door waarneming van hoog-frequente membraan potentiaal veranderingen), en hierna zichzelf of een ander ion-kanaal kan activeren, welke in staat is om een stroom te activeren die sterk genoeg is om de ritmestoornis te termineren. Cellulaire en genetische interventies voor hartziekten is tot nog toe een moeizaam proces gebleken, waardoor snelle translatie naar de klinische praktijk grotendeels is uitgebleven. Recente ontwikkelingen hebben veel nieuwe inzichten geleverd van problemen die dienen te worden overwonnen, maar bieden tegelijkertijd nieuwe hoop voor individuele therapieën op cellulair of moleculair niveau.

List of Publications

Full papers

Engels MC[†], Majumder R[†], de Vries AA[†], Panfilov AV[†], Pijnappels DA[†]. Islands of spatially discordant APD alternans underlie arrhythmogenesis by promoting electrotonic dyssynchrony in models of fibrotic rat ventricular myocardium. *Sci. Rep.*, 2016;6:24334.

Engels MC[†], Askar SF[†], Jangsangthong W, Bingen BO, Majumder R, Feola I, Liu J, Versteegh MI, Braun J, Klautz RJ, Zeppenfeld K, Ypey DL, SchaliJ MJ, de Vries AA[†], Pijnappels DA[†]. Forced fusion of human ventricular scar cells with cardiomyocytes suppresses arrhythmogenicity in a co-culture model. *Cardiovasc Res.* 2015;107:601-612.

Bingen BO[†], Engels MC[†], SchaliJ MJ, Jangsangthong W, Neshati Z, Feola I, Ypey DL, Askar SF, Panfilov AV, Pijnappels DA[†], de Vries AA[†]. Light-induced termination of spiral wave arrhythmias by optogenetic engineering of atrial cardiomyocytes. *Cardiovasc Res.* 2014;104:194-205.

Sturzu AC, Rajarajan K, Passer D, Plonowska K, Riley A, Tan TC, Sharma A, Xu AF, Engels MC, Feistritzer R, Li G, Selig MK, Geissler R, Robertson KD, Scherrer-Crosbie M, Domian IJ, Wu SM. Fetal mammalian heart generates a robust compensatory response to cell loss. *Circulation.* 2015;132:109-121.

Engels MC, Rajarajan K, Feistritzer R, Sharma A, Nielsen UB, SchaliJ MJ, de Vries AA, Pijnappels DA, Wu SM. Insulin-like growth factor promotes cardiac lineage induction in vitro by selective expansion of early mesoderm. *Stem Cells.* 2014;32:1493-1502.

Chen JX, Krane M, Deutsch MA, Wang L, Rav-Acha M, Gregoire S, Engels MC, Rajarajan K, Karra R, Abel ED, Wu JC, Milan D, Wu SM. Inefficient reprogramming of fibroblasts into cardiomyocytes using Gata4, Mef2c, and Tbx5. *Circ Res.* 2012;111:50-55.

Rajarajan K[†], Engels MC[†], Wu SM. Reprogramming of mouse, rat, pig, and human fibroblasts into iPS cells. *Curr Protoc Mol Biol.* 2012;Chapter 23:Unit 23.15.

[†]These authors contributed equally to this work.

Selected peer-reviewed abstracts

Engels MC, Askar SFA, Jangsangthong W, Neshati Z, Feola I, Ypey DL, Klautz RJM, SchaliJ MJ, De Vries AAF, Pijnappels DA. Heterocellular fusion of human ventricular scar cells with neonatal

rat cardiomyocytes ameliorates pro-arrhythmia through APD shortening and MDP lowering by enhanced outward potassium current. *Eur Heart J.* 2014;34:1045.

Engels MC, Rajarajan K, Feistritzer R, Sharma A, Nielsen UB, Schalij MJ, de Vries AA, Pijnappels DA, Wu SM. IGF promotes Cardiac Lineage Induction by Selective Expansion of Mesoderm in vitro. *Circulation.* 2013;128:A17539.

Engels MC, Rajarajan K, Feistritzer R, Sharma A, Nielsen UB, Schalij MJ, de Vries AA, Pijnappels DA, Wu SM. IGF promotes cardiac lineage induction by selective expansion of cardiogenic mesoderm in vitro. *Eur Heart J.* 2013;310,P5037.

Acknowledgements

Many people have contributed to this thesis in various ways and I would like to thank all of them. Prof. dr. Schalijs, dank voor uw onafgebroken steun vanaf het allereerste moment. Daniël, ik ben er heel erg trots op dat ik bij jou heb mogen werken. Dank je wel voor alles. Twan, jouw onuitputtelijke kennis en kunde, gekoppeld aan jouw gevoel voor humor hebben meer voor mij betekend dan je waarschijnlijk kan vermoeden. Dick, hartelijk dank voor jouw onbeperkte enthousiasme en jouw aanstekelijke liefde voor de wetenschap. Minka, dank je wel voor het altijd klaar staan om te helpen en voor jouw zorg voor de mensen in het lab. Cindy, samen hadden we de grootste lol. Dank voor jouw relativerend vermogen. Margreet, we hadden aan een half woord genoeg. Ik bewonder jouw moed en kracht.

I'd like to thank all my former co-workers from the lab: Annemarie, Jia, Iolanda, Yoke, Sasha (kid), Emile, Niels, Zeinab, Saïd, Brian, Masaya and Ivan. Rupa, I had a great time working together with you. Thank you for being such a good friend. Arti, ik kon altijd bij jou terecht voor raad en advies (en een kleine aanmoediging).

Sean, it all started in your lab, thank you for giving me the opportunity to come to the US and for introducing me to the world of science. Boston friends, especially Raja, Ahmed, Kenta, Anke, Arvind, Nick (India man!), Emil, Maxine, Dani, JW, Peter-Paul, Travis, Anthony, Silvia, Lei, Xiaolin, Wen-Pin, Markus, Marcus-André, Jenny, Lisa, thank you for everything. Stanford friends: Guang, Arun, Wen-Po, I enjoyed spending time in California with you guys.

Dank aan al mijn familie en vrienden in Nederland en op Curaçao. Pano Maria, Walter Palm, Diane Eikelboom, onze vriendschappen zijn mij bijzonder dierbaar.

Ramón en Ivonne, jullie hebben mij opgevangen als jullie eigen kind toen ik in Nederland aankwam. Jullie nemen een speciaal plekje in mijn leven in.

A special thank you to the Feistritzer family for making me feel right at home: Dick, Nancye, Scott, Mary Kate, Jenna, Tim, Sara, Andy, Jack and Addy, Porter, Smitty, Lucy and Banjo.

Charla en Ludo, jullie hebben het allemaal van dichtbij meegemaakt. Charla, ik hoop dat ik net zo'n grote steun voor jou kan zijn als jij voor mij bent.

Pap en mam, zonder jullie onvoorwaardelijke liefde en steun was dit allemaal niet mogelijk geweest.

Becca, I started my PhD thinking I would make a big discovery. I did. I can't wait to explore the future together.

Curriculum Vitae

Marc C. Engels was born on May 17th, 1984 in Willemstad, Curaçao where he attended the Peter Stuyvesant College and graduated as the overall Valedictorian of the former Netherlands Antilles. He moved to the Netherlands in 2002 and completed his propedeutical exam in Life Science & Technology *cum laude* before attending medical school at Leiden University. After graduating, he joined the laboratory of Dr. Sean M. Wu at the Cardiovascular Research Center of the Massachusetts General Hospital (Harvard University, Boston, MA, USA) and later at Stanford University (Palo Alto, CA, USA) as a visiting PhD student. During his time in the Wu lab, he focussed on cardiac differentiation of embryonic stem cells. He moved back to the Netherlands to continue his PhD training at the Laboratory of Experimental Cardiology at Leiden University Medical Center under supervision of Prof. Dr. Martin J. Schalij, Dr. Daniël A. Pijnappels and Dr. Antoine A.F. de Vries. At Leiden University, he worked on electrophysiological aspects of cell and gene therapy for heart disease. The results of this work are presented in this thesis. Marc will start with clinical training in July 2016 at the Emory University School of Medicine internal medicine residency program in Atlanta, GA, USA (program director: Dr. Lorenzo Di Francesco).

